

The Formation, Dissociation and Reactivity of Gaseous Ions

A thesis submitted for the degree of Doctor of Philosophy

by

Kevin Mark Douglas

Department of Chemistry,

University of London

2011



Declaration

I, Kevin Mark Douglas, confirm that the work presented in this thesis is my own. Where information has been derived from other sources, I confirm that this has been indicated in the thesis.

Signed,

Acknowledgements

It is with great pleasure that I am able to thank everyone who has helped me in the completion of my PhD. First and foremost, I would like to thank my supervisor Steve Price, for his continued support throughout my PhD and the writing of my thesis.

I am also especially grateful to the other members of the Price Group, in particular to Mike Parkes for the substantial help he has given, and to Jessica Lockyear and James Fletcher who have made my time at UCL so enjoyable. I would also like to thank all the technical staff in the workshops for their expertise and help.

Finally I would like to thank all my other friends, both at UCL (white and black Mike, Super V, José) and outside of it (Gwen Anderson, Drunk Sam, Lukey), for making the four years I have spent in London some of the best of my life.

Publications

Below is a list of publications resulting from work carried out during my PhD. In addition expected future publications of work presented in this thesis are also given.

Current Publications:

“Studies of the fragmentation of the monocation and dication of methanol”, K. M. Douglas, S. D. Price, *Journal of Chemical Physics*, **131**, 224305 (2009)

“Generation of the ArCF_2^{2+} Dication”, J. F. Lockyear, K. M. Douglas, S. D. Price, M. Karwowska, K. J. Figalkowski, W. Grochala, M. Remes, J. Roithova, D. Schroder, *Journal of Physical Chemistry Letters*, **1**, 358 (2010)

“Electron ionization of hydrogen sulphide”, K. M. Douglas, S. D. Price, *International Journal of Mass Spectrometry*, **303**, 147 (2011)

Future Publications:

“Electron ionization of trifluoriodomethane”, K. M. Douglas, M. A. Parkes, S. D. Price

Abstract

This thesis presents the results of a series of experiential investigations into the formation, dissociation and reactivity of gaseous ions. Firstly, using a time-of-flight mass spectrometer coupled with a 2D ion coincidence technique, studies of the electron ionization of a number of small gas-phase molecules are presented. Relative partial ionization cross-sections (PICS) are derived for the formation of positively charged fragment ions, following electron ionization of H_2S , CH_3OH and CF_3I . The 2D ion coincidence technique enables fragment ions formed by dissociative single, double, triple and quadruple ionization to be distinguished and quantified. This information also allows precursor specific relative PICS to be determined. While the relative PICS quantify the overall yield of each fragment ion, the precursor specific relative PICS quantify the contribution from single, double, triple and quadruple ionization to the relative yields of each fragment ion. Such information is essential for the accurate modelling, and the understanding, of the chemical processes occurring in energetic environments, such as industrial plasmas and planetary atmospheres. Comparison of the relative PICS data to existing measurements of the PICS for these molecules generally shows good agreement for experiments in which the efficient collection of translationally energetic ions is demonstrated. In addition, information on the energetics and dissociation dynamics involved in the fragmentation of H_2S^{2+} , $\text{CH}_3\text{OH}^{2+}$, CF_3I^{2+} and CF_3I^{3+} are provided by interpretation of ion pair peaks recorded in the 2D ion coincidence spectra.

Secondly, this thesis also presents the results of an investigation into the photoionization of CF_3I , using the threshold photoelectron-photoion-photoion coincidence (iPEPICO) endstation on the vacuum-ultraviolet beamline at the Swiss Light Source. These experiments were part of a scoping study to see if this existing apparatus could be used to study multiple ionization. The photoionization spectra are interpreted and discussed, and issues with the current experimental arrangement, which may be improved for future visits, are addressed.

Finally, studies of I^{2+} collisions with OCS , carried out using a crossed ion beam experiment with a time-of-flight mass spectrometer, are presented. Two bond-forming reactions producing IO^+ and IS^+ are observed, together with the more ubiquitous electron transfer reactions. These electron transfer reactions are rationalised using the Reaction Window model.

Table of Contents

List of Abbreviations.....	12
Table of Figures.....	14
Table of Tables.....	20
Chapter 1: Introduction.....	22
1.1 Background.....	22
1.2 Laboratory Techniques for Forming Positive Ions.....	24
1.2.1 Electron Ionization.....	24
1.2.2 Photoionization.....	27
1.2.3 Interactions with Positive Ions.....	29
1.3 Product Ions.....	30
1.3.1 Product Ions from Single Ionization.....	31
1.3.2 Properties of Multiply Charged Ions.....	35
1.4 Electron Ionization Cross-Sections.....	39
1.4.1 Total Ionization Cross-Sections.....	40
1.4.2 Partial Ionization Cross-Sections and Precursor Specific PICSs.....	41
1.4.3 Relative Partial Ionization Cross-Sections.....	42
1.5 Experimental Techniques for the Measurement of PICSs	43
1.5.1 Method 1: Individual Parameter Determination.....	43
1.5.2 Method 2: Normalization Method	44
1.6 Summary.....	46
1.7 References.....	46
Chapter 2: Experimental Details.....	51
2.1 Introduction.....	51
2.2 Time-of-Flight Mass Spectrometry.....	51
2.2.1 Two-Field Time-of-Flight Mass Spectrometry.....	52

2.2.2	Space Focusing.....	53
2.2.3	Energy Focusing.....	55
2.2.4	Ion Turn-Around Time.....	56
2.3	Experimental Setup.....	57
2.3.1	Source Region.....	58
2.3.2	Detection and Data Collection.....	60
2.3.3	Ion Discrimination Effects.....	60
2.4	Data Sets.....	62
2.4.1	Singles Spectrum.....	62
2.4.2	Pairs Spectrum.....	64
2.4.2.1	False Coincidences	66
2.4.2.2	Time-of-Flight Difference Plots	67
2.4.2.3	Dynamics and Energetics of Multiply Charged Ion Dissociation	68
2.4.3	Triples Spectrum.....	69
2.5	Conclusions.....	70
2.6	References.....	70
Chapter 3:	Data Collection and Analysis.....	72
3.1	Introduction.....	72
3.2	Spectral Intensities.....	72
3.2.1	Singles Mass Spectra.....	72
3.2.2	Pairs Mass Spectra.....	74
3.2.2.1	False Ion Coincidence Correction	75
3.2.2.2	Energetic Ion Pair Loss Correction	76
3.2.2.3	Correction for Dead-Time Losses	78
3.2.3	Triples Mass Spectra.....	79
3.2.3.1	False Triple Ion Coincidence Correction	79
3.3	Relative Partial Ionization Cross-Sections.....	80
3.3.1	Peak Intensities in the Singles, Pairs, and Triples Mass Spectra.....	80
3.3.2	Relative PICS Determination.....	83
3.3.3	Ion Detection Efficiency.....	84

3.3.4	Precursor-Specific Relative PICS Determination.....	85
3.3.5	Positive Ion-Negative Ion Pair Formation.....	87
3.4	Dissociation Dynamics of Multiply Charged Molecular Ions.....	88
3.4.1	Interpretation of Experimental Peak Slopes.....	88
3.4.2	Two-Body Dissociation Reactions.....	89
3.4.3	Three-Body Dissociation Reactions.....	90
3.4.3.1	Instantaneous Explosion	90
3.4.3.2	Deferred Charge Separation	90
3.4.3.3	Secondary Fragmentation	91
3.5	Kinetic Energy Release Determination.....	92
3.5.1	Monte Carlo Simulation.....	93
3.5.1.1	Apparatus and Ion Parameters	95
3.5.1.2	Simulation Parameters	95
3.6	References.....	96
Chapter 4:	Electron Ionization of Hydrogen Sulphide.....	98
4.1	Introduction.....	98
4.1.1	Dissociative Ionization of H ₂ S.....	98
4.2	Experimental Procedures.....	99
4.3	Data Analysis.....	100
4.3.1	Singles Mass Spectra.....	100
4.3.2	Pairs Spectra.....	101
4.3.3	Triples Spectra.....	103
4.4	Relative Partial Ionization Cross-Sections.....	103
4.4.1	Results.....	103
4.5	Discussion.....	105
4.5.1	Relative PICSs (σ_r).....	105
4.5.2	Precursor-Specific Relative PICSs (σ_n).....	107
4.5.3	Energetics and Dissociation of H ₂ S ²⁺	110
4.6	Conclusions.....	113
4.7	References.....	114

Chapter 5: Electron Ionization of Methanol.....	116
5.1 Introduction.....	116
5.1.1 Dissociative Ionization of Methanol.....	116
5.2 Experimental Procedure.....	118
5.3 Data Analysis.....	118
5.3.1 Singles Mass Spectra.....	118
5.3.2 Pairs Spectra.....	120
5.3.3 Computational Analysis.....	122
5.4 Relative Partial Ionization Cross-Sections.....	122
5.4.1 Results.....	122
5.5 Discussion.....	124
5.5.1 Relative PICSs (σ_r).....	124
5.5.2 Precursor-Specific Relative PICSs (σ_n).....	127
5.5.3 Energetics and Dissociation of $\text{CH}_3\text{OH}^{2+}$	129
5.6 Conclusions.....	133
5.7 References.....	134
Chapter 6: Electron Ionization of Trifluoroiodomethane... 137	137
6.1 Introduction.....	137
6.1.1 Dissociative Ionization of Trifluoroiodomethane.....	137
6.2 Experimental Procedure.....	138
6.3 Data Analysis.....	139
6.3.1 Singles Mass Spectra.....	139
6.3.2 Pairs Spectra.....	141
6.3.3 Triples Spectra.....	143
6.4 Relative Partial Ionization Cross-Sections.....	144
6.4.1 Results.....	144
6.5 Discussion.....	146
6.5.1 Relative PICSs (σ_r).....	146
6.5.2 Precursor-Specific Relative PICSs (σ_n).....	149
6.5.3 Energetics and Dissociation of CF_3I^{2+} and CF_3I^{3+}	154

6.6	Conclusion.....	156
6.7	References.....	157
Chapter 7:	An Investigation into the Value of Double Photoionization Studies at the SLS: Trifluoroiodomethane.....	159
7.1	Introduction.....	159
7.1.1	Dissociative Ionization of Trifluoroiodomethane.....	159
7.2	Experimental.....	160
7.2.1	Instrumentation.....	160
7.2.2	Conversion for Double Ionization Studies.....	162
7.2.3	Experimental Conditions.....	162
7.3	Data Analysis.....	163
7.3.1	Singles Mass Spectra.....	164
7.3.2	Pairs Spectra.....	165
7.3.3	Relative Ion Yield Determinations.....	168
7.3.4	Determination of Ion Detection Efficiency f_i	168
7.4	Results.....	170
7.4.1	RIYs and Precursor-Specific RIYs.....	170
7.5	Discussion.....	176
7.5.1	RIYs for the Formation of a Threshold Electron.....	176
7.5.2	Dissociation of CF_3I^{2+} and CF_3I^{3+}	177
7.6	Further Work.....	178
7.7	Conclusions.....	180
7.8	References.....	180
Chapter 8:	Reactions of I^{2+} with OCS.....	182
8.1	Introduction.....	182
8.1.1	Bimolecular Reactivity of Molecular Dications.....	182
8.1.1.1	Electron Transfer Reactions	183
8.1.1.2	Collision-Induced Fragmentation	186
8.1.1.3	Bimolecular Reactivity of Dications	187
8.2	Experimental.....	187

8.2.1	Instrumentation.....	187
8.2.2	Experimental Conditions.....	191
8.3	Data Analysis.....	191
8.3.1	Collision and Background Mass Spectra.....	191
8.3.2	Centre-of-Mass Frame.....	193
8.4	Results.....	193
8.5	Discussion.....	197
8.5.1	Single Electron Transfer Reactions.....	197
8.5.2	Double Electron Transfer Reaction.....	200
8.5.3	Bond-Forming Reactions.....	201
8.6	Conclusions.....	203
8.7	References.....	203
Chapter 9:	Conclusions and Future Work.....	206
9.1	References.....	210
Appendix A:	Time-of-Flight Mass Spectrometry.....	211
Appendix B:	Relative Partial Ionization Cross-Sections.....	216
Appendix C:	Relative Ion Yield Equations.....	231
Appendix D:	Relative Ion Yields.....	233

List of Abbreviations

2D	two-dimensional
CFD	constant fraction discriminator
COM	centre-of-mass
CS	charge separating
DCT	double charge transfer
DET	double electron transfer
DIE	double ionization energy
EELS	electron energy loss spectroscopy
FTMS	Fourier-transform mass spectrometry
FTOF	focusing time-of-flight
FWHM	full-width half-maximum
ICS	ionization cross-section
iPEPICO	imaging threshold photoelectron-photoion coincidence
KE	kinetic energy
KER	kinetic energy release
KERD	kinetic energy release distribution
LAB	laboratory
M/M	multistart-multistop
MCP	multichannel plate
MS	mass spectrometer
NCS	non charge separating
PEFCO	photoelectron-fluorescence coincidence
PEPECO	photoelectron-photoelectron coincidence
PEPICO	photoelectron-photoion coincidence

PEPIPICO	photoelectron-photoion-photoion coincidence
PES	photoelectron spectroscopy
PFC	perfluorinated compound
PICS	partial ionization cross section
PSD	position sensitive detector
QET	quasiequilibrium theory
QMS	quadrupole mass spectrometer
RF	radio frequency
RII	relative ion intensity
RIY	relative ion yield
RP	repeller plate
RRKM	Rice, Ramsperger, Kasses and Marcus
SET	single electron transfer
SLS	Swill Light Source
TDC	time-to-digital converter
TICS	total ionization cross-section
TOF	time-of-flight
TOFMS	time-of-flight mass spectrometer
TOF-PEPECO	time-of-flight photoelectron-photoelectron coincidence
TOF-PEPICO	time-of-flight photoelectron-photoion coincidence
TPES	threshold photoelectron spectroscopy
VMI	velocity map imaging
VUV	vacuum ultraviolet
Δ TOF	time-of-flight difference

Table of Figures

Chapter 1: Introduction

- Figure 1.1: Schematic potential energy curves for the single ionization of the molecule AB. Process (a) represents a vertical transition from the ground electronic state of the neutral to a bound region of a cationic potential curve, while process (b) represents a vertical transition to a cationic potential energy curve at an energy above the dissociation asymptote, and hence dissociates to form a singly charged fragment ion and a neutral. Recreated from Ref. [59]. 32
- Figure 1.2: A schematic diagram showing how predissociation *via* curve crossing to dissociative potentials provides a common dissociation mechanism. Recreated from Ref. [65]. 34
- Figure 1.3: Schematic potential energy curve for a diatomic YZ^{2+} . Many dication electronic states are purely dissociative (state B), whereas some small molecular dications may possess metastable states which exhibit potential energy minima (states A and X). Recreated from Ref. [67]. 36
- Figure 1.4: Prototypical potential energy curves for a diatomic dication from an adiabatic (black lines, foreground) and non-adiabatic (grey lines, background) perspective. If the lowest energy dissociation asymptote lies above the bound minimum (a) the molecular dication is thermodynamically stable; however if the asymptote lies below the barrier but is separated by a barrier (b) the dication is metastable; if there is no barrier to dissociation (c) the dication is kinetically and thermodynamically unstable. Recreated from Ref. [74]. 37
- Figure 1.5: A schematic diagram of an electron ionization experiment. 40
- Figure 1.6: A schematic diagram of the Condenser-Plate apparatus used by Smith and co-workers,⁷⁰⁻⁸⁰ and similar to the apparatus used by Rapp *et. al.*^{4,5} for the determination of total (gross) ionization cross-sections. 41
- Figure 1.7: A schematic diagram of the experimental apparatus used by Straub and co-workers.^{19,88-92} 44
- Figure 1.8: A schematic diagram of the experimental apparatus used by Tian and Vidal.^{8,94,95} 45
The main components of the apparatus are labelled on the diagram as follows: FL = Filament, FC = Faraday cup, BP = Backing plate, XD/YD = x-deflector and y-deflector, FT = Flight tubes, 1 & 2, IL = Ion lens, MCP = Multichannel plate.

Chapter 2: Experimental Details

- Figure 2.1: Schematic diagram of the two-field TOFMS used in Chapters 4 – 6 (not to scale). 52
- Figure 2.2: Diagram showing the ‘turn-around’ time of an ion formed with an initial velocity directed away from the detector. 55
- Figure 2.3: A schematic diagram of the TOFMS used in Chapters 4 – 6 of this thesis. 57

Figure 2.4:	A schematic diagram of the electron gun, showing typical operating voltages and approximate dimensions.	59
Figure 2.5:	A summary of the pulse sequencing and timing used for the TOFMS.	59
Figure 2.6:	A schematic diagram showing the collection of translationally energetic ions at the detector.	62
Figure 2.7:	A singles mass spectrum of hydrogen sulphide (H ₂ S) recorded following electron ionization at 200 eV.	63
Figure 2.8:	A probability tree indicating the various ionization channels that contribution to the ion singles and 2D ion coincidence spectra recorded by the experiment. The ion detection efficiency of the apparatus is denoted by f_i .	65
Figure 2.9:	A section of the pairs mass spectrum of CF ₃ I formed following electron ionization at 200 eV, showing the ion pairs CF ⁺ + F ⁺ , F ⁺ + F ⁺ and F ⁺ + C ⁺ , together with a (small) false coincidence ion pair CF ⁺ + C ⁺ .	66
Figure 2.10:	A Δ TOF plot for I ⁺ + CF ₂ ⁺ ion pairs formed <i>via</i> dissociative double ionization of CF ₃ I, at 200 eV electron energy. The flat-topped distribution is indicative of a single-valued momentum release upon ion pair formation, isotropically distributed over all laboratory angles.	68
Figure 2.11:	A representative one-dimensional triples mass spectrum (left) of CF ₃ I recorded following electron ionization at 200 eV, together with the coincident pairs spectrum in which all ion pairs are also in coincidence with a F ⁺ ion.	69

Chapter 3: Data Collection and Analysis

Figure 3.1:	A diagram showing a typical measurement of the background count level in the singles mass spectrum of CH ₃ OH recorded at 200 eV.	93
Figure 3.2:	Representative ion pair peaks observed following electron ionization of CF ₃ I recorded at 200 eV, showing the ‘true’ I ⁺ + CF ₂ ⁺ ion pair peak, and the false coincidence CF ₃ I ⁺ + CF ₂ ⁺ peak.	75
Figure 3.3:	A diagram showing the collection of energetic ions at the detector. Ion pairs formed with a translational energy component of greater than 10.7 eV perpendicular to the TOF axis (top) results in the loss of ion pair counts in the centre of the Δ TOF plot.	77
Figure 3.4:	A Δ TOF plot for the I ²⁺ + F ⁺ XXX ion pairs formed <i>via</i> dissociative triple ionization of CF ₃ I, at 200 eV electron energy. The ‘hollowed’ centre of the peak indicates energetic ion losses, which can be corrected using an appropriate geometric construction.	77
Figure 3.5	A Δ TOF plot for the F ⁺ + F ⁺ ion pair formed following electron ionization of CF ₃ I at 200 eV. The dead-time losses are estimated by extrapolating the peak height to the $t_1 - t_2 = 0$ limit.	78
Figure 3.6:	Schematic potential energy curves showing the relationship between the asymptotic energy of the dissociation limit, the KER, and the energy of the dication precursor state giving rise to the ion pair. Adapted from Ref. [20].	92

Figure 3.7: A Δ TOF plot for the $I^+ + CF^+$ ion pair recorded in the pairs spectrum of CF_3I at 50 eV, compared to a Monte Carlo simulation of the reaction in the TOF mass spectrometer. Good agreement is observed between the simulation and the experimental data. 94

Chapter 4: Electron Ionization of Hydrogen Sulphide

Figure 4.1: A typical singles mass spectrum of H_2S following electron ionization at 200 eV 100

Figure 4.2: Representative pairs spectrum of H_2S at 200 eV showing; a) $HS^+ + H^+$, $S^+ + H^+$ and $S^+ + H_2^+$, b) $H^+ + H^+$ and c) the very weak $SH^{2+} + H^+$ and $S^{2+} + H^+$ ion pairs. 102

Figure 4.3: Relative PICSSs $\sigma_r[X^{m+}]$ for forming (a) H^+ following electron ionization of H_2S , relative to the summed cross-sections for forming the group of ions H_nS^+ , (b) S^+ (\blacktriangle), HS^+ (\blacksquare), and H^+ (\blacktriangledown), (c) H_2^+ (\blacktriangle), H_2S^{2+} (\blacksquare) and (d) S^{2+} (\blacktriangle) and H_2S^{2+} (\blacksquare) following electron ionization of H_2S relative to the cross-section for forming the parent ion H_2S^+ . Where available the corresponding relative PICSSs from the data of Lindsay *et al.*⁸ (graph (a)) and Rao *et al.*⁷ (graphs (b), (c) and (d)) are also shown as open symbols. The representative error bars show two standard deviations of four separate determinations. 106

Figure 4.4: Precursor-specific relative PICSSs for forming (a) H^+ , (b) H_2^+ , (c) S^{2+} , (d) HS^{2+} , (e) S^+ and (f) HS^+ fragment ions via single (\blacksquare), double (\blacktriangle) and triple (\circ) ionization, following electron ionization of H_2S , relative to the cross-section for forming the parent ion H_2S^+ . The representative error bars shows two standard deviations of four separate determinations, except for $\sigma_3[S^+]$ (panel (e), (\circ)), for which only one standard deviation is given 108

Figure 4.5: Contribution to the total ion yield from single, double and triple ionization, following electron ionization of H_2S . 109

Figure 4.6: Relative PICSSs $\sigma_r[X^+ + Y^{m+}]$ for forming ion pairs following electron ionization of H_2S . 110

Chapter 5: Electron Ionization of Methanol

Figure 5.1: Typical mass spectrum (singles spectrum) of methanol following ionization by 200 eV electrons. 119

Figure 5.2: Representative pairs spectrum of methanol recorded at an electron energy of 200 eV. 120

Figure 5.3: Relative PICSSs $\sigma_r[X^{m+}]$ for forming (a) CH_3O^+ (\blacktriangle), CHO^+ (\blacksquare), CH_3^+ (\blacktriangleright) and H^+ (\blacklozenge), (b) CH_2^+ (\blacktriangle), CH_2O^+ (\blacksquare) and CO^+ (\blacktriangledown), (c) CH^+ (\blacktriangledown), C^+ (\blacksquare) and H_2^+ (\blacktriangle) and (d) OH^+ (\blacktriangledown), O^+ (\times), OH_2^+ (\blacktriangleright), H_3^+ (\blackstar) and CH_3O^{2+} (\blacktriangle), following electron ionization of methanol. Where available the corresponding relative PICSSs from the data of Srivastava *et al.*¹¹ are also shown as open symbols. The error bars expressed in this figure represent two standard deviations of three separate determinations. 125

- Figure 5.4: Relative PICSs $\sigma_r[X^+]$ for forming $CH_n^+ + H_nO^+$ (■), H_2^+ (●) and H^+ (▲) 126 following electron ionization of methanol, relative to the summed cross-sections for forming the group of ions CH_nO^+ . Similar PICSs extracted from the data of Rejoub *et al.*¹² (open shapes) are also shown. The representative error bars expressed in this figure represent two standard deviations of three separate determinations.
- Figure 5.5: Precursor-specific relative PICSs for forming (a) CH_3O^+ (■) and CHO^+ (▲), (b) 128 CH_3^+ (■) and H^+ (▲), (c) CH_2O^+ (■) and CO^+ (▲), (d) CH_2^+ (■) and CH^+ (▲), (e) OH^+ (■) and C^+ (▲), (f) H_2^+ (■) and O^+ (▲) (g) OH_2^+ (■) and (h) H_3^+ (■) monocation fragments via single (closed shapes) and double (open shapes) ionization, following electron ionization of methanol. The representative error bars show two standard deviations of three determinations.
- Figure 5.6: Contributions to the total ion yield from single and double ionization following 129 electron ionization of methanol.

Chapter 6: Electron Ionization of Trifluoroiodomethane

- Figure 6.1: A typical singles mass spectrum of trifluoroiodomethane following electron 140 ionization at 200eV showing: a) the full mass spectrum, b) close up (x 100) of mass range $m/z = 0 - 92$.
- Figure 6.2: Representative pairs spectrum of CF_3I showing the major ion pair channels, 142 recorded at an ionizing electron energy of 200 eV
- Figure 6.3: Relative PICSs $\sigma_r[X^{m+}]$ for forming (a) I^+ (■) and CF_3^+ (▲), (b) CF_2I^+ (●) and 148 CF^+ (▼), (c) F^+ (■), C^+ (▲), CF_2^+ (●) and I^{2+} (▼), (d) CI^+ (■), FI^+ (▲), CF_2I^{2+} (●) and CFI^+ (▼), (e) CF_2^{2+} (■), FI^{2+} (✱), CF^{2+} (●) and F_2^+ (×) and (f) F^{2+} (■), C^{2+} (✱), CFI^{2+} (▲) and I^{3+} (×) following electron ionization of CF_3I relative to the cross-section for forming the parent ion CF_3I^+ . Where available the corresponding relative PICSs from the data of Jiao *et al.*⁷ (graph (a), (b) and (c)) are also shown as open symbols. The representative error bars show one or two standard deviations of four separate determinations (see Table B.7).
- Figure 6.4: Precursor-specific relative PICSs for forming (a) C^+ , (b) F^+ , (c) CF^+ , (d) F_2^+ , (e) 153 CF_2^+ , (f) CF_3^+ , (g) I^+ , (h) CI^+ , (i) FI^+ , (j) CFI^+ , (k) CF_2I^+ , (l) C^{2+} , (m) F^{2+} , (n) CF^{2+} , (o) CF_2^{2+} , (p) I^{2+} , (q) FI^{2+} and (r) I^{3+} fragments via single (■), double (▲), triple (●) and quadruple (▼) ionization, following electron ionization of CF_3I , relative to the cross-section for forming the parent ion CF_3I^+ . Closed symbols relate to the left axis, open symbols to the right. The representative error bars show one or two standard deviations (see Tables B.8 and B.9) of four separate determinations.
- Figure 6.5: Contribution to the total ion yield from dissociative single, double, triple and 154 quadruple ionization, following electron ionization of CF_3I

Chapter 7: An Investigation into the Value of Double Photoionization Studies at the SLS: Trifluoroiodomethane

- Figure 7.1: Beamline layout (not to scale) with bend magnet (BM), vertical and horizontal slits (Sv, Sh), X-ray blocker (XB), collimating mirror (M1), grating (G), refocusing mirror (M2), flip mirror (M3), gas filter (GF), exit slit (Se), and endstations 1 and 2 (E1, E2). Reproduced from Ref. [14]. 161
- Figure 7.2: Schematic of the iPEPICO endstation, showing the interaction region where the VUV beam enters, and the two drift tubes, one for threshold photoelectrons (tPE) and one for ions. Reproduced from Ref. [15]. 162
- Figure 7.3: Singles mass spectrum of trifluoroiodomethane showing the major ion fragments and the parent ion formed following photoionization at 37 eV. 165
- Figure 7.4: A close up of the CF_2^+ fragment ion peak in the singles spectra at 37 eV photon energy showing: (a) the “hollowing out” of the peak, (b) the inner (yellow) peak resulting from ions from NCS dissociative ionization $I_{\text{NCS}}[\text{CF}_2^+]$ and the outer (light blue) peaks resulting from ions from CS dissociative ionization, and (c) the energetic ion loss correction to the outer peaks (green) yielding $I_{\text{CS}}[\text{CF}_2^+]$. The total counts of CF_2^+ in the singles spectra $I_{\text{n}}[\text{CF}_2^+]$ is given by the sum of $I_{\text{NCS}}[\text{CF}_2^+] + I_{\text{CS}}[\text{CF}_2^+]$. 165
- Figure 7.5: Raw pairs spectrum of CF_3I recorded at a photon energy of 37 eV, showing : (a) the full pairs spectra, in which the major ion pairs can be seen, and (b) a close up of the $\text{I}^+ + \text{CF}^+$ ion pair, in which the hollowing of the pairs peak can be observed. 167
- Figure 7.6: Relative ion yields $\text{RIY}[X^{m+}]$ for forming (a) I^+ (■) and I^{2+} (▲), (b) CF^+ (■), CF_3^+ (▲) and CF_2^+ (●), (c) C^+ (■), F^+ (▲) and CF_2I^+ (●), (d) CI^+ (■) and CF_2I^{2+} (▲) and (e) FI^+ (■), FI^{2+} (▲), CF_2I^+ (●) and CF_2i^{2+} (▼) following photoionization of CF_3I in which a threshold electron is formed, relative to the cross-section for forming the parent ion CF_3I^+ . 171
- Figure 7.7: Precursor-specific relative ion yields $\text{RIY}_{\text{n}}[X^{m+}]$ for forming (a) C^+ , (b) F^+ , (c) CF^+ , (d) CF_2^+ , (e) CF_3^+ , (f) I^+ , (g) CI^+ , (h) CF_2I^+ and (i) I^{2+} ion fragments via single (■), double (▲) and triple (●) ionization, following photoionization of CF_3I in which a threshold electron is formed, relative to the ion yield for forming the parent ion CF_3I^+ . Closed symbols relate to the left axis, open symbols right. 173
- Figure 7.8: Contribution to the total ion yield from dissociative single, double and triple ionization, following photoionization of CF_3I 175

Chapter 8: Reactions of I^{2+} with OCS

- Figure 8.1: Diagram showing the interrelationship between species separation r and asymptotic exothermicity ΔH for SET reactions between a dication and a neutral species. The reaction window is a qualitative region for which SET is most efficient. Only interspections inside the reaction window have a significant probability of resulting in SET (i.e. ΔH_2), typically between 2 – 6 eV. Reproduced from Ref. [12]. 184

Figure 8.2:	Schematic potential energy curves for a direct DET reaction between M^{2+} and AB, showing the concerted (a) and sequential (b) pathways. (a) ΔH_a indicates the small reaction enthalpy which is required for the curve crossing to lie in the reaction window, for the concerted mechanism. (b) ΔH_1 and ΔH_2 schematically indicate the limiting reaction exothermicities for which this pair of curve crossings will lie in the reaction window, a markedly larger range of exothermicities than for the concerted mechanism illustrated in (a). Reproduced from Ref. [13].	186
Figure 8.3:	Schematic diagram of the crossed-beam time-of-flight mass spectrometer experimental apparatus. Reproduced from Ref. [20].	189
Figure 8.4:	Schematic layout of the time-of-flight mass spectrometer.	190
Figure 8.5:	A typical collision spectrum (black line) with the collision gas on and a background spectrum (red line) with the collision gas off, for the $I^{2+} + OCS$ collision system.	192
Figure 8.6:	Representative collision (black line) and background (red line) spectra for the $I^{2+} + OCS$ collision system, showing mass to charge ratio ranges of (a) 20 – 46, (b) 50 – 70 and (c) 120 – 170.	195
Figure 8.7:	Product ratios R_{OBS} for product ions observed following $I^{2+} + OCS$ collisions. Error bars show one standard deviation of four separate determinations.	197
Figure 8.8:	Composite energy level diagram for $I^{2+} + OCS$, indicating possible SET reactions. Shaded areas indicate the approximate position of the Reaction Window.	199
Figure 8.9:	Composite energy level diagram for $I^{2+} + OCS$, indicating possible DET reactions. Shaded areas indicate the approximate position of the Reaction Window.	201
Figure 8.10:	Schematic potentials showing the route from $X^{2+} + YZ$ to $XY^+ + Z^+$. The reactants must avoid switching potential surfaces at point A and switch potential surfaces at B. Reproduced from Ref. [20].	202

Table of Tables

Chapter 2: Experimental Details

Table 2.1:	Typical operating parameters for the TOFMS used in Chapters 4 – 6 of this thesis.	58
------------	---	----

Chapter 3: Data Collection and Analysis

Table 3.1:	Absolute PICS values of Bruce and Bonham for the formation of single ions ⁹ and ion pair ¹⁰ following electron ionization of CF ₄ . All values have units Å ² . Note that the two data sets were recorded separately, and that the single ion cross-section data contains contributions from both single ions and ion pairs.	84
Table 3.2:	Typical values of parameters used in Monte Carlo simulations	95
Table 3.3:	Typical values of parameters used in Monte Carlo simulations	96

Chapter 4: Electron Ionization of Hydrogen Sulphide

Table 4.1:	Kinetic energy releases (KERs, uncertainty ± 0.6 eV unless stated), and corresponding precursor state energies P , for selected dissociation reactions of H ₂ S ²⁺ . The weightings of the KERs are listed, together with an average KER to facilitate a direct comparison with literature. The electron energy of the spectral data used to determine the KERs are also given. The energies of the dissociation asymptotes, relative to the ground state of H ₂ S, involved in the determination of P are listed. Unless indicated, such asymptotes correspond to the formation of ground state products.	112
------------	---	-----

Chapter 5: Electron Ionization of Methanol

Table 5.1:	Ion pairs observed in the pairs spectrum recorded following electron ionization of methanol at 200 eV ionizing electron energy.	121
Table 5.2:	Kinetic energy releases (KERs) for two-body fragmentations following double ionization of methanol. Where available literature values are also given, along with the calculated precursor state energies E of the methanol dication. The weightings of the KERs are listed, together with an average KER to facilitate a direct comparison with the literature. ^a Values are taken from ref. [15]. ^b Values are taken from ref. [16].	130
Table 5.3:	Kinetic energy releases (KERs) for three- or four-body break ups following double ionization of methanol. Where available literature values are also given, along with the calculated precursor state energies of the methanol dication E . The experimental peak gradient is given, together with the peak gradient calculated using the given dissociation pathway. See text and Error! Reference source not found. for details. ^a Values are taken from ref. [15]. ^b Values are taken from ref. [16].	131

Chapter 6: Electron Ionization of Trifluoroiodomethane

Table 6.1:	Ion pairs observed in the pairs spectrum recorded following electron ionization of CF_3I at 200 eV ionizing electron energy.	143
Table 6.2:	Ion triples observed in the pairs spectrum recorded following electron ionization of CF_3I at 200 eV ionizing electron energy.	144
Table 6.3:	Kinetic energy releases and corresponding precursor state energies P , for selected dissociation reactions of CF_3I^{m+} . The energies of the dissociation asymptotes, relative to the ground state of CF_3I , involved in the determination of P are listed. These asymptotes correspond to the formation of ground state products. Because of the possibility of forming $X^3\text{P}^0 \text{I}^+$ in three spin-orbit states ($J = 2, 1, 0$), the average energy of these three states was used as the ground state energy of I^+ .	155

Chapter 7: Electron Ionization of Trifluoroiodomethane

Table 7.1:	Ion pairs observed in the pairs spectrum recorded following photoionization of CF_3I at 37 eV ionizing photon energy.	166
Table 7.2:	Ion detection efficiencies obtained for fragment ions at 37 eV photon energy. Errors calculated by taking the counting error in each ion peak used and carrying through. Average error taken as twice the standard deviation of the individual determinations	170

Chapter 8: Reactions of I^{2+} with OCS

Table 8.1:	Experimental parameters employed under normal operating conditions.	190
Table 8.2	Product ratios R_{II}^{OBS} for product ions observed following $\text{I}^{2+} + \text{OCS}$ collisions. The values in parenthesis indicate one standard deviation in the last figure.	196

Chapter 1 Introduction

1.1 Background

This thesis presents the results of experimental investigations on the electron ionization of a number of small molecules. The electron ionisation of molecules occurs within many environments including plasmas¹⁻⁴ and planetary atmospheres.^{2,3} In these highly energised media, collisions between ionizing electrons and neutral molecules may result in the formation of a variety of positively charged species. These species may be formed *via* dissociative and non-dissociative ionization processes, involving both single and multiple ionization. Thus, the accurate modelling of these environments requires reliable and accurate information on the formation efficiency of the parent and any fragment ions that may be formed. Such information is usually presented in the form of partial ionization cross-sections (PICSs).⁴

Partial ionization cross-sections are important as they provide information on the identity and abundance of the different charged species formed in ionizing electron-molecule collisions. In order to identify the products formed following electron ionization events, a mass spectrometric experiment is required. In using a mass spectrometer to produce accurate and reliable PICS measurements, the apparatus must be able to detect all positive ions with the same efficiency, regardless of their mass or initial kinetic energy. This can be particularly problematic when it comes to energetic ions, such as those formed from dissociative multiple ionization events. Indeed, as highlighted in a number of recent reviews, the main technical difficulty in measuring accurate PICSs is caused by the initial kinetic energy of ions formed by dissociative ionization processes.⁵⁻⁷ It has therefore been widely recognised that the reliability of some earlier PICS determinations is questionable,^{6,8} such as those involving quadrupole mass spectrometers or magnetic sector instruments that do not ensure the complete collection of ions formed with considerable kinetic energies. Indeed, the contribution to the total ion yield from multiple ionization was then thought to be of little importance and was thus often ignored.⁴ Recent studies of the electron ionization cross-sections of small molecules have shown that dissociative multiple ionization can contribute significantly to the fragment ion yields.⁹⁻¹⁸ Appreciation of the shortcomings of available PICS data has therefore prompted the development of new experimental techniques for the accurate determination of PICSs, for which complete collection of

energetic fragment ions can be demonstrated.^{8,19} However, despite this renewed interest, there still remains significant gaps in the availability of accurate electron ionization cross-sections, even for small molecules, and even where PICS data sets are available, the agreement between data sets often varies.

With the continued growth in the semiconductor industry and related industries, the demand for accurate electron ionization cross-sections for a large variety of gases used in the feed gas mixtures for plasma etching applications continues to increase. Indeed, a recent report from the National Research Council addressing the ‘Database Needs for Modeling and Simulation of Plasma Processing’²⁰ highlights the lack of reliable PICS data for many small molecules. It is the lack of reliable and available PICS data for the ionization of many molecules relevant to industrial plasmas and planetary atmospheres that provide the clear motivation for the electron ionization investigations discussed in this thesis.

In this thesis, time-of-flight mass spectrometry coupled with a 2D ion coincidence technique is used to investigate the electron ionization of H₂S, CH₃OH and CF₃I, in the ionizing energy range 30 – 200 eV. This experimental technique enables fragment ions formed *via* dissociative single, double, triple, and quadruple ionization processes to be detected, identified and quantified, and hence provides detailed information on the various ionization processes that take place following electron-molecule interactions. The key aspects of the apparatus design, experimental setup, and data sets produced are described in Chapter 2. The procedures used to analyse the experimental data and derive relative PICSs and precursor-specific relative PICSs are described in Chapter 3. Also presented in Chapter 3 is a description of the methods used for analysing the peaks produced from the 2D ion coincidence data, to derive information concerning the dynamics and energetics involved in the charge-separating dissociations of small molecular dications. Chapters 4 – 6 of this thesis present the results of the experimental work, and a discussion of the results for each target molecule.

In the final two chapters of this thesis the results of an investigation into the photoionization of CF₃I (Chapter 7) and the reactions between I²⁺ and OCS (Chapter 8) are discussed. The photoionization study was carried out using the threshold photoelectron-photoion-photoion coincidence (iPEPICO) endstation on the vacuum-ultraviolet beamline at the Swiss Light Source. The photoionization spectra obtained from this experiment are interpreted and discussed, and issues in the current

experimental setup which may be improved for future visits addressed. For the study of I^{2+} collisions with OCS, a crossed ion beam experiment with a time-of-flight mass spectrometer was employed. The reactions following these collisions are presented, including the observation of two bond-forming reactions producing IO^+ and IS^+ . More ubiquitous single electron transfer reactions are also observed, and rationalised using the Reaction Window model.²¹⁻²³

1.2 Laboratory Techniques for Forming Positive Ions

In order to form a positively charged ion, sufficient energy must be transferred to a neutral atom or molecule for it to eject an electron. The minimum energy required for this process is termed the ionization energy. There are many processes used in the formation of positively charged ions, including:



In this thesis, both electron and photo-ionization processes are employed in the formation of positively charged species. In the following sections, the ionization processes listed above are discussed in further detail.

1.2.1 Electron Ionization

Electron ionization generally involves the formation of ions following inelastic collisions between electrons and neutral gas species. The electrons are usually formed *via* thermionic emission from a filament, with subsequent acceleration and focusing by electric fields to produce a collimated beam. Electron beams of any desired energy and

varying current can therefore be easily generated, by modification of the applied electric fields and the filament current. For this reason electron ionization is a widely used technique in experiments to investigate the formation of positively charged ions.^{5,8,24,25}

If the energy of the electron beam is greater than the ionization energy of the target molecule (or atom), some of the target species will be ionized. However, as there is no restriction on the proportion of energy an electron may transfer to a target molecule during a collision, not all collisions may result in the formation of an ion. The majority of ions formed by electron ionization are singly charged, and generally include both parent ions (Equation 1.2a) and fragment ions (Equation 1.2b):⁴



The ionization of target molecules at electron energies close to their ionization threshold proceeds predominately *via* direct ionization processes, where the ejected electron and the scattered electron leave the target molecule within 10^{-16} s of one another.⁴ Direct ionization is a non-resonant process because the ejected electron is released into a continuum and therefore can accommodate any excess kinetic energy. The relationship between the cross-section σ_{ion} for forming an ion *via* single ionization, to the amount of energy by which a system exceeds the ionization energy E , is given by the Wannier law:²⁶

$$\sigma_{ion} \propto E^{1.127} \quad (1.3)$$

As the Wannier law is a threshold law, it only applies to energies just above the ionization threshold, when E is small.²⁷

As the ionizing electron energy is increased above the single ionization threshold, multiply charged ions may also be formed by multiple electron ionization:



where $m \geq 2$. Wannier also considered the multiple ionization process shown in Equation 1.4, predicting that in the absence of long range correlations between the outgoing electrons, the ionization cross-section should increase as the m^{th} power of the excess energy E .²⁸ Therefore, the ionization cross-section for double ionization

increases approximately proportional to E^2 . Although this energy dependence may be true for energies just above the double ionization threshold, at higher ionizing electron energies direct ionization processes are not the main means of multiple ionization.^{29,30}

In addition to the direct ionization process described above, electron-molecule collisions can also result in indirect ionization, where the scattered electron and the ejected electron leave the molecule sequentially on a much longer timescale than 10^{-16} s. The indirect process is called autoionization.^{4,31} Autoionization occurs when, following an electron-molecule collision, the molecule is excited to a ‘super-excited’ neutral electronic state, AB^* , involving the promotion of one or a number of electrons to high-lying orbitals. These ‘super-excited’ states can decay in a number of ways, such as predissociation to form a pair of neutral fragments, fluorescence to a lower neutral electronic state, or by autoionization (Equation 1.5).



Autoionization occurs when the excess electronic energy is converted into the kinetic energy of an electron occupying a high-lying orbital. This process usually involves two electrons, where one falls into an orbital hole formed by the initial excitation of a non-valence electron, and the other is ejected from the molecule. Thus autoionization is a resonance process, as the energy transferred to the molecule by the electron (or other means of excitation) must match the energy of a transition involving the excitation of the non-valence electron.

At electron energies significantly in excess of threshold, ionization cross-sections are seen to drop off. This is a common trait of all electron-molecule interactions, in that the efficiency of the transfer of energy from the electron to the molecule decreases as the electron energy is increased. This drop in efficiency is due to the fact that higher energy electrons are moving faster. As the energy is increased, there reaches a point at which the electron is moving so fast it does not interact with the species at all and the cross-section, in principle, falls to zero.

In our experiments, as well as electron molecule interactions resulting in the formation of positive ions, so called ‘polar dissociation’ may take place. In polar dissociation positive ions are formed as part of a pair with accompanying negative ions (Equation 1.1g). Formation of positive ion-negative ion pairs can either be direct, or

proceed *via* the initial formation of an anion by the electron capture of a neutral molecule, which then dissociates forming a positive and a negative ion fragment and an outgoing electron. For this reason, positive ion-negative ion pair formation often competes with dissociative recombination (DR) processes,^{32,33} in which a molecule combines with an electron to form an anion, which then dissociates to form a neutral and an anionic fragment. As is the case with the other electron-molecule interactions described above, the efficiency of positive ion-negative ion pair formation as a function of electron energy initially rises to a maximum and then drops off. However, even at electron energies at which the efficiency of positive ion-negative ion pair formation is at a maximum, cross-sections for such processes are typically several orders of magnitude smaller than the corresponding cross-sections for positive ion formation.^{1,32-34}

1.2.2 Photoionization

Photoionization is a process in which a target gas is ionized following the absorption of a photon:



The photons are generally produced by a discharge lamp, a laser, or a synchrotron radiation source.^{29,35} In recent decades, improving laser technology, and the increased availability of synchrotron radiation sources providing either a pulsed or continuous source of ionizing photons of variable and high energy, means that photoionization is now a widely used method for the generation of positive ions. One of the advantages of photoionization is that as the energy of incident photon is, in principle, known, the energy transfer to the target molecule upon ionization is also known.³⁵

The absorption of a photon below the ionization threshold is a resonant process, generally involving the transition of an electron from one electronic state to another. These transitions are governed by selection rules, which arise due to the requirements of conservation of quantum variables such as angular momentum, spin and parity.³⁶ However, direct photoionization is a non-resonant process as the outgoing electron is released into the continuum and can accommodate any excess energy. There are also no strict selection rules governing photoionization, as the outgoing photoelectron may take on any value of angular momentum l in order to satisfy the conservation law:

$$\Delta l = \pm 1 \quad (1.7)$$

It is therefore possible to determine the nature of the orbital from which an electron is removed, by studying the angular distribution of the photoelectrons; such information can be provided by photoelectron imaging techniques.³⁷⁻⁴¹

In 1948, Wigner⁴² discussed the behaviour of photoionization cross-sections near threshold. Wigner stated that for a photoionization process, such as that shown in Equation 1.6, the ionization cross-section (σ) varies as the m^{th} power of the energy E by which the system exceeds the ionization energy E :⁴²

$$\sigma \propto E^m \quad (1.8)$$

The Wigner equation (Equation 1.8) is only applicable to direct photoionization processes near threshold, and when long range interactions between outgoing electrons are ignored. Of course, indirect photoionization processes may also contribute to the photoionization cross-section, particularly at photon energies high above the ionization threshold.^{43,44}

As mentioned above, one advantage of photoionization over electron ionization is that as in most cases the energy of the incident photon is known, then the energy transfer to the target molecule upon ionization is also known.³⁵ Thus, if the energy of the ejected photoelectron(s) is measured accurately, it is possible to define exactly the state of the molecular ion that is populated by the ionization event; this forms the basis of photoelectron spectroscopy (PES).³¹ It is also possible to examine the state-selective fragmentation dynamics of positive ions formed by photoionization, by detecting ions in coincidence with the energy analysed photoelectrons.⁴⁵ In the last few decades, a range of these electron-ion coincidence techniques have been developed and employed to study photoionization processes. One such technique, the photoelectron-photoelectron coincidence (PEPECO) technique, has shown that the double photoionization of many small molecules is an indirect process.²⁹ The indirect process proceeds with the initial formation of a ‘super-excited’ singly charged ion, which then autoionizes to the doubly charged final product. This means that doubly charged ions can also be formed outside the Frank-Condon zone due to the two-step nature of the transition.²⁹ Another variation of these coincidence techniques is where an energy analysed electron is detected in coincidence with a fluorescence photon (PEFCO); this technique can be used to determine whether an excited state of a molecular ion decays *via* a radiative process.⁴⁶

1.2.3 Interactions with Positive Ions

The energy required to ionize a target species may also be provided by collisions with positively charged ions. There are many ionization techniques that employ this method of ionization, including chemical ionization, double charge transfer^{47,48} (DCT) and charge-stripping^{49,50} (Equations 1.1d – 1.1f respectively).

Chemical ionization is the result of the reaction between target gas molecules and reagent ions.⁵¹ The reagent ions are generally formed from a reagent gas by electron ionization and subsequent ion-molecule collisions. Commonly used reagent gases include methane and hydrogen,⁵² which form the reagent ions CH_5^+ and H_3^+ respectively:



In order to achieve a high efficiency in the formation of the reagent ion a high pressure of reagent gas is generally required. For the two reagent ions illustrated above (CH_5^+ and H_3^+) ionization of the target gas generally occurs by proton transfer to form the protonated parent ion. One reason chemical ionization is sometimes chosen over other methods of ionization is that it is a softer ionization technique, generally imparting less energy to the target gas molecules, and enhancing the abundance of the molecular ion over fragment ions.

Double charge transfer is a process in which a fast moving positively charged ion M^+ , acquires two electrons *via* a double electron capture reaction with a neutral molecule AB. As the energy required to doubly ionize AB is usually greater than the energy released in the charge inversion of C^+ , DCT reactions are generally endoergic. The additional energy required for the DCT reaction is supplied by the translational energy of the ion C^+ .^{47,53} Therefore, by measuring the change in translational energy of the fast moving projectile ion following charge inversion, information on the double ionization energies (DIEs) of the neutral can be found.⁵⁴⁻⁵⁶ If the product anions are detected within a small angle of the original C^+ direction, the recoil energy of AB^{2+} can

be ignored, and thus the change in translational energy of the projectile ion ΔE_{trans} can be expressed as:

$$\Delta E_{\text{trans}} = \text{DIE}(\text{AB}) - \Delta E(\text{C}^+ \rightarrow \text{C}^-) \quad (1.11)$$

where $\text{DIE}(\text{AB})$ is the double ionization of AB and $\Delta E(\text{C}^+ \rightarrow \text{C}^-)$ is the energy released in the charge inversion of C^+ . The DIEs recorded by DCT experiments represent the vertical DIEs of the neutral molecule AB from the ground state. Therefore, DCT experiments are particularly useful in measuring the energies of dicationic electronic states which do not exist as stable species.^{57,58} It is also possible to populate exclusively electronic states of the dication with a single electron spin multiplicity by choosing a suitable projectile, as the total electron angular momentum must be conserved during the course of a DCT reaction.^{47,59,60}

In a charge stripping reaction, a fast moving projectile ion of interest AB^+ is ionized in a collision with a neutral species M, resulting in the formation of a dication AB^{2+} . As in the case of DCT reactions, the energy required to ionize AB^+ is supplied from the translational energy of the projectile ion itself. Therefore, measuring the change in translational energy of the fast moving projectile ion in a charge stripping experiment provides information on the vertical ionization energy of the ion AB^+ .⁴⁹ One limitation of this technique is that the dications formed must have a lifetime of at least several microseconds in order to be detected. However, charge stripping experiments are sometimes able to populate electronic states of a molecular dication that are inaccessible *via* a vertical transition at the geometry of the neutral molecule in the ground state. Thus, the charge stripping technique can be used to prepare a number of stable molecular dications that cannot be prepared by ionization involving single photons or collisions with electrons.^{50,61}

1.3 Product Ions

Following electron ionization of a target gas, a number of different product ions are formed. For the target molecules investigated in this thesis, these product ions are generally singly or doubly charged, and are formed from both dissociative and non-dissociative ionization. By simultaneously recording mass and coincidence spectra, the fragment ions formed *via* single, double, triple and quadruple ionization are

distinguished from one another. In this section, the different types of ions formed following electron-molecule collisions are examined in more detail.

1.3.1 Product Ions from Single Ionization

Single ionization of a neutral gas phase target molecule involves a transition between two well-defined electronic states of the molecule and the molecular ion. In this process an electron is removed from the neutral molecule and released into the continuum, resulting in the formation of a singly charged molecular ion. Vibrational and rotational excitation may also accompany the transition, however, the energy transferred into vibrational and rotational excitation is usually significantly smaller than that transferred during electronic excitation. The Frank-Condon principle states that during ionization there is no change in molecular geometry, as the electronic transition takes place on a much faster timescale than nuclear motion. Therefore, the transition from the ground electronic state to the electronic state of the molecular monocation is vertical, as is shown schematically in Figure 1.1. In the following Section, the Frank-Condon principle is discussed for the generic diatomic molecule AB, but it is of course also true for polyatomic molecules, for which the potential curves shown in Figures 1.1 and 1.2 represent cuts through the $3N-6$ dimensional potential energy surface.

Upon ionization, a number of different monocation electronic states may be accessed, depending on the relative shape of the neutral and cationic potential energy curves of the chosen molecular system, and the energy transferred by electron collision. As shown in Figure 1.1, the parent ion may be formed *via* a vertical transition from the ground state of the neutral to a bound region of a cationic potential curve. This bound region is typically a deep potential energy well supporting a number of vibrational and rotational energy levels. At the ionizing electron energies used in this thesis (30 – 200 eV), parent monocation formation is generally dominant (Equation 1.12).



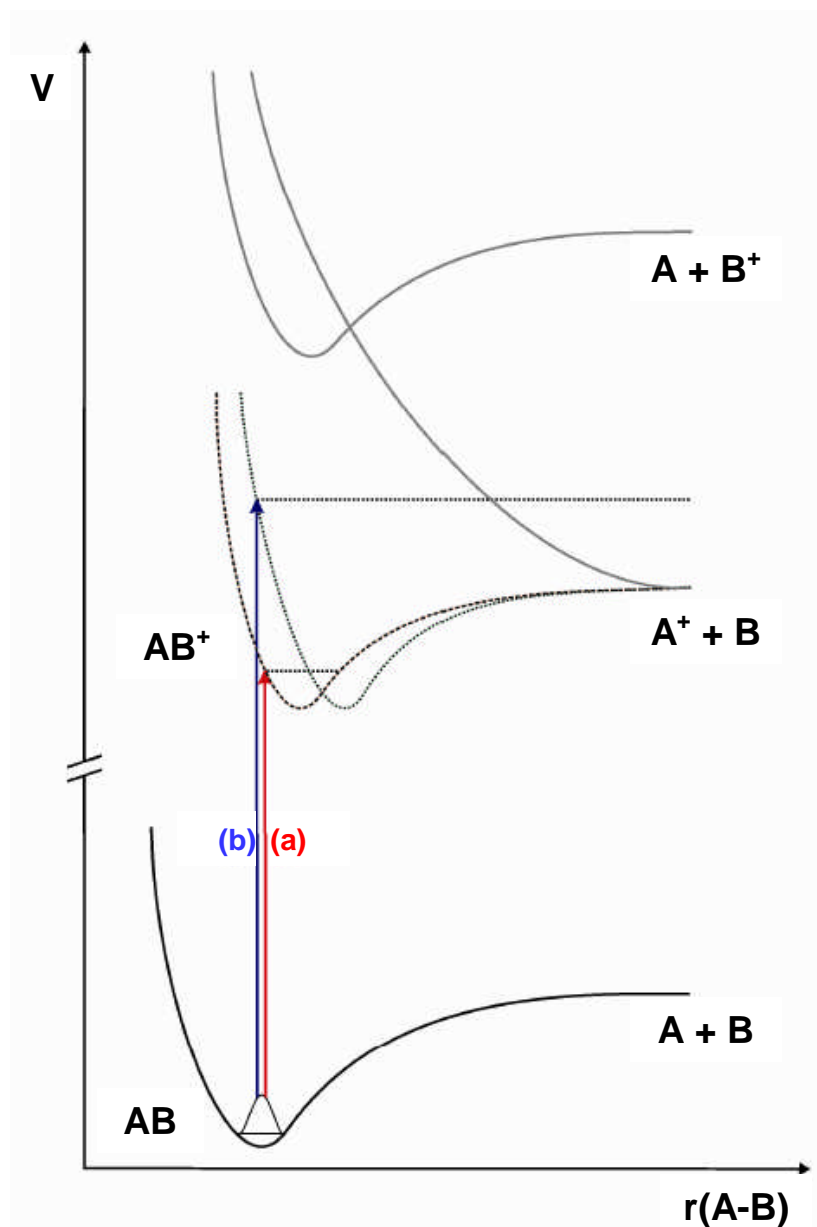


Figure 1.1: Schematic potential energy curves for the single ionization of the molecule AB. Process (a) represents a vertical transition from the ground electronic state of the neutral to a bound region of a cationic potential curve, while process (b) represents a vertical transition to a cationic potential energy curve at an energy above the dissociation asymptote, and hence dissociates to form a singly charged fragment ion and a neutral. Recreated from Ref. [62].

For some molecular systems, the relative shape of the monocation and neutral potential energy surfaces mean that the bound region of the cationic state cannot be accessed *via* a vertical transition from the ground electronic state of the neutral molecule. If no bound region can be accessed, the parent monocation rapidly fragments

to form a singly charged ion and a neutral product, $A^+ + B$, as shown in Equation 1.13 and Figure 1.1. The X^+ monocation is termed a fragment ion.



Of course, the cationic state accessed *via* a vertical transition may be a repulsive state. Once this state is populated the nuclei A^+ and B rapidly move apart and the excess energy of the system above the dissociation limit is converted into kinetic energy.

For the ionizing electron energies investigated in this thesis, fragment ion formation will not only proceed *via* the ground state, but by a wide range of highly excited electronic and vibrational energy levels, as shown in Equation 1.14:



It is therefore likely that many fragment ions will be formed by direct dissociation *via* predissociation, as shown schematically in Figure 1.2.⁶³ Electronic predissociation occurs when two potential curves of the molecular ion intersect; one a bound excited electronic state and the other a repulsive electronic state. When such a crossing occurs, monocations excited to vibrational levels near the crossing may jump from the bound potential curve to the dissociative curve; this transition is non-radiative, as no energy is absorbed or emitted.

In the case of polyatomic molecules, the multi-dimensional potential energy surfaces are complex, and the resulting polyatomic ion can undergo internal transitions leading to subsequent unimolecular dissociation.⁴ Therefore a statistical approach is required to predict the fragmentation of molecular ions in excited states. The two essentially identical statistical theories used for this purpose are the quasiequilibrium theory (QET) developed by Rosenstock *et. al.*,⁶⁴ and the Rice, Ramsperger, Kassel and Marcus (RRKM) theory.⁶⁵ Both theories assume that molecular ions formed in excited states relax rapidly by conversion of their electronic excitation energy into vibrational energy (internal conversion) of the molecular ion in its ground state. The internal energy in the excited atom is statistically distributed *via* transitions into the electronic ground state, normally within a few vibrational periods, and before fragmentation by vibrational predissociation. The RRKM/QET equation yields the rate constant for an

individual unimolecular dissociation reaction of a molecular ion, at a given energy. A more detailed description of statistical RRMK/QET theory calculations in mass spectrometry is given by Baer *et. al.*^{66,67}

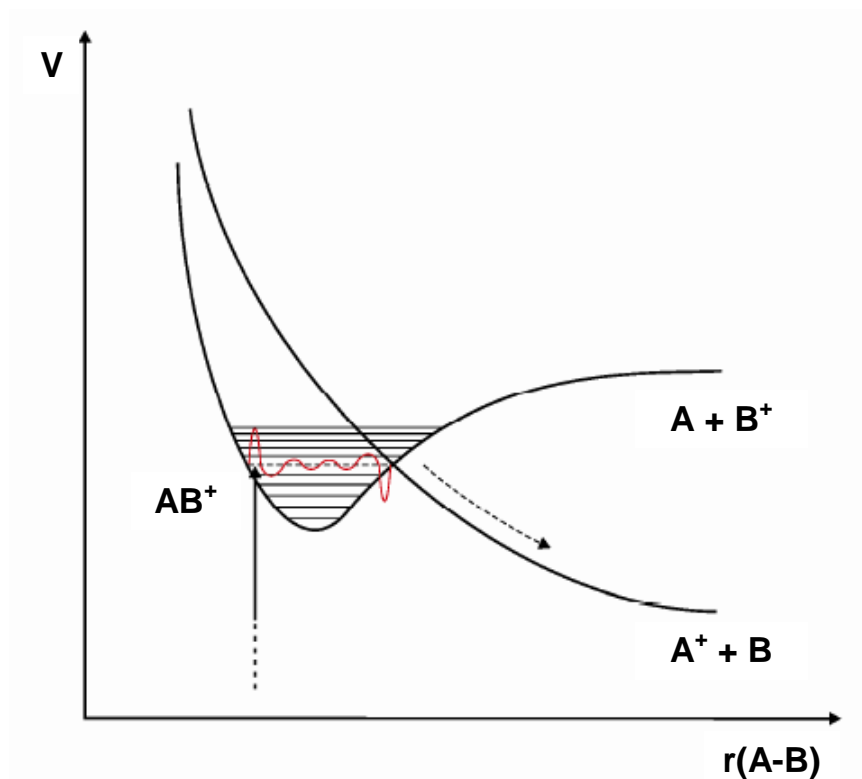


Figure 1.2: A schematic diagram showing how predissociation *via* curve crossing to dissociative potentials provides a common dissociation mechanism. Recreated from Ref. [68].

In general, the relative abundance of any fragment ion is related to its rate of formation and its rate of dissociation by unimolecular decomposition.⁴ Therefore, a mass spectrum is a record in time of the position of this ‘quasi-equilibrium’ of those rates, and hence, the respective partial ionization cross-sections of the fragment ions will depend on the time after formation of the parent ion.⁴ If the initial energy deposited into the parent ion is known or assumed, then the RRKM/QET statistical theories can be used to calculate a mass spectrum by determining the rate coefficients of formation and dissociation of the fragment ions.⁶⁹

In the ionizing electron energy range investigated in this thesis, the majority of ions formed are monocations, either parent or fragment. However, at ionizing electron energies above the double ionization threshold, many fragment monocations are formed *via* dissociative multiple ionization. The following section discusses the properties of

these multiply charged ions, and the method by which monocations formed *via* dissociative multiple ionization are distinguished from those formed *via* dissociative single ionization.

1.3.2 Properties of Multiply Charged Ions

At ionizing electron energies above the double ionization threshold, doubly charged parent and fragment ions, albeit in low abundances, are observed in the mass spectrum of a number of small gaseous molecules. The low abundance of such dications is due to the inherently small ionization cross-section for the formation of long-lived dications, even at ionization energies well in excess of the double ionization threshold.^{1,4} In fact, the majority of molecular dications are unstable and rapidly dissociate to yield a pair of singly charged ions, as shown in Equation 1.15:



However, the fact that molecular dications, such as CO^{2+} , have been observed and identified by mass spectrometric experiments, in which ions must survive for at least a microsecond to be detected, clearly indicates that not all dication electronic states are dissociative.

The non-adiabatic potential surface associated with a molecular dication asymptotically corresponds to a smaller (or atomic) dication and a neutral species (Figure 1.3). Simply through polarization interactions, such potential surfaces will always have a bound minimum, however weak. Molecular dications can decay by adiabatic transfer to a purely repulsive potential surface, corresponding to a monocation pair, that intersects the bound potential surface (Figure 1.3).

The stability of a molecular dication will depend upon the energy at which the intersection with the repulsive surface occurs relative to the energy of the bound minimum. This can be estimated using the depth of the bound minimum and the appropriate ionization potentials of the component atoms. For a dication XY^{2+} , the energy difference between the dication/neutral ($X^{2+} + Y$) asymptote and the monocation pair ($X^+ + Y^+$) can be calculated by the relative ionization potentials of X^+ and Y :

$$\Delta E = IP(X^+) - IP(Y) \quad (1.16)$$

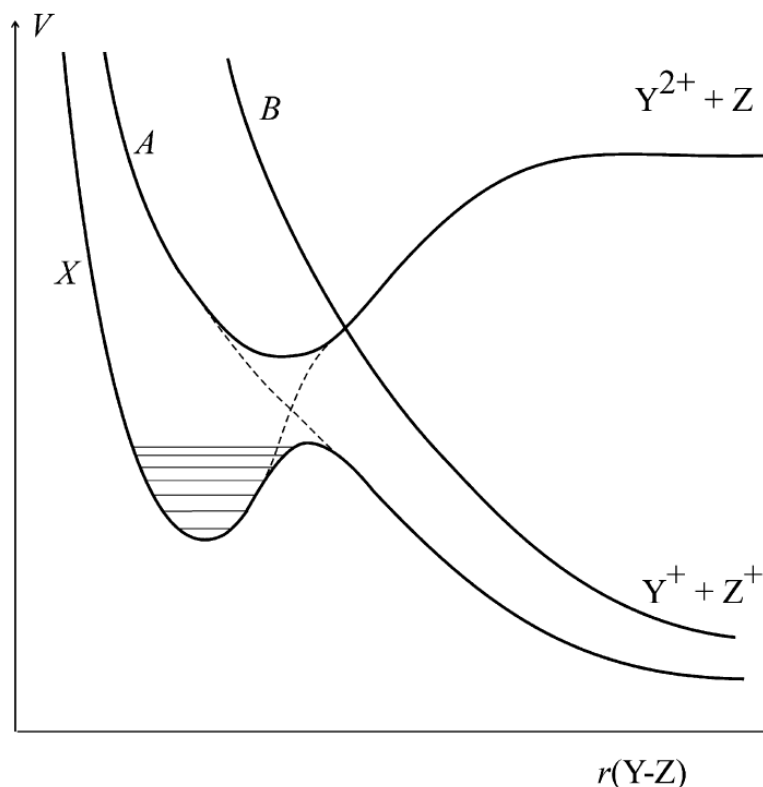


Figure 1.3: Schematic potential energy curve for a diatomic YZ^{2+} . Many dication electronic states are purely dissociative (state B), whereas some small molecular dications may possess metastable states which exhibit potential energy minima (states A and X). Recreated from Ref. [70].

In cases in which the two potential surfaces cross at all, there are three possible outcomes depending on the relative energetics (Figure 1.4):

- (a) If the monocation pair asymptote lies higher in energy than the bound minimum, then the molecular dication is thermodynamically stable and cannot spontaneously dissociate (Figure 1.4a). Several dications of heavy metal oxides and fluorides fall into this group, such as UO^{2+} and UF^{2+} .⁷¹
- (b) If the monocation pair asymptote lies slightly lower in energy than the bound minimum, an energy barrier to dissociation is created, inferring a degree of kinetic stability to the dication, depending on the height of the barrier (Figure 1.4b). As the dication is still thermodynamically unstable, with the asymptote to dissociation lying below the bound well, such dications are termed ‘metastable’. Many molecular dications possess at least one electronic state that has a bound well, with some even supporting vibrational levels.^{72,73}

- (c) If the monocation pair asymptote lies significantly lower in energy than the bound minimum, then the crossing between the surfaces will occur in the region of the bound minimum and the molecular dication will immediately dissociate (Figure 1.4c). This is the case for most small molecular dications composed of light elements.

As the bound minimum of a metastable state is not the global minimum (which corresponds to the asymptotic energy of the monocation pair), metastable dications are able to dissociate by tunnelling through the energy barrier confining the local minimum. The lifetime of a metastable state depends on the tunnelling rate, which in turn depends on the mass of the species, and more importantly the width of the energy barrier. As many molecular dications are observed in mass spectrometric experiments, many must have electronic states with a lifetimes of at least 1 μ s. In fact, storage ring experiments have shown that some molecular dications have significantly longer lifetimes, with the low-lying vibrational levels of the ground electronic states of CO^{2+} ,⁷⁴ N_2^{2+} ,⁷⁵ and SH^{2+} ⁷⁶ having lifetimes considerably longer than 1s.

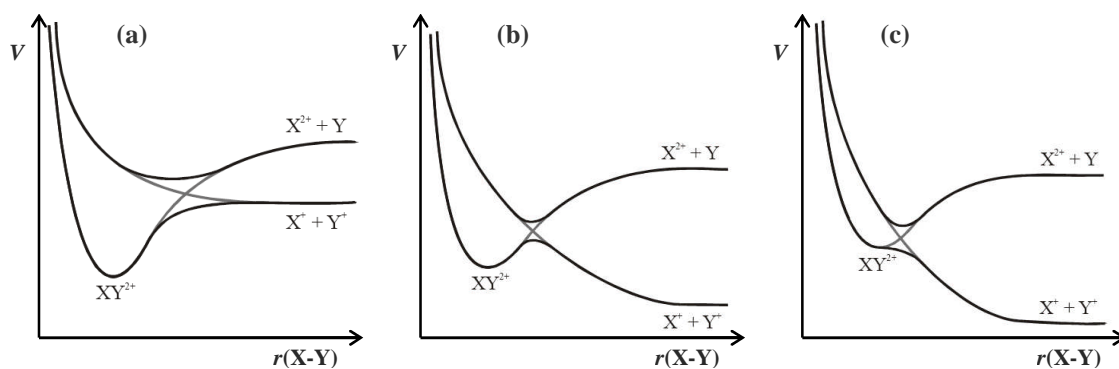


Figure 1.4: Prototypical potential energy curves for a diatomic dication from an adiabatic (black lines, foreground) and non-adiabatic (grey lines, background) perspective. If the lowest energy dissociation asymptote lies above the bound minimum (a) the molecular dication is thermodynamically stable; however if the asymptote lies below the barrier but is separated by a barrier (b) the dication is metastable; if there is no barrier to dissociation (c) the dication is kinetically and thermodynamically unstable. Recreated from Ref. [77].

In contrast to metastable molecular dications, which are commonly observed in the electron ionization and photoionization mass spectra of small gaseous molecules, very few observations of long-lived triply charged or higher ions, have been reported in

the literature.^{71,78} This is perhaps not surprising given that the stronger Coulomb repulsion between three like charges means that the majority of potential energy curves for molecular trications are purely repulsive. Furthermore, at ionizing energies in excess of the triple ionization threshold, the triple ionization cross-sections for small gaseous molecules are typically several orders of magnitude smaller than the corresponding cross-sections for single ionization.⁹⁻¹¹ However, a small number of molecular trications, including Cl_2^{3+} , SF^{3+} , OCS^{3+} and SO_2^{3+} , have been observed in mass spectrometric experiments, in which lifetimes of at least several microseconds are required for detection.⁷¹ Indeed, a tetracation, NbO^{4+} ,⁷⁹ has also been observed by mass spectrometry. The vast majority of molecular trications do however dissociate rapidly upon formation, to yield two or more positively charged fragment ions. For example, following triple ionization of the molecule ABC to form the trication ABC^{3+} , dissociation of the trication can result in the formation of three monocations (Equation 1.17a), or a dication-monocation pair (Equation 1.17b):



In order to distinguish between the different possible fragmentation channels of multiply charged ions, an ion coincidence technique is required. In the investigation of electron-molecule collisions presented in this thesis, the time-of-flight mass spectrometer (TOFMS) used is coupled with a 2D ion coincidence technique. This ion coincidence technique is similar to the photoelectron-photoion-photoion coincidence (PEPIPICO) technique pioneered by Eland and co-workers in the 1980s,⁸⁰ but uses electron ionization and records only the ion arrival times. This experimental setup enables single product ions, ion pairs and ion triples, formed following electron ionization, to be detected concomitantly, then identified and quantified. Such data allows monocations formed *via* dissociative single, double, triple, and, where it contributes at all, quadruple ionization, to be distinguished. In a similar manner, dications, formed *via* dissociative double, triple and quadruple ionization, and trications, formed *via* dissociative triple and quadruple ionization, are also distinguished.

1.4 Electron Ionization Cross-Sections

As has been described in previous sections, the electron ionization of a molecule involves a collision between an electron and a target molecule, and the subsequent formation of an ion. Ionization cross-sections (ICSs) provide a measure of the probability of such a reaction forming an ion. The cross-section for forming any positively charged ion, regardless of identity, is termed the total ionization cross-section (TICS).⁴ Partial ionization cross-sections quantify the cross-section for the production of a specific ion X^{m+} , and hence provide more detailed information about the electron ionization processes occurring.⁴ For ions formed *via* dissociative multiple ionization, the precursor-specific PICSs indicate the cross-sections for forming individual ions from single, double, triple and quadruple ionization.

Experimental determinations of electron ionization cross-sections usually involve an experimental arrangement similar to that shown in Figure 1.5, in which a monoenergetic beam of ionizing electrons intersects a beam of target gas molecules. Such an experimental arrangement gives rise to a finite volume in which electrons and neutral molecules may collide. Any ionization cross-section can be expressed mathematically using a variation of the Beer-Lambert law:

$$I = I_0 e^{-nl\sigma} \quad (1.18)$$

where I_0 is the initial electron flux, I is the electron flux after passing through the target gas, n is the number density of the gas, l is length of the interaction region between the electrons and molecules, and σ is the cross-section. Under conditions of low target gas pressure and low electron flux, i.e. $nl\sigma \ll 1$, equation 1.18 can be written as:

$$I - I_0 = I_0 nl\sigma \quad (1.19)$$

Assuming single collision conditions, the quantity $I - I_0$ corresponds to the number of ionization events N_{events} relating to the electron ionization process of interest. This gives rise to a generalised expression for the ionization cross-section:

$$\sigma = \frac{N_{\text{events}}}{I_0 nl} \quad (1.20)$$

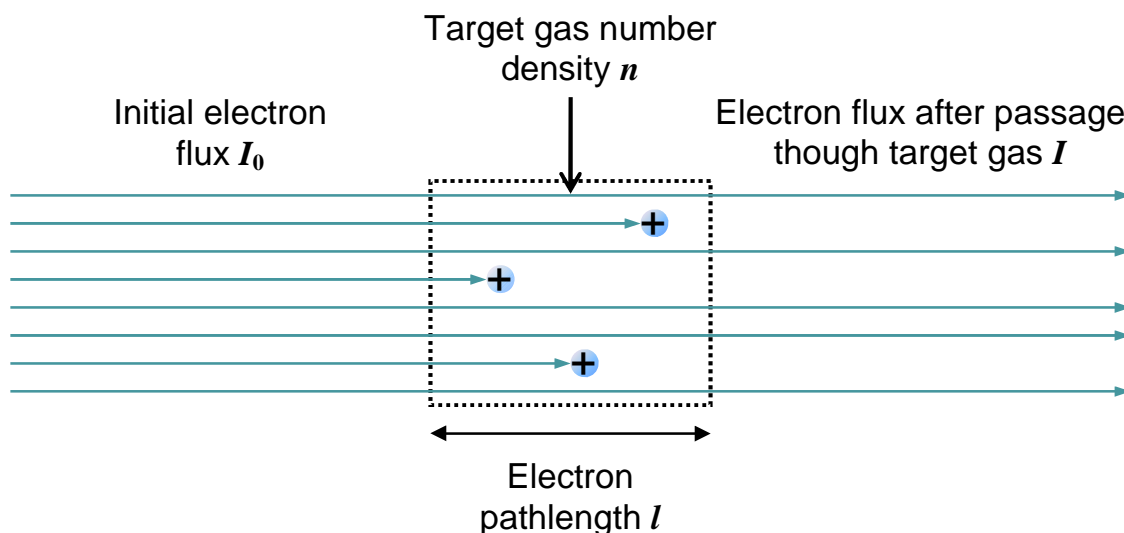


Figure 1.5: A schematic diagram of an electron ionization experiment.

1.4.1 Total Ionization Cross-Sections

The total ionization cross-section of a molecule is generally defined in one of two ways; the total charge ICS (gross ICS), or the counting TICS.⁴ The gross ICS describes the cross-section for the production of positive ion charge, following an electron-molecule collision. For the gross ICS, the term N_{events} in Equation 1.20 can be replaced by the positive ion flux I_{charge} produced by ionization events involving positive ion formation.⁵ The gross ICS (σ_T) is therefore defined as:

$$\sigma_T = \frac{I_{\text{charge}}}{I_0 n l} \quad (1.21)$$

The counting TICS describes the cross-section for forming any positively charged ion X^{m+} , regardless of its mass or charge. For the counting TICS the term N_{events} in Equation 1.20 can be replaced with by the total number of ions $\Sigma N[X^{m+}]$ formed by ionization events resulting in positive ion formation. The counting TICS (σ_C) is therefore defined as:

$$\sigma_C = \frac{\Sigma N[X^{m+}]}{I_0 n l} \quad (1.22)$$

As can be seen from Equations 1.21 and 1.22, a measurement of the TICS for a gaseous sample requires the determination of four quantities. Below, a brief description of the

principles involved in measurement of the four quantities given in Equation 1.21 is given using the classic Condenser-Plate apparatus developed by Smith and co-workers.⁸¹⁻⁸³ In fact, such apparatus has been used in many more recent determinations of TICs, with only slight modifications.^{4,84,85}

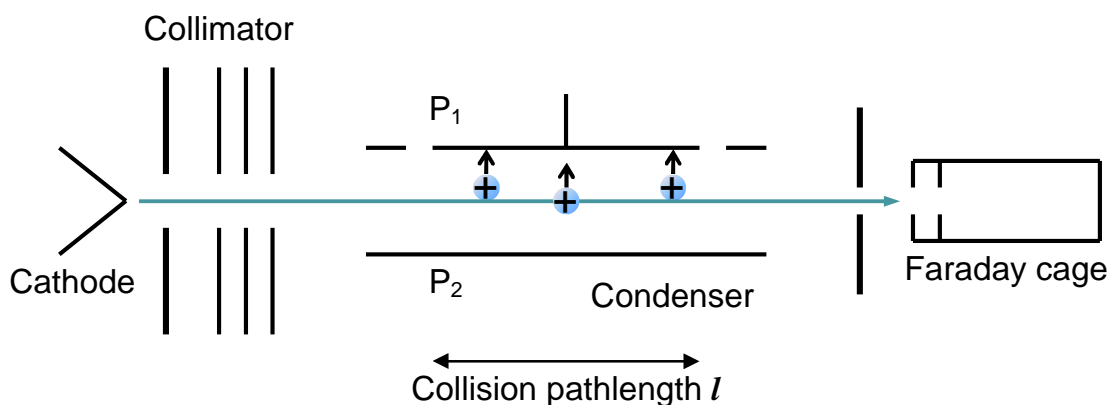


Figure 1.6: A schematic diagram of the Condenser-Plate apparatus used by Smith and co-workers,⁸¹⁻⁸³ and similar to the apparatus used by Rapp *et. al.*^{84,85} for the determination of total (gross) ionization cross-sections.

Electrons emerge from a cathode and pass through a collimator to be accelerated to a specified energy E , before entering a collision chamber filled with the target gas. An electric field is applied across the condenser plates, so that positive ions can be collected at P_1 and the total positive ion flux I_{charge} can be determined. An axial magnetic field prevents any electron beam deflection and suppresses secondary electron emission from P_1 . The electron beam is then trapped in a Faraday cage, so the electron flux I_0 can be determined. The collisional pathlength l is given by the length of the plate P_1 . Finally the number density n is evaluated using the gas pressure and temperature of the collision chamber.

1.4.2 Partial Ionization Cross-Sections and Precursor-specific PICs

As described above, PICs provide information on the identity and abundance of different charged species formed following electron ionization. The PIC $\sigma[X^{m+}]$ for the production of a specific ion X^{m+} , following an electron-molecule collision is defined as:

$$\sigma[X^{m+}] = \frac{N[X^{m+}]}{I_0 n l} \quad (1.23)$$

where $N[X^{m+}]$ represents the total number of ions X^{m+} formed by ionization events involving the formation of X^{m+} .¹⁹ Thus, mass spectrometric experiments are required for the measurement of PICSs, to allow the various ions formed *via* dissociative and non-dissociative ionization processes to be distinguished and quantified.

Precursor-specific PICSs express the probability for forming a particular fragment ion, *via* single, double, triple or quadruple ionization. The precursor-specific PICS $\sigma_n[X^{m+}]$ for the formation of a fragment ion X^{m+} , involving the loss of n electrons from the neutral target molecule, is defined as:

$$\sigma_n[X^{m+}] = \frac{N_n[X^{m+}]}{I_0 n l} \quad (1.24)$$

where $N_n[X^{m+}]$ represents the number of X^{m+} ions formed by ionization events involving the loss of n electrons from the target molecule. Such precursor-specific PICSs quantify the yield of each fragment ion from single ($n = 1$), double ($n = 2$), triple ($n = 3$) and quadruple ($n = 4$) ionization, and thus provides a more in-depth view of the various dissociative electron ionization processes leading to fragment ion formation.^{9,12-14}

1.4.3 Relative Partial Ionization Cross-Sections

As shown by Equations 1.23 and 1.24, the determination of absolute PICSs requires the accurate measurement of four experimental variables: the initial electron flux I_0 , the number density of the target gas n , the collisional pathlength l , and the number of ions $N_n[X^{m+}]$ formed by electron ionization events. Determination of some of these variables is experimentally non-trivial. A considerable experimental simplification is achieved by taking a ratio of the PICS for forming a selected fragment ion $\sigma[X^{m+}]$ against the PICS of another specific ion, commonly the parent monocation $\sigma[\text{parent}^+]$, to produce relative PICSs $\sigma_r[X^{m+}]$:^{9-16,81-89}

$$\sigma_r[X^{m+}] = \frac{\sigma[X^{m+}]}{\sigma[\text{parent}^+]} = \frac{N[X^{m+}]}{N[\text{parent}^+]} \quad (1.25)$$

Thus, the determination of relative PICSs requires only the number of X^{m+} ions and parent monocations formed during an experiment, which can be easily obtained from the measured mass spectral intensities. The parent monocation is chosen as the reference in Equation 1.25 as it is typically formed in large abundance, with a thermal

kinetic energy distribution, and can only be formed by single ionization. Thus parent monocations are least susceptible to ion discrimination effects in mass spectrometric experiments. The relative PICS data produced in this thesis can, where required, be placed on an absolute scale by normalization to available TICS or absolute PICS data, determined under similar experimental conditions of target gas pressure and temperature.

1.5 Experimental Techniques for the Measurement of PICSs

In this section two different experimental methods used to determine absolute PICSs are briefly reviewed. The first method involves the definitive determination of each of the variables expressed in Equation 1.24 ($N[X^{m+}]$, I_0 , l , n), which is experimentally non-trivial.⁹⁰ The second method involves two target gases, one target gas with well-defined absolute PICSs, such as argon or nitrogen, and the other target gas of interest. This method may be thought of as a normalisation technique.

1.5.1 Method 1: Individual Parameter Determination

For the discussion presented here, the focus is placed on the experimental arrangement used by Straub and co-workers,^{19,91-95} depicted in Figure 1.7. The apparatus of Straub and co-workers consists of an electron gun, TOF mass spectrometer with a position sensitive detector (PSD) and an absolute capacitance pressure gauge. A pulsed electron beam is directed through an interaction region filled with the target gas, located between two plates held at ground potential. After each electron pulse, a pulsed positive voltage is applied to the top plate to drive any positive ions formed towards the bottom plate. Some of these ions pass through an aperture in the bottom plate and impact upon the PSD, allowing the arrival time and the position of each product ion to be detected. While product ions are detected along the length of the PSD in the direction parallel to the electron beam, the transverse positional distribution of product ions arriving at the detector demonstrates the complete collection of energetic fragment ions, regardless of their initial kinetic energy or mass.

The number of particular ionization events $N[X^{m+}]$ is determined by recording a mass spectrum and counting the number of ions in an appropriate portion of the spectrum. The electron flux I_0 is found by collecting the electron beam in a Faraday cup and measuring the current with an electrometer. The collision length l is defined by the length of the aperture in the bottom plate directly above the PSD. Finally, the number

density of the target gas n is obtained from the pressure p , measured by a capacitance diaphragm gauge.⁹⁶ Measurement of these quantities allows the direct determination of absolute PICSs, but it is clear that the determination of these quantities is time consuming, particularly the target gas density.⁹⁶

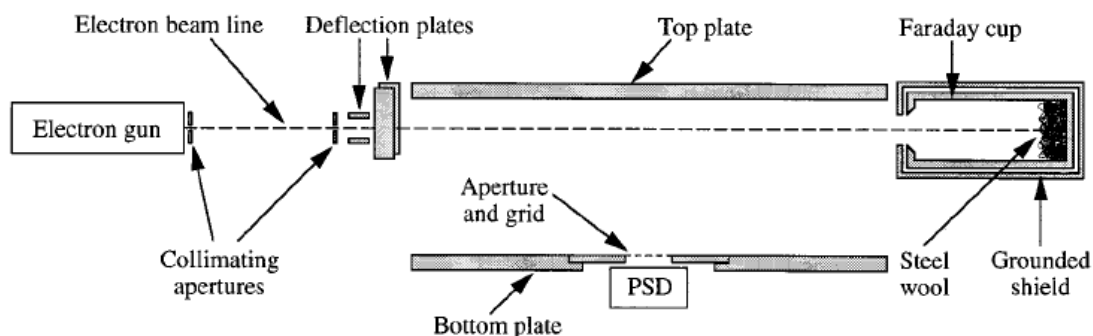


Figure 1.7: A schematic diagram of the experimental apparatus used by Straub and co-workers.^{19,91-95}

1.5.2 Method 2: Normalization Method

The second method involves two target gases, the target gas of interest, and a target gas which has a well-defined absolute PICS to normalise to, such as argon or nitrogen. Figure 1.8 shows a schematic diagram of the focusing time-of-flight (FTOF) mass spectrometer used by Tian and Vidal^{8,97,98} for the determination of absolute PICSs using the normalization method. The experimental arrangement bears many similarities to the two-field TOF mass spectrometer employed in the measurement of relative PICSs in this thesis, discussed in Chapter 2, with some modifications. In the FTOF, the drift tube is divided into two segments, FT1 and FT2, separated by a focusing mesh (IL). By applying an appropriate negative voltage across the focusing mesh, the equipotential curves inside the TOFMS behave as a symmetric spherical lens, focusing the diverging beam from the source region onto the MCP detector. By varying the deflector voltage applied to the deflector plates XD and YD (Figure 1.8) and monitoring the dependence of the ion count rate recorded at the detector, the complete collection of product ions is demonstrated.

For the normalization technique, the two target gases are premixed in a suitable ratio. A mass spectrum of the gas mixture is recorded to determine the number of product ions $N[X^{m+}]$ formed *via* electron ionization of the target gas of interest, and also

the number of product ions $N[\text{ref}^+]$ formed *via* electron ionization of the reference gas. The absolute PICS for the formation of each product ion X^{m+} is then found by normalisation to the absolute PICS forming the reference ion ref^+ , which can be obtained from the literature:

$$\sigma[X^{m+}] = \frac{N[X^{m+}]}{N[\text{ref}^+]} \times \frac{n_{\text{ref}}}{n_{\text{target}}} \times \sigma[\text{ref}^+] \quad (1.26)$$

where n_{ref} and n_{target} are the number densities of the premixed reference target gas and the target gas of interest.

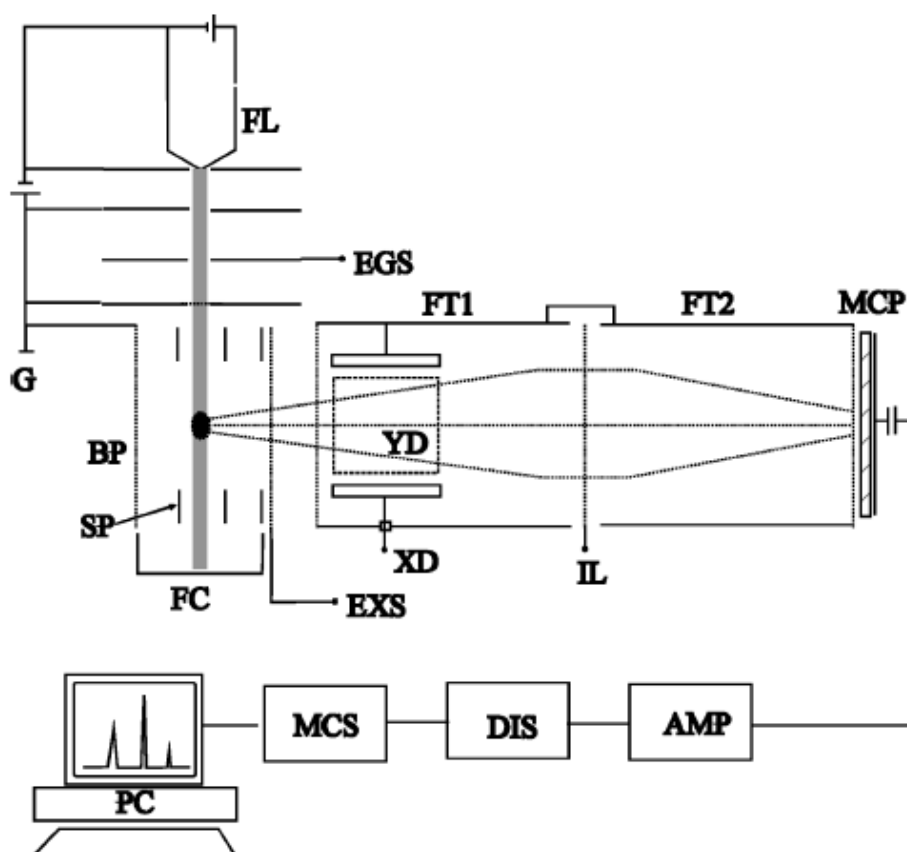


Figure 1.8: A schematic diagram of the experimental apparatus used by Tian and Vidal.^{8,97,98} The main components of the apparatus are labelled on the diagram as follows: FL = Filament, FC = Faraday cup, BP = Backing plate, XD/YD = x-deflector and y-deflector, FT = Flight tubes, 1 & 2, IL = Ion lens, MCP = Multichannel plate.

1.6 Summary

This chapter begins by providing clear motivation for the need to determine accurate electron ionization cross-sections for molecules used in plasmas and that are present in planetary atmospheres. The ionization methods used in this thesis are discussed, together with other available methods, and the type of ions that can be formed from such ionization events is presented. The various forms of electron ionization cross-sections determined are detailed, along with two of the more common experimental techniques employed in their measurement.

In this thesis, the formation and fragmentation of molecular ions formed following electron ionization are investigated, using a TOFMS coupled with a 2D ion coincidence technique. In the following chapters this experimental technique is discussed in detail, together with the data analysis procedures used to process the experimental data obtained into relative PICSs. The results of electron ionization investigations of the target gases H₂S, CH₃OH and CF₃I are then presented. In the final two chapters, the results of an investigation into the photoionization of CF₃I and of the reactions following I²⁺ + OCS collisions are presented.

1.7 References

- 1 L. G. Christophorou and J. K. Olthoff, *Fundamental Electron Interactions with Plasma Processing Gases* (Plenum, New York, 2004).
- 2 E. Herbst, *Annu. Rev. Phys. Chem.* **46**, 27 (1995).
- 3 M. J. McEwan, G. B. I. Scott, and V. G. Anicich, *Int. J. Mass Spectrom.* **172**, 209 (1998).
- 4 T. D. Mark and G. H. Dunn, *Electron Impact Ionization* (Springer-Verlag, 1985).
- 5 T. D. Mark, *Plasma Phys. Control. Fusion* **34**, 2083 (1992).
- 6 R. F. Stebbings and B. G. Lindsay, *J. Chem. Phys.* **114**, 4741 (2001).
- 7 H. U. Poll, C. Winkler, D. Margreiter, V. Grill, and T. D. Mark, *Int. J. Mass Spectrom. Ion Process.* **112**, 1 (1992).
- 8 C. C. Tian and C. R. Vidal, *J. Phys. B: At. Mol., Opt. Phys.* **31**, 895 (1998).
- 9 S. J. King and S. D. Price, *J. Chem. Phys.* **127**, 174307 (2007).
- 10 S. J. King and S. D. Price, *Int. J. Mass Spectrom.* **272**, 154 (2008).
- 11 K. M. Douglas and S. D. Price, *Int. J. Mass Spectrom.* **303**, 147 (2011).

- 12 N. A. Love and S. D. Price, *Phys. Chem. Chem. Phys.* **6**, 4558 (2004).
- 13 S. Harper, P. Calandra, and S. D. Price, *Phys. Chem. Chem. Phys.* **3**, 741 (2001).
- 14 N. A. Love and S. D. Price, *Int. J. Mass Spectrom.* **233**, 145 (2004).
- 15 P. Calandra, C. S. S. O'Connor, and S. D. Price, *J. Chem. Phys.* **112**, 10821 (2000).
- 16 K. M. Douglas and S. D. Price, *J. Chem. Phys.* **131**, 224305 (2009).
- 17 M. R. Bruce and R. A. Bonham, *Int. J. Mass Spectrom. Ion Process.* **123**, 97 (1993).
- 18 M. R. Bruce, L. Mi, C. R. Sporleder, and R. A. Bonham, *J. Phys. B At. Mol. Opt. Phys.* **27**, 5773 (1994).
- 19 H. C. Straub, P. Renault, B. G. Lindsay, K. A. Smith, and R. F. Stebbings, *Phys. Rev.* **52**, 1115 (1995).
- 20 *Database needs for modeling and simulation of plasma processing*, National Research Council (National Academy Press, 1996).
- 21 C. Zener, *Proc. Roy. Soc. London, Series A* **137**, 696 (1932).
- 22 S. A. Rogers, S. D. Price, and S. R. Leone, *J. Chem. Phys.* **98**, 280 (1993).
- 23 L. D. Landau, *Phys. Z. Sowjetunion* **2**, 46 (1932).
- 24 C. Q. Jiao, B. Ganguly, C. A. DeJoseph, and A. Garscadden, *Int. J. Mass Spectrom.* **208**, 127 (2001).
- 25 S. K. Srivastava, E. Krishnakumar, A. F. Fucaloro, and T. vanNote, *J. Geophys. Res., Planets* **101** (1996).
- 26 G. H. Wannier, *Phys. Rev.* **90**, 817 (1953).
- 27 F. H. Read, in *Electron Impact Ionization*, edited by T. D. Mark and G. H. Dunn (Springer-Verlag, New York, 1985).
- 28 G. H. Wannier, *Phys. Rev.* **100**, 1180 (1955).
- 29 J. H. D. Eland, *Vacuum Ultraviolet Photoionization and Photodissociations of Molecules and Clusters* (World Scientific, Singapore, 1991).
- 30 K. H. Becker and V. Tarnovsky, *Plasma Sources Sci. Technol.* **4**, 307 (1995).
- 31 J. H. D. Eland, *Photoelectron Spectroscopy* (Butterworths, London, 1984).
- 32 M. V. Kurepa and D. S. Belic, **11** (1978).
- 33 L. Mi, C. R. Sporleder, and R. A. Bonham, **251** (1996).
- 34 L. G. Christophorou and J. K. Olthoff, **28** (1999).
- 35 J. H. D. Eland, *Z. Phys. D Atoms Mol. Clusters* **4**, 31 (1986).
- 36 J. M. Hollas, *Modern Spectroscopy*, Fourth ed. (Wiley, 2005).

- 37 C. Bordas, F. Paulig, and H. Helm, *Rev. Sci. Instrum.* **67**, 2257 (1996).
- 38 A. T. J. B. Eppink and D. H. Parker, *Rev. Sci. Instrum.* **68**, 3477 (1997).
- 39 D. H. Parker and A. T. J. B. Eppink, *J. Chem. Phys.* **107**, 2357 (1997).
- 40 J. A. Davies, J. E. LeClaire, R. E. Continetti, and C. C. Hayden, *J. Chem. Phys.* **111**, 1 (1999).
- 41 A. Sanov and R. Mabbs, *Int. Rev. Phys. Chem.* **27**, 53 (2008).
- 42 E. P. Wigner, *Phys. Rev.* **73**, 1002 (1948).
- 43 S. Hsieh and J. H. D. Eland, *J. Phys. B* **30**, 4515 (1997).
- 44 S. Hsieh and J. H. D. Eland, *J. Phys. B: At., Mol. Opt. Phys.* **29**, 5795 (1996).
- 45 T. Baer, *Int. J. Mass Spectrom.* **200**, 443 (2000).
- 46 R. P. Tuckett, G. K. Jarvis, and K. J. Boyle, *J. Electron Spectrosc. Relat. Phenom.* **101-103**, 99 (1999).
- 47 R. M. Harris, *Int. J. Mass Spectrom. Ion Processes* **120**, 1 (1992).
- 48 J. Appell, J. Durup, and F. C. Fehsenfeld, *J. Phys. B: At. Mol. Phys.* **6**, 197 (1973).
- 49 C. J. Proctor, C. J. Porter, T. Ast, C. G. Herbert, J. H. Brenton, and J. H. Beynon, *Org. Mass Spectrom.* **16**, 454 (1983).
- 50 M. Rabrenovic, C. J. Proctor, T. Ast, C. G. Herbert, J. H. Brenton, and J. H. Beynon, *J. Phys. chem.* **87**, 3305 (1983).
- 51 W. J. Richter and H. Schwarz, **17**, 424-439 (1978).
- 52 A. G. Harrison and P. H. Lin, *Can. J. Chem.* **53**, 1314 (1975).
- 53 I. W. Griffiths, N. Jeffreys, A. R. Lee, and F. M. Harris, *Rapid Commun. Mass Spectrom.* **10**, 527 (1998).
- 54 S. R. Andrews, F. M. Harris, and D. E. Parry, *Chem. Phys.* **166**, 69 (1992).
- 55 I. W. Griffiths, D. E. Parry, and F. M. Harris, *Chem. Phys.* **238**, 21 (1998).
- 56 P. G. Fournier, J. Fournier, F. Salama, P. J. Richardson, and J. H. D. Eland, *J. Chem. Phys.* **83**, 241 (1985).
- 57 J. C. Severs, F. M. Harris, S. R. Andrews, and D. E. Parry, *Chem. Phys.* **175**, 467 (1993).
- 58 I. W. Griffiths, D. E. Parry, and F. M. Harris, *Int. J. Mass Spectrom.* **185-187**, 651 (1999).
- 59 R. P. Grant, F. M. Harris, S. R. Andrews, and D. E. Parry, *Int. J. Mass Spectrom. Ion Processes* **142**, 117 (1995).
- 60 S. R. Andrews and F. M. Harris, **253**, 403 (1996).

- 61 T. Ast, C. J. Porter, and J. H. Beynon, *Chem. Phys. Lett.* **78**, 439 (1981).
- 62 S. J. King, **PhD** *Studies of the Dissociation and Energetics of Gaseous Ions*, University College London, 2008.
- 63 G. Herzberg, *Electronic Spectra and Electronic Structure of Polyatomic Molecules* (D. Van Nostrand Company, New York, 1966).
- 64 H. M. Rosenstock and M. B. Wallenstein, *Proc. Nat. Acad. Sci. U.S.A.* **38**, 667 (1952).
- 65 R. A. Marcus and O. K. Rice, *J. Phys. chem.* **55**, 894 (1951).
- 66 T. Baer and W. L. Hase, *Unimolecular Reaction Dynamics: Theory and Experiments* (Oxford University Press, Oxford, 1996).
- 67 T. Baer and P. M. Mayer, *J. Am. Soc. Mass Spectrom.* **8**, 103 (1997).
- 68 N. A. Love, **PhD** *Studies of Electron Ionization*, University College London, 2005.
- 69 A. Maccoll, *Org. Mass Spec.* **26**, 234 (1991).
- 70 S. D. Price, **260**, 1 (2007).
- 71 D. Schroder and H. Schwarz, *J. Phys. chem.* **103**, 7385 (1999).
- 72 R. Abusen, F. R. Bennett, I. R. McNab, D. N. Sharp, R. C. Shiell, and C. A. Woodward, *J. Chem. Phys.* **108**, 1761 (1998).
- 73 F. R. Bennett and I. R. McNab, *Chem. Phys. Lett.* **251**, 405 (1996).
- 74 L. H. Andersen, J. H. Posthumus, O. Vahtras, H. Agren, N. Elander, A. Nunez, A. Scrinzi, M. Natiello, and M. Larsson, *Phys. Rev. Lett.* **71**, 1812 (1993).
- 75 J. Senekowitsch, S. Oniel, P. Knowles, and H. J. Werner, *J. Phys. chem.* **95**, 2125 (1991).
- 76 D. Mathur, L. H. Andersen, P. Hvelplund, D. Kella, and C. P. Safvan, *J. Phys. B* **28**, 3415 (1995).
- 77 P. W. Burnside, **PhD** *Mass spectrometric studies of dication reactions*, University of London, 2007.
- 78 D. Mathur, *Phys. Rep.-Rev. Sec. Phys. Lett.* **391**, 1 (2004).
- 79 V. Brites, K. Franzreb, J. N. Harvey, S. G. Sayres, M. W. Ross, D. E. Blumling, A. W. Castleman, and M. Hochlaf, *Phys. Chem. Chem. Phys.* **13**, 15233 (2011).
- 80 J. H. D. Eland, F. S. Wort, and R. N. Royds, *J. Elec. Spect. Rel. Phen.* **41**, 297 (1986).
- 81 P. T. Smith, *Phys. Rev.* **36**, 1293 (1930).
- 82 P. T. Smith, *Phys. Rev.* **37**, 808 (1931).

- 83 J. T. Tate and P. T. Smith, *Phys. Rev.* **39**, 270 (1932).
- 84 D. Rapp, P. Englander-Golden, and D. D. Briglia, *J. Chem. Phys.* **42**, 4081 (1965).
- 85 D. Rapp and P. Englander-Golden, *J. Chem. Phys.* **43**, 1464 (1965).
- 86 C. S. S. O'Connor and S. D. Price, *Int. J. Mass Spectrom.* **184**, 11 (1999).
- 87 C. S. S. O'Connor, N. C. Jones, K. Oneale, and S. D. Price, *Int. J. Mass Spectrom. Ion Process.* **154**, 203 (1996).
- 88 C. S. S. O'Connor, N. C. Jones, and S. D. Price, *Int. J. Mass Spectrom. Ion Process.* **163**, 131 (1997).
- 89 C. S. S. O'Connor, N. Trafadar, and S. D. Price, *J. Chem. Soc. Faraday Trans.* **94**, 1797 (1998).
- 90 B. G. Lindsay, H. C. Straub, K. A. Smith, and J. Stebbings, *J. Geophys. Res. Planets* **101**, 21151 (1996).
- 91 B. G. Lindsay, M. A. Mangan, H. C. Straub, and R. F. Stebbings, *J. Chem. Phys.* **112**, 9404 (2000).
- 92 H. C. Straub, D. Lin, B. G. Lindsay, K. A. Smith, and R. F. Stebbings, *J. Chem. Phys.* **106**, 4430 (1997).
- 93 H. C. Straub, B. G. Lindsay, K. A. Smith, and R. F. Stebbings, *J. Chem. Phys.* **105**, 4015 (1996).
- 94 H. C. Straub, B. G. Lindsay, K. A. Smith, and R. F. Stebbings, *J. Chem. Phys.* **108**, 109 (1998).
- 95 H. C. Straub, P. Renault, B. G. Lindsay, K. A. Smith, and R. F. Stebbings, *Phys. Rev.* **54**, 2146 (1996).
- 96 H. C. Straub, P. Renault, B. G. Lindsay, K. A. Smith, and R. F. Stebbings, *Rev. Sci. Instrum.* **65**, 3279 (1994).
- 97 C. C. Tian and C. R. Vidal, *J. Chem. Phys.* **108**, 927 (1998).
- 98 C. C. Tian and C. R. Vidal, *Phys. Rev. A* **58**, 3783 (1998).

Chapter 2 Experimental Details

2.1 Introduction

In this thesis a range of experimental techniques, all involving time-of-flight (TOF) mass spectrometry, have been employed to investigate the electron ionization of H₂S, CH₃OH and CF₃I, the photoionization of CF₃I, and dication-neutral reactions between I²⁺ and OCS. In this Chapter the basic principles of time-of-flight mass spectrometry (TOFMS) are discussed, with particular attention paid to the experimental setup employed to investigate the electron ionization of H₂S, CH₃OH and CF₃I, as reported in Chapters 4 – 6. Further details of the experimental setups used in the investigation of the photoionization of CF₃I and dication-neutral reaction between I²⁺ and OCS are given in Chapters 7 and 8 respectively.

In Chapters 4 – 6, the electron ionization of H₂S, CH₃OH and CF₃I are investigated using time-of-flight (TOF) mass spectrometry coupled with a two-dimensional (2D) ion coincidence technique. This experimental arrangement allows single product ions, ion pairs and ion triples formed following electron collisions with individual precursor gas molecules to be detected, identified and quantified. Such experiments enable the determination of both relative partial ionization cross-sections (PICSSs) and precursor-specific relative PICSSs for these molecules. These precursor-specific relative PICSSs, as described in the next Chapter, quantify the relative cross-sections for forming a fragment ion after single, double, triple and quadruple ionization. In addition, the 2D ion coincidence technique provides information on the energetics of the dissociation of the multiply charged ions formed in electron-molecule collisions.

2.2 Time-of-Flight Mass Spectrometry

The concept of time-of-flight mass spectrometry (TOFMS) is based on the principle that ions of different masses, when accelerated through an electric field to the same kinetic energy, will have different velocities and, therefore, different flight times over a set distance. The relationship between the flight time t_{tof} of an ion and its mass m , can be derived using a combination of Newtonian mechanics and electrostatics, as shown in Appendix A; this analysis yields a relationship between t_{tof} and the square root of the ions mass to charge ratio m/z :

$$t_{tof} = k\sqrt{\frac{m}{z}} + c \quad (2.1)$$

where k and c are constants. The value of k is dependent on the geometry of the apparatus and the voltage conditions used, while c arises due to the delays in the in the electronic timing equipment.

A major advantage of TOFMS over other types of mass spectrometric techniques is that it can be used to detect ions of all masses formed with all initial energies, continuously and simultaneously. This makes TOF mass spectrometry highly suited to the measurement of PICs and for the study of multiply charged ions, since both require the use of a multiplex mass analysis technique.

2.2.1 Two-Field Time-of-Flight Mass Spectrometry

The TOFMS used for the experiments reported in Chapters 4 – 6 in this thesis is based upon the standard Wiley-McLaren¹ two-field design, and is shown schematically in Figure 2.1.

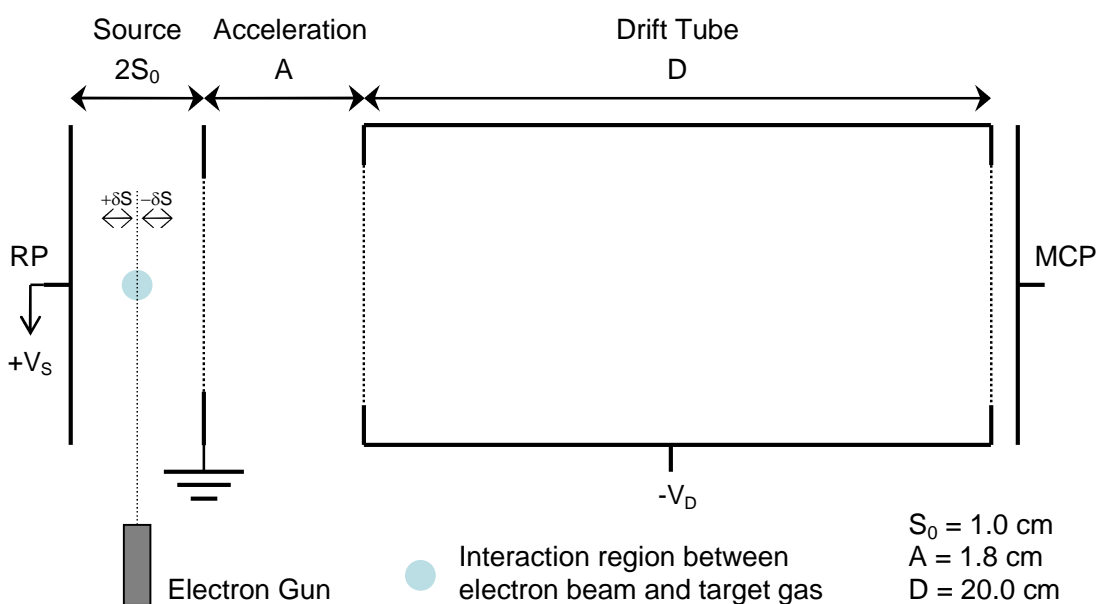


Figure 2.1: Schematic diagram of the two-field TOFMS used in Chapters 4 – 6 (not to scale).

The spectrometer can be divided into three distinct regions: the source, the acceleration region, and a field free drift tube. Ions are formed in the source region by electron ionization. The ions are accelerated out of the source region through a distance

S , by an electric field E_S formed by the application of a positive voltage to the repeller plate (RP). The ions then enter the acceleration region where they are further accelerated by a second electric field E_A , formed by a grid held at a negative potential at the entrance to the drift tube. Finally the ions enter the field free drift tube and travel at a constant velocity before impinging on a multi-channel plate (MCP) detector. Ideally ions with the same m/z should have an identical TOF in the TOFMS. However, resolution is limited by the initial spatial and kinetic energy distributions of ions formed in the source region. Methods used to reduce the time deviation for ion masses formed with an initial spatial or kinetic energy distribution, termed space and energy focusing respectively, are described below.

2.2.2 Space Focusing

In the source region of the TOFMS, there is an initial spatial distribution with which the ions are formed. This spatial distribution is in part due to the finite width of the electron beam used to ionize the target gas. Therefore, when the electric field is applied to the source region each ion will have an initial potential energy that is dependent on its initial position in the source region. After acceleration the final kinetic energy of identical mass ions will therefore not be single valued, resulting in a distribution of ion flight times centred around the ‘predicted’ ion flight time, and a reduction in the mass resolution of the TOF spectrum recorded.

The two- field MS used in Chapters 4 – 6 of this thesis is designed to reduce this time deviation in the flight times for ions of identical mass formed within a narrow range of initial positions in the source region ($S = S_0 \pm \delta S$). In this description S_0 represents the position of an ion formed in the centre of the source region with a zero initial kinetic energy. Space focusing utilises the fact that ions formed towards the back of the source (closer to the repeller plate and further from the detector) acquire a greater kinetic energy in the source field than ions formed towards the front of the source (further from the repeller plate and closer to the detector). Therefore, ions formed further away from the detector will traverse the drift region with a greater velocity, and may eventually overtake the slower moving ions formed closer to the detector. Consequently there is a plane within the drift region where ions formed within a narrow range of positions in the source region, arrive simultaneously; this is the space focus plane.¹ For ions formed initially with zero kinetic energy ($U_0 = 0$), the position of the space focus plane can be found, to first order, by:

$$\left(\frac{\delta t_{tof}}{\delta S} \right)_{U_0=0, S_0} = 0 \quad (2.2)$$

Equation 2.2 can then be applied to the equation for the total flight time of an ion in a two-field TOFMS (Equation A.13), to obtain an expression for the drift length defining the plane of focus:

$$D = 2S_0 k_0 \left(1 - \frac{d}{S_0 (k_0 + k_0^{1/2})} \right) \quad (2.3)$$

where:

$$k_0 = \frac{S_0 E_S + A E_A}{S_0 E_S} = 1 + \frac{A E_A}{S_0 E_S} \quad (2.4)$$

Equation 2.4 shows that it is the ratios of electric field strength and lengths in the source and acceleration regions that are key in the space focusing conditions. Therefore, for fixed values of S_0 and A , the plane of space focus can be moved in a two-field TOFMS, to a shorter or longer distance from the ion source, by adjusting the ratio of E_A/E_S . The aim is to therefore choose a set of voltage conditions such that the plane of space focus coincides with the plane of the detector. Table 2.1 summarises the typical operating voltages used in Chapters 4 – 6 of this thesis, which were chosen to provide a good first-order space focus for ions, whilst maintaining a high collection efficiency for translationally energetic ions (Section 2.3.2). Such manipulation of the space focus plane is not achievable in a one-field TOFMS, which only has geometric ‘space focusing’ independent of the electric field strengths.¹

In 1993, Eland² demonstrated that second-order space focusing could also be achieved by setting both the first and second order derivatives of the flight time expression (Equation A.13) to zero. Second-order space focusing means that the spread of TOFs for ions of the same m/z with different initial source positions is even smaller than for first-order focusing. What is more, the space focusing conditions apply over a wider range of initial S . However, for a two-field TOFMS of fixed geometry, only a single solution to the second order space focusing condition exists:

$$\frac{A}{D} = 2 + \frac{6}{(k_0 - 3)} \quad (2.5)$$

The principal result of this second-order focusing condition is to significantly lengthen the acceleration region in proportion to the source. For the current experimental geometry (Figure 2.1), Equation 2.5 yields a negative value of k_0 , implying that second order focusing conditions cannot be achieved without geometric modification of the apparatus. However, such a modification to the apparatus would not necessarily be beneficial for the measurement of PICSSs, as the increase in the length of the acceleration region would likely result in greater losses of energetic ions.

2.2.3 Energy Focusing

In the source region of the TOFMS, ions are formed with an initial distribution of velocities. This is true of all ions as each ion will possess at least a small amount of thermal kinetic energy. Consider two ions (A and B) of identical mass and formed at the same initial position S in the source region, with equal, but oppositely directed speeds. Ion A is formed with an initial velocity towards the detector ($+v_x$) while ion B is formed with an equal but oppositely directed velocity away from the detector ($-v_x$). As ion B moves away from the detector, it is decelerated due to E_S , until it stops. Ion B will then be accelerated back to its original position in the source S , where it will have an equal and opposite velocity ($+v_x$) to when it was formed (Figure 2.2). Subsequently, the motion of ion B is identical to that of ion A which it continues to lag by the ‘turn-around’ time.¹ It is this ‘turn-around’ time which results in a broadening of peaks in the mass spectrum, caused by the initial velocity distribution of the ions.

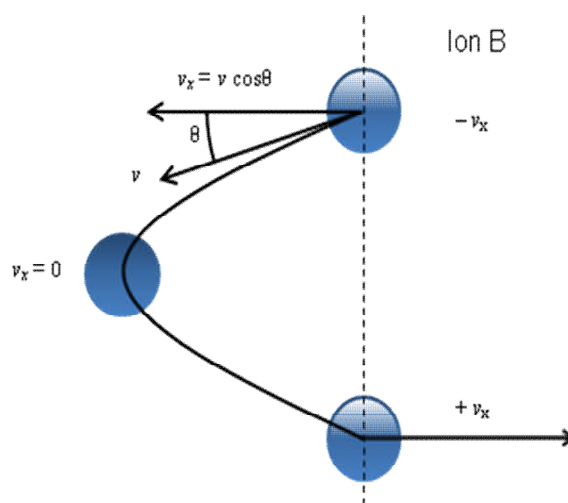


Figure 2.2: Diagram showing the ‘turn-around’ time of an ion formed with an initial velocity directed away from the detector.

One method that can be used to correct for the turn-around time in a two-field TOFMS is known as time-lag energy-focusing.¹ In this method, a time lag is introduced between the time of ion formation and the application of the accelerating pulse. During this time lag, ions with an initial velocity component directed away from the detector will move to a position in the source region of higher potential energy. Upon application of the source electric field, such ions will be accelerated to a greater kinetic energy than ions formed with initial velocity components directed towards the detector, which they may eventually overtake in the drift tube. For a given combination of E_S and E_A , it is therefore possible to choose a time lag which corrects for the initial velocity distribution of ions of equal mass.

However, this method of energy focusing can only be used with limited success to improve mass resolution, due to a number of issues. Firstly, as the conditions for time-lag focusing are mass dependent, they can only be used to achieve energy focusing within a narrow range of ion masses. Secondly, the conditions of time-lag focusing require that $\delta t_{\text{tof}}/\delta S$ is negative, and are therefore not compatible with the conditions for space-focusing. Finally, the introduction of a time lag prior to the application of the source electric field may result in the loss of translationally energetic ions. Therefore, in the experimental setup used in Chapters 4 – 6 of this thesis, the time-lag is minimised to eliminate such energetic ion losses. In fact, the absence of a time-lag enables useful information regarding the initial kinetic energy of ions to be extracted from the experimental peak shapes (Section 3.5).

2.2.4 Ion Turn-Around Time

Under the space focusing conditions used in Chapters 4 – 6 of this thesis, the ion turn-around time t_t of an ion can be derived using Newtonian mechanics:

$$t_t = \frac{v_x - (-v_x)}{a} = \frac{2v \cos \theta}{a} \quad (2.6)$$

where v_x is the component of an ions initial velocity along the flight axis (Figure 2.2), v is the ions total initial velocity at an angle θ relative to the flight axis ($\theta = 0^\circ$ is parallel and $\theta = 90^\circ$ is perpendicular to the flight axis), and a is the ion acceleration in the source electric field E_S . Substituting Equations A.3 and A.5 gives:

$$t_t = \frac{2p \cos \theta}{qE_S} = \frac{2(2mU_0)^{1/2} \cos \theta}{qE_S} \quad (2.7)$$

Equation 2.7 shows, that under space focusing conditions, the turn-around time is proportional to the component of initial ion momentum along the flight axis p . It follows that:

$$t_{tof} = t_0 - \frac{p \cos \theta}{qE_s} \quad (2.8)$$

where t_0 is the flight time of an ion formed with a zero momentum component along the flight axis. Equation 2.8 shows that the time deviation distribution in a mass spectrum is therefore equivalent to the distribution of initial momentum components along the spectrometer axis. This means that ions formed with a single valued initial momentum release, isotropically distributed over all laboratory angles θ , will give rise to a flat-topped time distribution in the mass spectrum,³ centred at t_0 and with width $2p/qE_s$. It is therefore possible to extract information on the initial kinetic energy release of ions U_0 , by analysis of the peak widths in TOF mass spectra,⁴ as described in Section 3.5.

2.3 Experimental Setup

A schematic diagram of the TOFMS used in Chapters 4 – 6 of this thesis is shown in Figure 2.3. The spectrometer is housed in a stainless steel chamber evacuated by a diffusion pump. A turbomolecular pump mounted by the detection region maintains a low gas-pressure in the vicinity of the MCP detector. Typical operating parameters for the TOFMS used to record mass spectra are given in Table 2.1.

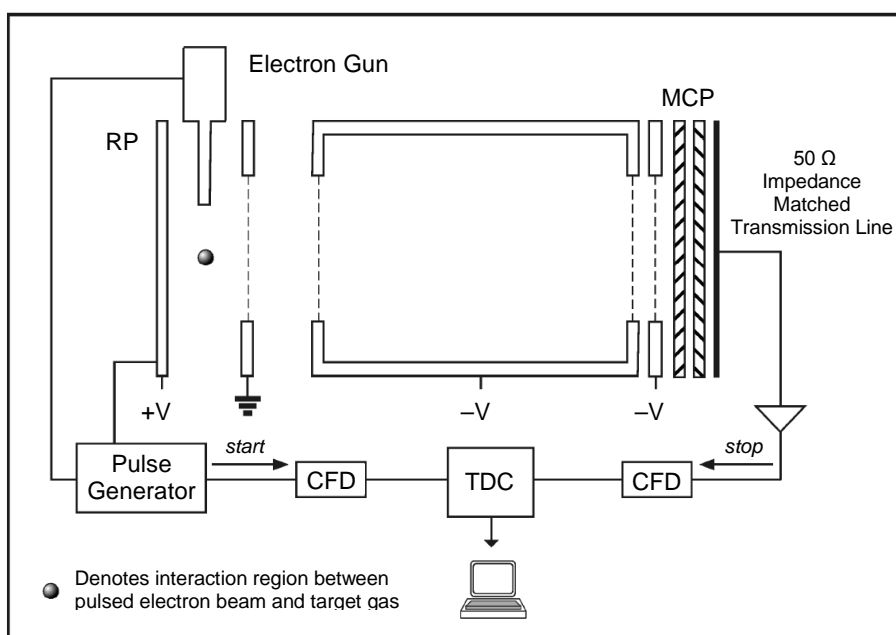


Figure 2.3: A schematic diagram of the TOFMS used in Chapters 4 – 6 of this thesis.

Table 2.1: Typical operating parameters for the TOFMS used in Chapters 4 – 6 of this thesis.

Parameter	Typical Value	Parameter	Typical Value
RP Voltage	+ 400 V	CFD dead-time	32 ns
Drift Tube Voltage	– 1600 V	Discriminator Threshold	25 mV
MCP Front Voltage	– 2050 V	Ion Count Rate	< 300 ion s ⁻¹
MCP Back Voltage	– 250 V	Target Gas Pressure	~ 1 × 10 ⁻⁶ Torr

2.3.1 Source Region

Target gas molecules are ionized in the source region of the MS following the interaction with a pulsed beam of electrons. Both the target gas beam and pulsed electron beam are transported to the centre of the source region *via* hypodermic needles. These needles are mounted perpendicular to one another and are both aligned perpendicular to the TOF axis.

The experiment is controlled by a pulse generator, running at 50 kHz, which pulses the electron gun and repeller plate (RP), and produces ‘start’ signals to begin each timing cycle of the data collection electronics. The electron gun (Figure 2.4) consists of a filament, a stainless steel base plate and optics (extraction lens and focusing lens), which serve to extract and transport the electrons from the filament to the needle entrance in the source region. In the absence of a trigger pulse from the pulse generator, the base plate is held at a negative potential to stop the electrons reaching the needle entrance. When a ‘start’ trigger is received from the pulse generator, a pulsed voltage is applied to the base plate to allow a pulse of ionizing electrons to pass through the needle entrance, and into the source region. The electron gun produces approximately 30 ns pulses of ionizing electrons in the energy range 30 – 200 eV, at a repetition rate of 50 kHz, with an estimated energy resolution of 0.5 eV FWHM. To obtain well-resolved spectra, the applied pulse and bias voltages are optimised at each electron energy. Using a pulsed electron beam ensures that ionization occurs immediately before ion extraction, reducing the time ions reside in the source region and minimising losses that may occur due to translationally energetic ions.

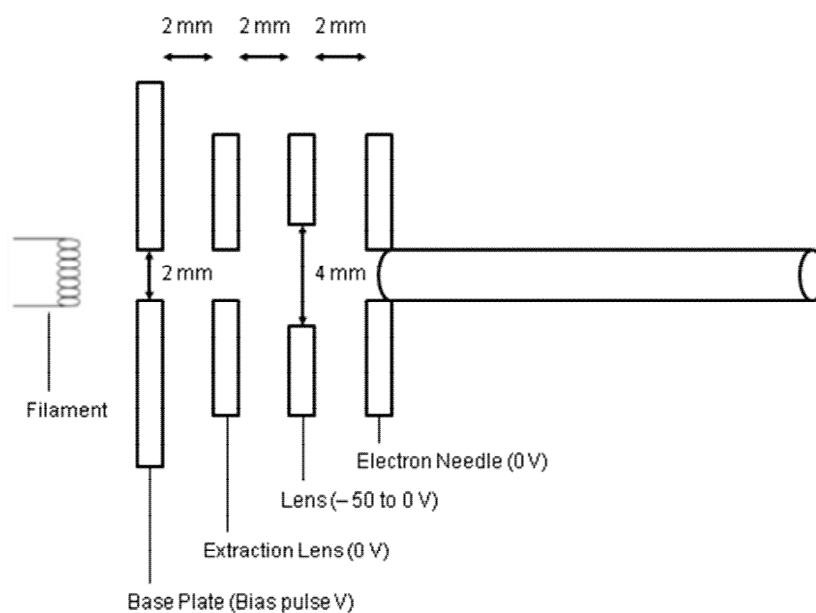


Figure 2.4: A schematic diagram of the electron gun, showing typical operating voltages and approximate dimensions.

Following the passage of electrons through the source region, the repeller plate is pulsed from 0 to +400 V to extract all positive ions formed in the source region into the acceleration region. After the ions are accelerated further, they pass into the field-free drift tube before impinging on the MCP detector. The time delay x between the pulse of ionizing electrons and the repeller plate pulse (Figure 2.5) is minimised to ensure that there is limited time for energetic fragment ions to leave the focused volume in the source region. However, a small delay is required to ensure the repeller plate is not pulsed 'on' before the pulse of ionizing electrons has passed through the source region; in this event electrons are deflected towards, and collide, with the repeller plate, giving rise to an increase in level of background noise and ion signals.

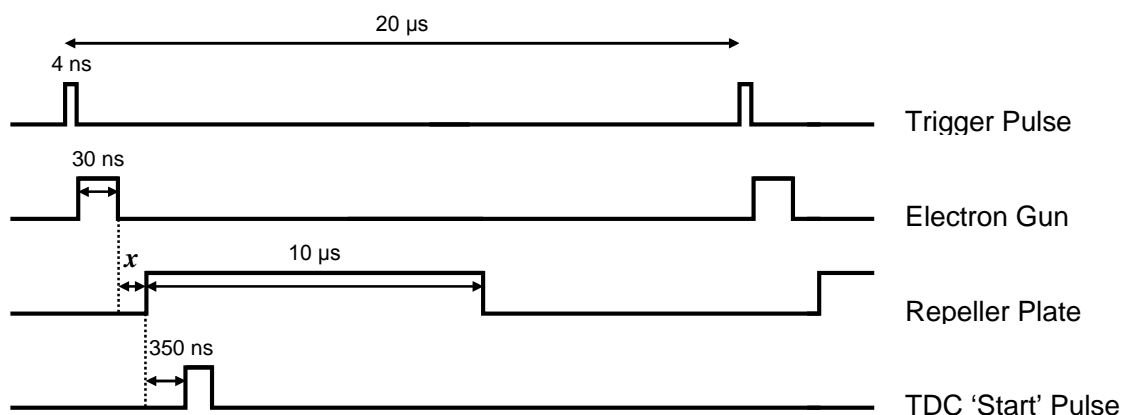


Figure 2.5: A summary of the pulse sequencing and timing used for the TOFMS.

350 ns after the repeller plate pulse a ‘start’ signal is sent from the pulse generator to the time-to-digital (TDC) converter *via* a constant fraction discriminator (CFD). The ‘start’ signal is sent to the data collection electronics after application of the extraction voltage to prevent any radio frequency (RF) noise formed by the pulsing of the repeller plate being detected and recorded.

2.3.2 Detection and Data Collection

The MCP detector is of a commercial design, comprised of two identical parallel glass plates of diameter 40 mm. Each plate is composed of an array of micro-channels of approximately 15 μm in diameter. These channels have a low work-function coating that releases electrons when an ion impacts their surface, effectively working as miniature electron multipliers.⁵ The channel axes are biased at a small angle to the normal of the MCP input surface, and the two plates are aligned to form a chevron arrangement. Ions impinging on the front surface of the MCP result in an output pulse of approximately 10^6 electrons, which is collected by a copper anode. The resulting signal is then amplified, discriminated using a CFD, and passed as a ‘stop’ pulse to the TDC. The CFD has a dead-time of 32 ns during which time further output pulses from the detector cannot be processed.

After each ‘start’ pulse the TDC is capable of receiving up to 32 ‘stop’ pulses from the detector within a 6000 ns time window. If during this time window a single stop pulse is received, one ion flight time is stored as an event in the memory. If the TDC receives two or three stop pulses in the time window, then two or three ion flight times are stored, as a single event in each case. The data is accumulated in a 512 kb memory module *via* a fast encoding and readout analog-to-digital conversion system interface, and is transferred periodically to a personal computer. Hence, this method allows the simultaneous recording of both TOF mass spectra and ion coincidence spectra.

2.3.3 Ion Discrimination Effects

In extracting quantitative data from a pulsed electron-beam TOFMS, it is important to ensure that all ions are detected with equal efficiency regardless of their mass. Through careful measurement of the Ar^{2+} to Ar^+ ratio following the electron ionization of argon, Bruce and Bonham⁶ investigated a number of experimental parameters that may give rise to mass-dependent discrimination effects. Following their

investigation, Bruce and Bonham⁶ found that the relative intensity of the Ar^{2+} and Ar^+ ions was dependent on the background gas pressure, the MCP bias voltage, and the CFD threshold setting. In accordance with the recommendations of Bruce and Bonham,⁶ and Straub *et. al.*,⁷ a MCP detector bias voltage greater than 2000 V was used for the experiments reported in Chapters 4 – 6 of this thesis, together with an experimentally optimised CFD threshold setting. In addition, the experiments reported in Chapters 4 – 6 were performed with a background gas pressure below 2×10^{-7} Torr. These experimental operating conditions, together with those listed in Table 2.1, ensure that no mass discrimination effects occurs in the experimental apparatus used in Chapters 4 – 6 of this thesis, as confirmed by the good agreement of the measured $\text{Ar}^{2+}/\text{Ar}^+$ ratio to that optimised by Bruce and Bonham.⁶

In addition to ensuring that no mass discrimination effects are occurring, to accurately determine PICSs is it crucial that the apparatus also detects all ions with equal efficiency regardless of their initial kinetic energy.⁸ This is of particular importance when studying fragmentation processes involving multiple ionization, as such events usually involve large kinetic energy releases (KERs).^{3,9}

Assuming that ionization occurs at the centre of the source region, the maximum component of initial velocity perpendicular to the TOF axis v_y an ion may possess and still impact on the detector (Figure 2.6), is given by:

$$v_y < \frac{r_{\text{det}}}{t_{\text{tof}}} \quad (2.9)$$

where r_{det} is the radius of the detector (20 mm) and t_{tof} is the flight time of an ion of mass m . This velocity can be related to the to the maximum component of translational kinetic energy perpendicular to the TOF axis an ion may possess and still be detected:

$$E_y = \frac{1}{2} m v_y^2 \quad (2.10)$$

therefore:

$$E_y < \frac{m}{2} \left(\frac{r_{\text{det}}}{t_{\text{tof}}} \right)^2 \quad (2.10)$$

Of course, Equation 2.10 is independent of the mass of the ion considered, as the flight time of an ion is proportional to the square of the ions mass ($t_{tof} \propto \sqrt{m}$). Using the flight time of an Ar^+ ion (2780 ns), a value of $E_y < 10.7$ eV is obtained.

Curtis and Eland⁹ determined that the total KER from the dissociation of small molecular dications to be, commonly, less than 9 eV; therefore the majority of energetic fragment ions formed *via* dissociative double ionization should reach the detector in this apparatus. However, ions with a translational energy component greater than 10.7 eV perpendicular to the TOF axis will miss the detector, as shown schematically in Figure 2.6. Ion losses due to translationally energetic ions ($E_y > 10.7$ eV) can however be identified and corrected, from the ion coincidence data, as described in Section 3.2.2.2.

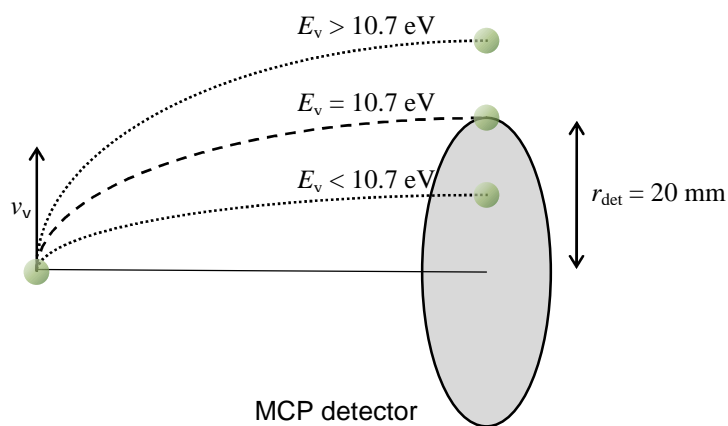


Figure 2.6: A schematic diagram showing the collection of translationally energetic ions at the detector.

2.4 Data Sets

2.4.1 Single Spectrum

Following each ionizing pulse of electrons, events in which a single ion is detected are termed ‘singles’, and are recorded as a list of individual flight times by the TDC. A singles spectrum, as shown in Figure 2.7, is a histogram of these flight times, showing the number of ions counts in each time-of-flight channel. Singles spectra are calibrated by measuring the flight times of two known ion peaks. Using these times, together with the m/z of the ions, a pair of simultaneous equations can then be constructed using the TOF expression $t_{tof} = k\sqrt{m} + c$ and solved to find the constants k and c .

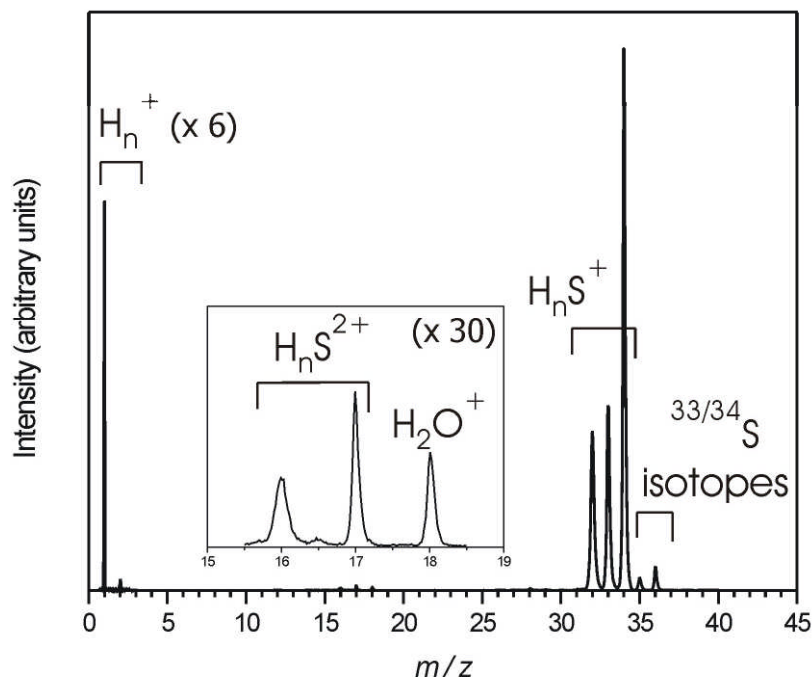


Figure 2.7: A singles mass spectrum of hydrogen sulphide (H_2S) recorded following electron ionization at 200 eV.

In the ionizing electron energy range investigated in Chapters 4 – 6 of this thesis, detection of a single ion mainly results from ionization events in which only a single positively charged ion is formed. However, due to the ion detection efficiency f_i of the apparatus being less than unity, multiple ionization events in which an ion pair or triple are formed may also contribute to the singles spectrum. For example, if an ion from dissociative double ionization is detected at the MCP but its correlated ion pair partner is missed, this ion flight time will be assigned to the data set containing single ion flight times, and plotted in the singles spectrum. Figure 2.8 indicates the various ionization channels that can contribute to the singles spectra. In this figure f_i represents the probability that an ion formed is detected by the apparatus, whereas $(1 - f_i)$ represents the probability that an ion formed will not be detected by the apparatus. In the experiments described in Chapters 4 – 6 of this thesis, ionization events removing 5 or more electrons are neglected, due to the low intrinsic probability of such events in the energy regime under investigation.¹⁰ Figure 2.8 also neglects the possibility of

detecting a tetracation (X^{4+}) in the singles spectra, due to absence of any observed tetracations following electron ionization of H_2S , CH_3OH and CF_3I in Chapters 4 – 6.

The contribution of fragment ions from dissociative multiple ionization to the singles spectrum is impossible to prevent experimentally. It is, however, possible to distinguish between fragment ions formed *via* dissociative single ionization and those formed *via* dissociative double, triple and quadruple ionization using, an ion coincidence technique. The 2D ion coincidence technique employed in Chapters 4 – 6 of this thesis allow the contribution of fragment ions from dissociative multiple ionization to the singles spectrum to be determined numerically, and corrected for in the data processing, as described below and in more detail in Chapter 3.

2.4.2 Pairs Spectrum

Events in which two ions are detected following a single ionizing pulse of electrons are termed ‘pairs’. A pairs spectrum (Figure 2.9) is generated by plotting flight times of coincident ion pairs in a 2D histogram. The flight time of the lightest ion t_1 is plotted on the y -axis, against the flight time of its correlated partner t_2 on the x -axis. The pairs spectra is therefore a histogram of ion pair peak intensities as a function of the flight times of the ion pairs formed *via* a dissociative ionization event. In the energy regime investigated in Chapters 4 – 6 of this thesis, the majority of ion pairs recorded are monocation-monocation ion pairs, largely formed *via* dissociative double ionization (Figure 2.8). In addition, dication-monocation pairs, largely formed *via* dissociative triple ionization, and dication-dication, trication-monocation pairs, largely formed *via* quadruple ionization, may also contribute to the pairs spectrum. As discussed previously, contributions to the mass spectra from quintuple or higher ionization are assumed to be negligible at electron energies below 200 eV. The pairs spectra therefore allows fragment ions X^+ formed *via* dissociative double, triple and quadruple ionization, to be distinguished from those formed *via* dissociative single ionization, shown in the singles spectra. By the same principle, the pairs spectra allows the dication fragment ions X^{2+} formed *via* dissociative triple and quadruple ionization, to be distinguished from those formed *via* dissociative double ionization. Thus, by collecting pairs data concurrently with conventional TOF mass spectra, a more detailed understanding of the formation and fragmentation of a molecule following ionization is obtained.

See page 235 for Figure 2.8

Figure 2.8: A probability tree indicating the various ionization channels that contribute to the ion singles and 2D ion coincidence spectra recorded by the experiment. The ion detection efficiency of the apparatus is denoted by f_i .

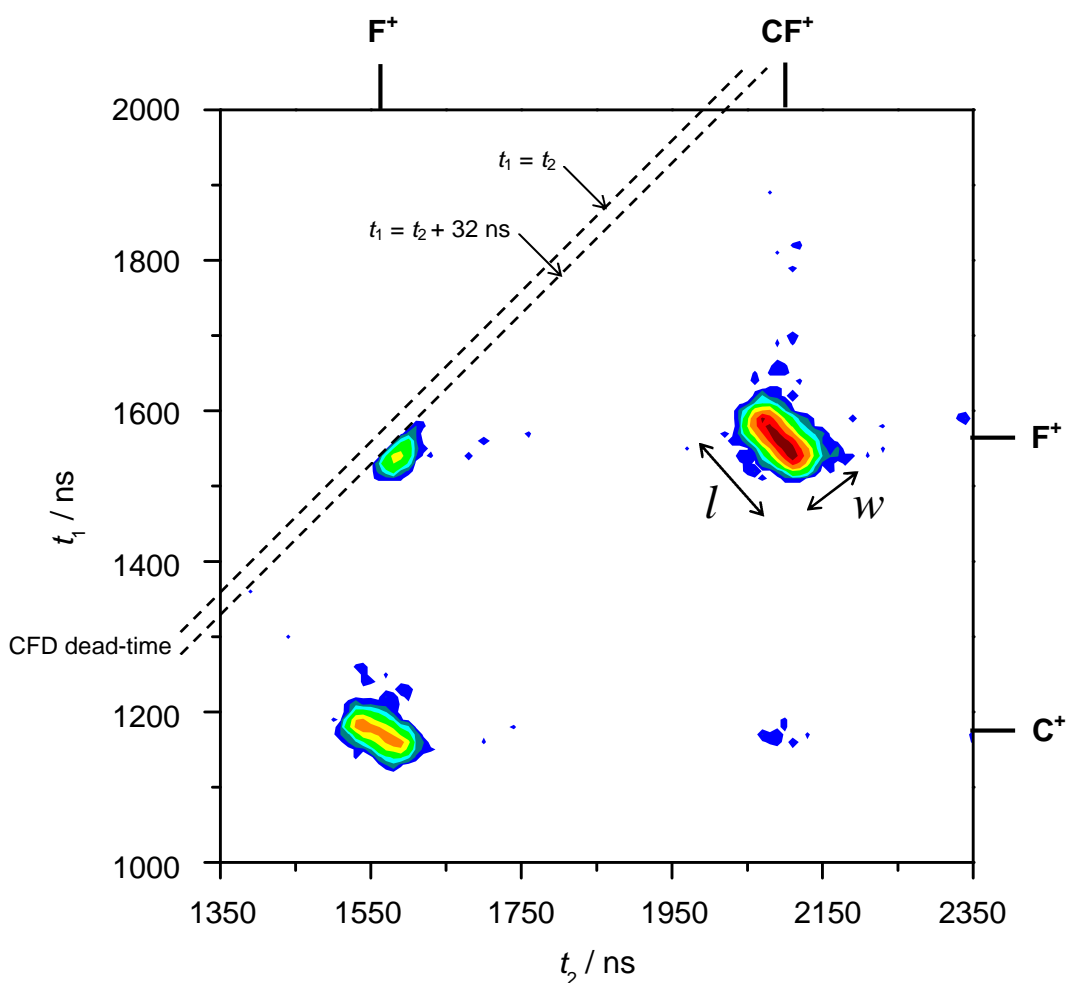


Figure 2.9: A section of the pairs mass spectrum of CF_3I formed following electron ionization at 200 eV, showing the ion pairs $\text{CF}^+ + \text{F}^+$, $\text{F}^+ + \text{F}^+$ and $\text{F}^+ + \text{C}^+$, together with a (small) false coincidence ion pair $\text{CF}^+ + \text{C}^+$.

2.4.2.1 False Coincidences

To produce a ‘real’ ion pair, both ions must originate from the same ionization event in the source region and be detected. There will however be a contribution to the pairs spectra from ‘false’ coincidences, where two ions formed by separate ionization events in the source are detected in coincidence following a single pulse of ionizing electrons. These false coincidences can be minimised by operating at low target gas pressures and low ionization rates, however they are impossible to eliminate completely as this would require infinitely long data acquisition times with infinitely low ionization rates. False coincidences can, however, be estimated, and thus subtracted from the pairs

spectrum, using an autocorrelation function as described in detail in Section 3.2.2.1. Typical operating pressures in the TOFMS used in Chapters 4 – 6 of this thesis were of the order 1×10^{-6} Torr, as recorded by an ion gauge. These low pressures employed in conjunction with low ionization rates of < 300 ions per second (controlled by adjusted the filament emission current), ensure that on average there is very much less than one ionization event in the source per ionizing pulse of electrons, thereby reducing the number of false coincidences to acceptable levels.¹¹

2.4.2.2 Time of Flight Difference Plots

In addition to presenting ion pair data as a 2D histogram, one dimensional spectra can also be produced in which the ion pair counts are plotted as a function of the difference between the two ions TOFs ($t_2 - t_1$). These one dimensional spectra are termed time-of-flight difference (Δ TOF) plots, and are usually constructed for a single ion pair peak in the pairs spectrum. Figure 2.10 shows a Δ TOF plot for the $I^+ + CF_2^+$ ion pair formed *via* dissociative double ionization of CF_2I . Ion pairs formed with a single-valued momentum release will typically give rise to a flat-topped distribution in the Δ TOF plot. If the momentum release is not single-valued, or more complicated dynamics are involved in the dissociation process, then a stepped or more rounded distribution may be observed. These Δ TOF plots are particularly useful in identifying energetic ion losses, which appear as a ‘hollowing out’ in the centre of the plot. Where energetic ion loss is observed the number of counts lost can be estimated using the fact that the peak shape should be flat-topped, as discussed in detail in Section 3.2.2. Δ TOF plots also allow corrections to be made for dead-time losses. Due to the dead-time of the discrimination circuitry, an ion pair will not be detected if the second ion arrives at the detector within 32 ns of the first ion. In this event, the flight time of the first ion is recorded as a single ion, and placed in the singles spectra. This affects ion pairs in which the two ions have very similar or identical mass to charge ratios. For the majority of identical ion pairs this dead-time does not obscure the whole ion pair peak, as the ion pairs that have a large difference in flight times (> 32 ns) are still detected and assigned to the pairs spectrum. These dead-time losses can be quantified and thus corrected for using a simple geometric procedure, as described in Section 3.2.2.3.

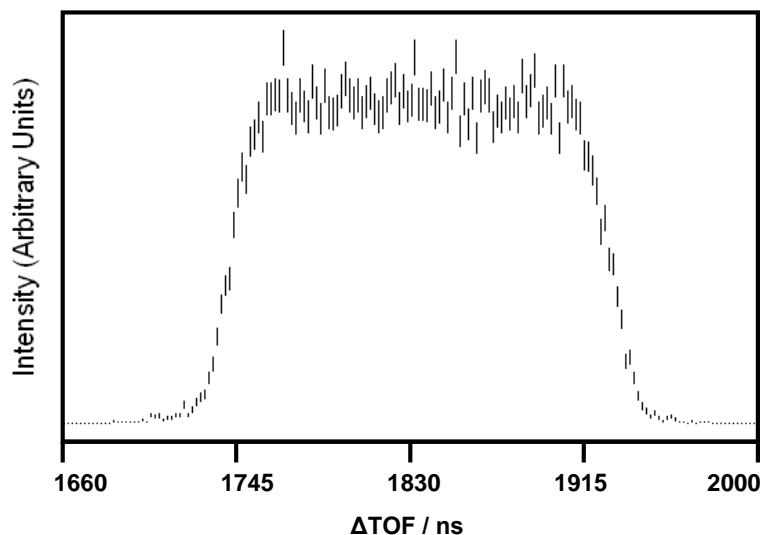


Figure 2.10: A Δ TOF plot for $\text{I}^+ + \text{CF}_2^+$ ion pairs formed *via* dissociative double ionization of CF_3I , at 200 eV electron energy. The flat-topped distribution is indicative of a single-valued momentum release upon ion pair formation, isotropically distributed over all laboratory angles.

2.4.2.3 Dynamics and Energetics of Multiply Charged Ion Dissociations

By inspection of the ion pair peaks appearing in a pairs spectrum, it is possible to obtain information on the dissociation dynamics and energetic involved in the dissociation of the multiply charged ions forming the ion pairs.^{3,12,13} As shown in Figure 2.9, peaks in the pairs spectra are typically lozenge shaped, with varying slopes, lengths (l) and widths (w). It was previously shown that the time deviation of ions in the mass spectrum is proportional to the component of initial momentum along the spectrometer axis (Equation 2.8). Therefore, the gradient or slope of an ion pair peak provides a measure of the correlated momentum between the two ions.³ Hence, the gradient of an ion pair peak observed in the pairs spectra can provide information on the mechanism of a given multiply charged ion dissociation, as described in detail in Section 3.4. The length l of an ion pair peak (Figure 2.9) relates to the distribution of initial ion momenta along the TOF axis, and provides information on the KER involved in ion pair formation.³ The width w of the ion pair peaks arise from random thermal velocities of the target gas before ionization and dissociation, the temporal resolution of the apparatus¹⁴ and the dissociation mechanism. The determination of KERs and dissociation pathways by interpretation of ion pair peaks is discussed in greater detail in Chapter 3.

2.4.3 Triples

Events involving the arrival of three ions at the detector following a single pulse of ionizing electrons are termed ‘triples’. Ion triples are initially displayed as a one-dimensional histogram, called a triples mass spectrum, showing the number of ion counts against ion flight times (Figure 2.11 Left). A TOF range is then specified for a particular reference ion, and all ion triples containing at least one ion whose arrival time falls within this specified range extracted. The flight times of the remaining two ions forming the ion triple are then plotted as 2D histogram (t_2 versus t_3), resulting in a pairs spectrum in which each ion pair is formed in coincidence with the selected reference ion, called a coincident pairs spectrum (Figure 2.11 Right).

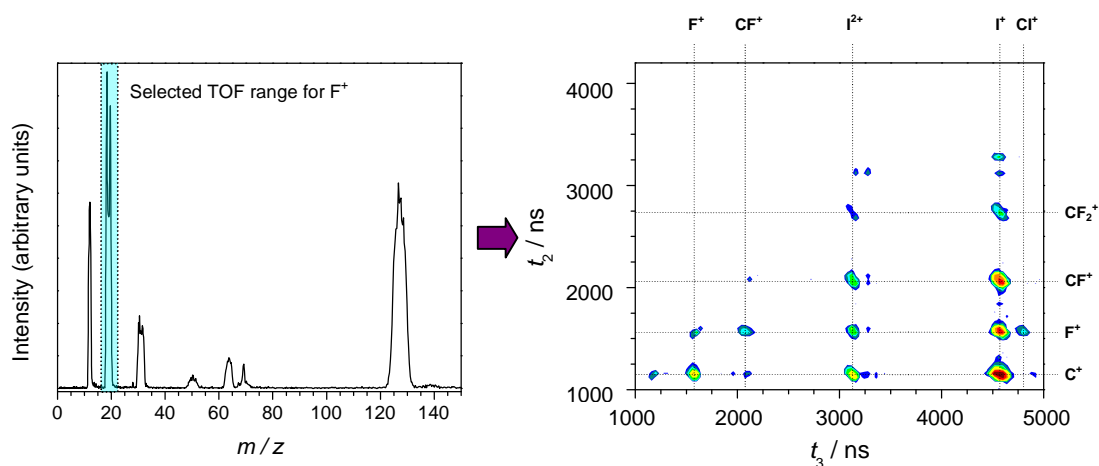


Figure 2.11: A representative one-dimensional triples mass spectrum (left) of CF_3I recorded following electron ionization at 200 eV, together with the coincident pairs spectrum in which all ion pairs are also in coincidence with a F^+ ion.

The majority of ion triples recorded are monocation triples, formed *via* dissociative triple ionization, however in some cases triples in which a dication is observed in coincidence with two monocations are recorded, formed *via* dissociative quadruple ionization. As discussed previously, contributions to the mass spectra from quintuple or higher ionization are assumed to be negligible at electron energies below 200 eV. Contributions from ion quadruples is also neglected, since following extended runs in which the data collection time was significantly increased, the number of events in which four ions were detected in coincidence was still negligible.

To produce a ‘real’ ion triple, all three ions must originate from the same ionization event in the source region and be detected. All triples spectra will however

contain contributions from ‘false’ triples, events in which three ions detected following a single pulse of ionizing electrons originate from more than one ionization event in the source. Under the typical operating conditions used in the experiment, false ion triples are composed mainly of real ion pairs formed from a charge separating dissociative ionization event, detected in coincidence with a single ion from a separate ionization event. These false ion triples can be quantified and thus subtracted from the triples mass spectrum using an extended form of the ion autocorrelation function,¹⁵ as described in Section 3.2.3.1.

2.5 Conclusion

This Chapter presented the basic principle of time-of-flight mass spectrometry, together with space and energy focusing techniques that can be employed to improve mass resolution. Following this a detailed description of the experimental setup used in the investigation of electron-molecule collisions reported in Chapters 4 – 6 was presented. This description included details of the TOFMS and 2D ion coincidence technique used, together with details of the singles, pairs and triples data sets that are produced by the experiment. In the following Chapter, the various analysis procedures that are used to process these data sets are presented. Firstly the procedures used to extract ion intensities from the singles, pairs and triples spectra are presented, followed by how these ion intensities are processed to yield relative and precursor-specific relative PICSs. Finally, the methods for analyzing the ion pairs peaks recorded in the 2D coincidence spectra, used to derive information regarding the dynamics and energetics involved in charge separating dissociations of molecular dications, is presented.

2.6 References

- 1 W. C. Wiley and I. H. McLaren, *Rev. Sci. Instrum.* **26**, 1150 (1955).
- 2 J. H. D. Eland, *Meas. Sci. Technol.* **4**, 1522 (1993).
- 3 J. H. D. Eland, *Mol. Phys.* **61** (1987).
- 4 J. L. Franklin, P. M. Hierl, and D. A. Whan, *J. Chem. Phys.* **47**, 3148 (1967).
- 5 J. L. Wiza, *Nucl. Instrum. Meths.* **162**, 587 (1979).
- 6 M. R. Bruce and R. A. Bonham, *Z. Phys. D* **24**, 149 (1992).
- 7 H. C. Straub, M. A. Mangan, K. A. Lindsay, K. A. Smith, and R. F. Stebbings, *Rev. Sci. Instrum.* **70**, 4238 (1999).

- 8 R. F. Stebbings and K. A. Lindsay, *J. Chem. Phys.* **114**, 4741 (2001).
- 9 D. M. Curtis and J. H. D. Eland, *Int. J. Mass Spectrom. Ion Processes* **63** (1985).
- 10 C. C. Tian and C. R. Vidal, *Phys. Rev. A* **58**, 3783 (1998).
- 11 L. J. Frasinski, P. A. Stankiewicz, P. A. Hatherly, and K. Codling, *Meas. Sci. Tech.* **3**, 1188 (1992).
- 12 J. H. D. Eland, *Vacuum Ultraviolet Photoionization and Photodissociations of Molecules and Clusters* (World Scientific, Singapore, 1991).
- 13 J. H. D. Eland, *Laser Chem.* **11**, 259 (1991).
- 14 P. J. Richardson, J. H. D. Eland, P. G. Fournier, and D. L. Cooper, *J. Chem. Phys.* **84**, 3189 (1986).
- 15 S. J. King and S. D. Price, *J. Chem. Phys.* **127**, 174307 (2007).

Chapter 3 Data Collection and Analysis

3.1 Introduction

This chapter presents the various analysis procedures used to process the data recorded by the pulsed TOF mass spectrometer and 2D ion coincidence technique, described in Chapter 2. Firstly, the procedures used to extract ion intensities from the mass spectra are described, followed by how these intensities are processed to produce relative partial ionization cross-sections (PICSs) and precursor-specific relative PICSs. Finally, the methods for analysing the ion pair peaks recorded in the 2D coincidence spectra are described, from which information concerning the fragmentation dynamics and energetics of multiply charged dissociations can be derived.

3.2 Spectral Intensities

3.2.1 Singles Mass Spectra

The intensities of ion peaks in the in the singles spectra, $I_1[X^+]$ for monocations, $I_2[X^{2+}]$ for dications, and $I_3[X^{3+}]$ for trications, are determined by summing the counts in the peak, and applying a small correction to account for the nonzero baseline due to background counts. For each ion peak the level of background is evaluated in a nearby region of the spectrum where no ion peaks are observed (Figure 3.1). This background level is then scaled appropriately to give the number of background counts that contribute to the peak of interest, and subtracted from the raw peak intensity.

In the singles mass spectra recorded in Chapters 4 – 6 of this thesis, there is a small but unavoidable contribution from ions arising due to the ionization of the background gas (air and water) in the vacuum chamber. These residual gas signals are the result of the low target-gas pressures employed in the experiment to minimise false coincidences. If these residual gas ions add to the number of counts in the various ion peaks of interest, they can be subtracted using a simple procedure, described using the following example. In the singles spectra of CF_3I (Chapter 6), ionization of residual O_2 results in the formation O_2^+ at $m/z = 32$, which contributes to the intensity of the broad CF^+ peak at $m/z = 31$. In addition, ionization of residual H_2O results in H_2O^+ at $m/z = 18$, which contributes to the intensity of the broad F^+ peak at $m/z = 19$. To quantify these background contributions, the relative intensity of O_2^+ with respect to N_2^+ ,

$\sigma[\text{O}_2^+/\text{N}_2^+]$, following electron ionization of air was measured, as a function of electron energy, and the relative intensity of H_2O^+ with respect to OH^+ , $\sigma[\text{H}_2\text{O}^+/\text{OH}^+]$, following electron ionization of water was measured, as a function of electron energy. The subtraction of ions from the residual gas can then be made by normalization to the N_2^+ and OH^+ peaks in each singles spectrum:

$$I_1[\text{CF}^+] = I[31] - I[28] \times \sigma \left[\frac{\text{O}_2^+}{\text{N}_2^+} \right] \quad (3.1)$$

$$I_1[\text{F}^+] = I[19] - I[17] \times \left[\frac{\text{H}_2\text{O}^+}{\text{OH}^+} \right] \quad (3.2)$$

where $I[31]$, $I[28]$, $I[19]$ and $I[17]$, represent the measured peak intensities at $m/z = 31$, 28, 19 and 17 respectively, after the subtraction of background counts (due to the peaks at $m/z = 31$ and 19 being broad, they span the mass ranges 30 – 32 and 18 – 20 respectively). The final intensity of CF^+ and F^+ ions in the singles spectrum formed by dissociative ionization of CF_3I , is then given by $I_1[\text{CF}^+]$ and $I_1[\text{F}^+]$ respectively.

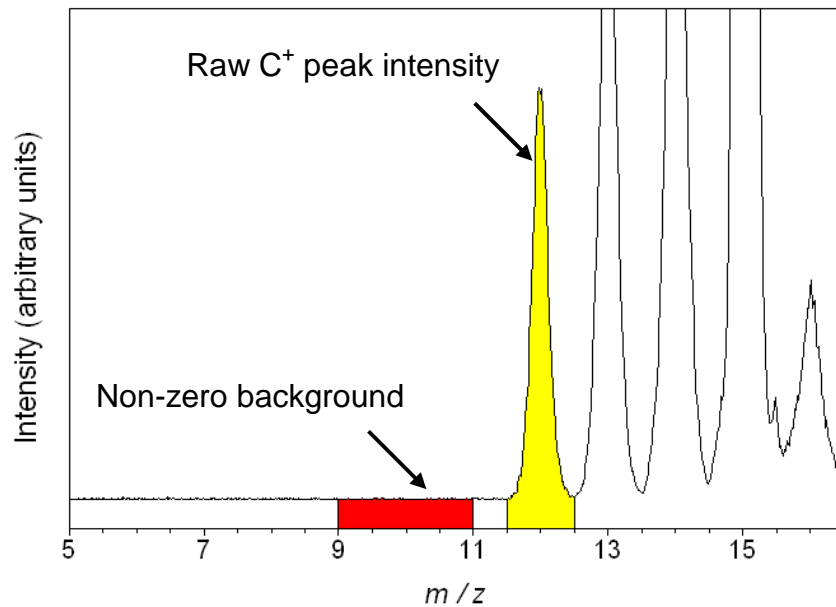


Figure 3.1: A diagram showing a typical measurement of the background count level in the singles mass spectrum of CH_3OH recorded at 200 eV.

In the singles mass spectrum, it is not possible to distinguish between isotopes of fragment ions occurring at the same mass, for example $\text{H}_2^{32}\text{S}^+$, H^{33}S^+ and $^{34}\text{S}^+$ ions at $m/z = 34$ formed by electron ionization of H_2S (Chapter 5). In these events, the measured ion intensities were corrected numerically for isotopic speciation using the natural isotopic distribution, for example $^{32}\text{S}:^{33}\text{S}:^{34}\text{S}$ (95.0%:0.8%:4.2%). Such a correction is demonstrated below for the above example:

$$I[\text{S}^+] = I[32] \times \frac{100}{95.0} \quad (3.3)$$

$$I[\text{HS}^+] = \left(I[33] - I[\text{S}^+] \frac{0.8}{100} \right) \times \frac{100}{95} \quad (3.4)$$

$$I[\text{H}_2\text{S}^+] = \left(I[34] - I[\text{S}^+] \frac{4.2}{100} - I[\text{HS}^+] \frac{0.8}{100} \right) \times \frac{95.0}{100} \quad (3.5)$$

where the final intensity of S^+ and HS^+ and H_2S^+ ions in the singles spectrum formed by dissociative ionization of H_2S is then given by $I_1[\text{S}^+]$, $I_1[\text{HS}^+]$ and $I_1[\text{H}_2\text{S}^+]$ respectively.

3.2.2 Pairs Mass Spectra

As previously discussed in Chapter 2, the pairs spectrum is displayed as a 2D histogram of the respective ion flight times (t_1 vs. t_2) of the two ions in a pair (Figure 3.2). The intensity of a peak in the pairs spectrum, for example, $P[\text{X}^+ + \text{Y}^+]$, is found by summing the counts in the peak lying within a specified region, as shown in Figure 3.2. The contribution of a fragment ion to the pairs spectrum, for example, $P_2[\text{X}^+]$, is then obtained by summing the counts in all appropriate peaks involving the ion X^+ . A distinction is made between ion counts from pairs of monocations, $P_2[\text{X}^+]$, monocation-dication pairs, $P_3[\text{X}^+]$ and $P_3[\text{X}^{2+}]$, monocation-trication pairs, $P_4[\text{X}^+]$ and $P_4[\text{X}^{3+}]$, and dication-dication pairs, $P_4[\text{X}^{2+}]$. Contributions from ion triples to intensities of ion pairs may arise when only two ions of an ion triple are detected, due to the ion detection efficiency of the apparatus being less than unity (Figure 2.8). As described previously, ion quadruples (the formation of four separate ions in a single ionization event) are neglected in our analysis.

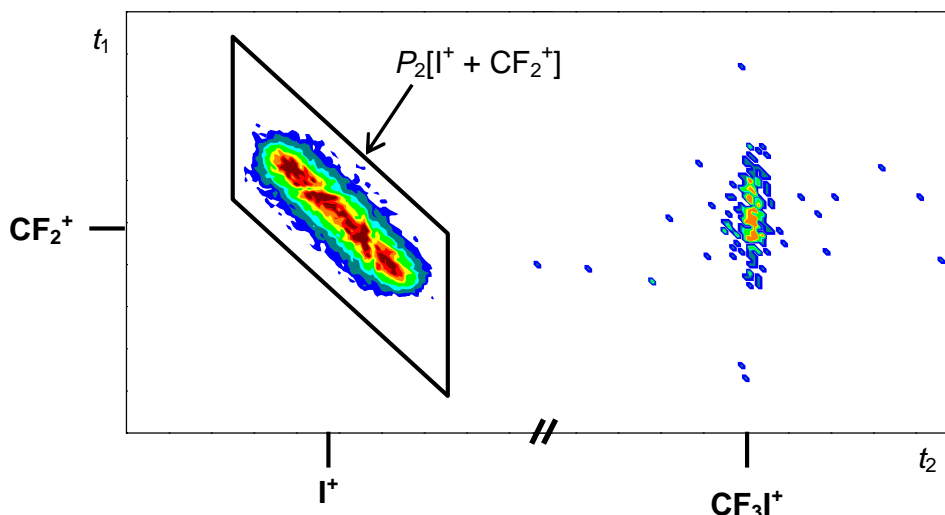


Figure 3.2: Representative ion pair peaks observed following electron ionization of CF_3I recorded at 200 eV, showing the ‘true’ $\text{I}^+ + \text{CF}_2^+$ ion pair peak, and the false coincidence $\text{CF}_3\text{I}^+ + \text{CF}_2^+$ peak.

3.2.2.1 False Ion Coincidence Subtraction

As discussed in Section 2.4.2.1, all pairs spectra will contain a contribution from false coincidences, events in which two ions are detected in coincidence that did not originate from the same ionization event; for example, two singly charged ions formed from the dissociation of two parent ions formed in the same pulse of ionizing electrons. Any purely false coincidence ion pair peaks in the pairs spectrum can be readily identified by their characteristic ‘round’ shape (Figure 3.2), formed as the ions show no momentum correlation, resulting from their separate formation. False ion pair peaks therefore usually consist of two ion pair masses that cannot be formed from the same dissociative ionization event, such as the parent ion and another fragment ion.

There is also a contribution from false coincidences to real ion pair peaks. These false coincidences are subtracted manually from the raw ion pair peak intensity using an ion auto-correlation function.^{1,2} Firstly, a number of purely false coincidences are identified in the pairs spectrum, for example the $\text{CF}_3\text{I}^+ + \text{CF}_2^+$ peak observed in the pairs spectrum of CF_3I^+ (Figure 3.2). The intensity of each false pair peak is then divided by the product of the relevant ion intensities in the corresponding singles mass spectrum to obtain a normalization factor α :

$$\alpha = \frac{P[\text{CF}_3\text{I}^+ + \text{CF}_2^+]}{I[\text{CF}_3\text{I}^+]I[\text{CF}_2^+]} \quad (3.6)$$

The single ion intensities used in Equation 3.6 are the raw peak intensities measured in the corresponding singles spectrum, prior to any correction for background counts or residual gasses. The individual normalization factors are then used to derive an average normalization factor, α' . The number of false coincidence counts, $F[X^+ + Y^{m+}]$, that contribute to a real ion-pair peak, for example $I^+ + F^+$, can be calculated using α' and the corresponding single ion intensities:

$$F[X^+ + Y^{m+}] = \alpha' I[X^+] I[Y^{m+}] \quad (3.7)$$

The ‘true’ number of counts in the ion pair $P_n[X^+ + Y^{m+}]$ is then found by subtracting the number of false coincidences from the raw pair peak intensity. The low count rates ($< 300 \text{ ion s}^{-1}$) employed in Chapters 4 – 6 of this thesis minimise the contribution to the pairs spectra from false coincidences, which were typically found to be less than 1 – 3 % of a real ion-pair peak intensity at an electron energy of 200 eV.

3.2.2.2 Energetic Ion Pair Loss Correction

As discussed in section 2.3.3, under the voltage conditions used in the apparatus, fragment ions with a translational energy component of up to 10.7 eV perpendicular to the TOF axis will be efficiently collected at the detector. Curtis and Eland³ determined the kinetic energy release (KER) from a dication dissociation to be commonly less than 9 eV, so the majority of energetic fragment ions formed *via* dissociative double ionization should reach the detector. However, ions formed with a translational energy component of greater than 10.7 eV perpendicular to the TOF axis will miss the detector. If these energetic ions comprise ion pairs, they can, however, be quantified and corrected for, by forming a Δ TOF plot for the ion pair (Section 2.4.2.2). As shown by Figure 3.3, the ion pairs that are missed are those where the KER between the two ion fragments is aligned perpendicular to the TOF axis; such ion pairs contribute to the central region of the Δ TOF plot. Thus, a ‘hollowing’ of the central region of the Δ TOF plot clearly indicates energetic ion losses.⁴ To correct for such losses, an appropriate geometric construction is used to estimate the number of counts missed, as shown in Figure 3.4, which is then added to the pairs peak intensity $P_n[X^+ + Y^{m+}]$. It should be noted, however, that ion losses from any single ion fragments formed with a translational energy component of greater than 10.7 eV perpendicular to the TOF axis, cannot be quantified.

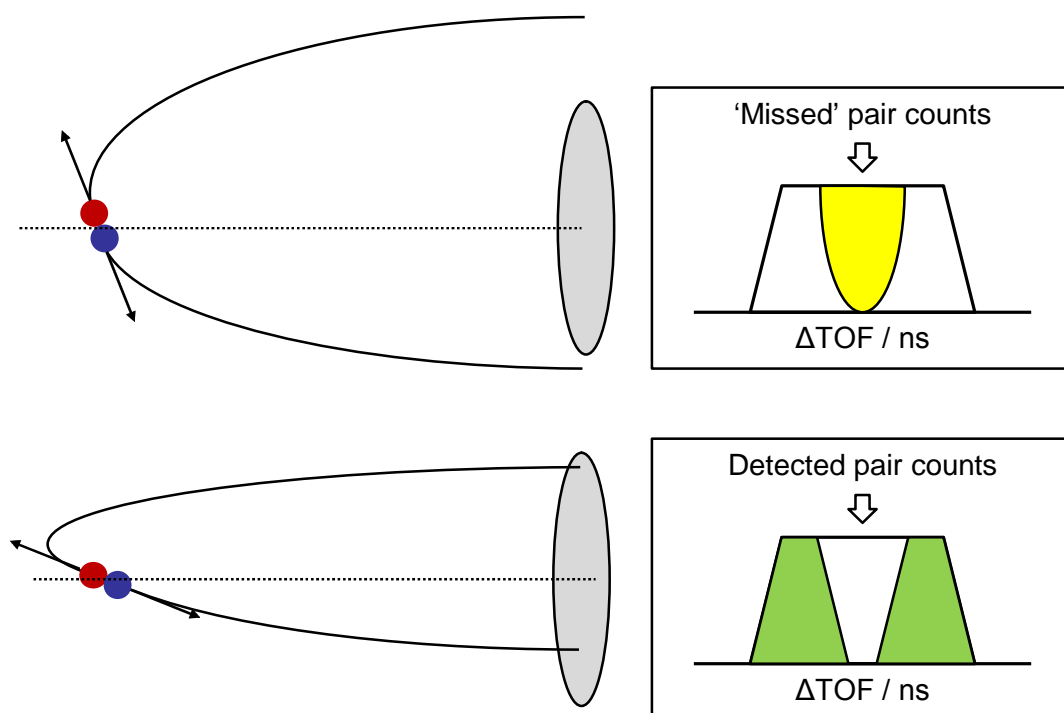


Figure 3.3: A diagram showing the collection of energetic ions at the detector. Ion pairs formed with a translational energy component of greater than 10.7 eV perpendicular to the TOF axis (top) results in the loss of ion pair counts in the centre of the ΔTOF plot.

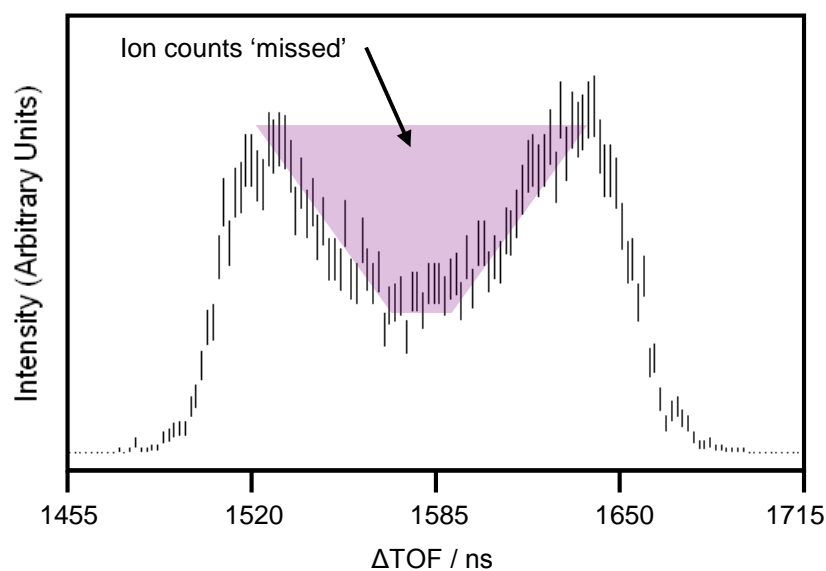


Figure 3.4: A ΔTOF plot for the $\text{I}^{2+} + \text{F}^+$ ion pair formed *via* dissociative triple ionization of CF_3I , at 200 eV electron energy. The 'hollowed' centre of the peak indicates energetic ion losses, which can be corrected using an appropriate geometric construction.

3.2.2.3 Correction for Dead-Time Losses

As described in Chapter 2, an ion will not be detected if it arrives at the detector within 32 ns of another ion due to the dead-time of the discriminatory circuitry. Therefore, there exists a region in the pairs spectrum close to the diagonal ($t_1 = t_2$) in which no ion pairs are recorded, called the dead region (Figure 2.9). This affects ion pairs in which the two ions have very similar or identical mass to charge ratios. For such ion pairs, a portion of the ion pair peak is missing from the pairs spectrum, as shown for the $F^+ + F^+$ ion pair in Figure 2.9. These dead-time ion losses can be easily estimated by first creating a Δ TOF plot for the affected ion pair (Figure 3.5). As can be seen from Figure 3.5, ion pairs within the 32 ns dead-region are missing. The number of missing ion pairs is then found by appropriately extrapolating, using simple geometry, the peak height to the limit of $t_1 - t_2 = 0$. The number of lost counts is then added to the measured peak intensity to correct for the dead-time losses. This extrapolation utilises the fact that, in most cases, the time difference distribution is flat-topped⁵ in the dead-time region. However, if the width of the distribution is smaller than the dead-time width of 32 ns, the full peak height will not be reached by the observable portion of the ion pair peak. In this event, the extrapolation represents a lower limit of the true number of ion pairs lost.

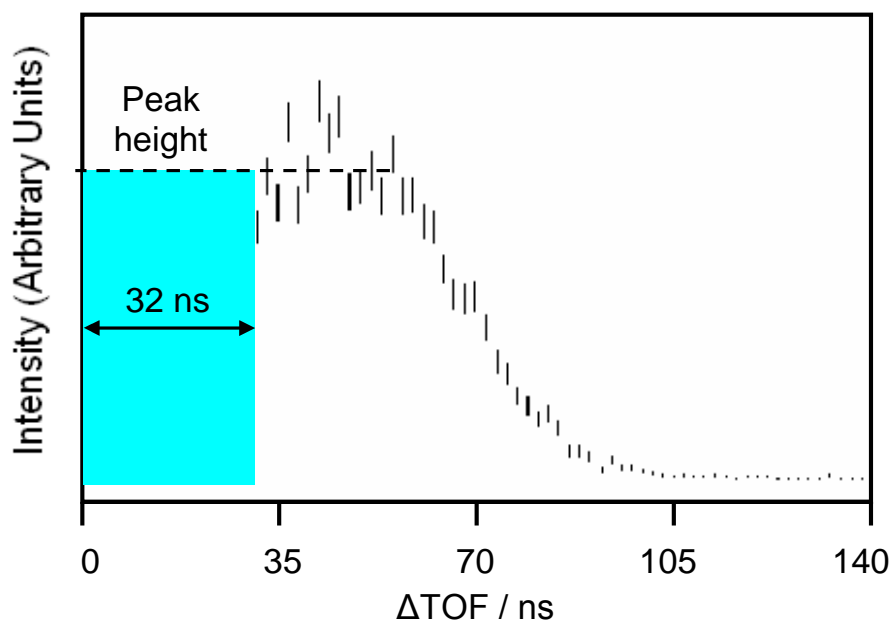


Figure 3.5: A Δ TOF plot for the $F^+ + F^+$ ion pair formed following electron ionization of CF_3I at 200 eV. The dead-time losses are estimated by extrapolating the peak height to the $t_1 - t_2 = 0$ limit.

3.2.3 Triples Mass Spectra

As previously described in Section 2.4.3, ion triples are processed by first specifying a time-of-flight range for a particular ion, and then extracting all ion triples containing at least one ion whose arrival time falls within this window. The remaining two flight times are then plotted as a 2D histogram (t_2 vs. t_3). The intensity of each peak in the triples spectrum, $T_n[X^+ + Y^+ + Z^{m+}]$, is found by summing the number of counts in each peak. The contribution of a fragment ion to the triples spectrum, for example $T_3[X^+]$, is then obtained by summing the counts in all appropriate peaks involving the ion X^+ . A distinction is made between ion counts from triples of monocations, $T_3[X^+]$, and from a dication-monocation-monocation triple, $T_4[X^+]$ and $T_4[X^{2+}]$. As previously mentioned in Chapter 2, possible contributions from ion quadruples, or quintuple or higher ionization, are neglected.

3.2.3.1 False Triple Ion Coincidence Correction

As previously discussed, to produce a real ion triple, all three ions detected must originate from the same ionization event. However, as for the pairs spectra, triples spectra will also contain contributions from false ion triples. These false ion triples may arise in one of two ways:

- (i) Following a single pulse of electrons, three separate ionization events form three separate single ions that are detected in coincidence.
- (ii) Following a single pulse of electrons, two separate ionization events form a 'real' ion pair and an ion single, which are detected in coincidence.

To effectively quantify the number of false coincidences that contribution to a real ion triple peak, the contribution from both possible routes needs to be evaluated. For the first false coincidence route, in which three ions from three separate ionization events are detected, a purely false ion triple peak $A^+ + B^+ + C^+$ is selected, for which no contributions from real ion pairs detected in coincidence with a single ion from a separate ionization event (i.e. false coincidences from route ii) are possible. For example, in the triples spectrum of CF_3I (Chapter 6) the $CF_3I^+ + CF_3^+ + CF^+$ triple peak would be such a false coincidence, as neither $CF_3I^+ + CF_3^+$, $CF_3I^+ + CF^+$ or $CF_3^+ + CF^+$ are real ion pairs. The triples peak intensity is then divided by the product of the corresponding single ion intensities recorded in the singles mass spectrum, to obtain a normalization factor γ , relating to the number of false coincidences formed by three separate ionization events (Equation 3.8):

$$\gamma = \frac{T[A^+ + B^+ + C^+]}{I[A^+]I[B^+]I[C^+]} \quad (3.8)$$

To evaluate false triple coincidences from the second route, another purely false ion triple peak $D^+ + E^+ + F^+$ is selected, for which contributions from both two or three separate ionization events are possible. For example, the $CF_3I^+ + I^+ + CF_2^+$ peak in the triples spectrum of CF_3I . A normalization factor β relating to the number of false triples formed by two separate ionization events, involving one ion pair and a single ion, can then be derived as:

$$\beta = \frac{T[D^+ + E^+ + F^+] - \gamma I[D^+]I[E^+]I[F^+]}{I[D^+]P[E^+ + F^+] + I[E^+]P[D^+ + F^+] + I[F^+]P[D^+ + E^+]} \quad (3.9)$$

In Equation 3.8, the numerator is the number of false ion triples due to two separate ionization events, obtained from the raw triples peak intensity minus the contribution of false ion triples from three separate ionization events (Equation 3.8). The denominator is all possible combinations of two separate ionization events involving a real ion pair and a single ion giving rise to the false ion triple. Analysis has shown that the vast majority of false ion triples arises from two separate ionization events, and that $\gamma \approx 0$. Thus, contributions from three separate ionization events may be neglected when calculating the number of false ion-triple counts. Therefore, the number of false ion-triples, $F[X^+ + Y^+ + Z^+]$, that contribute to a real ion-triple, $X^+ + Y^+ + Z^+$, can be found using Equation 3.10:

$$F[X^+ + Y^+ + Z^+] = \beta (I[X^+]P[Y^+ + Z^+] + I[Y^+]P[X^+ + Z^+] + I[Z^+]P[X^+ + Y^+]) \quad (3.10)$$

3.3 Relative Partial Ionization Cross-Sections

The ion intensities recorded in the singles, pairs, and triples spectra are processed to yield relative PICSs and precursor-specific relative PICSs. The relative PICSs for the formation of fragment monocations X^+ are represented as $\sigma_r[X^+]$, for dications X^{2+} as $\sigma_r[X^{2+}]$, and for trications X^{3+} as $\sigma_r[X^{3+}]$, and are expressed relative to the cross-section for forming the parent ion. Similarly, precursor-specific relative PICSs for the formation of fragment ions are symbolized by $\sigma_n[X^{m+}]$ ($m = 1, 2$ or 3 for monocations, dications and trications respectively), and represent the cross-section for

forming a fragment ion by single ($n = 1$), double ($n = 2$), triple ($n = 3$) or quadruple ($n = 4$) ionization, relative to the cross-section for forming the parent ion. As described previously, contributions to the ion yield from ion quadruples, and quintuple or higher order ionization, are neglected in the data analysis. The PICSs derived in this thesis are expressed relative to the cross-section for forming the parent monocation, as the parent monocation is typically formed in large abundance, making it suitable as a reference ion. In addition, as parent monocations are initially formed with a thermal kinetic energy distribution, they are least susceptible to ion discrimination effects in most mass spectrometric experiments.^{6,7} Thus, existing PICS data reported in the literature for the formation of the parent monocation is generally the most reliable, enabling a comparison between the relative PICSs reported in this thesis and those derived from existing literature data. In the following sections, the data reduction algorithms used to derive these relative PICSs are presented in detail.

3.3.1 Peak Intensities in the Singles, Pairs and Triples Mass Spectra

The intensity of a fragment monocation X^+ in the singles spectrum can be related to the number of ions formed by ionization events during the data acquisition period, as shown by Equation 3.11:

$$I_1[X^+] = f_i N_1[X^+] + f_i(1 - f_i) N_2[X^+] + f_i(1 - f_i) N_{3pair}[X^+] + f_i(1 - f_i) N_{4pair}[X^+] + f_i(1 - f_i)^2 N_{3trip}[X^+] + f_i(1 - f_i)^2 N_{4trip}[X^+] \quad (3.11)$$

In this equation, f_i denotes the experimental ion detection efficiency of the apparatus, while $N_n[X^+]$ represent the number of fragment ions X^+ formed *via* the loss of n electrons from the parent molecule. A distinction is made between the number of ions formed *via* dissociative triple ionization in which a monocation-dication pair is formed $N_{3pair}[X^+]$, and in which a monocation-triple is formed $N_{3trip}[X^+]$. Similarly, a distinction is made between the number of ions formed *via* dissociative quadruple ionization in which a monocation-trication pair is formed $N_{4pair}[X^+]$, and in which a monocation-monocation-dication triple is formed $N_{4trip}[X^+]$. The ion detection efficiency is included to account for the transmission efficiency of the grids that define the electric fields in the apparatus, and the less than unity efficiency of the electronics and detector. Thus, Equation 3.11 contains six contributions to the intensity of X^+ in the singles spectrum, as summarised by the probability tree shown in Figure 2.8. These are

ions detected from dissociative single ionization, three contributions from ions pairs formed by dissociative double, triple or quadruple ionization, where X^+ is detected in the absence of its correlated partner, and two contributions from ion triples formed by dissociative triple or quadruple ionization, where X^+ is detected in the absence of the other two correlated ions of the ion triple.

Similarly, the intensity of a fragment monocation X^+ in the pairs and triples spectra, $P_n[X^+]$ and $T_n[X^+]$, can be related to the number of ions formed by ionization events, as shown by Equations 3.12 – 3.16:

$$P_2[X^+] = f_i^2 N_2[X^+] + 2f_i^2(1-f_i)N_{3trip}[X^+] + f_i^2(1-f_i)N_{4trip}[X^+] \quad (3.12)$$

$$P_3[X^+] = f_i^2 N_{3pair}[X^+] + f_i^2(1-f_i)N_{4trip}[X^+] \quad (3.13)$$

$$P_4[X^+] = f_i^2 N_{4pair}[X^+] \quad (3.14)$$

$$T_3[X^+] = f_i^3 N_{3trip}[X^+] \quad (3.15)$$

$$T_4[X^+] = f_i^3 N_{4trip}[X^+] \quad (3.16)$$

The corresponding expressions for the spectral intensities of fragment dications X^{2+} and trications X^{3+} are shown in Equations 3.17 – 3.20 and 3.21 – 3.22 respectively. The number of parent ions $N_1[\text{Parent}^+]$ formed in each experiment is also related to the intensity of the parent ion observed in the singles mass spectrum $I[\text{Parent}^+]$, as shown in Equation 3.23.

$$I_2[X^{2+}] = f_i N_2[X^{2+}] + f_i(1-f_i)N_{3pair}[X^{2+}] + f_i(1-f_i)N_{4pair}[X^{2+}] + f_i(1-f_i)^2 N_{4trip}[X^{2+}] \quad (3.17)$$

$$P_3[X^{2+}] = f_i^2 N_{3pair}[X^{2+}] + 2f_i^2(1-f_i)N_{4trip}[X^{2+}] \quad (3.18)$$

$$P_4[X^{2+}] = f_i^2 N_{4pair}[X^{2+}] \quad (3.19)$$

$$T_4[X^{2+}] = f_i^3 N_{4trip}[X^{2+}] \quad (3.20)$$

$$I_3[X^{3+}] = f_i N_3[X^{3+}] + f_i(1 - f_i) N_{4pair}[X^{3+}] \quad (3.21)$$

$$P_4[X^{3+}] = f_i^2 N_{4pair}[X^{3+}] \quad (3.22)$$

$$I_1[Parent^+] = f_i N_1[Parent^+] \quad (3.23)$$

3.3.2 Relative PICS Determination

In Chapters 4 – 6 of this thesis, relative PICSs are derived for the formation of all fragment ions detected. To determine these σ_r values, it is noted that $\sigma_r[X^+]$, the relative PICS for the formation of a fragment ion X^+ with respect to the parent ion, is by definition equal to the sum of the corresponding precursor-specific relative PICSs:

$$\sigma_r[X^+] = \frac{\sum_{n=1}^{n=4} \sigma_n[X^+]}{\sigma[Parent^+]} = \sigma_1[X^+] + \sigma_2[X^+] + \sigma_3[X^+] + \sigma_4[X^+] \quad (3.24)$$

$$\sigma_r[X^{2+}] = \frac{\sum_{n=2}^{n=4} \sigma_n[X^{2+}]}{\sigma[Parent^+]} = \sigma_2[X^{2+}] + \sigma_3[X^{2+}] + \sigma_4[X^{2+}] \quad (3.25)$$

$$\sigma_r[X^{3+}] = \frac{\sum_{n=3}^{n=4} \sigma_n[X^{3+}]}{\sigma[Parent^+]} = \sigma_3[X^{3+}] + \sigma_4[X^{3+}] \quad (3.26)$$

Under the experimental conditions of low electron flux and low ionization rates used in this thesis, it can be shown that $N_n[X^{m+}]$ is proportional to $\sigma_n[X^{m+}]$ (Section 1.4):

$$\sigma_n[X^{m+}] = k N_n[X^{m+}] \quad (3.27)$$

Where k is a constant for each experiment and is dependent on experimental variables such as the target gas pressure, electron flux, and ionization volume.⁸ The relative PICSs in Equations 3.25 – 3.27 can therefore be expressed in terms of the number of ions formed by different ionization events N_n , and thus in the terms of the measured spectral intensities, using equations 3.11 – 3.23:

$$\begin{aligned} \sigma_r[X^+] &= \frac{N_1[X^+] + N_2[X^+] + N_3[X^+] + N_4[X^+]}{N_1[Parent^+]} \\ &= \frac{I_1[X^+] + P_2[X^+] + P_3[X^+] + T_3[X^+] + P_4[X^+] + T_4[X^+]}{I_1[Parent^+]} \end{aligned} \quad (3.28)$$

$$\begin{aligned}\sigma_r[X^{2+}] &= \frac{N_2[X^{2+}] + N_3[X^{2+}] + N_4[X^{2+}]}{N_1[Parent^+]} \\ &= \frac{I_2[X^{2+}] + P_3[X^{2+}] + P_4[X^{2+}] + T_4[X^{2+}]}{I_1[Parent^+]}\end{aligned}\quad (3.29)$$

$$\sigma_r[X^{3+}] = \frac{N_3[X^{3+}] + N_4[X^{3+}]}{N_1[Parent^+]} = \frac{I_3[X^{3+}] + P_4[X^{3+}]}{I_1[Parent^+]} \quad (3.30)$$

From Equations 3.28 – 3.30 it can be seen that the σ_r values are independent of the ion detection efficiency f_i . However, if the value of f_i can be determined, the data reduction can be extended to derive precursor-specific relative PICSs σ_n , quantifying the contributions to each ion yield from single, double, triple and quadruple ionization.

3.3.3 Ion Detection Efficiency

The ion detection efficiency can be determined experimentally by recording the singles and pairs spectra of CF_4 at an ionizing electron energy of 100 and 200 eV. CF_4 is chosen, as the PICSs are well characterised for this molecule, and can be extracted from published literature. Bruce and Bonham have measured absolute PICSs for the formation of single fragment ions σ_s and ion pairs σ_p following electron ionization of CF_4 , using both pulsed TOF mass spectrometry⁹ and a covariance mapping technique.¹⁰ Table 3.1 summarises the results of these separate investigations. Contributions from ion triples and quadruple or higher levels of ionization are assumed to be small and are neglected in the analysis.

Table 3.1: Absolute PICS values of Bruce and Bonham for the formation of single ions⁹ and ion pairs¹⁰ following electron ionization of CF_4 . All values have units \AA^2 . Note that the two data sets were recorded separately, and that the single ion cross-section data contains contributions from both single ions and ion pairs.

E / eV	$\sigma[C^+]$	$\sigma[F^+]$	$\sigma[CF^+]$	$\sigma[CF_2^+]$	$\sigma[CF_3^+]$	$\sigma[CF_2^{2+}]$	$\sigma[CF_3^{2+}]$	$\sum\sigma_s$
100	0.291	0.494	0.402	0.364	3.732	0.028	0.059	5.370
200	0.296	0.583	0.38	0.341	3.472	0.033	0.062	5.167

E / eV	$\sigma[C^+ + F^+]$	$\sigma[CF^+ + F^+]$	$\sigma[CF_2^+ + F^+]$	$\sigma[CF_3^+ + F^+]$	$\sigma[F^+ + F^+]$	$\sigma[CF_2^{2+} + F^+]$	$\sum\sigma_p$
100	0.041	0.142	0.076	0.071	0.025	-	0.355
200	0.144	0.261	0.099	0.083	0.117	0.002	0.706

By relating the σ_s and σ_p values of Bruce and Bonham to the total number of ions recorded in a singles spectrum, ΣI (Equation 3.31), and the total number of ions recorded in the pairs spectrum, ΣP (Equation 3.32), an expression for f_i can be derived:

$$\Sigma I = f_i k \Sigma \sigma_s \quad (3.31)$$

$$\Sigma P = 2 f_i^2 k \Sigma \sigma_p \quad (3.32)$$

$$f_i = \left(\frac{\Sigma P}{\Sigma I} \right) \left(\frac{\Sigma \sigma_s}{2 \Sigma \sigma_p} \right) \quad (3.33)$$

For each determination of the ion detection efficiency, an average value of f_i is derived from four independent experiments, two at each ionizing energy. A value for f_i was determined for each experimental study in this thesis, and is presented within each individual results chapter (Chapters 4 – 6). The average value of f_i determined over the course of all experimental investigations is approximately 0.26, in good agreement with the absolute values of f_i reported in the literature,^{3,5} values which are the product of the transmission efficiency of the apparatus and the detector efficiency.

3.3.4 Precursor-specific Relative PICS Determination

Having determined a value for the ion detection efficiency f_i , precursor-specific relative PICSs can be defined for the formation of all fragment ions. These cross-sections quantify the contribution of single, double, triple and quadruple ionization to the ion yield of a particular ion. These precursor-specific relative PICSs are first expressed in terms of the relative numbers of ions formed by ionization events N_n , then rewritten in terms of spectral intensities by substitution of Equations 3.11 – 3.23:

$$\sigma_1[X^+] = \frac{N_1[X^+]}{N_1[Parent^+]} = \frac{I_1[X^+] - \left(\frac{1-f_i}{f_i} \right) (P_2[X^+] + P_3[X^+] + P_4[X^+]) + \left(\frac{1-f_i}{f_i} \right)^2 (T_3[X^+] + T_4[X^+])}{I_1[Parent^+]} \quad (3.34)$$

$$\sigma_2[X^+] = \frac{N_2[X^+]}{N_1[Parent^+]} = \frac{\left(\frac{1}{f_i}\right)P_2[X^+] - \left(\frac{1-f_i}{f_i^2}\right)(2T_3[X^+] + T_4[X^+])}{I_1[Parent^+]} \quad (3.35)$$

$$\sigma_3[X^+] = \frac{N_3[X^+]}{N_1[Parent^+]} = \frac{\left(\frac{1}{f_i}\right)P_3[X^+] + \left(\frac{1}{f_i^2}\right)T_3[X^+] - \left(\frac{1-f_i}{f_i^2}\right)T_4[X^+]}{I_1[Parent^+]} \quad (3.36)$$

$$\sigma_4[X^+] = \frac{N_4[X^+]}{N_1[Parent^+]} = \frac{\left(\frac{1}{f_i}\right)P_4[X^+] + \left(\frac{1}{f_i^2}\right)T_4[X^+]}{I_1[Parent^+]} \quad (3.37)$$

$$\sigma_2[X^{2+}] = \frac{N_2[X^{2+}]}{N_1[Parent^+]} = \frac{I_2[X^{2+}] - \left(\frac{1-f_i}{f_i}\right)(P_3[X^{2+}] + P_4[X^{2+}]) + \left(\frac{1-f_i}{f_i}\right)^2 T_4[X^{2+}]}{I_1[Parent^+]} \quad (3.38)$$

$$\sigma_3[X^{2+}] = \frac{N_3[X^{2+}]}{N_1[Parent^+]} = \frac{\left(\frac{1}{f_i}\right)P_3[X^{2+}] - \left(\frac{1-f_i}{f_i^2}\right)2T_4[X^{2+}]}{I_1[Parent^+]} \quad (3.39)$$

$$\sigma_4[X^{2+}] = \frac{N_4[X^{2+}]}{N_1[Parent^+]} = \frac{\left(\frac{1}{f_i}\right)P_4[X^{2+}] + \left(\frac{1}{f_i^2}\right)T_4[X^{2+}]}{I_1[Parent^+]} \quad (3.40)$$

$$\sigma_3[X^{3+}] = \frac{N_3[X^{3+}]}{N_1[Parent^+]} = \frac{I_3[X^{3+}] - \left(\frac{1-f_i}{f_i}\right)P_4[X^{3+}]}{I_1[Parent^+]} \quad (3.41)$$

$$\sigma_4[X^{3+}] = \frac{N_4[X^{3+}]}{N_1[Parent^+]} = \frac{\left(\frac{1}{f_i}\right)P_4[X^{3+}]}{I_1[Parent^+]} \quad (3.42)$$

Using these precursor-specific relative PICSSs, the contribution to the total ion yield from single, double, triple and quadruple ionization, as a percentage of the total ion yield, can be easily found using Equations 3.43 – 3.46 below:

$$\% \text{ Single Ionization} = \frac{\sum \sigma_1}{\sum \sigma_r} \times 100 \quad (3.43)$$

$$\% \text{ Double Ionization} = \frac{\sum \sigma_2}{\sum \sigma_r} \times 100 \quad (3.44)$$

$$\% \text{ Triple Ionization} = \frac{\sum \sigma_3}{\sum \sigma_r} \times 100 \quad (3.45)$$

$$\% \text{ Quadruple Ionization} = \frac{\sum \sigma_4}{\sum \sigma_r} \times 100 \quad (3.46)$$

In practice, contributions from triple and quadruple ionization are usually very small at all ionizing electron energies investigated. This significantly simplifies the equations used to derive precursor-specific relative PICSSs. In fact, quadruple ionization is only observed following electron ionization of CF₃I at energies of 125 eV and above (Chapter 6), with no contribution from quadruple ionization observed following electron ionization of H₂S and CH₃OH (Chapters 4 and 5).

3.3.5 Positive Ion-Negative Ion Pair Formation

Using the experimental apparatus described in Chapter 2, only positive ions will be detected. Positive ion-negative ion pairs (Equation 3.47) formed in our experiments will therefore be indistinguishable from the formation of a positive ion plus a neutral.



Positive ions from such reactions will contribute to the recorded ion intensities, and thus be included in the relative PICS values determined. However, in the energy range investigated in this thesis (30 – 200 eV), the cross-sections for forming positive ion-negative ion pairs following electron ionization of small molecules are typically several orders of magnitude smaller than the corresponding total ionization cross-sections.¹¹

Thus, contributions from these ion pairs to the relative PICSSs reported in this thesis are therefore expected to be minor.

3.4 Dissociation Dynamics of Multiply Charged Molecular Ions

As discussed in Section 2.4.2.3, information concerning the fragmentation mechanism involved in a given dissociation reaction forming an ion pair peak can be extracted from the shape of the ion pair peak in the pairs spectrum.¹²⁻¹⁵ For this purpose the most useful parameter that can be extracted from the ion pair data is the gradient b of the ion-pair peak, sometimes referred to as the ‘peak slope’. The gradient of the chosen ion-pair peak is the gradient of a linear regression between t_1 and t_2 within the area of the chosen peak (Figure 3.2), determined using a least-squares fit method.¹⁶ Both t_1 and t_2 are given equal weightings since both ion flight times have an equal uncertainty. In determining the gradient of a chosen ion pair peak, it is important to limit the number of stray ion counts included in the peak area. These ‘stray’ counts describe any counts that do not correspond to the formation of the ion pair of interest, and include false ion coincidences. If the proportion of stray counts included in the selected peak area is too large, the fitting procedure produces a biased peak gradient. In this event, any information gained from this peak gradient would not necessarily be a true representation of the dissociation mechanism.

3.4.1 Interpretation of Experimental Peak Slopes

As described in Section 2.2.4, under the space-focusing conditions used, the flight time of an ion is proportional to the component of initial momentum along the TOF axis:

$$t_{tof} = t_0 - \frac{p \cos \theta}{qE_s} \quad (3.48)$$

where t_0 is the ideal flight time of an ion initially at rest and with no initial kinetic energy, q is the ion charge, E_s is the source electric field and p is the magnitude of initial ion momentum release at an angle θ to the flight axis. Equation 3.48 shows that the deviation of the flight time δt of an ion from the ideal t_0 is directly proportional to the

initial momentum component along the TOF axis. Therefore, for an ion pair $A^+ + B^+$ observed in the pairs spectrum, the peak gradient can be defined as:

$$b = \frac{\delta t_B}{\delta t_A} = \frac{p_B \cos \theta_B}{p_A \cos \theta_A} \left(\frac{q_A}{q_B} \right) \quad (3.49)$$

where ion B^+ is the first ion to arrive at the detector. As can be seen from Equation 3.49, the peak slope provides a measure of the correlated momentum components of the two ions of an ion pair. Therefore, by comparing the peak gradient obtained from an experiment to values predicted using simple models of the dication or trication dissociation process, information regarding fragmentation pathways can be obtained.

3.4.2 Two-Body Dissociation Reactions

In a two-body dissociation reaction there is only one possible fragmentation pathway, the direct dissociation of the molecular dication to form a pair of product ions:



Conservation of linear momentum requires that the two ions separate collinearly with an equal and opposite momentum:

$$-p_A = p_{BC} \quad (3.51)$$

Substitution of Equation 3.51 into Equation 3.49 yields a value of -1 for the peak gradient. Therefore, two-body dissociation reactions forming a pair of monocations will result in a peak in the pairs spectrum with a gradient of -1.

If the two-body dissociation reaction involves the formation of a dication-monocation pair, the ion charges must also be considered when predicting the peak slope. Substitution of Equation 3.51 into 3.49 produces two possible values of the peak gradient, depending on whether the dication or monocation fragment arrives at the detector first:

Dication fragment detected first	$ABC^{3+} \rightarrow A^{2+} + BC^+$	$b = \frac{p_A}{p_{BC}} \left(\frac{1}{2} \right) = -0.5$	(3.52)
-------------------------------------	--------------------------------------	--	--------

Dication fragment detected second	$ABC^{3+} \rightarrow A^+ + BC^{2+}$	$b = \frac{p_A}{p_{BC}} \left(\frac{2}{1} \right) = -2$	(3.53)
--------------------------------------	--------------------------------------	--	--------

3.4.3 Three-Body Dissociation Reactions

For a three-body dissociation reaction, such as that shown in Equation 3.54, in which two detectable fragment ions and one unobserved neutral species are formed, the dynamics upon dissociation can be far more complex, as these reactions can occur *via* a variety of different pathways.



These different pathways can be approximately separated into three classes of dissociation mechanism: instantaneous explosion, deferred charge separation and secondary fragmentation. In this section, these model reaction mechanisms are presented for the charge separating decay of a molecular dication ABC^{2+} forming an ion pair and a single neutral fragment, and a value of the peak gradient derived for each one.

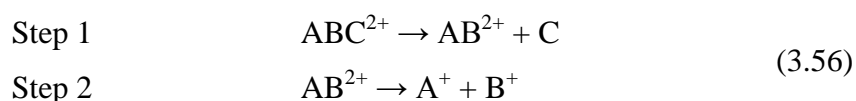
3.4.3.1 Instantaneous Explosion

An instantaneous explosion describes a reaction in which all the bonds are broken simultaneously upon ionization (Equation 3.55). Providing there are no collisions between the fragments, the two monocations separate immediately under the influence of electrostatic forces, and the neutral fragment receives no impulse. This dissociation mechanism, termed unobstructed instantaneous explosion, produces an ion pair peak with a gradient of -1 in the pairs spectrum, due to the correlation in momenta of the fragment ions, as described above for a two-body dissociation.



3.4.3.2 Deferred Charge Separation

Deferred charge separation involves the initial loss of a neutral fragment (C), followed by the charge separation of the resulting double charged fragment (AB^{2+}) in a second distinct step, as shown by Equation 3.56.

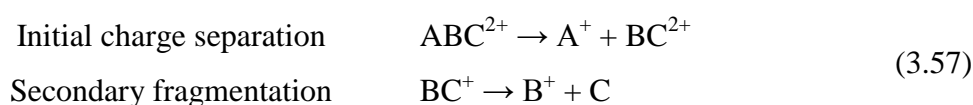


As the dominant energy release will occur on the second dissociation step, this mechanism is comparable to a simple two-body dissociation, thus producing an ion peak gradient of -1 in the pairs spectrum.^{14,17} Hence, it is difficult to distinguish

deferred charge separation from a mechanism involving an unobstructed instantaneous explosion. However, supporting evidence for a deferred charge separation reaction may appear in the pairs spectrum in the form of a ‘metastable tail’ originating from the $A^+ + B^+$ peak to the diagonal $t_1 = t_2$ of the dissociated dication.^{13,18}

3.4.3.2 Secondary Fragmentation

A secondary fragmentation describes a reaction in which, following initial charge separation of a molecular dication ABC^{2+} , one of the fragment ions undergoes a secondary fragmentation to form a daughter fragment ion and a daughter neutral fragment (Equation 3.57):



In the case of the initial charge separation, the monocations formed will have equal and opposite momenta:

$$-p_A = p_{BC} \quad (3.58)$$

However, the secondary fragmentation affects the momenta, by introducing a factor involving a mass ratio of fragment ions:

$$p_B = m_B v_{BC} = \frac{m_B}{m_{BC}} p_{BC} \quad (3.59)$$

therefore:

$$p_B = -\frac{m_B}{m_{BC}} p_A \quad (3.60)$$

Thus the peak slope predicted for a secondary fragmentation reaction is equal to the mass ratio $-m_A/m_{BC}$ or $-m_{BC}/m_B$, depending on whether B^+ is the first or second ion to arrive at the detector, respectively. However, this gradient illustrates the limiting case where the ion BC^+ has sufficient time to freely rotate and leave the Coulomb field of the other monocation before the secondary fragmentation occurs. If the ion BC^+ dissociates within the Coulomb field of its correlated partner A^+ (a fast dissociation), the daughter

monocation produced from the secondary fragmentation B^+ will possess an increased momentum and thus the gradient will move towards -1. Hence, fast secondary fragmentation reactions will produce a peak in the pairs spectrum with a gradient between the limiting cases of -1 and $-m_A/m_{BC}$ or $-m_{BC}/m_B$, depending on whether B^+ is the first or second ion to arrive at the detector, respectively.

3.5 Kinetic Energy Release Determination

It is possible to estimate the kinetic energy released upon fragmentation of a molecular dication (or triation), by interpretation of the shape of the resulting ion pair peak in the pairs spectrum.^{4,19} This is achieved by first constructing a Δ TOF plot for a particular ion pair, and then performing a Monte Carlo simulation of the dissociation process in the mass spectrometer, as described below.

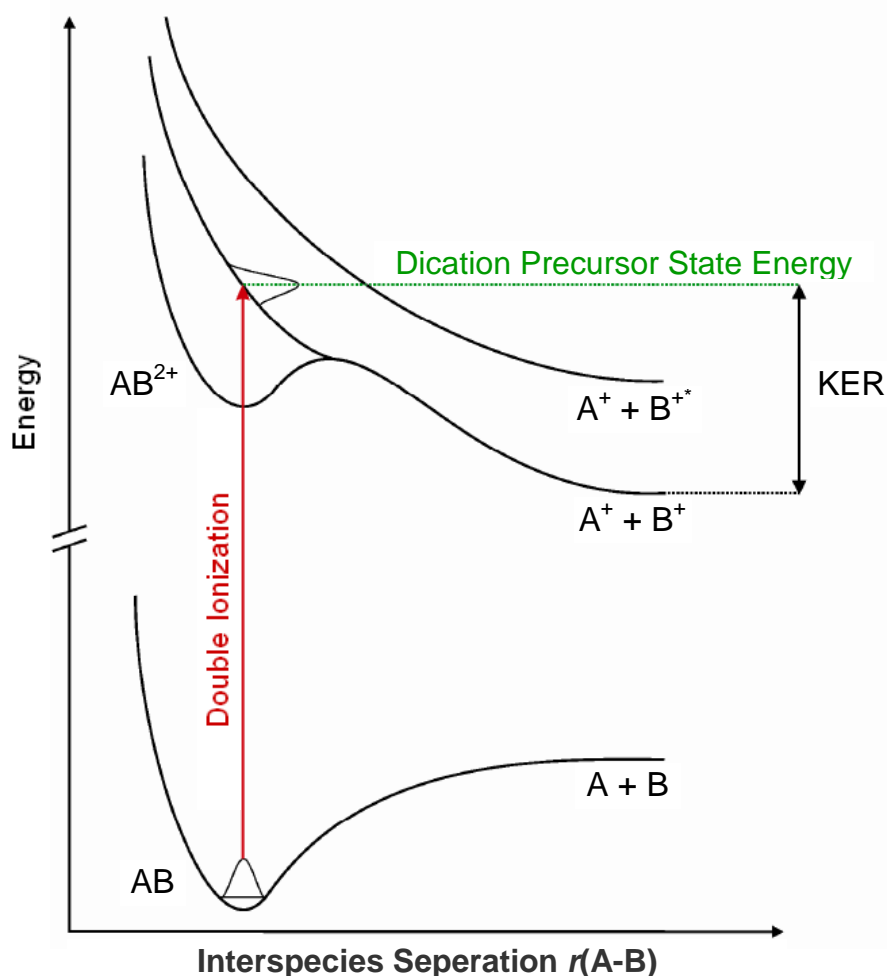


Figure 3.6: Schematic potential energy curves showing the relationship between the asymptotic energy of the dissociation limit, the KER, and the energy of the dication precursor state giving rise to the ion pair. Adapted from Ref. [20].

If the asymptotic energy E_{frag} of the dissociation limit is known, measurement of the KER enables an estimate to be made of the energy of the dication (or trication) precursor state $E(\text{AB}^{2+})$ which dissociates to form the ion pair of interest (Figure 3.6 and Equation 3.61).

$$E(\text{AB}^{2+}) = \text{KER} + E_{\text{frag}} \quad (3.61)$$

The value of E_{frag} is commonly derived using data from standard thermodynamic tables,²¹ usually assuming that the products of the dissociation are formed in their ground states. As the degree of internal excitation of the ionic fragments (and neutral fragments) is often unknown, the precursor state energies derived represent a lower limit for the electronic state energies of the molecular dication. Despite this, precursor states energies derived in this manner have been shown to be in good agreement with existing experimental and theoretical data on the electronic structure of small molecular dications.²²⁻²⁶

All ion-pair peaks recorded in the pairs spectrum exhibit an additional degree of broadening due to the finite length of the ionizing electron pulse (30 ns). This additional ion pair width adds to the uncertainty when evaluating the KER(s) for a particular ion pair. Hence, the KER values obtained by the apparatus used in Chapters 4 – 6 of this thesis are not as precise as those obtained by more advanced techniques such as PEPIICO spectroscopy¹⁹ and position sensitive coincidence methods.²⁷ However, as such complementary KER data is only available in the reported literature for a limited number of small molecular dications, KER determinations have been made, where possible, for the ion pairs observed following electron ionization of H_2S , CH_3OH and CF_3I (Chapters 4 – 6).

3.5.1 Monte Carlo Simulation

The Monte Carlo simulation used to fit ΔTOF distributions and extract KERs, uses repeated ion trajectories and calculates the ion flight times under an electrostatic model of the experimental conditions, and allows the inclusion of all experimental parameters affecting the peak shape, such as the size of the ionizing region and the distribution of KERs. The dication (or trication) dissociation is modelled with a Gaussian kinetic energy release distribution (KERD), and Gaussian spatial distribution of ionization events about the centre of the source region. The initial velocity of the

neutral molecule before ionization is represented by a Maxwell-Boltzmann distribution. The KERDs are modelled as a sum of the Gaussian energy release distributions as the KERD of the detected fragments is expected to be a direct function of the reflection of the Gaussian ground state wavefunction on the respective repulsive potential energy curves of the dication states in the Franck-Condon region (reflection approximation).^{3,17}

The weighting of initial ion velocity vectors in the simulation is also important. The initial direction of motion and orientation of the parent molecule before ionization is random, and so the motion of the ions formed by dicationic dissociation will be isotropic. However, the detection of the ions is only on a single plane. Most ions detected will therefore have a significant velocity component perpendicular to the TOF axis. To allow for the projection of a spherical velocity distribution onto the plane of the detector, the distribution of initial velocities must be sinusoidally weighted, thus ensuring that a higher proportion of ions have large velocity components perpendicular to the TOF axis. This modelling results in the satisfactory production of a square-topped peak^{5,28} in the Δ TOF plot (Figure 3.7).

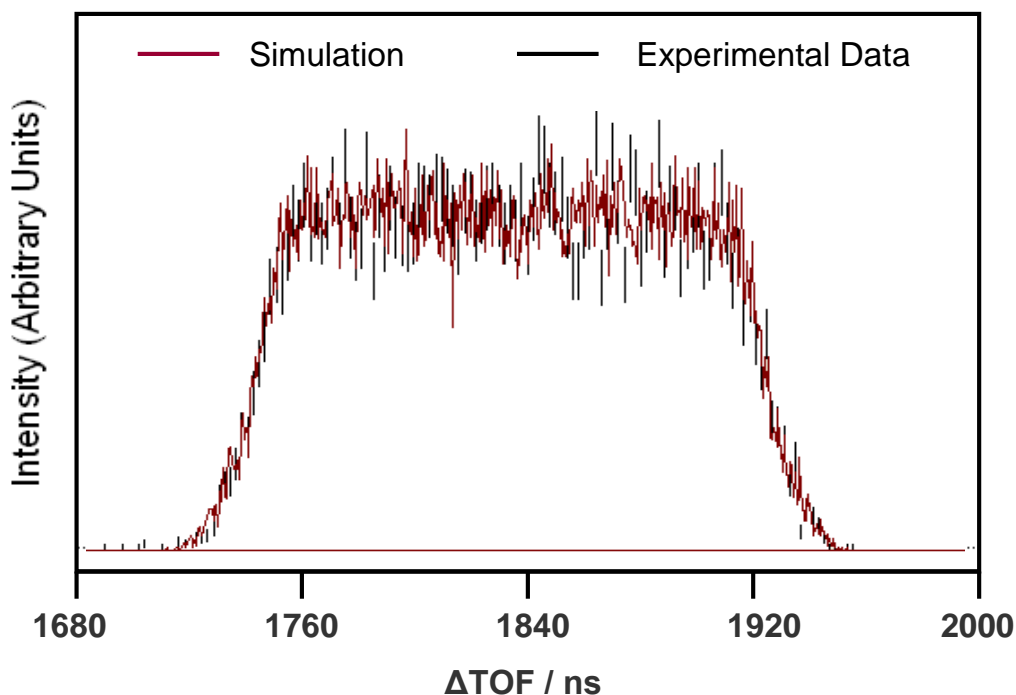


Figure 3.7: A Δ TOF plot for the $I^+ + CF^+$ ion pair recorded in the pairs spectrum of CF_3I at 50 eV, compared to a Monte Carlo simulation of the reaction in the TOF mass spectrometer. Good agreement is observed between the simulation and the experimental data.

3.5.1.1 Apparatus and Ion Parameters

To set up a simulation the apparatus parameters are entered: the source length, acceleration length, drift tube length, source voltage, and the voltage on the drift tube (Table 3.2). These parameters form a description of the electrostatic model of the TOF mass spectrometer under the experimental conditions. The values concerning the dissociation reaction under investigation are then entered; firstly the masses of the detected ion pair and the mass of the parent dication. Then, if the ion pair was formed *via* a secondary fragmentation pathway (Section 3.4.3.3) the mass of the primary ionic fragments (precursor ions) formed in the initial dication dissociation are entered. Such mechanistic information is provided through the analysis of the corresponding ion pair peak gradient. The simulation assumes that there is no component of KER involved in the secondary fragmentation step.

Once a suitable description of the dication fragmentation pathway has been constructed, the energetic of the dissociation are entered. Initially an estimate of the KER upon dissociation is entered, or a combination of weighted components of KER if the reaction KER is multi-valued. The detector radius, initial gas temperature along the jet axis and perpendicular to the jet axis are then defined and entered into the program (Table 3.3).

Table 3.2: Typical values of parameters used in Monte Carlo simulations.

Apparatus/Ion Parameter	Value	Simulation Parameter	Value
Source length (S)	1.0 cm	Source voltage	+400 V
Acceleration length (A)	18 cm	Drift tube voltage	-1600 V
Drift tube length (D)	20.0 cm		

3.5.1.2 Simulation Parameters

The simulation parameters consist of the number of ion trajectories required, the half-width of the KER distribution for each ion pair and the half-width of the Gaussian distribution of ionization events in the source region. The time jitter distribution of the detector output is also considered in the simulation. Once all the apparatus, ion and simulation parameters have been entered into the program, the simulation is run and the data output used to construct a simulated Δ TOF plot, which is then compared with the experimental data (Figure 3.7). The parameters of the simulation are then refined until a good fit between the simulated and experimental Δ TOF plots is achieved. Satisfactory

agreement between the simulated and experimental Δ TOF plots is evaluated visually. The uncertainties in the values of the KERs determined are estimated by the deviations necessary to significantly degrade the fit with experimental data, and are typically in the order of ± 0.6 eV.

Table 3.2: Typical values of parameters used in Monte Carlo simulations.

Apparatus/Ion Parameter	Value	Simulation Parameter	Value
Detector Radius	20 mm	Ion trajectories	50000
Initial gas T along jet axis	300 K	Half-width of Gaussian KERD	~ 1.5 eV
Initial gas T perpendicular to jet axis	300 K	Half-width of Gaussian spatial distribution in source	1 mm
		Half-width of time jitter distribution	1 ns

3.6 References

- 1 L. J. Frasinski, K. Codling, and P. A. Hatherly, *Sci.* **246**, 1029 (1989).
- 2 L. J. Frasinski, P. A. Stankiewicz, P. A. Hatherly, and K. Codling, *Meas. Sci. Tech.* **3**, 1188 (1992).
- 3 D. M. Curtis and J. H. D. Eland, *Int. J. Mass Spectrom. Ion Process.* **63**, 241 (1985).
- 4 J. H. D. Eland, *Vacuum Ultraviolet Photoionization and Photodissociations of Molecules and Clusters* (World Scientific, Singapore, 1991).
- 5 J. H. D. Eland, F. S. Wort, and R. N. Roynolds, *J. Mass Spectrom. Ion Process.* **123**, 97 (1986).
- 6 S. Feil, A. Bacher, M. Zangerl, W. Schustereder, K. Gluch, and P. Scheier, *Int. J. Mass Spectrom.* **233**, 325 (2004).
- 7 R. F. Stebbings and B. G. Lindsay, *J. Chem. Phys.* **114**, 4741 (2001).
- 8 H. C. Straub, P. Renault, B. G. Lindsay, K. A. Smith, and R. F. Stebbings, *Phys. Rev. A* **52**, 1115 (1995).
- 9 M. R. Bruce and R. A. Bonham, *Int. J. Mass Spectrom. Ion Process.* **123**, 97 (1993).
- 10 M. R. Bruce, C. Ma, and R. A. Bonham, *J. Phys. B* **27**, 5773 (1994).
- 11 L. G. Chrisophorou and J. K. Olthoff, *Fundamental Electron Interactions with Plasma Processing Gasses* (Plenum, New York, 2004).

- 12 C. Maul and K. H. Gericke, *Int. Rev. Phys. Chem.* **16**, 1 (1997).
- 13 J. H. D. Eland, *Laser Chem.* **11**, 259 (1991).
- 14 J. H. D. Eland, *Mol. Phys.* **61**, 725 (1987).
- 15 R. Thissen, J. Delwiche, J. M. Robbe, D. Dufлот, J. P. Plament, and J. H. D. Eland, *J. Chem. Phys.* **99**, 6590 (99).
- 16 D. York, *Can. J. Phys.* **44**, 1079 (1966).
- 17 M. Lange, O. Pfaff, U. Muller, and R. Brenn, *Chem. Phys.* **230**, 117 (1998).
- 18 J. H. D. Eland and B. J. Trevesbrown, *Int. J. Mass Spectrom. Ion Process.* **113**, 167 (1992).
- 19 R. Thissen, J. Delwiche, J. M. Robbe, D. Dufлот, J. P. Plament, and J. H. D. Eland, *J. Chem. Phys.* **99**, 6590 (1993).
- 20 S. J. King, **PhD Studies of the Dissociation and Energetics of Gaseous Ions**, University College London, 2008.
- 21 *NIST Chemical WebBook; NIST Standard Reference Database Number 69*, Vol., edited by P. J. Linstrom and W. G. Mallard (National Institute of Standards and Technology, Gaithersburg MD, 20899, 2008).
- 22 K. M. Douglas and S. D. Price, *Int. J. Mass Spectrom.* **303**, 147 (2011).
- 23 K. M. Douglas and S. D. Price, *J. Chem. Phys.* **131**, 224305 (2009).
- 24 S. J. King and S. D. Price, *Int. J. Mass Spectrom.* **272**, 154 (2008).
- 25 S. J. King and S. D. Price, *J. Chem. Phys.* **127**, 174307 (2007).
- 26 N. A. Love and S. D. Price, *Phys. Chem. Chem. Phys.* **6**, 4558 (2004).
- 27 S. Hseih and J. H. D. Eland, *J. Phys. B* **30**, 4515 (1997).
- 28 S. Leach, J. H. D. Eland, and S. D. Price, *J. Phys. Chem.* **93**, 7575 (1989).

Chapter 4 Electron Ionization of Hydrogen Sulphide

4.1 Introduction

Hydrogen sulphide (H_2S) is a colourless, poisonous and flammable gas that has a characteristic odour of rotten eggs. A minor constituent of the Earth's atmosphere, it is produced by a range of biological processes, as well as being present in volcanic and natural gases.¹ Hydrogen sulphide has also been detected in extra-terrestrial environments including interstellar clouds,^{2,3} comets⁴ and planetary atmospheres.⁵ To model the role of hydrogen sulphide in these energized environments requires, amongst other factors, a reliable quantification of the consequences of electron- H_2S collisions. Accurate and reliable electron ionization cross-sections of H_2S are therefore essential for the modelling of planetary atmospheres.

4.1.1 Dissociative Ionization of H_2S

A range of experimental techniques have been used to study the dissociative ionization of hydrogen sulphide, employing both electron ionization and photoionization. Considering electron ionization, the technique employed in this study, absolute total cross-sections following electron ionization have been measured by Belic *et al.*⁶ Absolute PICSs have also been measured by Rao and Srivastava⁷, using a TOF and a quadrupole mass spectrometer in the energy range 0 – 1000 eV, and by Lindsay *et al.*⁸ in the energy range 16 – 1000 eV using a time-of-flight mass spectrometer (TOFMS) coupled with a position sensitive detector. The electron ionization of hydrogen sulphide has also been investigated theoretically.^{9,10}

Experimentally, Lindsay *et al.*⁸ have demonstrated the efficient collection of all ion fragments in their experiment irrespective of their kinetic energy, an important consideration for determining accurate PICSs.⁸ However, in the data of Lindsay *et al.*⁸, ion collection efficiency comes at the expense of mass resolution, meaning that their data are reported as groups of ions with similar masses, rather than for individual ion fragments. In a step forward, the mass resolution of our data allows unambiguous identification of all the different fragment ions formed following electron- H_2S collisions.

Over the electron energy range investigated in this study (30-200 eV) multiple ionization, particularly double ionization, of H_2S can contribute significantly to the ion

yield. Several previous studies have probed the double photoionization of hydrogen sulphide. Initial studies of the fragmentation of H_2S^{2+} were made using an ion coincidence technique.¹¹ Later, employing threshold photoelectrons coincidence (TPEsCO) and photoelectron-photoion-photoion coincidence (PEPIPICO) techniques, Eland *et al.*^{12,13} investigated the double ionization of H_2S in the energy range 28 – 48 eV and reported kinetic energy releases for some of the major charge separation channels. The ground and several excited electronic states of H_2S^{2+} have also been probed by Cesar *et al.*¹² using Auger spectroscopy, computational chemistry and double charge transfer experiments.

In this study, the electron ionization of H_2S in the energy range 30 – 200 eV is investigated using TOF mass spectrometry coupled with a two-dimensional (2D) ion coincidence technique. This experimental method allows single product ions, ion pairs and ion triples, formed following electron ionization of H_2S , to be detected, identified and quantified. From this data we extract precursor-specific relative PICSs $\sigma_n[\text{X}^{m+}]$ ($n = 1-3$) for all the fragment ions observed. These precursor-specific cross-sections quantify the contribution to individual fragment ion yields from each level of ionization (single $n = 1$, double $n = 2$ and triple $n = 3$), as described in Chapters 2 and 3. These measurements represent the first complete description of the consequences of the single and multiple ionization of H_2S at electron energies below 200 eV. In addition, the 2D ion coincidence technique shows that population of the excited states of H_2S^{2+} provides the dominant route to ion pair formation at electron energies between 50 and 100 eV.

4.2 Experimental Procedures

All experiments were carried out using the TOFMS described in Chapter 2. The operating conditions employed involve using low target gas pressure, together with low electron fluxes, ensures that on average there is considerably less than one ionization event per ionizing electron pulse. This significantly reduces the number of ‘false coincidences’ in our spectra, as described in chapters 2 and 3. The hydrogen sulphide gas used was a commercial sample of $\geq 99.5\%$ purity. The voltage conditions employed are given in Table 2.1, and allow the efficient collection of ions formed with up to 10.7 eV of initial translational energy.

4.3 Data Analysis

Mass and coincidence spectra of hydrogen sulphide were recorded at ionising electron energies in the range 30 – 200 eV using the experimental apparatus described in Chapter 2. For each ionising electron energy used, four separate experimental cross-sections determinations were made.

4.3.1 Singles Mass Spectra

A representative mass spectrum of H_2S following electron ionization at 200 eV is shown in Figure 4.1. In addition to the H_2S^+ parent ion peak, this mass spectrum shows peaks corresponding to the fragment ions HS^+ , S^+ , H_2S^{2+} , HS^{2+} , S^{2+} , H_2^+ and H^+ , formed by the dissociation of H_2S^{m+} . The intensities of these individual ion peaks $I[\text{X}^{m+}]$ appearing in the singles spectra, were extracted using the procedure described in Section 3.2.

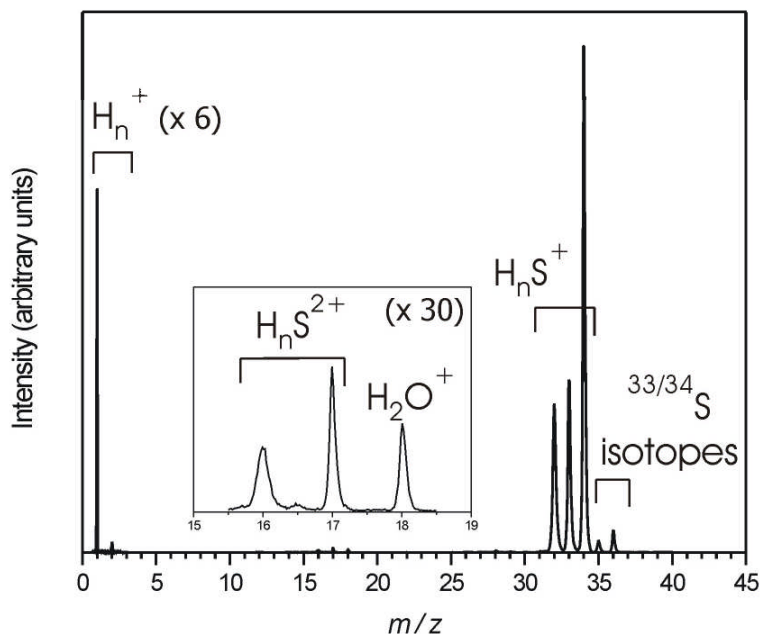


Figure 4.1: A typical singles mass spectrum of H_2S following electron ionization at 200 eV.

Due to the low target gas pressures used, the singles spectrum also shows traces of ions resulting from the ionization of residual air and water in our vacuum chamber. Ionization of residual air results in O_2^+ ions that contribute to the intensity of the $^{32}\text{S}^+$ ion peak, and O^+ ions that contribute primarily to the intensity of the $^{32}\text{S}^{2+}$ peak.

Ionization of residual water results in OH^+ ions that contribute primarily to the intensity of the $\text{H}_2^{32}\text{S}^{2+}$ ion peak, O^+ ions that contribute to the intensity of the $^{32}\text{S}^{2+}$ peak, and H_2^+ and H^+ ions. These minor contributions to the mass spectrum are removed by normalisation to the N_2^+ and H_2O^+ peaks, as described in Section 3.2. Contributions to the raw ion intensities from these residual gases were typically much less than 1 % for the S^+ , H_2^+ and H^+ ion peaks, and typically less than 10 % for the small peaks primarily due to $\text{H}_2^{32}\text{S}^{2+}$ and S^{2+} . As we are unable to distinguish between the isotopologues of a number of sulphur containing ions which occur at the same mass in the singles spectrum, for example, $\text{H}_2^{32}\text{S}^+$, H^{33}S^+ and $^{34}\text{S}^+$, the measured ion intensities were corrected numerically for isotopic speciation using the natural isotopic distribution ^{32}S : ^{33}S : ^{34}S (95.0%: 0.8%: 4.2%).

4.3.2 Pairs Spectra

Schematic pairs spectra of H_2S recorded at 200 eV ionising electron energy are shown in Figure 4.2. At this energy four monocation-monocation pair peaks are observed, $\text{H}^+ + \text{H}^+$, $\text{S}^+ + \text{H}^+$, $\text{S}^+ + \text{H}_2^+$ and $\text{HS}^+ + \text{H}^+$, and two dication-monocation pair peaks are observed, $\text{S}^{2+} + \text{H}^+$, $\text{HS}^{2+} + \text{H}^+$. Above the double ionization threshold, the ion pair yield is dominated (>90%) by the formation of $\text{SH}^+ + \text{H}^+$ and $\text{S}^+ + \text{H}^+$, with the former channel the most intense at electron energies up to 65 eV and the latter channel more intense above that electron energy. The ion pairs involving dications are only present, and then with low intensities, at electron energies above 75 eV. The contribution of a particular ion to the pairs spectra were extracted using the procedure described in Section 3.2. The number of false coincidences, events in which two ions are detected in coincidence that did not originate from the same ionization event, are evaluated manually for each peak using the autocorrelation of the singles spectrum, as described in Section 3.2.2.1. As in the singles spectra, corrections are also made to some ion pairs for ion contributions arising from residual water in the apparatus. Contributions from these residual gasses to the counts of the weak $\text{H}^+ + \text{H}^+$ and $\text{S}^{2+} + \text{H}^+$ ion pair peaks were typically less than 1 % and 10 % respectively. In our experimental arrangement, due to the ‘dead-time’ of the discrimination circuitry, an ion-pair will not be detected if the second ion arrives at the detector within 32 ns of the first. This results in a ‘dead region’ in the pairs spectrum affecting the $\text{H}^+ + \text{H}^+$ peak. An estimation of the losses within this dead region can be made by first plotting the time-of-flight difference (ΔTOF) between pairs of ions making up the visible part of the affected pairs peak.

Extrapolation of this Δ TOF plot can then be made, using simple geometry, to quantify the counts lost in the dead region,¹³ as described in Section 3.2.2.3. Inspection of the Δ TOF plots for all other ion pairs observed can also indicate whether there are any losses due to energetic ions. The missing centre of the Δ TOF plot for the ion pair $S^{2+} + H^+$ indicated such losses due to energetic ions. Correction of these losses indicated that approximately 40% of the $S^{2+} + H^+$ ion pairs were lost due to energetic ions. As in the singles spectra, corrections were also made for isotopic speciation of sulphur to a number of pairs peaks using the natural isotopic distribution.

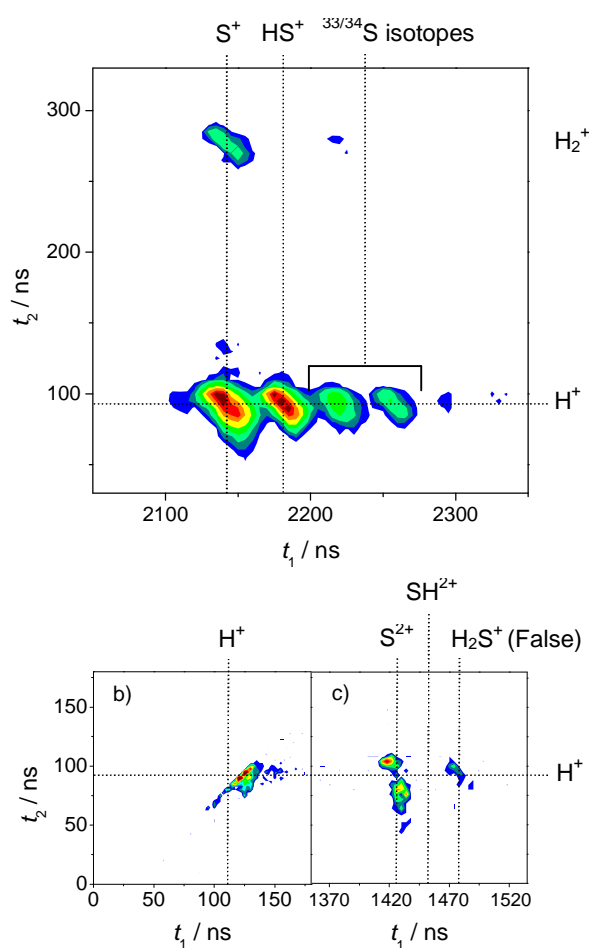


Figure 4.2: Representative pairs spectrum of H_2S at 200 eV showing; a) $HS^+ + H^+$, $S^+ + H^+$ and $S^+ + H_2^+$, b) $H^+ + H^+$ and c) the very weak $SH^{2+} + H^+$ and $S^{2+} + H^+$ ion pairs.

4.3.3 Triples Spectra

As discussed in Section 3.2 the triples data is quantified in a similar way to the pairs data. First the TOF range of a particular ion is selected, and all ion triples with an ion falling into this range are extracted. The remaining two TOFs are then plotted as a pairs spectrum, and the intensity of each ion triple peak found by summing the number of counts in the peak. The contribution of a fragment ion to the triples spectrum, $T[X^+]$, is then obtained by summing the counts of all appropriate peaks involving the ion X^+ . In practice, the only true triple event we detect following electron ionization of H_2S is $S^+ + H^+ + H^+$, justifying our neglect of quadruple and higher levels of ionization.

4.4 Relative Partial Ionization Cross-sections

4.4.1 Results

Mass and coincidence spectra of hydrogen sulphide were recorded at ionising electron energies in the range 30 – 200 eV. These spectra were processed, as described in Section 3.3, to yield relative PICSs $\sigma_r[X^{m+}]$ for the formation of all fragment ions observed: HS^+ , S^+ , H_2S^{2+} , HS^{2+} , S^{2+} , H_2^+ and H^+ . These σ_r values are expressed relative to the H_2S^+ ion yield and are displayed as a function of electron energy in Figure 4.3 and Table B.1. Precursor-specific relative PICSs $\sigma_n[X^{m+}]$ were also derived for these fragment ions, using the procedure described in Section 3.3. These $\sigma_n[X^{m+}]$ ($n = 1 - 3$) values are expressed relative to the H_2S^+ ion yield, and are displayed as a function of electron energy in Figure 4.4 and Table B.2. As discussed in Section 1.4.3, producing absolute PICSs requires the accurate measurement of four experimental variables: the initial electron flux, the number density of the target gas, the collisional pathlength and number of ions formed by electron ionization events. Determination of the first three of these variables is experimentally non-trivial, and thus we report relative PICSs. These relative values can be readily placed on an absolute scale using the measurements of the total ionization cross-sections discussed above. For example, to produce an absolute value for $\sigma[H^+]$ simply requires an absolute value for the cross-section for forming the parent monocation, H_2S^+ , $\sigma[H_2S^+]$:

$$\sigma[H^+] = \sigma_r[H^+] \times \sigma[H_2S^+] \quad (4.1)$$

As discussed in Section 1.4.3, one advantage of producing relative PICSs relative to the parent monocation is that the parent monocation is formed with a thermal distribution and thus the least likely to suffer from ion discrimination effects. Therefore, even previous cross-section determinations in which the efficient collection of energetic ions is not accounted for should produce accurate $\sigma[\text{parent}^+]$ values.

In the coincidence spectra, we observe four ion pairs generated predominantly by the dissociation of H_2S^{2+} ($\text{H}^+ + \text{H}^+$, $\text{S}^+ + \text{H}^+$, $\text{S}^+ + \text{H}_2^+$ and $\text{HS}^+ + \text{H}^+$) and two ion pairs clearly formed from the dissociation of H_2S^{3+} ($\text{S}^{2+} + \text{H}^+$ and $\text{HS}^{2+} + \text{H}^+$). Above the double ionization threshold, the ion pair yield is dominated (>90%) by the formation of $\text{SH}^+ + \text{H}^+$ and $\text{S}^+ + \text{H}^+$, with the former channel the most intense at electron energies up to 65 eV and the latter channel more intense above that energy. A similar dominance of these two ion pair decay channels is observed for H_2S^{2+} formed by photoionization.¹⁴ We also observe one ion triple channel from the dissociation of H_2S^{3+} ($\text{H}^+ + \text{H}^+ + \text{S}^+$). The overall contributions from single, double and triple ionization to the total ion yield is shown in Figure 4.5 and Table B.3. Figure 4.5 shows that as the ionizing electron energy is increased from 30 to 200 eV the relative contribution to the ion yield from single ionization broadly drops (50 eV:89%, 100 eV:80%, 200 eV:82%). This drop coinciding with an increase in the contribution to the ion yield from double ionization (50 eV:11%, 100 eV:20%, 200 eV:18%) and triple ionization. However, the contribution from triple ionization is negligible below 85 eV and very small (0.1-0.3 %) above 85 eV.

As can be seen from Figures 4.3 and 4.4, as the ionizing electron energy is increased, the general trend of the cross sections is to increase from threshold to a maximum, after which they gently drop off. As discussed in Section 1.4.3., such a trend is observed for all electron-molecule interactions, as the efficiency at which the electron interacts with a molecule decreases with increasing electron energy. This is due to the fact that higher energy electrons are moving faster. As the energy is increased, there, in principle, reaches a point at which the electron is moving so fast it does not interact with the species at all and the cross section falls to zero.

As discussed in Section 3.3, a value for the ion detection efficiency f_i is required to enable us to derive $\sigma_n[\text{X}^{m+}]$ values. Measurement of f_i for our apparatus, using the methodology described in Section 3.3.3, resulted in a value of 0.26 ± 0.01 , in good agreement with previous determinations.¹⁶⁻²⁰

4.5 Discussion

4.5.1 Relative PICSSs (σ_r)

The values of $\sigma_r[X^{m+}]$ we have derived from our data are displayed in Figure 4.3 and given numerically in the Table B.1. Given that these results present the first measurement of precursor-specific relative PICSSs, it is only by constructing the relative PICSSs from our data that we can compare our results with previous work. Our relative PICSSs are compared with values derived from the data of Rao *et al.*⁷ (Figure 4.3b-4.3d). To enable a direct comparison with the results of Lindsay *et al.*,⁸ who report PICSSs for H^+ and the group of ions H_nS^+ ($n = 0 - 2$), we have also calculated the relative PICSSs for H^+ relative to the summed cross-section for the H_nS^+ group of ions, as shown in Figure 4.3a.

Comparison of our $\sigma_r[H^+]$ values to those derived from the work of Lindsay *et al.*,⁸ in which the efficient collection of all ion fragments with considerable translational energy was demonstrated, show good agreement at all ionizing electron energies investigated (Figure 4.3a). By contrast, there is a significant difference between some of the values of $\sigma_r[X^+]$ we determine and those derived from the data of Rao *et al.*⁷ Specifically, good agreement is observed for the heavier ion fragments (HS^+ and S^+), and for the fragment ion S^{2+} the $\sigma_r[X^{m+}]$ values agree within mutual error limits, although our values are systematically slightly higher. However, for the lighter ion fragments (H_2^+ and H^+) the values of $\sigma_r[X^+]$ derived in the current work are significantly higher than those of Rao *et al.*⁷ These differences for H^+ and H_2^+ can be explained by the inefficient collection of translationally energetic ions in this earlier work, as has been discussed before.¹⁵⁻¹⁷

Indeed, better agreement is observed comparing our $\sigma_1[X^{m+}]$ values for H^+ and H_2^+ to the $\sigma_r[X^+]$ values derived from the work of Rao *et al.*,⁷ indicating the majority of ion losses in this earlier work are from dissociative double or triple ionization. Another significant difference between our data and that of Rao *et al.*⁷ involves the values we obtain for $\sigma_r[H_2S^{2+}]$; here, conversely, our values are about half of that reported in the previous work. A possible explanation for these differences in the values of $\sigma_r[H_2S^{2+}]$ is due to the lifetime of the metastable H_2S^{2+} ion. Specifically, the lifetime of a subset of the H_2S^{2+} ions formed in our electron molecule collisions is clearly of the order of a few hundred nanoseconds, as readily evidenced by the metastable tail from the $HS^+ + H^+$ peak in the pairs spectrum. In our experiments the flight time of an H_2S^{2+} ion is 1820 ns. If, in the experiments of Rao *et al.*⁷, the H_2S^{2+} ions lived for a significantly shorter time

than 1820 ns before their detection then the $\sigma_r[\text{H}_2\text{S}^{2+}]$ values derived from the data of Rao *et al.*⁷ would be larger than our data.

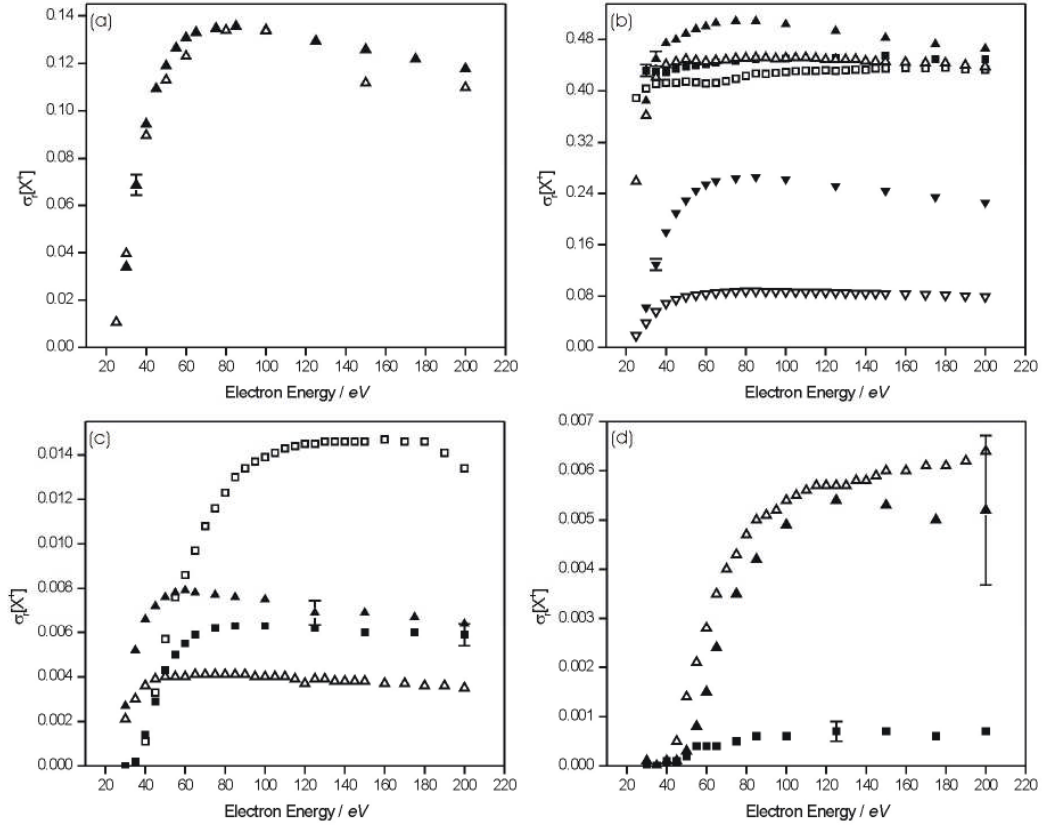


Figure 4.3: Relative PICs $\sigma_r[X^{m+}]$ for forming (a) H^+ following electron ionization of H_2S , relative to the summed cross-sections for forming the group of ions H_nS^+ , (b) S^+ (\blacktriangle), HS^+ (\blacksquare), and H^+ (\blacktriangledown), (c) H_2^+ (\blacktriangle), H_2S^{2+} (\blacksquare) and (d) S^{2+} (\blacktriangle) and H_2S^{2+} (\blacksquare) following electron ionization of H_2S relative to the cross-section for forming the parent ion H_2S^+ . Where available the corresponding relative PICs from the data of Lindsay *et al.*⁸ (graph (a)) and Rao *et al.*⁷ (graphs (b), (c) and (d)) are also shown as open symbols. The representative error bars show two standard deviations of four separate determinations.

We are also able to compare our $\sigma_r[X^{m+}]$ values to those derived from theoretical calculations by Khare *et al.*⁹ at 100 eV ionizing electron energy. At this energy, the relative PICs for the fragment ions H^+ , S^+ and HS^+ as derived from the theoretical data of Khare *et al.*⁹ are lower than those reported in this study by 39 %, 46 % and 16 % respectively.

An estimate for the appearance energy of the S^{2+} , HS^{2+} and H_2S^{2+} ions was determined by extrapolation of a linear fit to the first three data points at which the relative PICS values are non-zero within error. In all three cases a least-squares fit was used, in which the differing uncertainty in each point is taken into account. For S^{2+} , taking the three data points above 50 eV an appearance energy of 50.2 ± 0.5 eV is obtained, for HS^{2+} , taking the three data points above 35 eV an appearance energy of 35.3 ± 0.5 eV is obtained, and for H_2S^{2+} , taking the three data points above 30 eV an appearance energy of 34.5 ± 0.1 eV is obtained.

4.5.2 Precursor-Specific Relative PICSs (σ_n)

The values of σ_1 , σ_2 and σ_3 for the formation of fragment ions formed following electron ionization of H_2S are displayed in Figure 4.4 and given numerically in Table B.2. Figure 4.5 indicates the contribution from single, double and triple ionization to the total ion yield. As can be seen from Figure 4.5, the greatest contribution to the total ion yield at all ionizing electron energies is from single ionization. The contribution from double ionization increases steadily with increasing ionizing electron energy, rising from 0.2 % at 30 eV to reach a maximum of 19.5 % at 100 eV, above which it gently declines. Contribution from triple ionization remains effectively zero below 85 eV, remains small as the ionization electron energy is increased, and still only accounts for 0.3 % of the total ion yield at 200 eV.

For all singly charged fragment ions, H^+ , H_2^+ , S^+ and HS^+ , the greatest contribution to their ion yields is from dissociative single ionization. However it can still be seen that double ionization does make a significant contribution to the ion yields of these singly charged fragment ions. For H^+ and H_2^+ , the contributions to their ion yields from dissociative double ionization rise rapidly between 35 eV and 60 eV, after which they begin to level off, reaching a maximum of 43.8 % and 29.6 % at 200 eV for H^+ and H_2^+ respectively. For S^+ and HS^+ , contributions from dissociative double ionization rise rapidly as the ionizing electron energy is increased from 40 eV, reaching a maximum of 13.4 % at 100 eV for S^+ and 10.5 % at 65 eV for HS^+ , after which both gradually decrease up to 200 eV. Contributions from triple ionization to the ion yield for H^+ are effectively zero within error below an ionizing electron energy of 85 eV, and above which they gradually increase to a maximum of 0.7 % at 200eV. Due to the small number of counts present in the triple channel $H^+ + H^+ + S^+$, the only channel that contributes to $\sigma_3[S^+]$, large errors are associated with these values. However the general

trend of these $\sigma_3[S^+]$ values can be seen to be in line with other $\sigma_3[X^{m+}]$ values, rising from around 85 eV to reach a plateau at 125 eV. This indicates that despite the large errors associated with the $\sigma_3[S^+]$ values, they can be taken to be negligible below 85 eV, and non-zero above 85 eV.

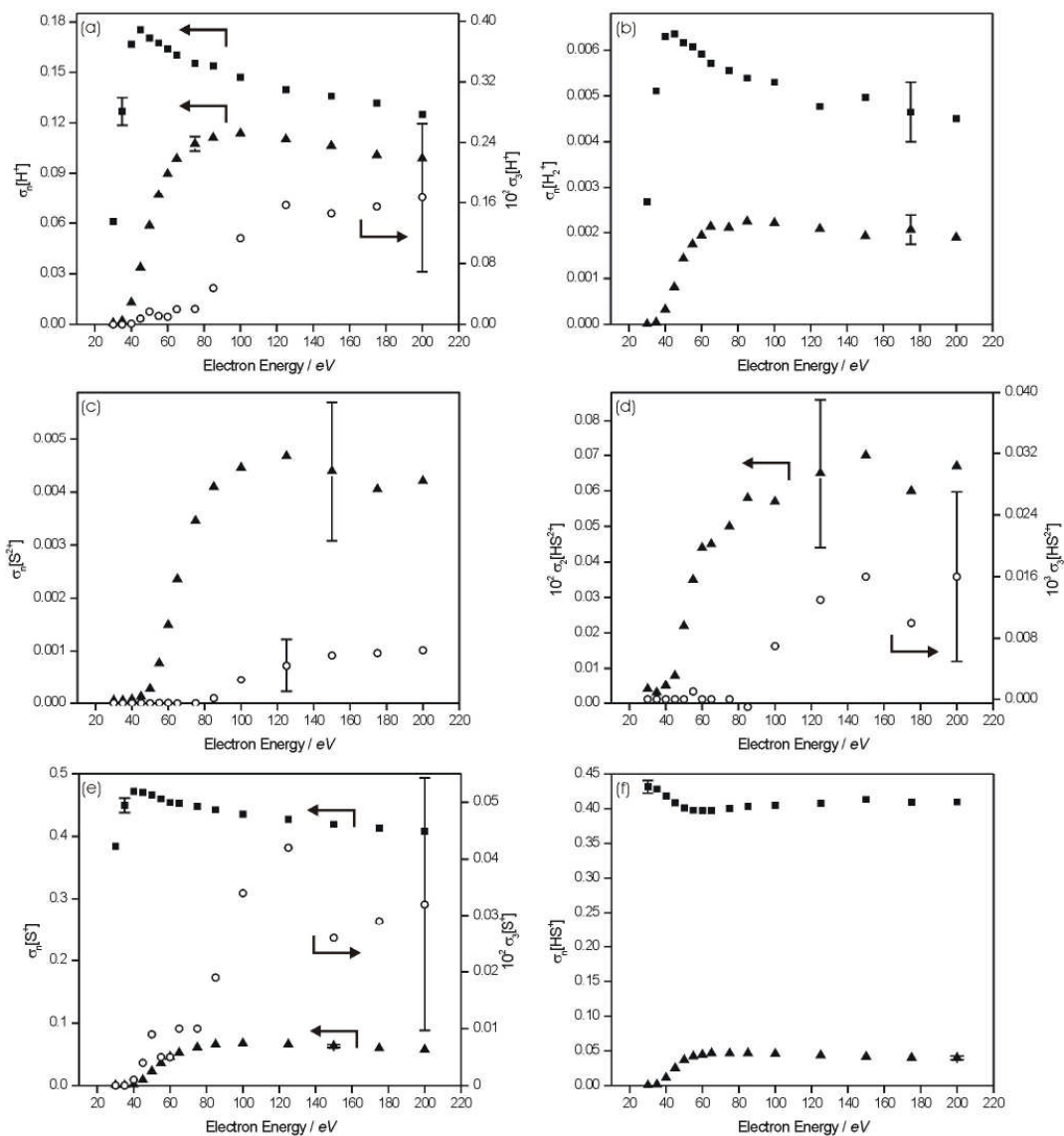


Figure 4.4: Precursor-specific relative PICSSs for forming (a) H^+ , (b) H_2^+ , (c) S^{2+} , (d) HS^{2+} , (e) S^+ and (f) HS^+ fragment ions via single (\blacksquare), double (\blacktriangle) and triple (\circ) ionization, following electron ionization of H_2S , relative to the cross-section for forming the parent ion H_2S^+ . The representative error bars shows two standard deviations of four separate determinations, except for $\sigma_3[S^+]$ (panel (e), (\circ)), for which only one standard deviation is given.

For the doubly charged fragment ions, S^{2+} and HS^{2+} , at ionizing electron energies above which they are observed the greatest contribution to their ion yields is from dissociative double ionization. Contributions from triple ionization begin at 85 eV for S^{2+} and at 100 eV for HS^{2+} , and increase with increasing electron energy, reaching a maximum of 19.5 % and 2.3 % at 200 eV for S^{2+} and HS^{2+} respectively.

In comparison with H_2O , where the maximum contribution of double ionization to the ion yield is 5 %¹⁵, the presence of a sulphur atom in H_2S , an atom from the second row of the periodic table with associated greater electron correlation, raises the maximum contribution of double ionization to the ion yield to 20%.

The σ_r values for the formation of ion pairs following dissociation of H_2S^{n+} are displayed in Figure 4.6. Above the double ionization threshold, the ion pair yield is dominated (>90%) by the formation of $SH^+ + H^+$ and $S^+ + H^+$, with the former channel the most intense at electron energies up to 65 eV and the latter channel more intense above that energy. A similar dominance of these two ion pair decay channels is observed for H_2S^{2+} formed by photoionization.¹⁴

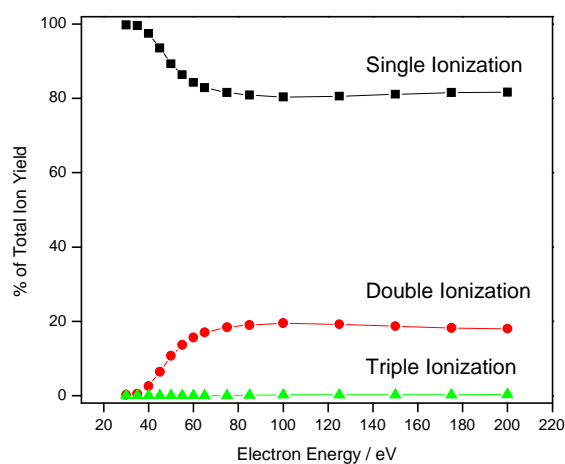


Figure 4.5: Contribution to the total ion yield from single, double and triple ionization, following electron ionization of H_2S .

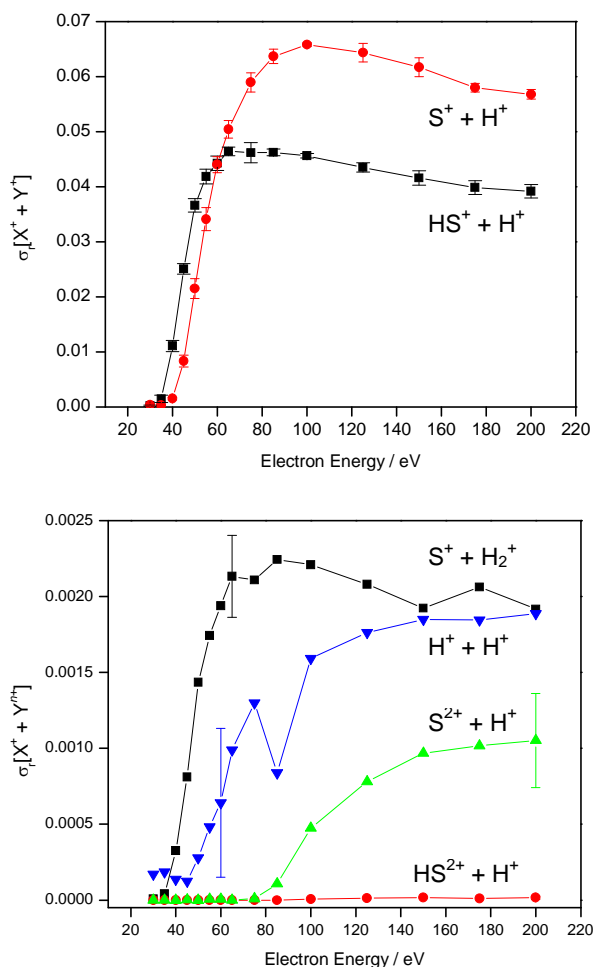


Figure 4.6: Relative PICs $\sigma_r[X^+ + Y^{m+}]$ for forming ion pairs following electron ionization of H_2S .

4.5.3 Energetics and Dissociation of H_2S^{2+}

As described in Chapter 3, the peak shapes in the pairs spectra can be used to determine estimates of the kinetic energy released when the doubly charged parent ion dissociation. We extract kinetic energy release distributions for the different fragmentation channels of H_2S^{2+} , by fitting the experimental ΔTOF spectrum¹¹ with a Monte-Carlo simulation of the dissociation. For each channel we use the data at the lowest electron energy which generates a statistically significant ΔTOF spectrum. For two-body dissociations the Monte Carlo simulation can be directly employed to model the ΔTOF peaks, directly yielding the KER. The KERs we have determined from the pairs spectra are shown Table 4.1. As can be seen from Table 4.1, more than one KER value was required to satisfactorily fit the experimental ΔTOF spectra, if the width of

the (Gaussian) KER distribution was restricted to realistic values, below 1.5 eV. The H_2S^{2+} precursor state energies derived from these KER measurements should be viewed as lower limits as they neglect any internal energy in the dissociation products. Good agreement is observed between the average of our KER values (Table 4.I) and the results of Eland *et al.*¹⁴ and Curtis and Eland¹¹ recorded following photoionization of hydrogen sulphide.

For the ion pair $\text{HS}^+ + \text{H}^+$, the lowest H_2S^{2+} precursor state energy we derive is 31.3 ± 0.6 eV, given that,^{14,18} due to spin correlations, that the ground ($^1\text{A}_1$) state of H_2S^{2+} does not dissociate to the ground state products but to $\text{H}^+ + \text{HS}^+(\text{a}^1\Delta)$. This precursor state energy is in good agreement with the experimentally determined energy of the ground state of H_2S^{2+} (31.6 eV). However, the ground $^1\text{A}_1$ state of H_2S^{2+} is metastable with a barrier of approximately 2 eV to dissociation.¹⁸ Thus it seems clear that this precursor energy must correspond to the population of the dissociative monocation states lying close to the vertical double ionization energy. These states have been implicated in the formation of monocation pairs from H_2S at energies below the double ionization potential.¹⁴

Cesar *et al.*¹² have presented (their Table VII) the energies of the states of H_2S^{2+} determined from double charge transfer spectroscopy, Auger spectroscopy and theory. Comparing the state energies presented by Cesar *et al.*¹² with the latest value of the double ionization energy of H_2S ,¹⁹ it seems clear that for the lower states of H_2S^{2+} the theoretical values of Cesar *et al.*¹² should be shifted upwards by about 1 eV, whilst the energies determined by double charge transfer experiments should be shifted down in energy by about 1 eV. In the light of this adjustment, the assignment of the $\text{H}^+ + \text{HS}^+$ precursor state we observe at 33.7 ± 0.6 eV to the second excited state ($^1\text{B}_1$) of H_2S^{2+} appears logical. Population of this precursor state (Table 4.I) dominates the product flux in the $\text{H}^+ + \text{HS}^+$ channel. Our assignment implies that curve crossings to other dissociative states allow the $^1\text{B}_1$ state of H_2S^{2+} to dissociate to the, nominally spin-forbidden, ground state products.

The final precursor state energy we extract from the $\text{H}^+ + \text{HS}^+$ energy release spectrum lies at 38.2 eV. The energy of this state agrees well with the first $^1\text{B}_2$ excited state of H_2S^{2+} revealed by Cesar *et al.*¹², recalling that the precursor state energy is a lower limit. However, given that this state lies over 7 eV above the ground state of H_2S^{2+} where the electronic state density is likely to be high, this assignment can at best be described as tentative.

Table 4.1: Kinetic energy releases (KERs, uncertainty ± 0.6 eV unless stated), and corresponding precursor state energies P , for selected dissociation reactions of H_2S^{2+} . The weightings of the KERs are listed, together with an average KER to facilitate a direct comparison with literature. The electron energy of the spectral data used to determine the KERs are also given. The energies of the dissociation asymptotes, relative to the ground state of H_2S , involved in the determination of P are listed. Unless indicated, such asymptotes correspond to the formation of ground state products.

Ion pair	Electron energy /eV	KER /eV	Weight /%	Average KER		Asymptote ²⁰ /eV	P / eV
				This work	Lit. ^{11,12}		
$\text{HS}^+ + \text{H}^+$	55	2.2	25	6.0	5.4 ± 0.4	29.1	31.3 ^a
		5.8	50			27.9	33.7
		10.3	25				38.2
$\text{S}^+ + \text{H}_2^+$	100	3.5	50	5.1	5.2 ± 0.5	28.9	32.4
		5.6	35				34.5
		9.5 ± 1.0	15				38.4
$\text{S}^+ + \text{H}^+$	55	2.6	30	6.2	5.5	31.6	34.2
		6.0	40				37.6
		10.0	30				41.6

^a This precursor state and asymptote correspond to the formation of the first excited singlet state of HS^+ . See text for details.

The two lowest energy precursor states we derive from the KERs (Table 4.I) in the $\text{S}^+ + \text{H}_2^+$ channel match well with the energies of the first two excited states of H_2S^{2+} , the $^3\text{B}_1$ state lying at 32.6 eV and $^1\text{B}_1$ state at 34.1 eV.¹² The highest energy precursor state in the $\text{S}^+ + \text{H}_2^+$ channel (38.4 ± 0.6 eV) agrees well with the highest energy precursor state in the $\text{H}^+ + \text{HS}^+$ channel (38.2 eV), which we tentatively assigned to the first $^1\text{B}_2$ excited state of H_2S^{2+} .¹²

To extract the KER values for the three-body dissociation of H_2S^{2+} , where a neutral H fragment is formed together with S^+ and H^+ , the mechanism of the dissociation is first required. As described above, in principle, this mechanistic information can be extracted from the gradient of the peak in the pairs spectrum.^{11,21} The gradient of the $\text{S}^+ + \text{H}^+$ peak in the pairs spectrum indicates^{11,21} an initial separation of H_2S^{2+} into $\text{S}^+ + \text{H}_2^+$, followed by a secondary dissociation of the H_2^+ into $\text{H}^+ + \text{H}$. The calculated gradient for such a dissociation pathway is -0.50, in good agreement with the observed gradient of -0.52. Using this mechanism, three KERs were required to

satisfactorily fit the experimental Δ TOF spectrum (Table 4.I). The lowest precursor state energy (34.2 eV) corresponding to these KERs (Table 4.I) agrees well with the energy of the 1B_1 state, which we concluded above also dissociates to $H_2^+ + S^+$. Satisfyingly, as discussed above, the slope of the $H^+ + S^+$ peak in the pairs spectrum indicates that this three body reaction proceeds *via* initial formation of the $H_2^+ + S^+$ ion pair. Thus it seems clear that the 1B_1 state initially dissociates to form $H_2^+ + S^+$ with some of the H_2^+ ions being sufficiently excited to dissociate to $H^+ + H$. Given the state energies of Cesar *et al.*¹², the $H^+ + S^+$ precursor state at 37.6 eV can be tentatively assigned to the first excited 1A_1 state and the state at 41.6 eV to the second excited 1A_1 state.

Satisfyingly, our precursor state energies and assignments in the $HS^+ + S^+$ and $H^+ + S^+$ channels agree well with observed threshold energies for energetic H^+ formation, above the double ionization potential, measured by Dunn *et al.*²² For the remaining ion pairs observed ($H^+ + H^+$, $SH^{2+} + H^+$ and $S^{2+} + H^+$), at all ionizing electron energies investigated, insufficient count were available to produce statistically significant KERs.

4.6 Conclusions

Relative and precursor partial ionization cross-sections for fragment ions formed following electron ionization of hydrogen sulphide have been measured using time-of-flight mass spectrometry coupled with a 2D ion coincidence technique. These cross-sections are reported relative to the H_2S^+ ion, at ionizing energies from 30-200 eV. A comparison of these relative PICSs has been made with previous measurements of the partial ionization cross-sections of H_2S . Good agreement is found between our data and the recently published absolute partial ionization cross-sections of Lindsay *et al.*⁸ Conversely, discrepancies are observed with the absolute partial ionization cross-sections of Rao *et al.*⁷ discrepancies we attribute to the loss of translationally energetic fragment ions. Precursor-specific relative partial ionization cross-sections have also been derived. These cross-sections allow the contribution from single, double and triple ionization to the individual fragment ion yields, following ionization of hydrogen sulphide, to be quantified for the first time. Our analysis shows that the contribution of double ionization to the total ion yield reaches a maximum of 20% at 100 eV. Through analysis of peaks observed in the pairs spectra, the kinetic energy released when doubly charged H_2S dissociates have also been determined. From these kinetic energy releases,

estimates of the energies of the electronic states of H_2S^{2+} which are responsible for the different fragmentation channels can be made. These estimates, in comparison with other data on the electronic states of H_2S^{2+} , reveal that at higher electron energies, the population of excited electronic states of H_2S^{2+} are major pathways to charge separation.

4.7 References

- 1 C. H. Lin, I. F. Mao, P. H. Tsai, H. Y. Chuang, Y. J. Chen, and M. L. Chen, *Environ. Res.* **110**, 536 (2010).
- 2 P. Thaddeus, R. W. Wilson, M. L. Kutner, K. B. Jefferts, and A. A. Penzias, *Astrophys. J.* **176**, L73 (1972).
- 3 Y. C. Minh, W. M. Irvine, and L. M. Ziurys, *Astro. J.* **345**, L63 (1989).
- 4 J. Crovisier, D. Despois, D. Bockeleemorvan, P. Colom, and G. Paubert, *Icarus* **93**, 246 (1991).
- 5 V. A. Krasnopolsky, *Icarus* **197**, 377 (2008).
- 6 D. S. Belic and M. V. Kurepa, *Fizika (Zagreb)* **17**, 117 (1985).
- 7 M. Rao and S. K. Srivastava, *J. Geophys. Res.* **98**, 13137 (1993).
- 8 B. G. Lindsay, R. Rejoub, and R. F. Stebbings, *J. Chem. Phys.* **118**, 5894 (2003).
- 9 S. P. Khare and W. J. Meath, *J. Phys. B* **20**, 2101 (1987).
- 10 Y. K. Kim, W. Hwang, N. M. Weinberger, M. A. Ali, and M. E. Rudd, *J. Chem. Phys.* **106**, 1026 (1997).
- 11 D. M. Curtis and J. H. D. Eland, *Int. J. Mass Spectrom. Ion Processes* **63**, 241 (1985).
- 12 A. Cesar, H. Agren, A. N. Debrito, S. Svensson, L. Karlsson, M. P. Keane, B. Wannberg, P. Baltzer, P. G. Fournier, and J. Fournier, *J. Phys. Chem.* **93**, 918 (1990).
- 13 M. R. Bruce, L. Mi, C. R. Sporleder, and R. A. Bonham, *J. Phys. B: At., Mol. Opt. Phys.* **27**, 5773 (1994).
- 14 J. H. D. Eland, P. Lablanquie, M. Lavollee, M. Simon, R. I. Hall, M. Hochlaf, and F. Penent, *J. Phys. B: At. Mol. Opt. Phys.* **30**, 2177 (1997).
- 15 S. J. King and S. D. Price, *Int. J. Mass Spectrom.* **277**, 84 (2008).
- 16 S. J. King and S. D. Price, *J. Chem. Phys.* **127**, 174307 (2007).
- 17 C. C. Tian and C. R. Vidal, *J. Phys. B: At. Mol., Opt. Phys.* **31**, 895 (1998).

- 18 S. A. Pope, I. H. Hillier, and M. F. Guest, *Faraday Symp. Chem. Soc.*, 109 (1984).
- 19 J. H. D. Eland, **294** (2003).
- 20 *NIST Chemical WebBook; NIST Standard Reference Database Number 69*, Vol., edited by P. J. Linstrom and W. G. Mallard (National Institute of Standards and Technology, Gaithersburg MD, 20899, 2008).
- 21 J. H. D. Eland, *Mol. Phys.* **61**, 725 (1987).
- 22 K. F. Dunn, R. Browning, M. A. MacDonald, C. R. Browne, and C. J. Latimer, *J. Phys. B.* **31**, 4173 (1998).

Chapter 5 Electron Ionization of Methanol

5.1 Introduction

Methanol (CH_3OH), the simplest alcohol, is a volatile, colourless and flammable liquid. Natural gas is the most widely used feedstock for the production of methanol, however many varieties of bacteria produce methanol via anaerobic metabolism. The ionization of methanol is an important fundamental process. Ionization of methanol is also of relevance in terrestrial and extra-terrestrial environments. For example, alcohols are increasingly found in the polluted atmosphere associated with industrial areas,^{1,2} and methanol is one of the more abundant interstellar molecules, detected in a variety of astrophysical environments such as in comets³⁻⁵ and protostellar regions,^{6,7} where ionization events are relatively common. To model the role of methanol in the above environments requires accurate and reliable data on the partial ionization cross-sections (PICSs).

5.1.1 Dissociative Ionization of Methanol

There have been numerous experimental investigations of the ionization of methanol, employing both electrons and photons as the ionizing agent. Focusing on electron ionization, the subject of this study, both Duric *et al.*⁸ and Hudson *et al.*⁹ have measured total absolute ionization cross-sections in the energy range of 12 – 500 eV, while Zaviopulo *et al.*¹⁰ measured the relative electron ionization cross-sections in the energy range of 5 – 60 eV. Hudson *et al.*⁹ also compare their data to theoretical calculations made using both the Deutsch-Märk additive method and the Binary-encounter Bethe method, finding that both overestimate the maximum cross-section. PICSs have also been measured by Srivastava *et al.*,¹¹ in the energy range 20 – 500 eV using a quadrupole mass spectrometer (QMS), and by Rejoub *et al.*,¹² in the energy range 13 – 1000 eV using a time-of-flight mass spectrometer (TOFMS) coupled with a position sensitive detector (PSD). Rejoub *et al.* have demonstrated the efficient collection of all ion fragments in their experiment irrespective of their kinetic energy, an important consideration.¹² However, such ion collection efficiency is at the expense of mass resolution, meaning that the data of Rejoub *et al.*¹² are reported as PICSs for groups of ions with similar masses, rather than for individual ion fragments. Using electron energy loss spectroscopy (EELS), coupled with a TOFMS, Burton *et al.*¹³ have

reported absolute oscillator strengths for photoabsorption and photoionization of methanol, along with product branching ratios, in the energy range 6 – 360 eV. The fragmentation of ionized methanol following photoionization has also been studied by Pilling *et al.*¹⁴ and the Eland group.^{15,16} Employing photoelectron-photoion-photoion coincidence spectroscopy, together with photons in an energy range from below the double ionization potential up to 48 eV, the Eland group^{15,16} characterized the mechanisms and energetics of the charge-separating dissociation channels of the methanol dication. These studies also used isotopic substitution to show, for example, that the hydrogen atoms making up the H_3^+ product ion, which arises from dissociative double ionization, all originate from the methyl group.¹⁶ In addition, Pilling *et al.*¹⁴ used 100 – 310 eV photons, together with the photoelectron-photoion coincidence (PEPICO) technique, to report partial ion yields and the absolute cross-sections for dissociative and non-dissociative ionization of methanol.

The dissociation of methanol following multiple ionization by highly-charged ion impact has also been investigated,¹⁷ and the observed fragmentation pathways and kinetic energy releases reported. In addition, there has been considerable recent interest^{17,18} in the astrophysical consequences of H_3^+ formation following ionization of methanol, a fragment ion which is formed principally *via* multiple, not single, ionization.¹⁹

This chapter presents an investigation of the electron ionization of methanol in the energy range 30 – 200 eV, using TOF mass spectrometry coupled with a 2D ion coincidence technique. Relative PICSs, $\sigma_r[\text{X}^{m+}]$, for the formation of all fragment ions detected are reported, expressed relative to the formation of the parent ion CH_3OH^+ , as a function of ionizing electron energy. In addition precursor-specific relative PICSs, $\sigma_n[\text{X}^{m+}]$, which quantify the relative cross-sections for forming a fragment ion X^{m+} after single ($n = 1$), double ($n = 2$) and, in principle, triple ($n = 3$) ionization are also presented. These measurements represent the first complete description of the single and multiple ionization of methanol at electron energies below 200 eV. In addition, our 2D ion coincidence technique provides information on the energetics of the dissociation of the multiply charged ions formed in electron-methanol collisions.

5.2 Experimental Procedure

As described in Chapter 2, all experiments were carried out using the TOFMS described in Chapter 2. The operating conditions employed involve using low target gas pressure, together with low electron fluxes, ensures that on average there is considerably less than one ionization event per ionizing electron pulse. This significantly reduces the number of ‘false coincidences’ in our spectra, as described in chapters 2 and 3. The methanol sample, of analytical quality with a purity of 99.99 %, was thoroughly degassed *via* a series of freezing, thawing and pumping cycles prior to the experiment. The methanol sample was then held at a constant temperature of 273 K using a water-ice bath.

Our first mass spectra of methanol showed some broad peaks at high m/z ratios. Following several attempts to identify and remove these peaks, we replaced the tungsten filament in the electron gun with a yttria coated tungsten filament. Following this modification the “impurity” peaks in the mass spectrum disappeared, leading us to believe that these signals were caused by methanol reacting on the hot tungsten filament in the original electron gun. All experiments to determine the relative PICSs of methanol were therefore carried out using yttria-coated tungsten filaments in the electron gun.

5.3 Data Analysis

Mass and coincidence spectra of methanol were recorded at ionising electron energies in the range 30 – 200 eV using the experimental apparatus described in Chapter 2. For each ionising electron energy used, three separate experimental cross-sections determinations were made.

5.3.1 Singles Mass Spectra

A representative mass spectrum of methanol following electron ionisation at 200 eV is shown in Figure 5.1. This figure shows the various ion peaks observed in the singles mass spectra, including the parent monocation, CH_3OH^+ , and ion fragments arising from the dissociation of $\text{CH}_3\text{OH}^{m+}$: CH_3O^+ , CH_2O^+ , CHO^+ , CO^+ , OH_2^+ , OH^+ , O^+ , CH_3^+ , CH_2^+ , CH^+ , C^+ , H_3^+ , H_2^+ , H^+ and CH_3O^{2+} . The intensities of these individual ion peaks $I[X^{m+}]$ appearing in the singles spectra are extracted by summing the counts in each peak, after applying a small correction to account for the non-zero baseline which arises due to stray ions, as described in Section 3.2.1. Additional corrections are also

made to the intensities of the CH_3OH^+ , CO^+ , O^+ and CH_2^+ peaks, due to ions arising from residual air in the apparatus. Such residual gas signals are the result of the low target gas pressures employed in the experiment to minimise false coincidences. Specifically, ionization of O_2 results in the formation of O_2^+ ions, indistinguishable from CH_3OH^+ ions as both have $m/z = 32$, and O^+ ions at $m/z = 16$. Ionization of N_2 results in the formation of N_2^+ ions, indistinguishable from CO^+ ions as both have $m/z = 28$, and N^+ ions, indistinguishable from CH_2^+ ions as both have $m/z = 14$. To quantify these background contributions, the relative intensities of O_2^+ , N_2^+ , O^+ and N^+ with respect to Ar^+ were measured in separate experiments following electron ionization of air, as a function of ionizing electron energy. The subtraction of the ion signals resulting from ionization of the residual gas can then be made by normalisation to the small Ar^+ peak in each methanol mass spectrum, as described in Section 3.2.1. Contributions to the raw ion intensities from the background gases were typically much less than 2 %. No reliable correction could be made for the contribution from the ionization of background water molecules to our mass spectra. However, we believe that only a small contribution to the counts of H_2O^+ , OH^+ , O^+ , H_2^+ and H^+ in the singles spectra result from the ionization of background water molecules, as discussed in Section 5.3.2. As we are unable to distinguish between the isotopologues of a number of carbon containing ions which occur at the same mass in the singles spectrum, for example, $^{13}\text{CH}_3\text{O}$ and $^{12}\text{CH}_3\text{OH}$, the measured ion intensities were corrected numerically for isotopic speciation using the natural isotopic distribution $^{12}\text{C}: ^{13}\text{C}$ (98.93%: 1.07%).

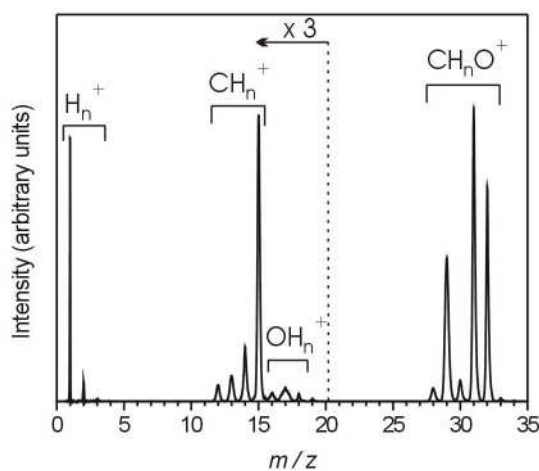


Figure 5.1: Typical mass spectrum (singles spectrum) of methanol following ionization by 200 eV electrons.

5.3.2 Pairs Spectra

A representative pairs mass spectrum of methanol recorded at an ionizing electron energy of 200 eV is shown in Figure 5.2. At this energy 36 different ion pairs formed from the dissociation of $\text{CH}_3\text{OH}^{2+}$ are observed, as listed in Table 5.1. The contribution of a particular ion to the pairs spectra were extracted using the procedure described in Section 3.2.2. As can be seen in Figure 5.2, a number of false coincidences, events in which two ions are detected in coincidence that did not originate from the same ionisation event, are present in the pairs spectra (e.g. $\text{CH}_3\text{OH}^+ + \text{H}^+$). As described in Section 3.2.2.1, these false coincidences are evaluated manually for each peak using the autocorrelation of the singles spectrum.

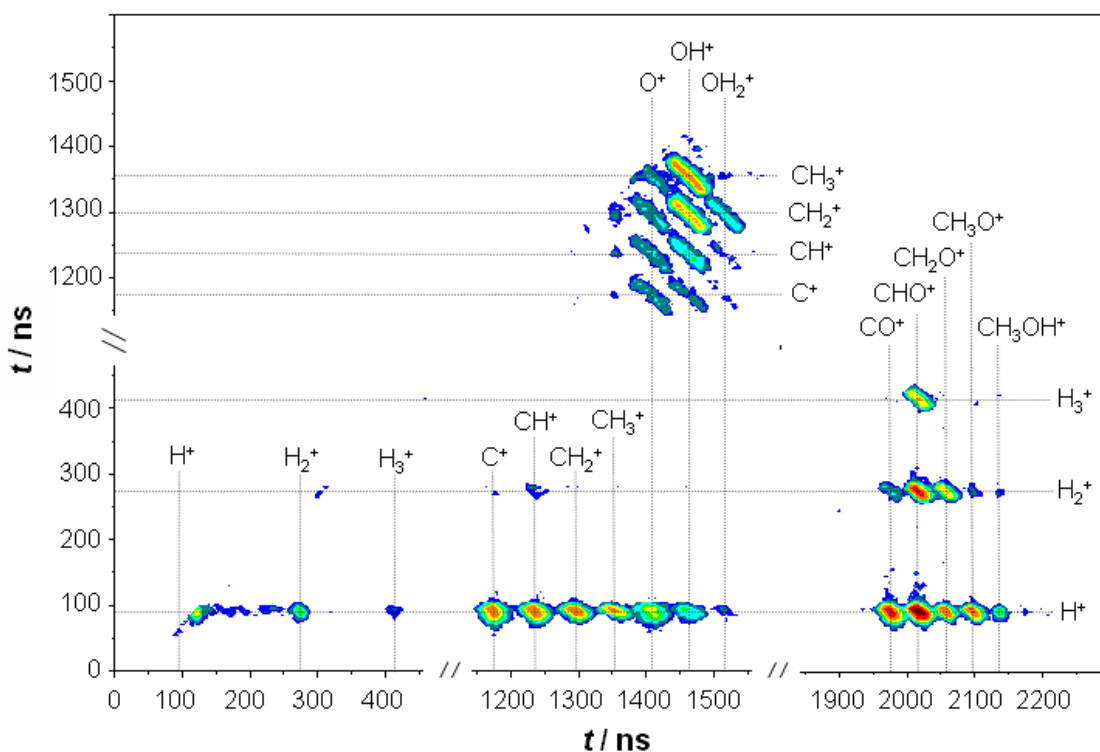


Figure 5.2: Representative pairs spectrum of methanol recorded at an electron energy of 200 eV.

No reliable correction could be made for the contribution from the ionization of background water molecules to our pairs mass spectra. However, we believe that only a small contribution to the counts of H_2O^+ , OH^+ , O^+ , H_2^+ and H^+ in both the pairs and singles spectra result from the ionization of background water molecules. We draw this conclusion from the typical “lozenge” shape of the peaks in the pairs spectrum (Figure

5.2) that involve a $m/z=18$ ion: the $\text{OH}_2^+ + \text{C}^+$, $\text{OH}_2^+ + \text{CH}^+$ and $\text{OH}_2^+ + \text{CH}_2^+$ coincidence peaks. The peak shapes for these channels indicate ion momentum correlations and tell us these ions must have originated from $\text{CH}_3\text{OH}^{2+}$. If a significant amount of background water was present, these peaks would be dominated by ‘false’ coincidences and have a distinctive circular shape. The relative intensity of the OH_2^+ and OH^+ peaks, $\sim 1:4$ in our mass spectra of methanol and $\sim 1:0.3$ in the mass spectrum of H_2O at 200 eV, also indicate a minimal number of background water ions are present in our mass spectra. We are therefore confident that background counts from water are negligible, and we can safely report relative PICSs for the formation of the ions OH_2^+ , OH^+ , O^+ , H_2^+ and H^+ from methanol.

As discussed in Chapter 2, in our experimental arrangement no ion pairs are recorded if the second ion arrives at the detector within 32 ns of the first. This results in a ‘dead region’ in the pairs spectrum affecting the $\text{H}^+ + \text{H}^+$ and $\text{H}_2^+ + \text{H}_2^+$ peaks. As described in Section 3.2.2.3, an estimation of the losses within this dead region can be made by first plotting the time-of-flight difference (ΔTOF) between pairs of ions making up the visible part of the affected pairs peak. Extrapolation of this ΔTOF plot can then be made, using simple geometry, to quantify the counts lost in the dead region.²⁰

Table 5.1: Ion pairs observed in the pairs spectrum recorded following electron ionization of methanol at 200 eV ionizing electron energy.

		Ion 1																	
		H^+	H_2^+	H_3^+	C^+	CH^+	CH_2^+	CH_3^+	O^+	OH^+	OH_2^+	CO^+	CHO^+	CH_2O^+	CH_3O^+	H^+			
Ion 2	H^+	H^+	H^+	H^+	H^+	H^+	H^+	H^+	H^+	H^+	H^+	H^+	H^+	H^+	H^+	H^+	H^+		
	H_2^+	H_2^+	H_2^+		H_2^+	H_2^+	H_2^+		H_2^+	H_2^+		H_2^+	H_2^+	H_2^+			H_2^+		
	H_3^+											H_3^+	H_3^+				H_3^+		
	C^+	C^+							C^+	C^+	C^+							C^+	
	CH^+	CH^+							CH^+	CH^+	CH^+							CH^+	
	CH_2^+	CH_2^+							CH_2^+	CH_2^+	CH_2^+							CH_2^+	
	CH_3^+								CH_3^+	CH_3^+								CH_3^+	
	O^+	O^+			O^+	O^+	O^+	O^+											O^+
	OH^+	OH^+			OH^+	OH^+	OH^+	OH^+											OH^+
	OH_2^+				OH_2^+	OH_2^+	OH_2^+												OH_2^+
	CO^+	CO^+	CO^+																CO^+
	CHO^+	CHO^+	CHO^+																CHO^+
	CH_2O^+	CH_2O^+																	CH_2O^+

5.3.3 Computational Analysis

Due to the absence of any experimental and theoretical data on the double ionization potential of CH₃OH, Gaussian 98²¹ was used to estimate the vertical double ionization energy of methanol. To test our computational methodology, the vertical single ionization energy of methanol was first determined. The structure of neutral methanol was first optimized at an MP2 level of theory, using the aug-cc-pVTZ basis set. Using this optimized structure the energy of neutral and singly charged methanol were calculated at the CCSD(T) level using the cc-pVTZ basis set; the augmented basis being too large to run under CCSD(T) in our implementation. From these calculations the vertical single ionization energy of methanol was calculated to be 10.9 eV, in excellent agreement with the experimental value of 10.8 eV.²² In an analogous manner we determine a vertical double ionization energy of 32.4 eV for populating the first singlet state of CH₃OH²⁺ and 32.5 eV to form the first triplet state. Adiabatic ionization energies could not be calculated as no stable structure for the CH₃OH²⁺ isomer of methanol could be located. It should be noted, however, that a minimum does exist on the [CH₄O]²⁺ potential energy surface at the geometry of the methyleneoxonium dication (CH₂OH₂²⁺).^{23,24}

5.4 Relative Partial Ionisation Cross-sections

5.4.1 Results

Mass and coincidence spectra of methanol were recorded at ionizing electron energies in the range 30 – 200 eV. These spectra were processed, as described in Section 3.3.2, to yield the relative PICSs $\sigma_r[X^{m+}]$ for the formation of all fragment ions observed: CH₃O⁺, CH₂O⁺, CHO⁺, CO⁺, OH₂⁺, OH⁺, O⁺, CH₃⁺, CH₂⁺, CH⁺, C⁺, H₃⁺, H₂⁺, H⁺ and CH₃O²⁺. These $\sigma_r[X^{m+}]$ values are expressed relative to the CH₃OH⁺ ion yield, and are displayed as a function of electron energy in Figure 5.3 and Table B.4. Precursor-specific relative PICSs $\sigma_n[X^{m+}]$ were also derived for these fragment ions, using the procedure described in Section 3.3.4. These $\sigma_n[X^{m+}]$ ($n = 1 - 3$) values are expressed relative to the H₂S⁺ ion yield, and are displayed as a function of electron energy in Figure 5.5 and Table B.5. As discussed in Section 1.4.3, producing absolute PICSs requires the accurate measurement of four experimental variables: the initial electron flux, the number density of the target gas, the collisional pathlength and number of ions formed by electron ionization events. Determination of the first three of

these variables is experimentally non-trivial, and thus we report relative PICSs. These relative values can be readily placed on an absolute scale using the measurements of the total ionization cross-sections discussed above. For example, to produce an absolute value for $\sigma[H^+]$ simply requires an absolute value for the cross-section for forming the parent monocation, CH_3OH^+ , $\sigma[CH_3OH^+]$:

$$\sigma[H^+] = \sigma_r[H^+] \times \sigma[CH_3OH^+] \quad (5.1)$$

As discussed in Section 1.4.3, one advantage of producing relative PICSs relative to the parent monocation is that the parent monocation is formed with a thermal distribution and thus the least likely to suffer from ion discrimination effects. Therefore, even previous cross-section determinations in which the efficient collection of energetic ions is not accounted for should produce accurate $\sigma[\text{parent}^+]$ values.

We observe 36 different ion pairs formed from the dissociation of CH_3OH^{2+} in our pairs spectra, as listed in Table 5.1. At all ionizing electron energies contribution from ion triples was negligible, as the small number of counts in each triples channel was effectively reduced to zero, within error, following false coincidence correction. Therefore, we report no contributions from triple ionization to the ionization cross-sections of methanol. The overall contributions from single and double ionization as a percentage of the total ion yield are given in Figure 5.6 and Table B.6.

The relative PICSs reported for the formation of CH_3O^{2+} , the only dicationic species observed in our mass spectra, are given as an upper limit. This is due to the difficulty in accurately evaluating the counts in the CH_3O^{2+} peak in the ‘singles’ mass spectrum, due to the overlap of this weak signal with the adjacent CH_3^+ and O^+ peaks.

As can be seen from Figures 5.3 and 5.5, as the ionizing electron energy is increases, the general trend of the cross sections is to increase from threshold to a maximum, after which they gently drop off. As discussed in Section 1.4.3., such a trend is observed for all electron-molecule interactions, as the efficiency at which the electron interacts with a molecule decreases with increasing electron energy. This is due to the fact that higher energy electrons are moving faster. As the energy is increased, there, in principle, reaches a point at which the electron is moving so fast it does not interact with the species at all and the cross section falls to zero.

As discussed in Section 3.3, a value for the ion detection efficiency f_i is required to enable us to derive $\sigma_n[X^{m+}]$ values. Measurement of f_i for our apparatus, using the

methodology described in Section 3.3.3, resulted in a value of 0.26 ± 0.01 , in good agreement with previous determinations.²⁵⁻²⁸

5.5 Discussion

5.5.1 Relative PICSSs (σ_r)

The values of σ_r we have derived are displayed in Figure 5.3 and given numerically in Table B.4. Where appropriate these values are compared with values of relative PICSSs derived from the data of Srivastava *et al.*¹¹ To enable a direct comparison with the results of Rejoub *et al.*,¹² who report PICSSs for the groups of ions CH_nO^+ and $\text{OH}_n^+ + \text{CH}_n^+$, and for the ionic fragments H_2^+ and H^+ , we have also calculated relative PICSSs for the same groups of ions and ion fragments relative to the summed cross-section for the CH_nO^+ group of ions, as shown in Figure 5.4. As can be seen from Figure 5.3, CH_3O^+ is the most abundant ion formed at all ionizing electron energies investigated.

Comparison of our $\sigma_r[\text{X}^+]$ values to those derived from the work of Rejoub *et al.*,¹² in which the efficient collection of all ion fragments with considerable transitional energy was demonstrated, show good agreement at all ionizing electron energies investigated (Figure 5.4). By contrast, there is a significant difference between the values of $\sigma_r[\text{X}^+]$ we determine and those derived by Srivastava *et al.*¹¹ (Figure 5.3), with our values being considerably higher for all ionic fragments except H_2^+ . These differences can be explained by the inefficient collection of translationally energetic fragment ions in the earlier work, as has been discussed before.²⁸⁻³⁰ As mentioned above, contrary to all the other fragment ions, the $\sigma_r[\text{H}_2^+]$ values derived from the data of Srivastava *et al.*¹¹ are considerably higher than the values we obtain. The reasons for this discrepancy are unclear; however, it should be noted that our $\sigma_r[\text{H}_2^+]$ values and those obtained by Rejoub *et al.*¹² are in good agreement.

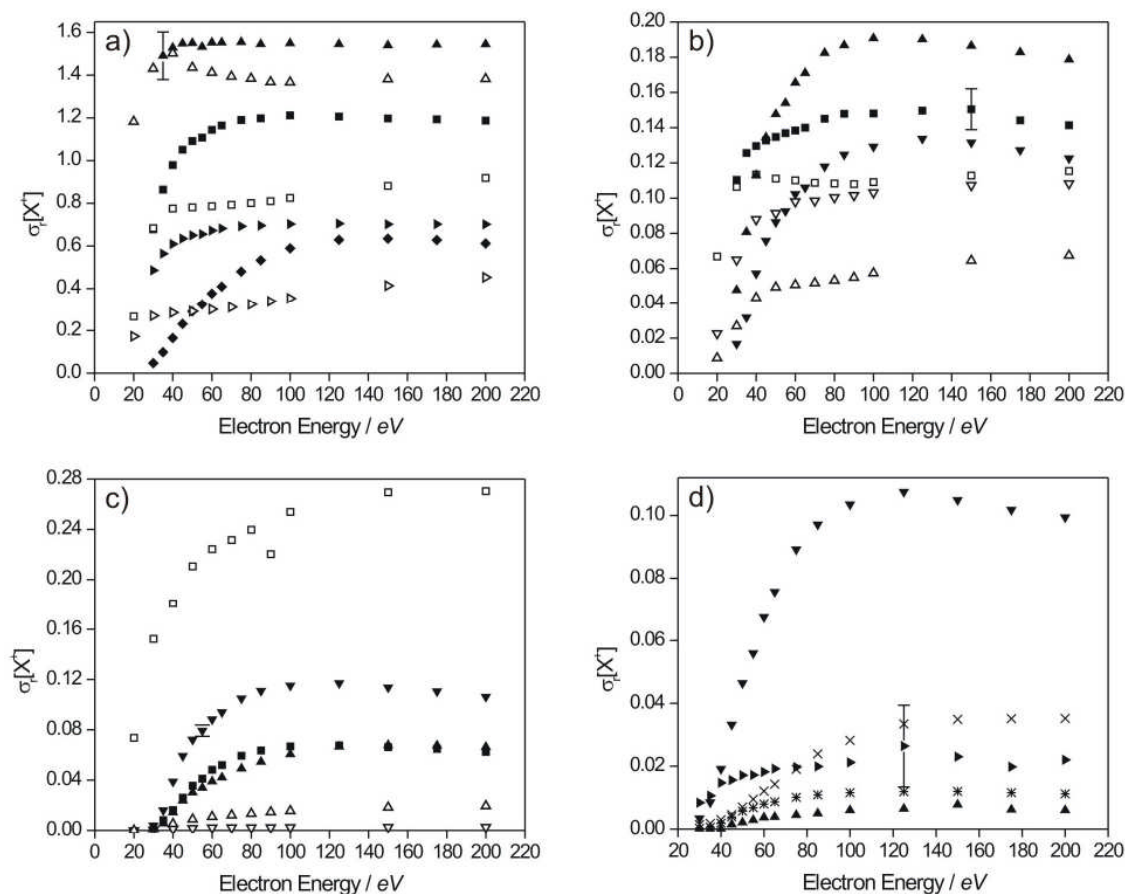


Figure 5.3: Relative PICSSs $\sigma_r[X^{m+}]$ for forming (a) CH_3O^+ (\blacktriangle), CHO^+ (\blacksquare), CH_3^+ (\blacktriangleright) and H^+ (\blacklozenge), (b) CH_2^+ (\blacktriangle), CH_2O^+ (\blacksquare) and CO^+ (\blacktriangledown), (c) CH^+ (\blacktriangledown), C^+ (\blacksquare) and H_2^+ (\blacktriangle) and (d) OH^+ (\blacktriangledown), O^+ (\times), OH_2^+ (\blacktriangleright), H_3^+ (\blackstar) and CH_3O_2^+ (\blacktriangle), following electron ionization of methanol. Where available the corresponding relative PICSSs from the data of Srivastava *et al.*¹¹ are also shown as open symbols. The error bars expressed in this figure represent two standard deviations of three separate determinations.

Comparison of our $\sigma_r[X^+]$ values to those derived from the (e,2e) pseudo-photoinduced fragmentation data of Burton *et al.*¹³ and the photodissociation data of Pilling *et al.*¹⁴ have also been made. For the majority of fragment ions, the relative PICSSs for forming fragment ions at ionizing electron energies of 40, 60 and 100 eV in our study agree relatively well with those obtained by Burton *et al.*¹³ at photon energies of 30, 40 and 50 eV respectively. However relative PICSSs obtained from the data of Burton *et al.*¹³ above a photon energy of 50 eV are generally considerably higher than those we obtain at any ionizing electron energy up to 200 eV. Similar trends are apparent when comparing our data with the relative PICSSs obtained from the photodissociation work of Pilling *et al.*¹⁴ Specifically, the PICSSs obtained for the

majority of fragment ions formed *via* photodissociation of methanol at 100 eV are significantly higher than any reported in our dataset for methanol ions formed *via* electron ionization.¹⁴

No thresholds for the formation of any fragment ions are noted in the ionizing energy range investigated (30-200 eV), with the exception of the CH_3O^{2+} dication. An estimate for the appearance energy of CH_3O^{2+} was made by extrapolation of a linear fit to the three PICS points above 40 eV, yielding a threshold of 33.7 ± 2.0 eV, in good agreement with a previous determination of 33 to 35 eV by Eland *et al.*¹⁶ This value lies above the double ionization potential of methanol, calculated to be 32.4 eV. Despite an estimated appearance energy of 33.7 ± 2.0 eV, no CH_3O^{2+} signal is discernable in our mass spectra at ionizing electron energies of 35 and 40 eV. This lack of signal is attributed to the poorer experimental mass resolution at lower ionizing electron energies, where the strong adjacent CH_3^+ ($m/z = 15$) and O^+ ($m/z = 16$) signals mask any weak CH_3O^{2+} signals at $m/z = 15.5$. The maximum relative yield of CH_3O^{2+} is observed at 150 eV ionizing electron energy.

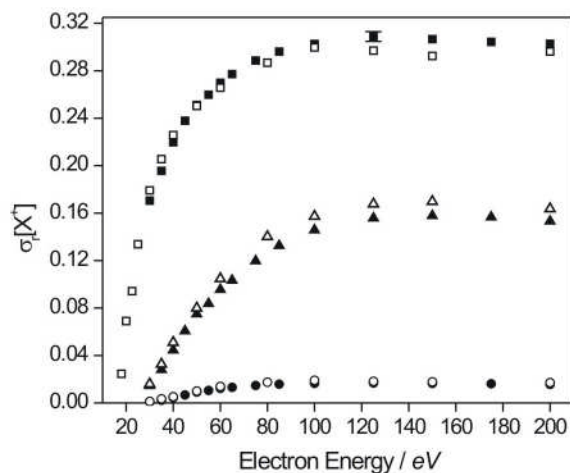


Figure 5.4: Relative PICSs $\sigma_r[X^+]$ for forming $\text{CH}_n^+ + \text{H}_n\text{O}^+$ (\blacksquare), H_2^+ (\bullet) and H^+ (\blacktriangle) following electron ionization of methanol, relative to the summed cross-sections for forming the group of ions CH_nO^+ . Similar PICSs extracted from the data of Rejoub *et al.*¹² (open shapes) are also shown. The representative error bars expressed in this figure represent two standard deviations of three separate determinations.

5.5.2 Precursor-Specific Relative PICSSs (σ_n)

A comparison of the values of σ_1 and σ_2 for the formation of monocation fragments formed following electron ionization of methanol are displayed in Figure 5.5 and given numerically in Table B.5. Figure 5.6 indicates the contribution from single and double ionization to the total ion yield. The most significant contribution to the majority of ion yields is from dissociative single ionization. The exceptions to this generalization are the fragment ions OH^+ , O^+ , H_3^+ , H_2^+ , and H^+ . For the fragment ions OH^+ , O^+ , H_2^+ and H^+ , contributions from dissociative single ionization rise rapidly between 30-60 eV, after which they level off or decrease up to 200 eV. However the contributions to the ion yields of OH^+ , O^+ , H_2^+ and H^+ from dissociative double ionization continue to increase monotonically with increasing electron energy, so that at 200 eV dissociative double ionization contributes 83.2 %, 74.8 %, 89.4 % and 53.3 % to the yields for these ions respectively.

The ion yield of H_3^+ is almost entirely from dissociative double ionization at all ionizing electron energies. This is an observation in agreement with other data, which suggests the majority of all H_3^+ ions seen in the mass spectra of simple compounds come from charge separation of the doubly-charged precursor ions.¹⁹ The majority of H_3^+ ions are thus formed with significant amounts of kinetic energy, which results in a broadening of the H_3^+ peak in the singles spectrum. This peak results principally from events where an H_3^+ ion formed from dissociative double ionization is detected but its ionic partner is missed due to our experimental detection efficiency being less than unity. Since the formation of H_3^+ is not a major channel following the electron ionization of methanol (Figure 5.3 and Table B.4), the broad wings of the H_3^+ peak are hard to discern in the singles spectrum and become lost in the baseline, so the limits of the H_3^+ peak have to be estimated. These problems result in significant uncertainty in $\sigma_1[\text{H}_3^+]$ (Figure 5.5 and Table B.5).

The contribution from double ionization to the ion yield (Figure 5.6), effectively zero at an ionizing electron energy of 30 eV, increases considerably between energies of 40-125 eV, then remains effectively constant up to 200 eV where the contribution is 20%.

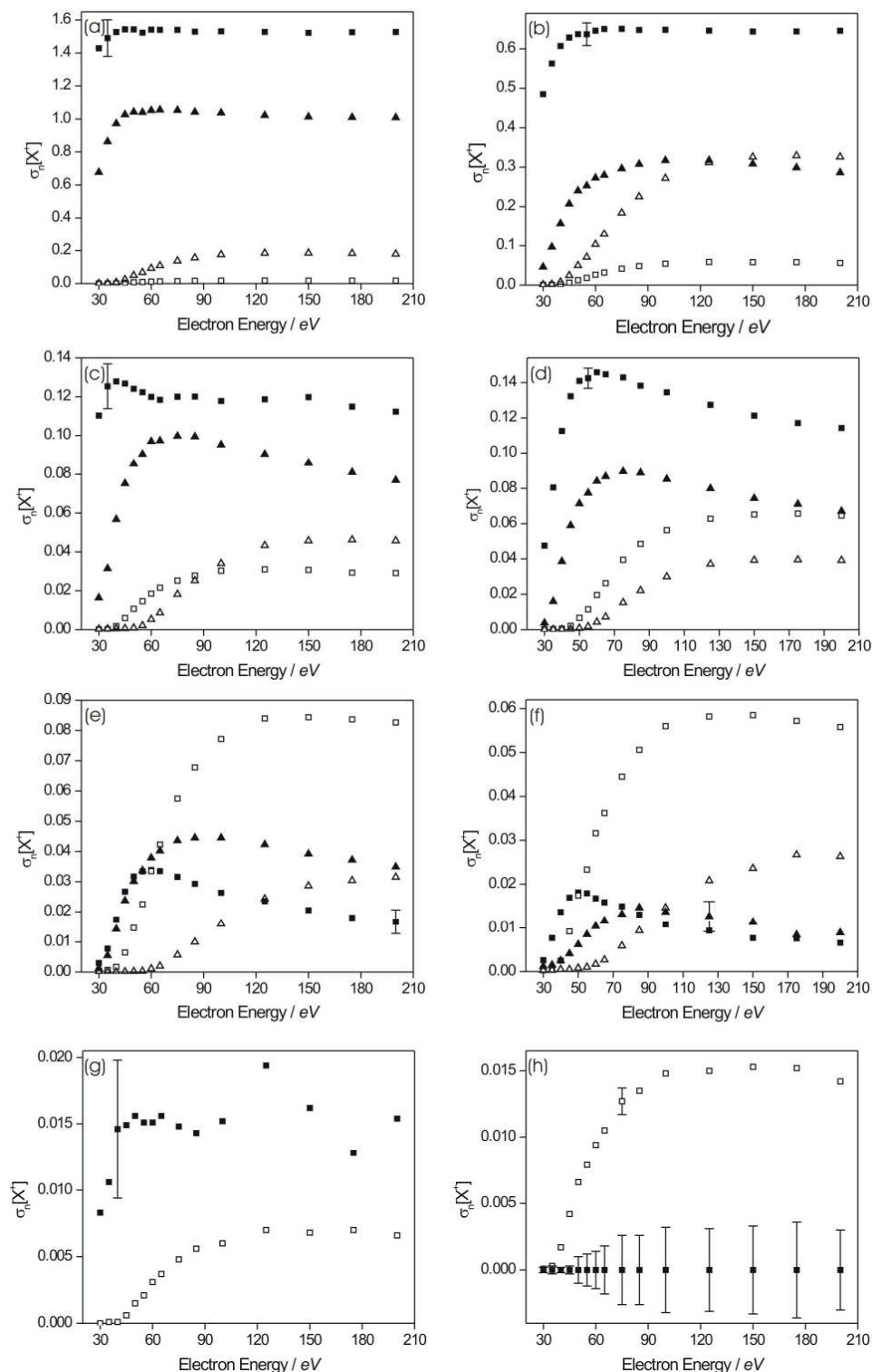


Figure 5.5: Precursor-specific relative PICSS for forming (a) CH_3O^+ (■) and CHO^+ (▲), (b) CH_3^+ (■) and H^+ (▲), (c) CH_2O^+ (■) and CO^+ (▲), (d) CH_2^+ (■) and CH^+ (▲), (e) OH^+ (■) and C^+ (▲), (f) H_2^+ (■) and O^+ (▲) (g) OH_2^+ (■) and (h) H_3^+ (■) monocation fragments via single (closed shapes) and double (open shapes) ionization, following electron ionization of methanol. The representative error bars show two standard deviations of three determinations.

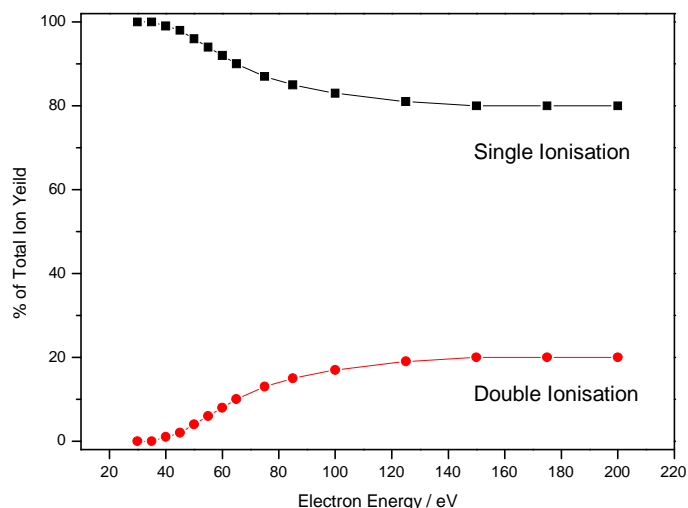


Figure 5.6: Contributions to the total ion yield from single and double ionization following electron ionization of methanol.

5.5.3 Energetics and Dissociation of $\text{CH}_3\text{OH}^{2+}$

As described in Section 3.4, from the pairs data at a given electron energy, a time-of-flight difference (ΔTOF) spectrum³¹ can be constructed for the events making up each dissociation channel of the methanol dication. The shape and width of the ΔTOF plot is determined by the KER and angular distribution of the dissociation, as well as several apparatus parameters. For a two-body dissociation (Table 5.2), where the mechanism of the fragmentation is not in question, Monte Carlo simulations can be directly employed to model the ΔTOF peaks, thus yielding the KER for a given two-body fragmentation pathway of $\text{CH}_3\text{OH}^{2+}$. As can be seen from Table 5.2 and Table 5.3, for several of the dissociation channels of $\text{CH}_3\text{OH}^{2+}$ more than one KER value was required to satisfactorily fit the experimental ΔTOF spectrum, if the width of the (Gaussian) KER distribution was restricted to realistic values, below 2.5 eV. A summary of the KERs we extract for the two-body fragmentations following double ionization of methanol is given in Table 5.2. Good agreement is observed between our two-body KER values and the data of Eland and Trevesbrown¹⁶ recorded following photoionization of methanol at 40.8 eV. Good agreement is also noted between our two-body KER values and those obtained by Rühl *et. al.*¹⁵ following photoionization of methanol at 40.8 eV, with the exception of the ion pair $\text{OH}_2^+ + \text{CH}_2^+$, for which the values lie just outside their mutual error limits.

Table 5.2: Kinetic energy releases (KERs) for two-body fragmentations following double ionization of methanol. Where available literature values are also given, along with the calculated precursor state energies E of the methanol dication. The weightings of the KERs are listed, together with an average KER to facilitate a direct comparison with the literature.

Ion pair	Electron energy/ eV	KERs	Weighting (%)	Average KER		E / eV
				Current work	Lit. ^(a,b)	
$\text{CH}_3\text{O}^+ + \text{H}^+$	65	1.8 ± 1.0	50	3.2 ± 1.0	$4.5 \pm 0.6^{(a)}$	30.7
		4.5 ± 1.0	50		$4.4 \pm 1.4^{(b)}$	33.4
$\text{CH}_2\text{O}^+ + \text{H}_2^+$	65	4.1 ± 1.0	100	4.1 ± 1.0	$3.4 \pm 1.4^{(b)}$	31.4
$\text{CHO}^+ + \text{H}_3^+$	65	5.1 ± 1.0	100	4.1 ± 1.0	$4.8 \pm 0.4^{(a)}$	28.5
					$3.6 \pm 1.0^{(b)}$	
$\text{OH}_2^+ + \text{CH}_2^+$	175	5.2 ± 1.0	100	5.1 ± 1.0	$2.9 \pm 1.6^{(b)}$	31.7
$\text{OH}^+ + \text{CH}_3^+$	65	5.2 ± 1.0	100	5.2 ± 1.0	$5.9 \pm 0.4^{(a)}$	32.1

^a Values are taken from Ref. [15].

^b Values are taken from Ref. [16].

To extract the KER values for the three-body dissociations of $\text{CH}_3\text{OH}^{2+}$, fragmentations where one or more neutral is formed in addition to the pair of monocations, we require the mechanism of the dissociation. As described in Section 3.4, this mechanistic information, in principle, can be extracted from the gradient of the relevant peak in the pairs spectrum.^{31,32} However, for several of the three-body dissociation channels we observe, there are several possible dissociation pathways that would give peak slopes which match the experimental value. For example, for the ion pair $\text{O}^+ + \text{H}^+$ the experimental peak gradient from the pairs spectrum was -0.25 ± 0.03 (Table 5.3). One possible dissociation pathway for forming this ion pair involves a primary dication dissociation to form CH_4^+ and O^+ , followed by CH_4^+ undergoing a secondary dissociation into CH_3 and H^+ . This secondary decay mechanism would have a limiting peak gradient of -0.06 , which is potentially consistent with the observed experimental value of -0.25 if the decay of the primary CH_4^+ product occurred within the field of the O^+ ion; in such a situation the actual peak gradient lies between the limiting value (-0.06) and -1 .^{32,33} However, another possible dissociation pathway with a limiting peak gradient of -0.07 involves a primary dissociation of $\text{CH}_3\text{OH}^{2+}$ into CH_3^+ and OH^+ , with the primary product ions then fragmenting to form H^+ and O^+ respectively. To distinguish between these two possible decay pathways we note that only the primary fragmentation of $\text{CH}_3\text{OH}^{2+}$ to CH_3^+ and OH^+ is observed as a two-

body reaction in the pairs spectrum (Table 5.2). This observation hints strongly, but does not conclude definitively, that the primary fragmentation to $\text{CH}_3^+ + \text{OH}^+$ is the more likely route to the $\text{O}^+ + \text{H}^+$ ion pair. For the observed three-body dissociation reactions of $\text{CH}_3\text{OH}^{2+}$ where more than one potential fragmentation pathway is possible from the initial consideration of the peak slopes, considering which two-body fragmentations are observed in the pairs spectrum always allows a unique dissociation pathway to be assigned.

Table 5.3: Kinetic energy releases (KERs) for three- or four-body break ups following double ionization of methanol. Where available literature values are also given, along with the calculated precursor state energies of the methanol dication E . The experimental peak gradient is given, together with the peak gradient calculated using the given dissociation pathway. See text and Table 5.2 for details.

Ion pair	Dissociation pathway	Peak gradient		Electron energy (eV)	KERs	Weightings (%)	Average KER (eV)		E / eV	
		Calc.	Exp.				Current work	Lit. ^(a,b)		
$\text{CH}_2\text{O}^+ + \text{H}^+$	$\text{CH}_3\text{OH}^{2+} \rightarrow \text{CH}_2\text{O}^+ + \text{H}_2^+$	-0.50	-0.51(2)	65	2.6 ± 1.0	100	2.6 ± 1.0	4.0 ± 0.6 ^(a)	32.6	
	$\text{H}_2^+ \rightarrow \text{H}^+ + \text{H}$							3.3 ± 1.1 ^(b)		
$\text{CHO}^+ + \text{H}_2^+$	$\text{CH}_3\text{OH}^{2+} \rightarrow \text{CHO}^+ + \text{H}_3^+$	-0.67	-0.71(3)	65	2.8 ± 1.0	100	2.8 ± 1.0	4.4 ± 0.5 ^(a)	31.1	
	$\text{H}_3^+ \rightarrow \text{H}_2^+ + \text{H}$							3.7 ± 1.1 ^(b)		
$\text{CHO}^+ + \text{H}^+$	$\text{CH}_3\text{OH}^{2+} \rightarrow \text{CH}_2\text{O}^+ + \text{H}_2^+$	-0.52	-0.48(3)	65	2.3 ± 1.0	40	4.4 ± 1.0	3.6 ± 0.4 ^(a)	37.6	
	$\text{CH}_2\text{O}^+ \rightarrow \text{CHO}^+ + \text{H}$				5.8 ± 1.0			60		4.5 ± 1.0 ^(b)
$\text{CO}^+ + \text{H}^+$	$\text{CH}_3\text{OH}^{2+} \rightarrow \text{CH}_2\text{O}^+ + \text{H}_2^+$	-0.52	-0.54(9)	65	2.2 ± 1.0	50	4.5 ± 1.0		35.3	
	$\text{CH}_2\text{O}^+ \rightarrow \text{CO}^+ + \text{H}_2$				6.8 ± 1.0			50		39.9
$\text{H}_2^+ \rightarrow \text{H}^+ + \text{H}$	$\text{H}_2^+ \rightarrow \text{H}^+ + \text{H}$									
	$\text{CH}_3\text{OH}^{2+} \rightarrow \text{CH}_2\text{O}^+ + \text{H}_2^+$									
$\text{OH}^+ + \text{CH}_2^+$	$\text{CH}_3\text{OH}^{2+} \rightarrow \text{OH}^+ + \text{CH}_3^+$	-0.93	-0.96(2)	65	4.8 ± 1.0	100	4.8 ± 1.0	5.3 ± 1.0 ^(a)	37.0	
	$\text{CH}_3^+ \rightarrow \text{CH}_2^+ + \text{H}$							4.2 ± 1.6 ^(b)		
$\text{OH}^+ + \text{CH}^+$	$\text{CH}_3\text{OH}^{2+} \rightarrow \text{OH}^+ + \text{CH}_3^+$	-0.87	-0.87(2)	100	5.2 ± 1.0	100	5.2 ± 1.0		37.5	
	$\text{CH}_3^+ \rightarrow \text{CH}^+ + \text{H}_2$									
$\text{O}^+ + \text{H}^+$	$\text{CH}_3\text{OH}^{2+} \rightarrow \text{OH}^+ + \text{CH}_3^+$	-0.07	-0.25(3)	125	1.8 ± 1.0	40	4.9 ± 1.0		42.2	
	$\text{OH}^+ \rightarrow \text{O}^+ + \text{H}$				6.4 ± 1.0			45		46.8
	$\text{CH}_3^+ \rightarrow \text{H}^+ + \text{CH}_2$				8.5 ± 1.0			15		48.9
$\text{CH}_3^+ + \text{H}^+$	$\text{CH}_3\text{OH}^{2+} \rightarrow \text{CH}_3^+ + \text{OH}^+$	-0.06	-0.25(1)	65	1.2 ± 1.0	35	3.5 ± 1.0		33.1	
	$\text{OH}^+ \rightarrow \text{H}^+ + \text{O}$				4.6 ± 1.0			55		36.5
	$\text{CH}_3^+ \rightarrow \text{H}^+ + \text{CH}_2$				5.2 ± 1.0			10		37.1
$\text{CH}_2^+ + \text{H}^+$	$\text{CH}_3\text{OH}^{2+} \rightarrow \text{CH}_3^+ + \text{OH}^+$	-0.06	-0.29(4)	65	1.9 ± 1.0	50	3.1 ± 1.0		39.1	
	$\text{CH}_3^+ \rightarrow \text{CH}_2^+ + \text{H}$				4.3 ± 1.0			50		41.8
	$\text{OH}^+ \rightarrow \text{H}^+ + \text{O}$									
$\text{CH}^+ + \text{H}^+$	$\text{CH}_3\text{OH}^{2+} \rightarrow \text{CH}_3^+ + \text{OH}^+$	-0.07	-0.34(3)	75	1.6 ± 1.0	35	3.8 ± 1.0		38.9	
	$\text{CH}_3^+ \rightarrow \text{CH}^+ + \text{H}_2$				4.5 ± 1.0			45		41.8
	$\text{OH}^+ \rightarrow \text{H}^+ + \text{O}$				6.1 ± 1.0			20		43.4

^a Values are taken from ref. 15.

^b Values are taken from ref. 16.

For those peaks in the pairs spectra that contain sufficient counts to produce statistically significant results, the dissociation pathways and KERs that have been determined using the above methodology are summarized in Table 5.3. As indicated in Table 5.3 the data analyzed for each reaction channel was that recorded at the lowest

electron energy at which there were sufficient counts to produce a statistically significant result.

For the three-body dissociation channels for which complementary KER determinations have been made by Eland and Trevesbrown¹⁶ good agreement is observed between the two sets of KER values, with the exception of the $\text{CHO}^+ + \text{H}_2^+$ ion pair, for which the two values lie just outside the mutual error limits. Agreement is also seen for the majority of our derived dissociation mechanisms, with those proposed by Eland and Trevesbrown.¹⁶ However differences are observed for the dissociation mechanisms for the ion pairs $\text{CH}_2\text{O}^+ + \text{H}^+$, $\text{CHO}^+ + \text{H}_2^+$, $\text{CHO}^+ + \text{H}^+$ and $\text{CH}_2^+ + \text{H}^+$. For these ion pairs, Eland and Trevesbrown¹⁶ observe peak gradients that are indistinguishable from -1, suggesting the dissociation mechanism for these four channels is *via* deferred charge separation. In the current work the peak gradients for the four ion pairs are far removed from -1, suggesting the dissociation mechanism for these four channels involves secondary decay of one or both of the initial primary ion fragments (Table 5.3). These differences in the dissociation mechanisms are likely to be the result of the different ionization energies used in the two set of experiments. The pairs data from which we extract peak slopes are recorded at higher ionizing energies than the photoionization experiments of Eland and Trevesbrown.¹⁶ Thus a large number of higher lying electronic states of the methanol dication are accessible in our experiments. These higher lying states clearly decay *via* secondary dissociations in contrast to the low-lying states populated by 40.8 eV photoionization. Indeed, Eland and Trevesbrown¹⁶ clearly observed a metastable tail from the $\text{CH}_2\text{O}^+ + \text{H}^+$ peak in the pairs spectrum; no such delayed dissociation is apparent in our data, reinforcing the suggestion that different energy levels are being populated in the photoionization and electron ionization experiments. Good agreement is also observed between our three-body KER values and the data of Rühl *et. al.*¹⁵ The exception to this agreement is again the ion pair $\text{CHO}^+ + \text{H}^+$, for which Rühl *et. al.*¹⁵ also suggest a dissociation mechanism involving the initial loss of a neutral H_2 fragment, followed by deferred charge separation. Again this difference can be accounted for by the population of higher energy states of $\text{CH}_3\text{OH}^{2+}$ in our experiments.

Using the calculated KERs, along with thermochemical data²² on the products of the break-up reactions, we are also able to estimate precursor state energies of the methanol dication before fragmentation. These precursor state energies are given in Table 5.2 and Table 5.3, but given the paucity of information on the electronic states of

$\text{CH}_3\text{OH}^{2+}$ only some general observations can be made concerning these values. Firstly, several of the precursor state energies lie below the calculated double ionization potential of methanol (32.4 eV, see above). This clearly suggests that the products from these dissociation channels are formed with significant internal excitation, as the calculated precursor energies are for dissociation products in their ground states. Of course, the population of dissociative dication states *via* stepwise indirect double ionization at energies below the vertical double ionization potential is also well characterized.³⁴⁻³⁷ However, given the major chemical rearrangements involved in many of the dissociation reactions, internal excitation of the monocationic products is certainly to be expected. For the simple two-body dissociation reactions forming $\text{CH}_3\text{O}^+ + \text{H}^+$ and $\text{CH}_3^+ + \text{OH}^+$, where it appears that just simple bond cleavage is involved in the dissociation reaction, the precursor energies agree well with the calculated double ionization potential of methanol. Many of the precursor energies lie below 40 eV, indicating that the methanol dication has several electronic states in this energy regime and, probably, those states have complex potential energy landscapes allowing the dissociation to several product asymptotes. This observation highlights the need for further theoretical work on the nature of the electronic states of $\text{CH}_3\text{OH}^{2+}$.

5.6 Conclusions

Two-dimensional time-of-flight mass spectrometry has been used to measure relative and precursor-specific relative PICSs for the formation of all positive ion fragments following electron ionization of methanol in the energy range 30-200 eV. To the best of our knowledge this is the first time that precursor-specific relative PICSs have been derived for the electron ionization of methanol. The contribution from double ionization to the ion yield reaches a maximum between electron energies of 150 and 200 eV, accounting for 20 % of all ions formed, whereas contribution from triple ionization is negligible at all ionizing electron energies employed. Good agreement between our data and relative PICSs derived from the data of Rejoub *et al.*¹² has been demonstrated. Conversely, discrepancies are observed with the absolute partial ionization cross-sections of Srivistava *et al.*;¹¹ discrepancies we attribute to the loss of translationally energetic fragment ions. Measurements of the KER involved in several of the dissociation pathways have been made, and suggest many of the ionic and neutral products are formed in excited states.

5.7 References

- 1 K. Na, Y. P. Kim, K. C. Moon, I. Moon, and K. Fung, *Atmos. Environ.* **35**, 2747 (2001).
- 2 E. Cetin, M. Odabasi, and R. Seyfioglu, *Sci. Total Environ.* **312**, 103 (2003).
- 3 D. Bockeleemorvan, J. Crovisier, P. Colom, and D. Despois, *Astron. Astrophys.* **287**, 647 (1994).
- 4 J. Crovisier and D. Bockelee-Morvan, *Space Sci. Rev.* **90**, 19 (1998).
- 5 M. J. Mumma, N. Dello Russo, M. A. DiSanti, K. Magee-Sauer, R. E. Novak, S. Brittain, T. Rettig, I. S. McLean, D. C. Reuter, and L. H. Xu, *Sci.* **292**, 1334 (2001).
- 6 R. J. A. Grim, F. Baas, T. R. Geballe, J. M. Greenberg, and W. Schutte, *Astron. Astrophys.* **243**, 473 (1991).
- 7 K. M. Pontoppidan, E. F. van Dishoeck, and E. Dartois, *Astron. Astrophys.* **426**, 925 (2004).
- 8 N. Duric, I. Cadez, and M. Kurepa, *Fizika* **21**, 339 (1989).
- 9 J. E. Hudson, M. L. Hamilton, C. Vallance, and P. W. Harland, *Phys. Chem. Chem. Phys.* **5**, 3162 (2003).
- 10 A. N. Zvilopulo, F. F. Chipev, and L. M. Kokhtych, *Nucl. Instrum. Methods Phys. Res., Sect. B* **233**, 302 (2005).
- 11 S. K. Srivastava, E. Krishnakumar, A. F. Fucaloro, and T. vanNote, *J. Geophys. Res., Planets* **101**, 26155 (1996).
- 12 R. Rejoub, C. D. Morton, B. G. Lindsay, and R. F. Stebbings, *J. Chem. Phys.* **118** (2003).
- 13 G. R. Burton, W. F. Chan, G. Cooper, and C. E. Brion, *Chem. Phys.* **167**, 349 (1992).
- 14 S. Pilling, R. Neves, A. C. F. Santos, and H. M. Boechat-Roberty, *Astron. Astrophys.* **464**, 393 (2007).
- 15 E. Ruhl, S. D. Price, S. Leach, and J. H. D. Eland, *Int. J. Mass. Spectrom. Ion Processes* **97**, 175 (1990).
- 16 J. H. D. Eland and B. J. Trevesbrown, *Int. J. Mass Spectrom. Ion Processes* **113**, 167 (1992).
- 17 S. De, J. Rajput, A. Roy, P. N. Ghosh, and C. P. Safvan, *Phys. Rev. Lett.* **97**, 213201 (2006).

- 18 S. Pilling, D. P. P. Andrade, R. Neves, A. M. Ferreira-Rodrigues, A. C. F. Santos, and H. M. Boechat-Roberly, *Mon. Not. R. Astron. Soc.* **375**, 1488 (2007).
- 19 J. H. D. Eland, *Rapid Commun. Mass Spectrom.* **10**, 1560 (1996).
- 20 M. R. Bruce, L. Mi, C. R. Sporleder, and R. A. Bonham, *J. Phys. B: At., Mol. Opt. Phys.* **27**, 5773 (1994).
- 21 M. J. Frisch, G. W. Trucks, H. B. Schlegel, G. E. Scuseria, M. A. Robb, J. R. Cheeseman, V. G. Zakrzewski, J. A. M. Jr., R. E. Stratmann, J. C. Burant, S. Dapprich, J. M. Milliam, A. D. Daniels, K. N. Kudin, M. C. Strain, O. Farkas, J. Tomasi, V. Barone, M. Cossi, R. Cammi, B. Mennucci, C. Pomelli, C. Adamo, S. Clifford, J. Ochterski, G. A. Petersson, P. Y. Ayala, Q. Cui, K. Morokuma, D. K. Malick, A. D. Rabuck, K. Raghavachari, J. B. Foresman, J. Cioslowski, J. V. Ortiz, A. G. Baboul, B. B. Stefanov, G. Liu, A. Liashenko, P. Piskorz, I. Komaromi, R. Gomperts, R. L. Martin, D. J. Fox, T. Keith, M. A. Al-Laham, C. Y. Peng, A. Nanayakkara, M. Challacombe, P. M. W. Gill, B. Johnson, W. Chen, M. W. Wong, J. L. Andres, C. Gonzalez, M. Head-Gordon, E. S. Replogle, and J. A. Pople, *Gaussian 98, Revision A.9* (Gaussian, Inc., Pittsburgh PA, 1998).
- 22 *NIST Chemical WebBook; NIST Standard Reference Database Number 69*, Vol., edited by P. J. Linstrom and W. G. Mallard (National Institute of Standards and Technology, Gaithersburg MD, 20899, 2008).
- 23 W. J. Bouma and L. Radom, *J. Am. Chem. Soc.* **105**, 5484 (1863).
- 24 B. F. Yates, W. J. Bouma, and L. Radom, *J. Am. Chem. Soc.* **108**, 6545 (1986).
- 25 P. Calandra, C. S. S. O'Connor, and S. D. Price, *J. Chem. Phys.* **112**, 10821 (2000).
- 26 S. Harper, P. Calandra, and S. D. Price, *Phys. Chem. Chem. Phys.* **3**, 741 (2001).
- 27 N. A. Love and S. D. Price, *Phys. Chem. Chem. Phys.* **6**, 4558 (2004).
- 28 S. J. King and S. D. Price, *J. Chem. Phys.* **127**, 174307 (2007).
- 29 C. C. Tian and C. R. Vidal, *J. Phys. B: At. Mol., Opt. Phys.* **31**, 895 (1998).
- 30 S. J. King and S. D. Price, *Int. J. Mass Spectrom.* **277**, 84 (2008).
- 31 D. M. Curtis and J. H. D. Eland, *Int. J. Mass Spectrom. Ion Processes* **63**, 241 (1985).
- 32 J. H. D. Eland, *Mol. Phys.* **61**, 725 (1987).
- 33 J. H. D. Eland, *Chem. Phys. Lett.* **203**, 353 (1993).

- 34 A. E. Slattery, T. A. Field, M. Ahmad, R. I. Hall, J. Lambourne, F. Penent, P. Lablanquie, and J. H. D. Eland, *J. Chem. Phys.* **122**, 084317 (2005).
- 35 S. Hsieh and J. H. D. Eland, *J. Chem. Phys.* **103**, 1006 (1995).
- 36 J. H. D. Eland, S. S. W. Ho, and H. L. Worthington, *Chem. Phys.* **290**, 27 (2003).
- 37 S. J. King and S. D. Price, *Int. J. Mass Spectrom.* **272**, 154 (2008).

Chapter 6 Electron Ionization of Trifluoroiodomethane

6.1 Introduction

Trifluoroiodomethane (CF_3I) has been proposed as a possible plasma etching gas to replace other perfluorinated compounds (PFCs),^{1,2} as it provides copious amounts of CF_3^+ and CF_3 radicals via dissociative electron ionization and other dissociation processes.³ Studies have also been made into using CF_3I as an alternative to CF_3Br as a gaseous fire suppressant for in-flight aircraft and electronic equipment fires.^{4,5} The recent interest in using CF_3I for such replacements is due to it being a more “environmentally friendly” gas, having a much lower global warming potential than many current PFCs and fire suppression agents.¹⁻⁵ CF_3I also has a short atmospheric lifetime, meaning it does not significantly contribute to ozone depletion.⁶ For the accurate modelling and optimization of plasmas involving CF_3I , and also for atmospheric modelling, accurate electron ionization cross-sections for this molecule are essential.

6.1.1 Dissociative Ionization of Trifluoroiodomethane

There have been many studies of electron interactions with trifluoroiodomethane, as summarised in a review by Christophorou and Olthoff.³ However, considering electron ionisation, the technique employed in this study, the data available is limited.^{7,8} Total absolute ionization cross-sections have been measured by Beran *et. al.*,⁸ and calculated theoretically by Onthong *et. al.*⁹ Absolute partial ionization cross-sections (PICSs) have been measured by Jiao *et. al.*⁷, using a Fourier-transform mass spectrometer (FTMS) equipped with a cubic ion cyclotron resonance trapping cell, in the electron energy range 10 – 70 eV. The absolute PICSs reported by Jiao *et. al.*⁷ are presented only as figures, however the numerical values are reported in Table 9 of Ref. 3. Comparisons of the new data presented in this chapter to the data of Jiao *et. al.*⁷ are therefore taken from the numerical values reported in Ref. 3.

In the energy range employed in this study (30 – 200 eV) multiple ionization of CF_3I can contribute significantly to the ion yield. Again, the available data on the multiple ionization of CF_3I is limited. An investigation by Pilche-Clayton and Eland¹⁰ into the double photoionization of CF_3I in the energy range 23 – 47 eV, used a time-of-flight photoelectron-photoelectron coincidence (TOF-PEPECO) technique. The double

photoionization and dication fragmentation of CF_3I has also been studied by Eland *et al.*¹¹, employing a range of electron-ion coincidence techniques together with computational calculations. In this study by Eland *et al.*¹¹ the energies of the ground and several excited electronic states of CF_3I^{2+} are reported, together with the dication dissociation pathways.

In this study the electron ionization of CF_3I in the energy range 30 – 200 eV is investigated using TOF mass spectrometry and ion-ion coincidence techniques, as described in Chapters 2 and 3. Relative PICSs $\sigma_i[\text{X}^{m+}]$ for all fragment ions detected, expressed relative to the formation of the parent ion CF_3I^+ , are reported as a function of ionizing electron energy. Precursor-specific relative PICSs $\sigma_n[\text{X}^{m+}]$ are also reported, quantifying the contribution to the ion yield of an ion from single, double, triple, and quadruple ionisation, as explained in Section 3.3. These measurements, reported below, represent the first complete description of the consequences of the single and multiple ionization of CF_3I at electron energies below 200 eV. In addition, information on the energetics of the dissociation of the CF_3I dication and trication are provided by our 2D ion coincidence technique.

6.2 Experimental Procedure

All the experiments in this study were carried out using the TOFMS described in Chapter 2. The trifluoroiodomethane gas was a commercial sample of 99% purity, and was used without further purification. As described in Chapters 2 and 3, the operating conditions employed involve using low target gas pressures together with low electron fluxes. These conditions ensure that there is considerably less than one ionization event per ionizing pulse of electrons. This methodology markedly decreases the likelihood of any ‘false coincidences’ in our spectra, as described in previous Chapters.

In our mass spectra, following electron ionization of CF_3I , we observe the ions FI^+ , FI^{2+} and F_2^+ . To ensure these ions were not the result of bimolecular reactions between a CF_3I ion and a neutral CF_3I , a series of experiments were carried out in which the pressure of CF_3I in the source chamber was varied from 9×10^{-8} Torr to 1×10^{-6} Torr. If the FI^+ , FI^{2+} and F_2^+ ions were the result of bimolecular reactions, their intensities should increase as the square of the pressure. In these preliminary experiments, no change in the cross-sections derived for the FI^+ , FI^{2+} and F_2^+ ions was observed as the pressure of CF_3I was changed. This behaviour indicates these ions are

fragment ions formed from dissociative ionization of CF_3I , and are not formed by bimolecular reactions between CF_3I ions.

6.3 Data Analysis

Mass and coincidence spectra of trifluoroiodomethane were recorded at ionising electron energies in the range 30 – 200 eV using the experimental apparatus described in Chapter 2. For each ionising electron energy used, four separate determinations of the experimental cross-sections were made.

6.3.1 Singles Mass Spectra

A representative mass spectrum of CF_3I following electron ionisation at 200 eV is shown in Figure 6.1. The mass spectrum shows the various ion peaks observed in the singles mass spectrum, together with the parent monocation, CF_3I^+ , and ion fragments arising from the dissociation of CF_3I^{m+} : C^{2+} , F^{2+} , C^+ , F^+ , CF^{2+} , CF_2^{2+} , CF^+ , F_2^+ , I^{3+} , CF_2^+ , I^{2+} , CF_3^+ , FI^{2+} , CFI^{2+} , CF_2I^{2+} , I^+ , CI^+ , FI^+ , CFI^+ and CF_2I^+ . The intensities of these individual ion peaks $I[X^{m+}]$ appearing in the singles spectra are extracted by summing the counts in each peak, after applying a small correction to account for the non-zero baseline which arises due to stray ions, as described in Section 3.2.1. Due to the low target gas pressures used, the singles spectrum also shows traces of ions resulting from the ionization of residual air and water in our vacuum chamber. Ionization of O_2 and H_2O yields O^+ ions, resulting in a peak at $m/z = 16$ which overlaps with the small CF^{2+} peak at $m/z = 15.5$. Ionization of O_2 also yields O_2^+ ions, resulting in a peak at $m/z = 32$ which overlaps with the CF^+ peak at $m/z = 31$, and ionization of H_2O also yields H_2O^+ resulting in a peak at $m/z = 18$ which overlaps with the F^+ peak at $m/z = 19$. To quantify and remove these background contributions, the relative intensities of O^+ and H_2O^+ with respect to OH^+ , and O^+ and O_2^+ with respect to N_2^+ were measured in separate experiments following electron ionization of water and air, as a function of ionizing electron energy. The subtraction of the ion signals resulting from ionization of the residual gases can then be made by normalisation to the small OH^+ and N_2^+ peaks in each CF_3I mass spectrum, as described in Section 3.3.1.

In our mass spectra we also note a peak at $m/z = 44$, which we conclude to be a small CO_2 impurity in our CF_3I sample, although it is hard to see how CO_2 could be formed in the manufacturing process of CF_3I . We conclude this due to peaks observed in the pairs spectrum that are representative of electron ionization of CO_2 , as discussed in

Section 6.3.2. The possibility of this CO_2 resulting from background gas in our chamber has also been considered, however as the peak is of comparable size to the N_2^+ ion peak it cannot be the result of residual air. Ionization of CO_2 yields C^+ and O^+ ions, contributing the peaks at $m/z = 12$ and $m/z = 16$ respectively. To quantify and remove these background contributions, the relative intensities of C^+ and O^+ with respect to CO_2^+ were measured in separate experiments following electron ionization of CO_2 .¹² As described above and in Section 3.2.1, the ion signals resulting from the ionization of the CO_2 impurity can then be made by normalization to the small CO_2^+ peak in each CF_3I mass spectrum. In each mass spectrum, the CO_2^+ peak was usually much less than 0.1 % of the total ion count.

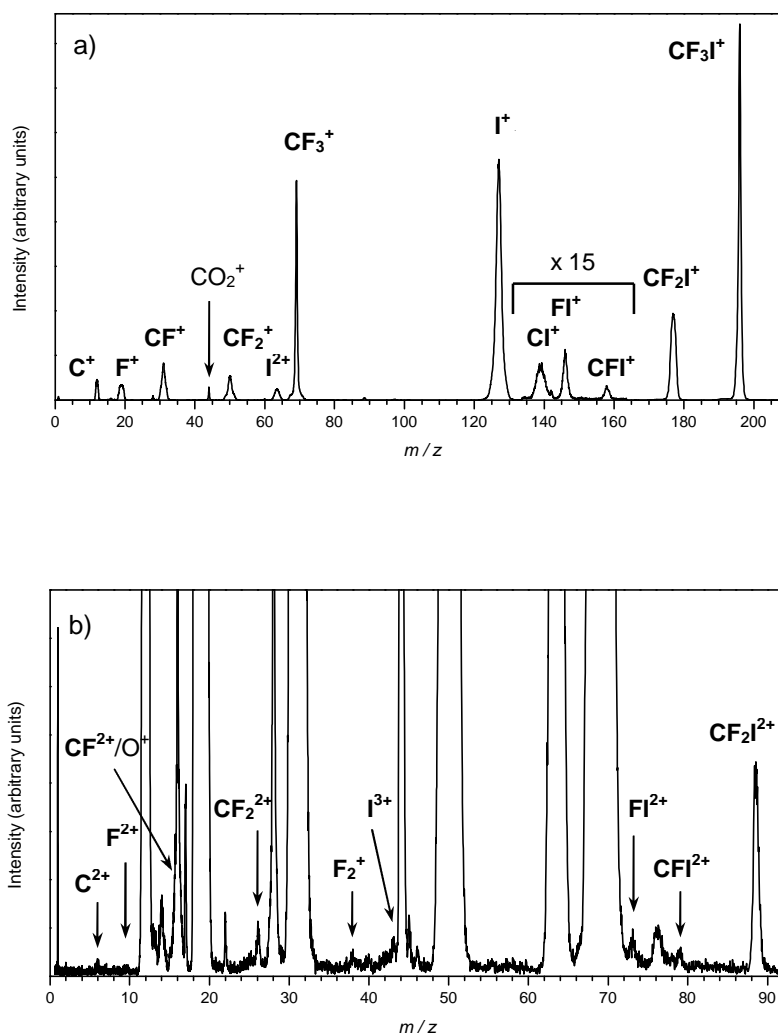


Figure 6.1: A typical singles mass spectrum of trifluoriodomethane following electron ionization at 200eV showing: a) the full mass spectrum, b) close up (x 100) of mass range $m/z = 0 - 92$.

Contributions to the raw fragment ion intensities from these background gases mentioned above were typically 5% for the CF^+ ion peak, and much less than 0.1 % for the C^+ ion peak. However, due to the very small number of counts in the CF^{2+} ion peak, we were unable to resolve the small CF^{2+} peak at $m/z = 15.5$ from the O^+ peak at $m/z = 16$. Therefore, we do not report $\sigma_2[\text{CF}^{2+}]$ values. However, as described below in Section 6.5.2, formation of CF^{2+} from dissociative double ionization of CF_3I appears to be negligible, and results solely from dissociative triple ionization.

6.3.2 Pairs Spectra

A representative pairs spectrum of CF_3I recorded at an ionizing electron energy of 200 eV, in which the major ion pair channels can be seen, is shown in Figure 6.2. At this energy a total of 41 different ion pairs are observed; 18 monocation-monocation pair peaks, 17 dication-monocation pair peaks, 4 dication-dication pair peaks and 2 trication-monocation pair peaks. These ion pairs are listed in table 6.1. Dication-monocation ion pairs are only observed at electron energies above 50 eV, dication-dication ion pairs are only observed at electron energies above 75 eV, and trication-monocation ion pairs are only observed at electron energies above 150 eV.

The contribution of a particular ion to the pairs spectra were extracted using the procedure described in Section 3.2.2. As can be seen in Figure 6.2, a number of false coincidences, events in which two ions are detected in coincidence that did not originate from the same ionisation event, are present in the pairs spectra (e.g. $\text{CF}_2\text{I}^+ + \text{CF}^+$). These false coincidences are subtracted manually for each peak using the autocorrelation of the singles spectrum, as described in Section 3.2.2.1.

In our pairs spectra, along with the ion pairs originating from the dissociation of multiply charged CF_3I , we also observed ion pairs at mass to charge ratios of $28 + 16$ and $16 + 12$. These two pair channels are a signature of the dissociation of multiply charged CO_2 . As mentioned above, we also observed a small peak at $m/z = 44$ in our singles spectra, and concluded that our sample contained a small carbon dioxide impurity. As the ion pairs resulting from the dissociation of multiply charged CO_2 do not coincide with any ion pairs resulting from the dissociation of multiply charged CF_3I , no correction was required for this impurity in the pairs spectra.

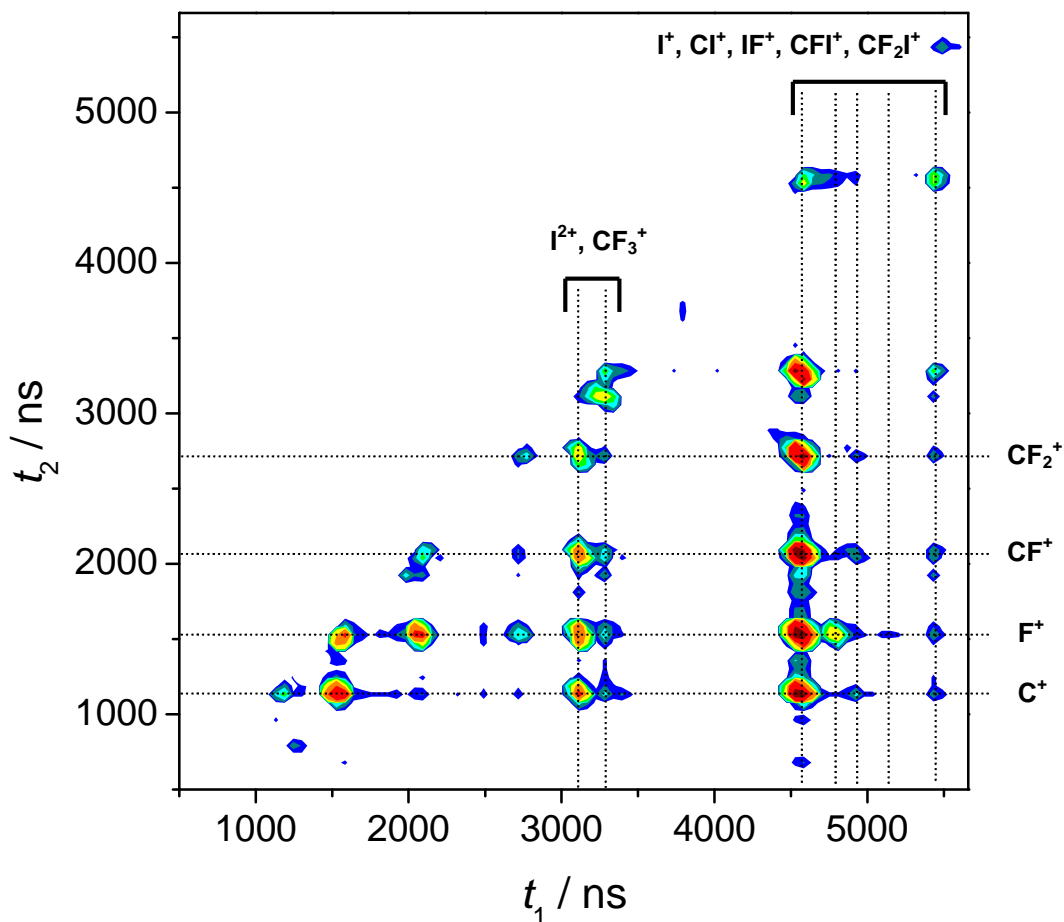


Figure 6.2: Representative pairs spectrum of CF_3I showing the major ion pair channels, recorded at an ionizing electron energy of 200 eV.

In our experimental arrangement, due to the ‘deadtime’ of the discriminatory circuitry, an ion pair will not be detected if the second ion arrives at the detector within 32 ns of the first ion. This results in a ‘dead region’ in the pairs spectrum affecting the $\text{F}^+ + \text{F}^+$ ion pair peak. As described in Section 3.2.2, an estimation of the losses within this ‘dead region’ can be made by first plotting the time-of-flight difference (ΔTOF) between pairs of ions making up the visible part of the affected pairs peak. Extrapolation of this ΔTOF plot can then be made, using simple geometry, to quantify the counts lost in the dead region.¹³ Section 3.2.2 also describes how inspection of these ΔTOF plots can also identify any losses due to energetic ions. The missing centre of the ΔTOF plots for the $\text{I}^{2+} + \text{C}^+$, $\text{I}^{2+} + \text{F}^+$, $\text{I}^{2+} + \text{CF}^+$ and $\text{F}^+ + \text{C}^+$ ion pairs indicated such losses due to energetic ions. Correction of these losses indicated that approximately 15% of the $\text{I}^{2+} + \text{C}^+$, $\text{I}^{2+} + \text{F}^+$, $\text{I}^{2+} + \text{CF}^+$ and $\text{F}^+ + \text{C}^+$ ion pairs were lost due to energetic ions.

Table 6.1: Ion pairs observed in the pairs spectrum recorded following electron ionization of CF₃I at 200 eV ionizing electron energy.

Monocation-monocation pairs		Dication-monocation pairs		Dication-dication pairs		Trication-monocation pairs	
CF ₂ I ⁺	+ F ⁺	FI ²⁺	+ C ⁺	I ²⁺	+ C ²⁺	I ³⁺	+ C ⁺
CFI ⁺	+ F ⁺		+ F ⁺		+ F ²⁺		+ F ⁺
FI ⁺	+ C ⁺		+ CF ⁺		+ CF ²⁺		
	+ F ⁺		+ CF ₂ ⁺		+ CF ₂ ²⁺		
	+ CF ⁺	I ²⁺	+ C ⁺				
	+ CF ₂ ⁺		+ F ⁺				
CI ⁺	+ F ⁺		+ CF ⁺				
I ⁺	+ C ⁺		+ CF ₂ ⁺				
	+ F ⁺		+ CF ₃ ⁺				
	+ CF ⁺	CF ₂ ²⁺	+ I ⁺				
	+ F ₂ ⁺	CF ²⁺	+ I ⁺				
	+ CF ₂ ⁺	F ²⁺	+ C ⁺				
	+ CF ₃ ⁺		+ F ⁺				
CF ₂ ⁺	+ F ⁺		+ CF ⁺				
F ₂ ⁺	+ C ⁺		+ I ⁺				
CF ⁺	+ F ⁺	C ²⁺	+ F ⁺				
F ⁺	C ⁺		+ I ⁺				
	F ⁺						

6.3.3 Triples Spectra

The triples data is quantified in a similar way to the pairs data, as discussed in Section 3.2.3. Briefly, the TOF range for a particular ion is first selected, for example F⁺, and all the ion triples containing at least one ion whose arrival time lies within this range are extracted. The remaining two TOFs are then plotted as a pairs spectrum, and the intensity of each ion triple peak found by summing the number of counts in the peak. The contribution of a fragment ion to the triples spectrum, $T_n[X^{m+}]$, is then obtained by summing the counts of all the appropriate peaks involving the ion X^{m+}. At an ionizing electron energy of 200 eV, a total of 15 ion triple channels are observed; 8 monocation-monocation-monocation channels and 7 dication-monocation-monocation channels. These ion triples are listed in Table 6.2. Ion triple channels involving three monocations are only observed at ionizing electron energies above 55 eV, and ion triple channels involving one dication and two monocations are only observed at ionizing electron energies above 85 eV. Similarly to the pairs data, corrections are also made to account for ion losses due to the “deadtime” of the detector and energetic ions. Specifically, “deadtime” losses are observed and corrected for in the CI⁺ + F⁺ + F⁺, I⁺ + F⁺ + F⁺, CF⁺ + F⁺ + F⁺, F⁺ + F⁺ + F⁺, C⁺ + F⁺ + F⁺ and I²⁺ + F⁺ + F⁺ ion triples, and energetic ion losses are observed and corrected for in the C⁺ + I⁺ + F⁺ ion triple.

Due to the significant number of ion triples observed at higher ionizing electron energies, extended runs were carried out at energies of 150, 175 and 200 eV to look for ion quadruples. In these extended runs, twice the usual number of ions were collected, however the number of ion quadruples collected was still negligible. Due to this, and the fact that no ion triples or pairs are observed originating from quintuple ionization of CF_3I , our subsequent neglect of ion quadruples, and quintuple and higher levels of ionization is justified.

Table 6.2: Ion triples observed in the pairs spectrum recorded following electron ionization of CF_3I at 200 eV ionizing electron energy.

Monocation-monocation-monocation triples			Dication-monocation-monocation triples		
CI^+	$+ \text{F}^+$	$+ \text{F}^+$	I^{2+}	$+ \text{C}^+$	$+ \text{F}^+$
I^+	$+ \text{C}^+$	$+ \text{F}^+$	I^{2+}	$+ \text{F}^+$	$+ \text{F}^+$
I^+	$+ \text{F}^+$	$+ \text{F}^+$	I^{2+}	$+ \text{F}^+$	$+ \text{CF}^+$
I^+	$+ \text{F}^+$	$+ \text{CF}^+$	I^{2+}	$+ \text{F}^+$	$+ \text{CF}_2^+$
I^+	$+ \text{F}^+$	$+ \text{CF}_2^+$	F^{2+}	$+ \text{C}^+$	$+ \text{I}^+$
CF^+	$+ \text{F}^+$	$+ \text{F}^+$	F^{2+}	$+ \text{F}^+$	$+ \text{I}^+$
F^+	$+ \text{C}^+$	$+ \text{F}^+$	C^{2+}	$+ \text{F}^+$	$+ \text{I}^+$
F^+	$+ \text{F}^+$	$+ \text{F}^+$			

6.4 Relative Partial Ionization Cross-Sections

6.4.1 Results

Mass and coincidence spectra of CF_3I were recorded at ionizing electron energies in the range 30 – 200 eV. These spectra were processed, as described in Section 3.3.2, to yield the relative PICSs $\sigma_r[\text{X}^{m+}]$ for the formation of all fragment ions observed: CF_2I^+ , CFI^+ , FI^+ , CI^+ , I^+ , CF_2I^{2+} , CFI^{2+} , FI^{2+} , CF_3^+ , I^{2+} , CF_2^+ , I^{3+} , F_2^+ , CF^+ , CF_2^{2+} , F^+ , CF^{2+} , C^+ , F^{2+} and C^{2+} . These $\sigma_r[\text{X}^{m+}]$ values are expressed relative to the CF_3I^+ ion yield, and are displayed as a function of electron energy in Figure 6.3 and Table B.7. Precursor-specific relative PICSs $\sigma_n[\text{X}^{m+}]$ were also derived for these fragment ions, using the procedure described in Section 3.3.4. These $\sigma_n[\text{X}^{m+}]$ ($n = 1 - 3$) values are expressed relative to the CF_3I^+ ion yield, and are displayed as a function of electron energy in Figure 6.4 and Tables B.8 and B.9. As discussed in Section 1.4.3, producing absolute PICSs requires the accurate measurement of four experimental variables: the initial electron flux, the number density of the target gas, the collisional pathlength and number of ions formed by electron ionization events. Determination of

the first three of these variables is experimentally non-trivial, and thus we report relative PICSSs. These relative values can be readily placed on an absolute scale using the measurements of the total ionization cross-sections discussed above. For example, to produce an absolute value for $\sigma[C^+]$ simply requires an absolute value for the cross-section for forming the parent monocation, CF_3I^+ , $\sigma[CF_3I^+]$:

$$\sigma[C^+] = \sigma_r[C^+] \times \sigma[CF_3I^+] \quad (6.1)$$

As discussed in Section 1.4.3, one advantage of producing relative PICSSs relative to the parent monocation is that the parent monocation is formed with a thermal distribution and thus the least likely to suffer from ion discrimination effects. Therefore, even previous cross-section determinations in which the efficient collection of energetic ions is not accounted for should produce accurate $\sigma[\text{parent}^+]$ values.

In our pairs spectra we observe 41 ion pairs; 18 monocation-monocation pair peaks, 17 dication-monocation pair peaks, 4 dication-dication pair peaks and 2 trication-monocation pair peaks (Table 6.1). At all ionizing electron energies investigated the ion pair yield is dominated by monocation-monocation pairs containing I^+ . Below 65 eV ionizing electron energy, $I^+ + CF_3^+$ is the most intense channel, however at 65 eV and above the yield of this channel decreases, and the $I^+ + CF^+$ channel becomes the most intense. Increasing the electron energy to 200 eV sees the yield of the $I^+ + CF_3^+$ channel decrease further, falling below the $I^+ + C^+$ and $I^+ + CF_2^+$ channels at 125 and 150 eV respectively. These results indicate, unsurprisingly, a greater degree of fragmentation of the CF_3I^{2+} ion as the ionising electron energy is increased. A greater degree of fragmentation of the trifluoroiodomethane trication (CF_3I^{3+}) is also noted as the ionizing electron energy is increased. Below 85 eV ionizing electron energy, the $I^{2+} + CF_3^+$ channel is the most intense, however at 85 eV and above the yield of this channel decreases, falling first below the $I^{2+} + CF^+$ channel, and then the $I^{2+} + C^+$ and $I^{2+} + F^+$ channels at 125 and 150 eV respectively.

Ion triples channels begin contributing to the ion yield at an ionizing electron energy of 60 eV. At 200 eV a total of 15 ion triple channels are observed; 8 monocation-monocation-monocation channels and 7 dication-monocation-monocation channels (Table 6.2). For the triple channels in which three monocations are detected, the ion yield is dominated by I^+ containing channels. Similarly, for the triple channels

in which one dication and two monocations are detected, the ion yield is dominated by I^{2+} containing channels.

The overall contributions from single, double, triple and quadruple ionization to the total ion yield is shown in Figure 6.5 and Table B.10. Figure 6.5 shows that as the ionizing electron energy is increased from 30 to 200 eV the relative contribution to the ion yield from single ionization broadly drops (50 eV:84 %, 100 eV:64 %, 200 eV:56 %). This decrease coincides with increases in the contributions from double (50 eV:12 %, 100 eV:34 %, 200 eV:31 %), triple (50 eV:0 %, 100 eV:2 %, 200 eV:12 %) and quadruple ionization. However, the contribution from quadruple ionization is negligible below 125 eV and very small (0.1 – 0.7 %) even above 125 eV. Figure 6.4 also shows the increase in contribution to the ion yield from double ionization peaks at 35% at 125 eV.

As can be seen from Figures 6.3 and 6.4, as the ionizing electron energy is increases, the general trend of the cross sections is to increase from threshold to a maximum, after which they gently drop off. As discussed in Section 1.4.3., such a trend is observed for all electron-molecule interactions, as the efficiency at which the electron interacts with a molecule decreases with increasing electron energy. This is due to the fact that higher energy electrons are moving faster. As the energy is increased, there, in principle, reaches a point at which the electron is moving so fast it does not interact with the species at all and the cross section falls to zero.

As discussed in Section 3.3, a value for the ion detection efficiency f_i is required to enable us to derive $\sigma_n[X^{m+}]$ values. Measurement of f_i for our apparatus, using the methodology described in Section 3.3.3, resulted in a value of 0.26 ± 0.01 , in good agreement with previous determinations.¹⁴⁻¹⁹

6.5 Discussion

6.5.1 Relative PICSSs (σ_r)

The values of σ_r we have derived are displayed in Figure 6.3 and given numerically in Table B.7. Given that these results present the first measurement of the precursor-specific relative PICSSs, it is only by constructing the relative PICSSs from our data that we can compare our results with previous work. Where appropriate, our relative PICSSs are compared with values derived from the data of Jiao *et. al.*⁷ (Figure 6.3a – 6.3c). As previously mentioned, the total cross-sections reported by Jiao *et. al.* in

Ref. 7 are only presented as figures. The values used for the comparisons in this study were instead taken from Ref. 3, in which the data of Jiao *et. al.*⁷ are presented numerically in Table 9. As can be seen from Figure 6.3, I^+ is the most abundant ion formed at ionizing electron energies of 40 eV and above, and is second only to the parent ion (CF_3I^+) below 40 eV.

Comparison of our $\sigma_r[X^+]$ values to those derived from the data of Jiao *et. al.*⁷ show significant differences between the two sets of data, with our values being, in general, significantly higher. For the lighter ion fragments, CF^+ and CF_2^+ , our values are around three times larger than the values derived from the data of Jiao *et. al.*⁷. For slightly heavier fragment ions, CF_3^+ and I^+ , our values are around 2 and 1.75 times higher respectively. Conversely, for the heaviest fragment ion reported by Jiao *et. al.*⁷ (CF_2I^+), our values are between 10 and 20 % lower, however here the two values lie within their mutual error limits.

A possible explanation for these differences in the values of $\sigma_r[X^+]$, is the loss of translationally energetic ions from the ion cyclotron resonance trapping cell used by Jiao *et. al.*⁷ Such ion losses in earlier measurements of electron ionization cross-sections have been observed before.^{12,14-16,20} Indeed, better agreement is observed comparing our $\sigma_1[X^+]$ values for CF^+ , CF_2^+ , CF_3^+ and I^+ to the $\sigma_r[X^+]$ values derived from the work of Jiao *et. al.*⁷, indicating the majority of ion losses in this earlier work are from dissociative double, triple, or quadruple ionization. The loss of translationally energetic ions in the earlier work would also explain why the differences between the $\sigma_r[X^+]$ values obtained in this study and the early work, increase with decreasing mass, as upon Coloumb explosion of a multiply charged species, the lighter fragment departs with more translational energy, and is thus less likely to be detected.

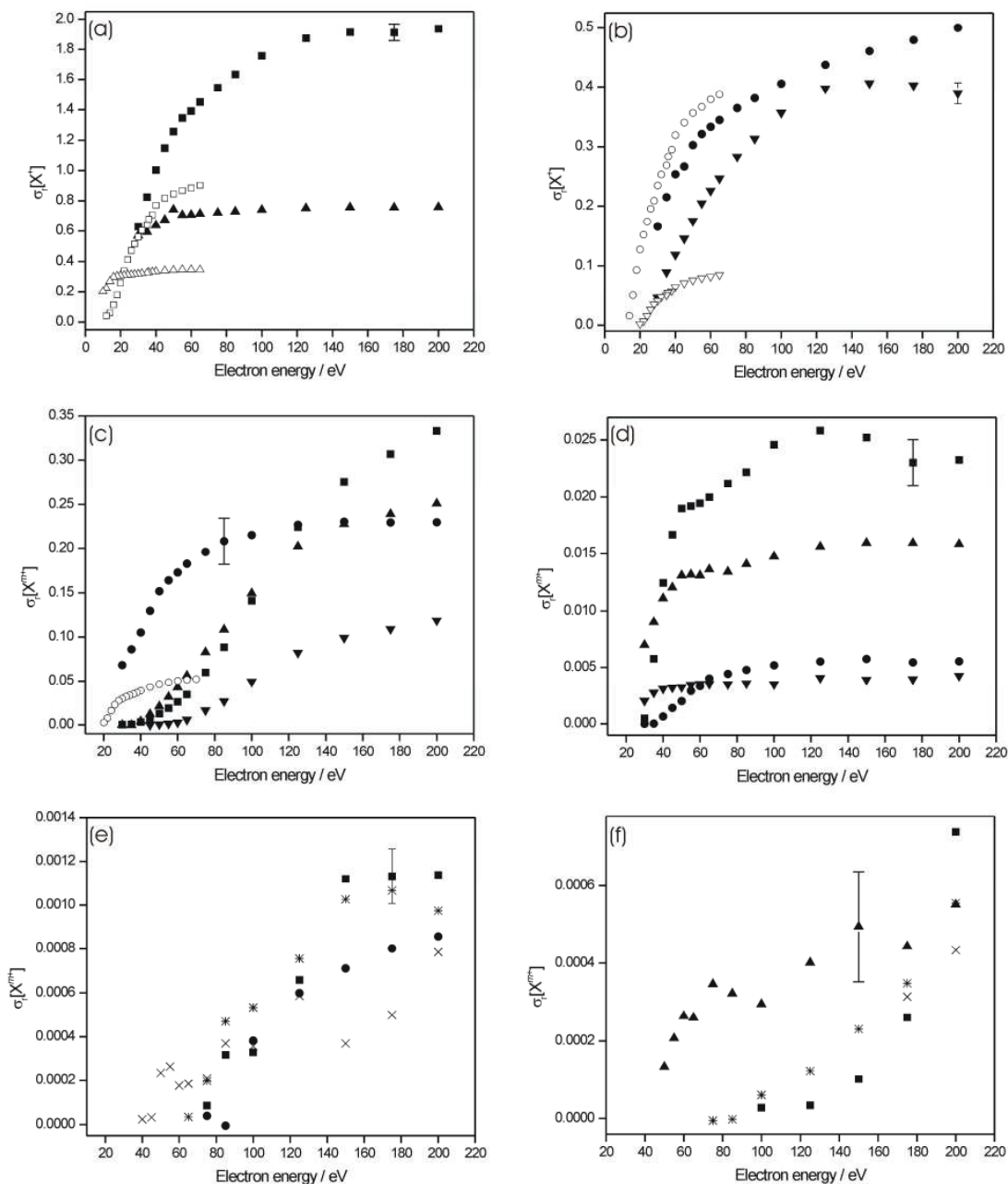


Figure 6.3: Relative PICSSs $\sigma_i[X^{m+}]$ for forming (a) I^+ (■) and CF_3^+ (▲), (b) CF_2I^+ (●) and CF^+ (▼), (c) F^+ (■), C^+ (▲), CF_2^+ (●) and I^{2+} (▼), (d) CF_2I^+ (●), CF^+ (▼), F^+ (■), C^+ (▲), CF_2^+ (●) and I^{2+} (▼), (e) CF_2^{2+} (■), FI^{2+} (✱), CF^{2+} (●) and F_2^+ (×) and (f) F_2^+ (×), F^{2+} (■), C^{2+} (✱), CFI^{2+} (▲) and I^{3+} (×) following electron ionization of CF_3I relative to the cross-section for forming the parent ion CF_3I^+ . Where available the corresponding relative PICSSs from the data of Jiao *et. al.*⁷ (graph (a), (b) and (c)) are also shown as open symbols. The representative error bars show one or two standard deviations of four separate determinations (see Table B.7).

6.5.2 Precursor-specific Relative PICs (σ_n)

The values of σ_1 , σ_2 , σ_3 , and σ_4 for the formation of fragment ions formed following electron ionization of CF_3I are displayed in Figure 6.4 and given numerically in Tables B.8 and B.9. Figure 6.5 indicates the contribution from single, double, triple and quadruple ionization to the total ion yield. As can be seen from Figure 6.5, and as discussed above, the greatest contribution to the total ion yield at all ionizing energies investigated is from single ionization.

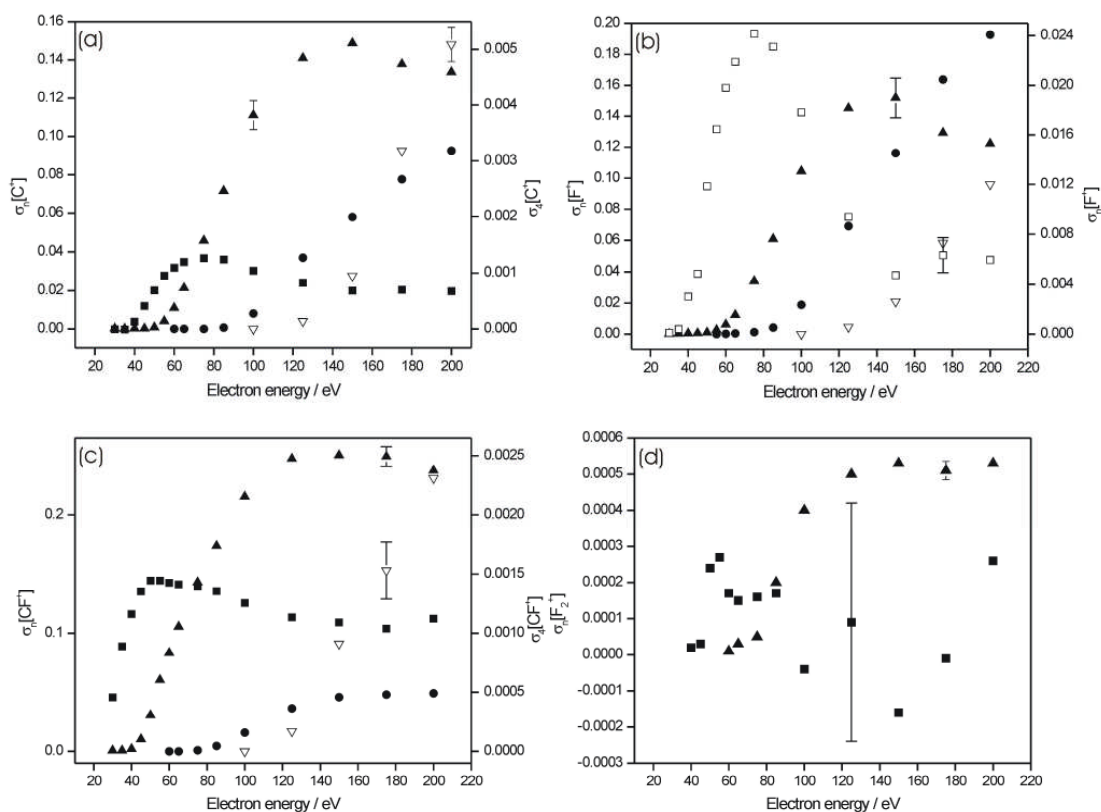
Looking at the contribution to individual ion fragment yields from different levels of ionization, some general observations can be made. Firstly, for singly charged fragment ions, at low ionizing electron energies, dissociative single ionization is unsurprisingly the greatest contribution to the individual fragment ion yields. For all the iodine containing monocation fragments (I^+ , CI^+ , FI^+ , CFI^+ and CF_2I^+), and those which have formed with minimal fragmentation of the parent ion (CF_3^+), single ionization remains the greatest contribution to their fragment ion yields as the ionizing electron energy is raised to 200 eV, followed by contributions from dissociative double, triple, and quadruple ionization respectively, if these latter processes contribute at all. However for the yields of the smaller monocation fragments (C^+ , F^+ , CF^+ and CF_2^+), many of which must have been formed following significant fragmentation of the parent ion, as the ionizing electron energy is raised to 100 eV the greatest contribution to the ion yield changes from dissociative single to dissociative double ionization. For the ion fragments CF^+ and CF_2^+ , as the ionizing electron energy is raised further to 200 eV, dissociative double ionization remains the greatest contribution to their ion yields, contributing 59 % and 52 % respectively; dissociative single ionization remains the second largest contribution to their ion yields, contributing 36 % and 44 % respectively. Dissociative triple ionization also contributes a significant amount to the CF^+ and CF_2^+ ion yields at 200 eV, contributing 12 % and 4% respectively, and dissociative quadruple ionization contributes 2 % to the CF^+ ion yield and <1 % to the CF_2^+ ion yield at 200 eV. For the lightest monocation fragment, C^+ , dissociative double ionization also remains the greatest contribution to its ion yield as the ionizing electron energy is raised from 100 to 200 eV, contributing 53 % at 200 eV. However, at 200 eV the second greatest contribution to the ion yield is from dissociative triple ionization, which reaches 37 %, followed by dissociative single (8 %) and dissociative quadruple (2 %) ionization. Interestingly, dissociative single ionization contributes almost negligibly to the F^+ ion

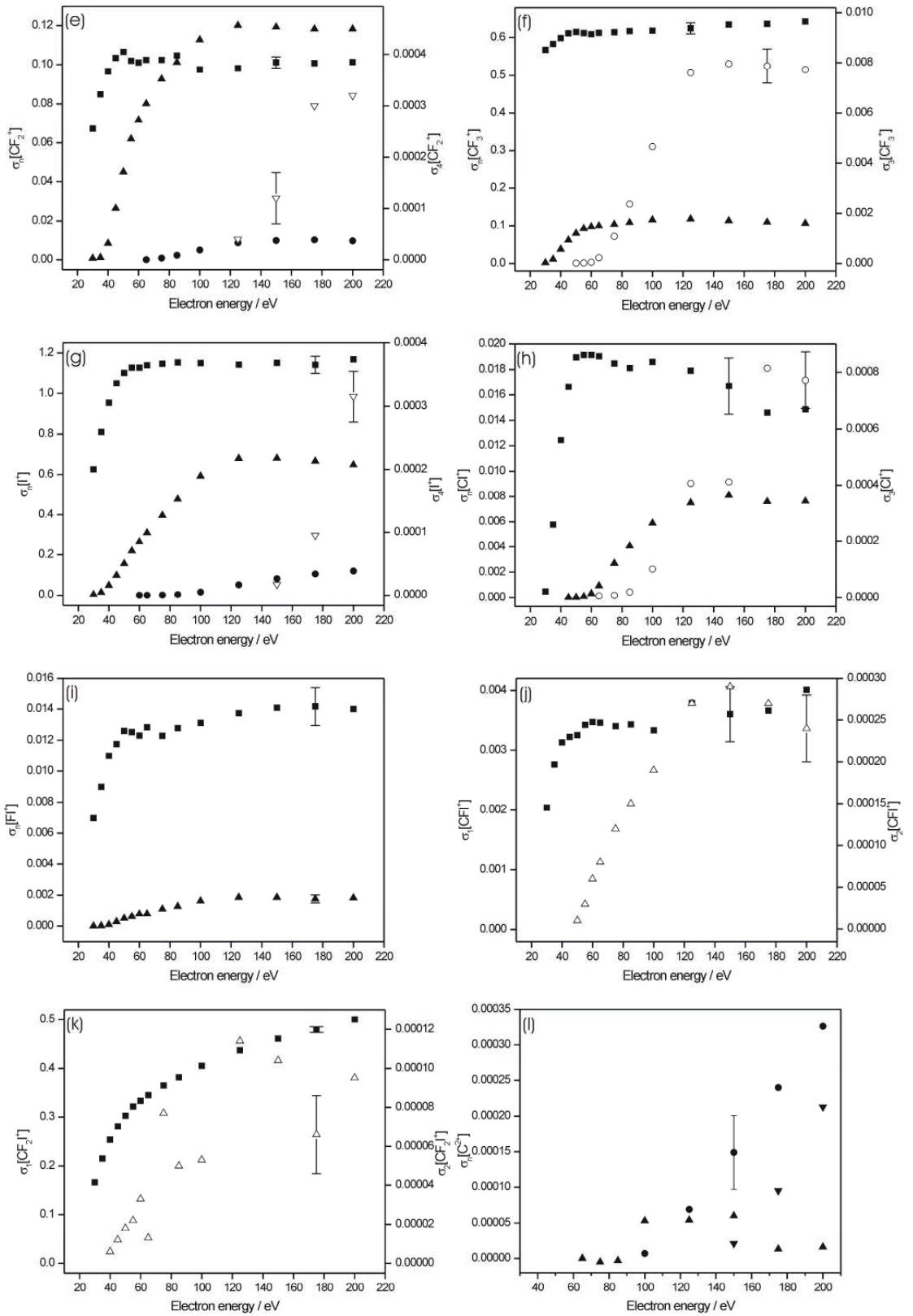
yield as the ionizing electron energy approaches 200 eV, with dissociative triple ionization making the greatest contribution to the F^+ ion yield (58 %) at 200 eV, followed by contributions from dissociative double and quadruple ionization respectively (37 % and 8 % respectively at 200 eV). A similar trend is observed following electron ionization of C_2F_6 , in which dissociative single ionization contributes almost negligibly to the F^+ ion yield at ionizing energies approaching 200 eV.²¹

For the last monocation fragment observed, F_2^+ , the $\sigma_1[F_2^+]$ values obtained remain close to zero, and have large errors associated with them. These large errors arise due to the difficulties in estimating the size of the small F_2^+ peak in the singles spectra. However, the $\sigma_2[F_2^+]$ values, which start at 60 eV, rapidly increase as the ionizing electron energy is raised to 125 eV, after which the values plateau. From these results, it is clear that the ion yield of F_2^+ is almost entirely from dissociative double ionization at all ionizing electron energies. Thus the majority of F_2^+ ions are formed with significant amounts of kinetic energy, resulting in a broadening of the F_2^+ peak in the singles spectra. This peak results principally from events where an F_2^+ ion formed from dissociative double ionization is detected but its ionic partner is missed, due to our experimental detection efficiency being less than unity. Since the formation of F_2^+ is not a major channel following the electron ionization of CF_3I (Figure 6.3e and Table B.7), the broad wings of the F_2^+ peak are hard to discern in the singles spectrum and become lost in the baseline, so the limits of the F_2^+ peak have to be estimated. These problems result in the significant uncertainty reported in our $\sigma_1[F_2^+]$ values (Figure 5.4f and Table B.8).

For doubly charged fragment ions, only the largest two, CFI^{2+} and CF_2I^{2+} , are observed at the lowest ionizing energy investigated (30 eV). The contribution to their ion yields is solely from dissociative double ionization at all ionizing electron energies (Figure 6.3d and f and Table B.9). For the remaining two iodine containing dication fragments, I^{2+} and FI^{2+} , which are observed at ionizing electron energies above 40 eV and 65 eV respectively, the greatest contribution to their ion yields remains dissociative double ionization up to 125 eV and 150 eV respectively, above which point the greatest contribution is from dissociative triple ionization. At 200 eV, the contribution from triple ionization to the dication fragment yields reaches 73 % for I^{2+} and 63 % for FI^{2+} , followed by contributions from dissociative double ionization (18 % and 37 % respectively), and for I^{2+} from dissociative triple ionization (9 %). For the four smaller dication fragments (C^{2+} , F^{2+} , CF^{2+} and CF_2^{2+}), at ionizing energies above their

thresholds, contributions to their ion yields are almost completely from dissociative triple or higher ionization. As in the case of F_2^+ , this means that the majority of these dication fragments are formed with significant amounts of kinetic energy, resulting in a broadening of their peaks in the singles spectra. As described above for F_2^+ , since the formation of these dication fragments are not major channels following electron ionization, this broadening makes the quantification of the C^{2+} , F^{2+} , CF^{2+} and CF_2^{2+} peaks in the singles mass spectra difficult. For the C^{2+} and F^{2+} dication fragments, this difficulty in quantifying the amount observed in the singles spectra has resulted in $\sigma_2[X^{2+}]$ with large errors associated with them. For the dication fragment CF_2^{2+} , the values of $\sigma_2[CF_2^{2+}]$ that we obtain can be seen to be zero within error, indicating that contribution to the CF_2^{2+} ion yield is negligible from dissociative double ionization, and results solely from dissociative triple ionization. As described above in Section 6.3.1, we were unable to resolve the small CF^{2+} peak at $m/z = 15.5$ from the O^+ impurity peak at $m/z = 16$, meaning we are unable to report $\sigma_2[CF^{2+}]$ values. However, the similar profiles of the $\sigma_3[X^{2+}]$ values for both CF^{2+} and CF_2^{2+} , and the fact that CF^{2+} and CF_2^{2+} are observed in the pairs spectra in coincidence with the same ions (I^+ and I^{2+}), lead us to believe that the amount of CF^{2+} formed from dissociative double ionization is negligible, as is the case for the dication fragment CF_2^{2+} , and that all CF^{2+} observed is formed by dissociative triple ionization.





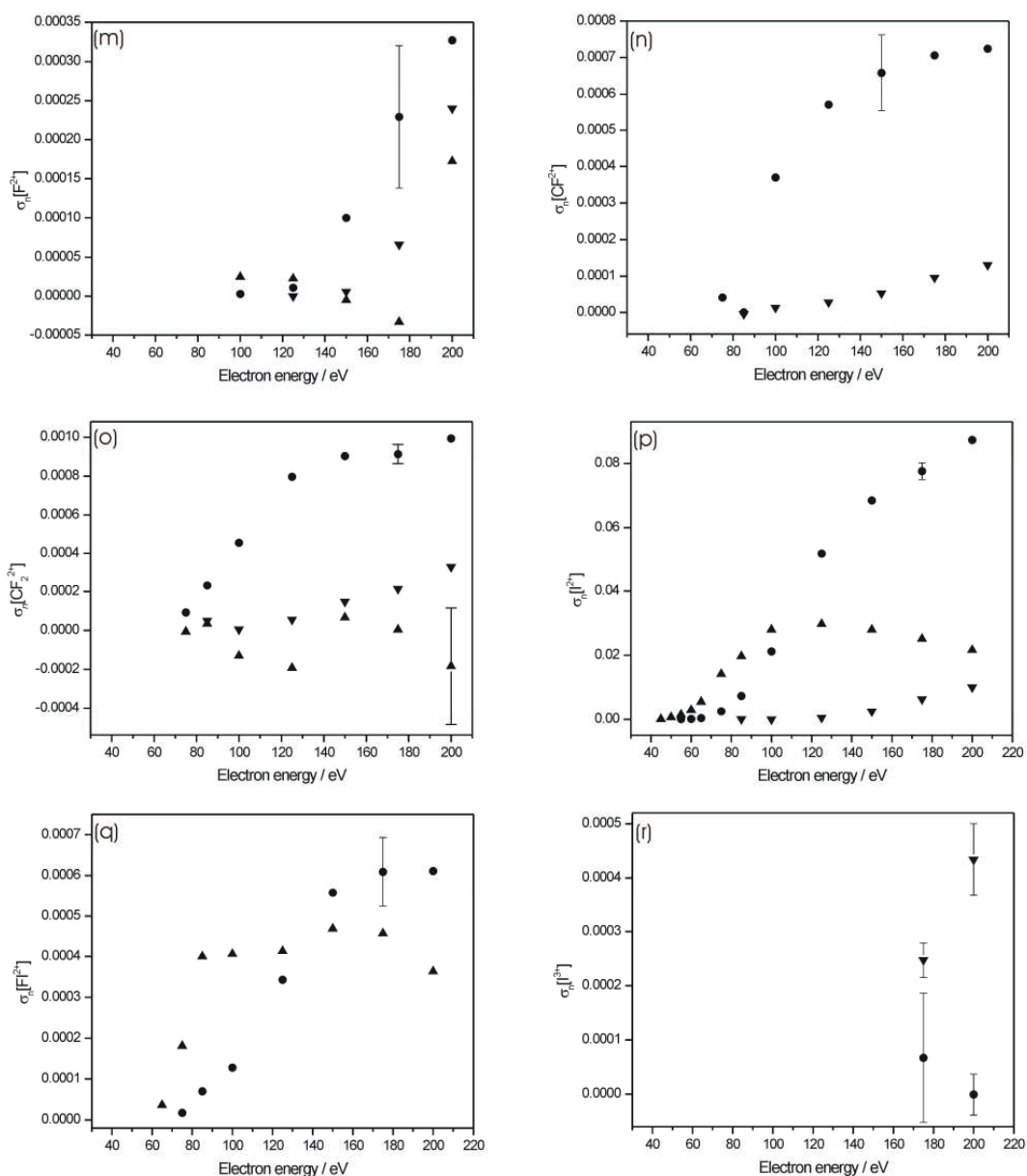


Figure 6.4: Precursor-specific relative PICs for forming (a) C^+ , (b) F^+ , (c) CF^+ , (d) F_2^+ , (e) CF_2^+ , (f) CF_3^+ , (g) I^+ , (h) CI^+ , (i) FI^+ , (j) CFI^+ , (k) CF_2I^+ , (l) C^{2+} , (m) F^{2+} , (n) CF^{2+} , (o) CF_2^{2+} , (p) I^{2+} , (q) FI^{2+} and (r) I^{3+} fragments via single (■), double (▲), triple (●) and quadruple (▼) ionization, following electron ionization of CF_3I , relative to the cross-section for forming the parent ion CF_3I^+ . Closed symbols relate to the left axis, open symbols to the right. The representative error bars show one or two standard deviations (see Tables B.8 and B.9) of four separate determinations.

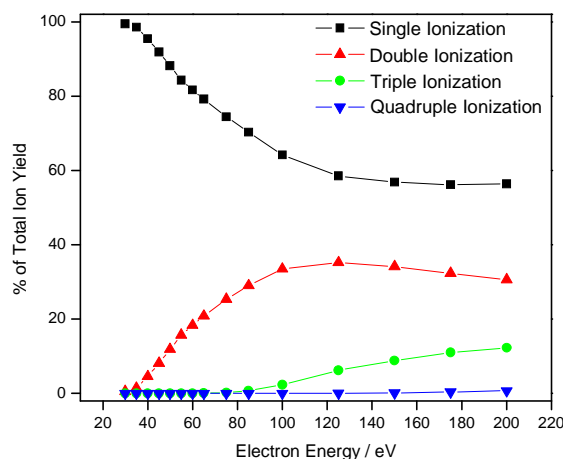


Figure 6.5: Contribution to the total ion yield from dissociative single, double, triple and quadruple ionization, following electron ionization of CF_3I .

6.5.3 Energetics and Dissociation of CF_3I^{2+} and CF_3I^{3+}

As described in Section 3.4, the peak shapes in the pairs spectra can be used to determine estimates of the kinetic energy released when the doubly and triply charged parent ions dissociate. We extract kinetic energy release distributions for the different fragmentation channels of CF_3I^{m+} , by fitting the experimental ΔTOF spectrum²² with a Monte-Carlo simulation of the dissociation. For each channel we use data from the lowest electron energy which generates a statistically significant ΔTOF spectrum. For two-body dissociations the Monte-Carlo simulations can be directly employed to model the ΔTOF peaks, and yield the KER. The KERs we have determined from the pairs spectra are shown in Table 6.3. Good agreement is observed between our KER value for the dissociation channel $\text{I}^+ + \text{CF}_3^+$, and that reported by Eland *et. al.*,¹¹ recorded following photoionization of CF_3I at 40.8 eV. Using the calculated KERs, along with thermochemical data²³ on the products of the break-up reactions, we are also able to estimate precursor state energies of the CF_3I dication and trication. These precursor state energies are given in Table 6.3.

For the ion pair $\text{I}^+ + \text{CF}_3^+$ we derive a precursor state energy of 27.9 ± 0.3 eV. This precursor state energy is in good agreement with the ground state of the CF_3I dication, $X^3\text{A}_2$, at 28 eV.¹¹ However, this precursor state is calculated using the average energy of the three possible spin-orbit states of $X^3\text{P}^0 \text{I}^+$ ($J = 2, 1, 0$). If the $X^3\text{P}^0 \text{I}^+$ is formed in the $J = 2$ spin-orbit state, the lowest in energy, we derive a precursor

state energy of 26.9 ± 0.3 eV, which lies below the double ionization potential of CF_3I at 28.0 eV.¹¹ This suggests that if the I^+ fragment is formed in the $X^3\text{P}^0 \text{I}^+$, $J = 2$ state then the CF_3^+ product from this dissociation channel is formed with significant internal excitation, as the calculated precursor energy is for CF_3^+ in the ground state. Indeed, since CF_3^+ is planar, whereas the CF_3 moiety in neutral CF_3I is non-planar, a considerable amount of internal vibrational energy of this product is to be expected.

For the ion pair $\text{CF}_3^+ + \text{I}^{2+}$ we are able to determine an estimate of a precursor state energy of the CF_3I trication. The precursor state energy we derive is 55.3 ± 0.3 eV. To the best of our knowledge, this is the first estimate of a precursor state energy of the CF_3I trication.

Table 6.3: Kinetic energy releases and corresponding precursor state energies P , for selected dissociation reactions of CF_3I^{m+} . The energies of the dissociation asymptotes, relative to the ground state of CF_3I , involved in the determination of P are listed. These asymptotes correspond to the formation of ground state products. Because of the possibility of forming $X^3\text{P}^0 \text{I}^+$ in three spin-orbit states ($J = 2, 1, 0$), the average energy of these three states was used as the ground state energy of I^+ .

Ion Pair	Electron energy / eV	KER / eV	Weight / %	Lit. ¹¹ KER	Asyptote ²³	P / eV
$\text{I}^+ + \text{CF}_3^+$	50	4.7 ± 0.3	100	4.4 ± 0.3	23.2	27.9
$\text{I}^+ + \text{CF}_2^+$	50	4.4 ± 0.5	75		29.4	33.8
		6.5 ± 0.5	25			35.9
$\text{CF}_3^+ + \text{I}^{2+}$	125	6.7 ± 0.3	100		48.6	55.3

To extract KER values for three-body dissociations of the CF_3I dication, the mechanism of the dissociation is first required. As described in Section 3.4, in principle this information can be extracted from the gradient of the peak in the pairs spectrum.^{22,24} At an ionizing electron energy of 50 eV, the observed gradient of the $\text{I}^+ + \text{CF}_2^+$ peak is -0.85 . This gradient indicates an initial separation of CF_3I^{2+} into CF_3^+ and I^+ , followed by a secondary dissociation of the CF_3^+ into CF_2^+ and a neutral F fragment. This dissociation pathway gives a calculated peak gradient of -0.72 , consistent with our observed value if the decay of the primary CF_3^+ fragment occurs within the field of the I^+ ion; in such a situation the observed peak gradient will lie between -0.72 and -1 . A disparity is noted between this dissociation pathway for the $\text{I}^+ + \text{CF}_2^+$ ion pair, and that proposed by Eland *et. al.*¹¹, who report an observed peak gradient of exactly -1 . This

peak gradient indicates the CF_3I^{2+} species initially ejects of a neutral F fragment to form CF_2I^{2+} , which then fragments to form the $\text{I}^+ + \text{CF}_2^+$ ion pair. A possible explanation for this observed difference, is that in the work of Eland *et. al.*,¹¹ in which ionization is achieved using 40.8 eV photons, a smaller range of electronic states of the CF_3I dication are likely to be accessed than when ionization is achieved using 50 eV electrons. This would also explain why the observed peak gradient of the $\text{I}^+ + \text{CF}_2^+$ peak lies between -0.72 and -1 , as the majority of CF_3I dication states accessed using 50 eV electrons dissociate *via* a CF_3^+ intermediate (calculated gradient of -0.72), whereas some of those accessed may dissociate as described by Eland *et. al.*¹¹ (calculated gradient of -1), resulting in the observed gradient (-0.85) being between the two. Indeed, looking at the $\text{I}^+ + \text{CF}_2^+$ ion pair peak when using an ionizing electron energy of 200 eV, in which different electronic states of the CF_3I dication may be accessed, the gradient of the peak can be seen to much closer to -1 , indicating a greater number of the electronic states accessed at 200 eV dissociate following the pathway described by Eland *et. al.*,¹¹ whereas fewer of those accessed dissociate *via* the CF_3^+ intermediate.

Using the dissociation pathway indicated by the $\text{I}^+ + \text{CF}_2^+$ peaks observed at an ionizing electron energy of 50 eV, more than one KER value was required to satisfactorily fit the experimental ΔTOF spectrum, if the width of the (Gaussian) KER distribution was restricted to realistic values, below 1.5 eV. The KERs obtained, shown in Table 6.3, resulted in estimated precursor state energies of 33.8 ± 0.5 and 35.9 ± 0.5 eV. These states lie higher in energy than any calculated theoretically by Eland *et. al.*¹¹ For this ion pair, no KER value is reported by Eland *et. al.*¹¹ for comparison.

For the remaining ion pairs observed in the pairs spectra, KER determinations were not made. This was either due to difficulties in obtaining the dissociation pathway, as several possibilities resulted in similar calculated gradients, or there being insufficient counts for a particular ion pair to produce statistically significant KERs.

6.6 Conclusions

Using time-of-flight mass spectrometry coupled with a 2D ion coincidence technique, relative and precursor-specific relative partial ionization cross-sections have been measured for the formation of all positive ion fragments following electron ionization of trifluoroiodomethane. These cross-sections are reported relative to the CF_3I^+ ion, at ionizing electron energies in the range 30 – 200 eV. To the best of our knowledge this is the first time that precursor-specific relative PICSs have been derived

for the electron ionization of CF_3I . The precursor-specific relative PICSs derived allow the contribution from single, double, triple and quadruple ionization to the individual fragment ion yields, following electron ionization of CF_3I , to be quantified. Our analysis shows that the contribution to the total ion yield from single ionization remains the most significant at all ionizing electron energies investigated. Contributions from double, triple and quadruple ionization reach a maximum of 35 %, 12 % and 1 % at ionizing electron energies of 125, 200 and 200 eV respectively. Comparison of our relative PICSs to those derived from the data of Jiao *et. al.*⁷ showed significant discrepancies. These discrepancies were attributed to the inefficient detection of translationally energetic fragmentation ions in the earlier work. Measurements of the KERs involved in several of the dissociation pathways have been made by analysis of peaks observed in the pairs spectra. From these KERs, estimates of the energies of the electronic states of the CF_3I dication, and for the first time the CF_3I trication, which are responsible for the different fragmentation channels have been made.

6.7 References

- 1 R. A. Levy, V. B. Zaitsev, K. Aryusook, C. Ravindranath, V. Sigal, S. Kesari, D. Rufin, J. Sees, and L. Hall, *J. Mat. Res.* **13**, 2643 (1998).
- 2 F. Fracassi and R. d'Agostino, *J. Vac. Sci. Technol. B* **16**, 1867 (1998).
- 3 L. G. Christophorou and J. K. Olthoff, *J. Phys. Chem. Ref. Data* **29**, 553 (2000).
- 4 J. C. Yang, M. R. Nyden, and S. L. Manzello, in *Halon Optics Technical Working Conference* (NIST, 2001), pp. 64.
- 5 *Fire Suppression System Performance of Alternative Agents in Aircraft Engine and Dry Bay Laboratory Simulations*, Vol. 1, edited by R. G. Gann (NIST, Gaithersburg, 1995).
- 6 S. Solomon, J. B. Burkholder, A. R. Ravishankara, and R. R. Garcia, *J. Geophys. Res.-Atmos.* **99**, 20929 (1994).
- 7 C. Q. Jiao, B. Ganguly, C. A. DeJoseph, and A. Garscadden, *Int. J. Mass Spectrom.* **208**, 127 (2001).
- 8 J. A. Beran and L. Kevan, *J. Phys. Chem.* **73**, 3866 (1969).
- 9 U. Onthong, H. Deutsch, K. Becker, S. Matt, M. Probst, and T. D. Mark, *Int. J. Mass Spectrom.* **214**, 56 (2002).
- 10 A. Pilcher-Clayton and J. H. D. Eland, *J. Electron. Spectrosc.* **142**, 313 (2005).
- 11 J. H. D. Eland, R. Feifel, and M. Hochlaf, *J. Phys. Chem.* **128**, 234303 (2008).

- 12 S. J. King and S. D. Price, *Int. J. Mass Spectrom.* **272**, 154 (2008).
- 13 M. R. Bruce, L. Mi, C. R. Sporleder, and R. A. Bonham, *J. Phys. B: At., Mol. Opt. Phys.* **27**, 5773 (1994).
- 14 K. M. Douglas and S. D. Price, *Int. J. Mass Spectrom.* **303**, 147 (2011).
- 15 K. M. Douglas and S. D. Price, *J. Chem. Phys.* **131**, 224305 (2009).
- 16 S. J. King and S. D. Price, *J. Chem. Phys.* **127**, 174307 (2007).
- 17 N. A. Love and S. D. Price, *Phys. Chem. Chem. Phys.* **6**, 4558 (2004).
- 18 S. Harper, P. Calandra, and S. D. Price, *Phys. Chem. Chem. Phys.* **3**, 741 (2001).
- 19 P. Calandra, C. S. S. O'Connor, and S. D. Price, *J. Chem. Phys.* **112**, 10821 (2000).
- 20 C. C. Tian and C. R. Vidal, *J. Phys. B: At. Mol., Opt. Phys.* **31**, 895 (1998).
- 21 S. J. King, **PhD Studies of the Dissociation and Energetics of Gaseous Ions**, University College London, 2008.
- 22 D. M. Curtis and J. H. D. Eland, *Int. J. Mass Spectrom. Ion Processes* **63**, 241 (1985).
- 23 *NIST Chemical WebBook; NIST Standard Reference Database Number 69*, Vol., edited by P. J. Linstrom and W. G. Mallard (National Institute of Standards and Technology, Gaithersburg MD, 20899, 2008).
- 24 J. H. D. Eland, *Mol. Phys.* **61**, 725 (1987).

Chapter 7 **An Investigation into the Value of Double Photoionization Studies at the SLS: Trifluoroiodomethane**

7.1 Introduction

As discussed in the previous chapter, trifluoroiodomethane (CF_3I) has been proposed as a possible plasma etching gas and a gaseous fire suppressant to replace other perfluorinated compounds (PFCs).¹⁻⁴ The recent interest in making such a replacement is due to CF_3I being a “more environmentally friendly” gas, having a much lower global warming potential than many currently used PFCs and fire suppressant agents,¹⁻⁵ as well as not significantly contributing to ozone depletion due to its short atmospheric lifetime.⁶

This chapter presents results from a preliminary visit to the vacuum ultra-violet (VUV) beamline at the Swiss Light Source (SLS), to evaluate the suitability of the imaging photoion-photoelectron coincidence (iPEPICO) endstation for studying double photoionization processes. As an initial investigation, the photoionization of CF_3I at energies above its double ionization energy (28.0 eV)⁷ was studied. The iPEPICO endstation at the SLS can be configured to produce singles and pairs spectra very similar to those produced by the electron ionization experiments reported in Chapters 4 – 6. These singles and pairs spectra can be processed to yield relative ion yields (RIYs) similar to the relative and precursor-specific relative partial ionization cross-sections reported in Chapters 4 – 6. One key difference, as described in detail below, is that the relative ion yields reported in this Chapter are for the formation of ions following photoionization processes that produce a threshold electron (≤ 800 meV).

7.1.1 Dissociative Ionization of Trifluoroiodomethane

Photoionization of CF_3I below the double ionisation threshold has been extensively studied in the past, using a range of ion and electron coincidence techniques.⁸⁻¹² Focusing on the photoionization of CF_3I at energies above its double ionization energy, as investigated in this chapter, the available data is limited. An investigation by Pilcher-Clayton and Eland¹³ in the energy range 23 – 47 eV, employed a time-of-flight photoelectron-photoelectron coincidence (TOF-PEPICO) technique, and

suggested the presence of a possible indirect mechanism for double photoionization. This indirect mechanism, which results in I^+ containing ion pairs, proceeds by initial ionization of CF_3I to an excited cation state (CF_3I^{+*}), which then undergoes dissociation to $CF_3^+ + I^*$ before autoionization of the atomic iodine fragment.¹³ The double photoionization and dicationic fragmentation of CF_3I has also been investigated by Eland *et. al.*,⁷ using a range of electron-ion coincidence techniques, together with computational calculations. In the study by Eland *et. al.*⁷ the energies of the ground and several excited electronic states of CF_3I^{2+} are reported, together with dication dissociation pathways leading to several of the observed ion pairs.

7.2 Experimental

7.2.1 Instrumentation

The experiments reported in this chapter were performed at the Swiss Light Source on the VUV beamline.¹⁴ The SLS storage ring is operated in top-up mode, and a continuous VUV light source is provided by a bend magnet port. A full description of the beamline can be found in Ref. 14, and only a brief overview is given here. A schematic diagram of the beamline optics is given in Figure 7.1. Radiation from the bending magnet is collimated using a copper mirror with a platinum reflective coating. A silicon grating with 1200 mm^{-1} line density is employed to produce monochromatic light in the energy range 15 – 100 eV. A second mirror focuses the collimated beam into a gas filter. These first three elements form a constant deviation angle monochromator, in which the grating is the only optical element moving during an energy scan. Hard radiation is blocked from the first mirror with an X-ray blocker, a water-cooled copper tube which cuts out the central ± 0.2 mrad of the vertical radiation responsible for 80 % of the overall heat load. Due to the characteristic vertical distribution of the bend magnet radiation, the X-ray blocker cuts out most of the hard X-rays, while losing only 15 % of the VUV flux. A 12° grazing angle on the first mirror yields a high reflectivity in the VUV range, while cutting off the flux for photon energies above 150 eV. The beamline is optimised to give a high photon flux and resolution in the energy range of 5 – 30 eV, with higher harmonic light from the beam monochromator being removed by a gas filter (above 20 eV) and the grazing of the diffraction grating, as mentioned above. However as these preliminary experiments were to study the photoionization of CF_3I above the double ionization threshold (28

eV), the gas filter was not employed, allowing the use of higher energy photons (up to 100 eV). This means that in the experiments reported here, there is the possibility of contamination of the photon beam by higher order light from the monochromator. The flux transmitted through the beamline, together with the resolution, is regulated by moving two motorized sets of slits in the front end of the beamline optics.

For the experiments reported here, the iPEPICO endstation (Figure 7.2) was attached to the beamline. Again only a brief description of this endstation is given, as a full description can be found in Ref. 15. The iPEPICO endstation is designed and optimized to detect coincident photoelectrons and photoions formed following single photoionization. Two drift tubes, one for electrons and one for ions, are aligned opposite each other across a small interaction region. In the interaction region, the sample is introduced as a continuous effusive jet of gas which crosses the beam of VUV photons. Any electron or ions formed are accelerated by a small electric field ($40 - 80 \text{ Vcm}^{-1}$) into their respective detection regions. Electrons fly vertically into a 265 mm long electron flight tube. The fields in the electron detection region are chosen to achieve velocity map imaging (VMI) of the electron beam at the detector. The detector used is a position sensitive detector, of the delay line type. Only electrons with energies below 800 meV will be focused onto the detector plate, although there will be a small contribution of high energy electrons whose initial velocities are directed towards the detector. Magnetic shielding of the electrons is achieved using two μ -metal pieces, one encapsulating the whole electrode stack, and the second acting as the electron flight tube. Any ions formed following photoionization are extracted into a standard time-of-flight (TOF) mass spectrometer and detected using a multi-channel plate detector.

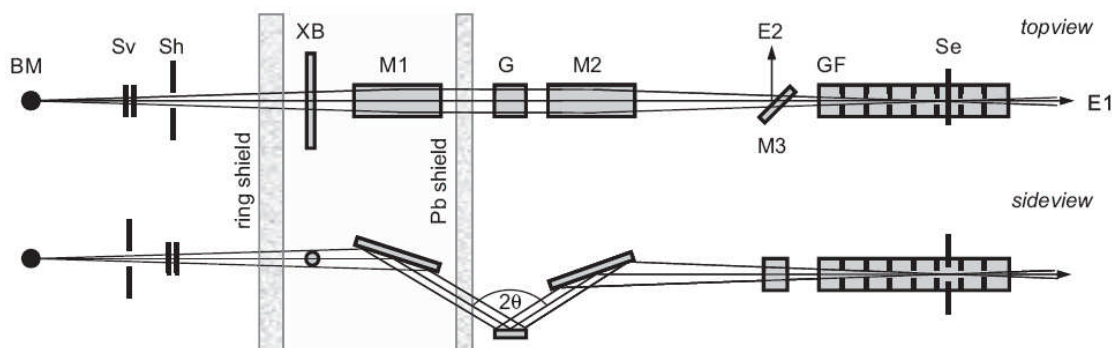


Figure 7.1: Beamline layout (not to scale) with bend magnet (BM), vertical and horizontal slits (Sv, Sh), X-ray blocker (XB), collimating mirror (M1), grating (G), refocusing mirror (M2), flip mirror (M3), gas filter (GF), exit slit (Se), and endstations 1 and 2 (E1, E2). Reproduced from Ref. [14].

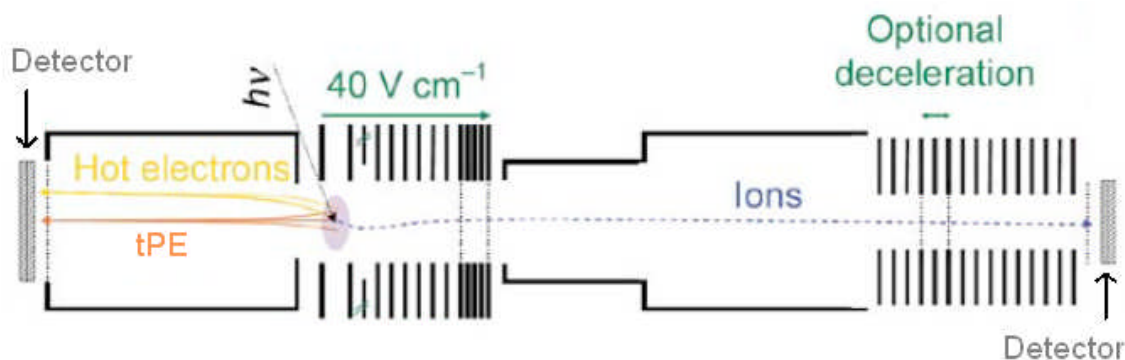


Figure 7.2: Schematic of the iPEPICO endstation, showing the interaction region where the VUV beam enters, and the two drift tubes, one for threshold photoelectrons (tPE) and one for ions. Reproduced from Ref. [15].

7.2.2 Conversion for Double Ionization Studies

As mentioned above, the VUV beamline and iPEPICO end station were designed and optimised to study single ionization of gas-phase species. In order to study the double ionization of gas-phase species some minor alterations were necessary. The original data acquisition system employs a multistart-multistop (M/M) mode of a time-to-digital converter (TDC) card, in which all detector data are collected. This M/M setup ensures the highest signal-to-noise ratio, a constant background, and fast data acquisition.¹⁶ To allow for studies of double ionization, the mode of the TDC was altered so that for every electron detected, more than one ion could also be recorded. Following an experimental run, the data was then analysed so that events in which only a single ion was detected were placed in a singles mass spectrum, while those events in which two ions were detected in coincidence were stored in a pairs spectrum. These spectra are at first glance very similar to those produced in the electron ionization experiments in Chapters 4 – 6, and are analysed as described in Section 7.3 below.

7.2.3 Experimental Conditions

For all experiments, the trifluoriodomethane used was a commercial sample of $\geq 99\%$ purity. The pressure in the interaction region of the iPEPICO endstation was maintained around $1 - 2 \times 10^{-6}$ mbar. As described above, the flux transmitted through the beamline, together with the resolution of the photon beam, is regulated by moving two motorized sets of slits in the front end the beamline optics. The best energy resolution is obtained by having a small distance between the slits. However, if more photon flux is required the distance between the slits can be increased; this will, of

course, come at the expense of the energy resolution of the beam, which will decrease. For the experiments carried out at 28, 31 and 34 eV, the slits were in a position to give the best possible energy resolution, of around 15 meV. However, as the flux from the monochromator shows oscillations in intensity,¹⁴ with one of the minima occurring at a photon energy of 37 eV, for the experiment at 37 eV it was necessary to open the slits wider to increase the flux from the monochromator, resulting in a decreased energy resolution of around 40 meV for this photon energy. Typical experimental run times were of the order of 2 hours.

As the iPEPICO end station was designed to study single ionization processes, there are several issues that arise when using it in the study of double ionization. It was these issues this set of preliminary experiments were designed to probe. Firstly, the conditions required to extract threshold electrons with a high-resolution mean that only a small field can be applied to extract ions into the TOF mass spectrometer. These small fields employed mean that energetic ions are more likely to miss the detector face, and not be detected. This effect is easily recognised as a “hollowing out” of peaks in both the 1D and 2D spectra (Figures 7.3 and 7.5). Such ion losses can straightforwardly be corrected using a simple geometry correction, as described in Sections 3.2.2.2 and 7.3 below. A second problem is the high count rates that arise due to the quasi-continuous nature of synchrotron radiation, and the difficulty in controlling photon flux. These high count rates result in a large number of false coincidences in the pairs spectra, events in which two ions are detected in coincidence together with a threshold electron, but all three species did not originate from the same ionization event. We have shown these false coincidences can be effectively removed using the autocorrelation of the singles spectrum, as described in Section 3.2.2.1.

7.3 Data Analysis

Singles and pairs mass spectra of trifluoroiodomethane were recorded at photon energies of 28, 31, 34 and 37 eV, at the SLS on the VUV beamline, using the experimental apparatus described in Section 7.2. As mentioned above, the detection of only low energy electrons in these experiments changes the data analysis markedly, as described below.

7.3.1 Singles Mass Spectra

A mass spectrum of CF₃I following photoionization at 37 eV, in which the major ion fragments can be seen, is shown in Figure 7.3. The mass spectrum shows the parent monocation, CF₃I⁺, together with the ion fragments formed from dissociation of CF₃I^{m+}: C⁺, F⁺, CF⁺, CF₂⁺, I²⁺, CF₃⁺, FI²⁺, CFI²⁺, CF₂I²⁺, I⁺, CI⁺, FI⁺, CFI⁺ and CF₂I⁺. The intensities of these individual ion peaks $I_n[X^{m+}]$ appearing in the singles spectra are extracted by summing the counts in each peak, after applying a small correction to account for the non-zero baseline which arises due to stray ions, as described in Section 3.2.1. A correction is also made to any ion peaks that show a “hollowing out” resulting from energetic ion loss. As can be seen in Figure 7.4, such a “hollowing out” of a peak in the singles spectra results in a central peak and two or more outer peaks. The central peak, which can be labelled $I_{\text{NCS}}[X^{m+}]$, results mainly from non charge separating (NCS) dissociative ionization events, e.g. CF₃I⁺ → CF₃⁺ + I and CF₃I²⁺ → CF₃ + I²⁺. In these NCS processes, in which there will only be a small kinetic energy release (KER) upon fragmentation, the ions will be formed with low translational energies and so only have small deviations from the ideal TOFs. The outer peaks are mainly the result of charge separating (CS) dissociative ionization events, in which one of the resulting ions is not detected due to the detection efficiency of the apparatus being less than unity, e.g. CF₃I²⁺ → CF₃⁺ [detected] + I⁺ [not detected]. Such CS dissociations are processes in which there is a large KER upon fragmentation, so that only ions formed with kinetic energies approximately parallel to the TOF axis will be detected (arriving either markedly earlier or later than their ideal TOFs), whereas those formed with kinetic energies perpendicular to the TOF axis will be missed. Therefore, to correct for those ions that are missed, a straight line is drawn between the two outer peaks, and the counts underneath summed (Fig. 7.4). This gives the corrected number of ions resulting from CS dissociation processes, in which one of the ions have been missed, $I_{\text{CS}}[X^{m+}]$. The correct value for the number of counts in a particular ion peak in the singles spectrum, $I_n[X^{m+}]$, can then be found by summing $I_{\text{NCS}}[X^{m+}]$ and $I_{\text{CS}}[X^{m+}]$ (see Figure 7.4).

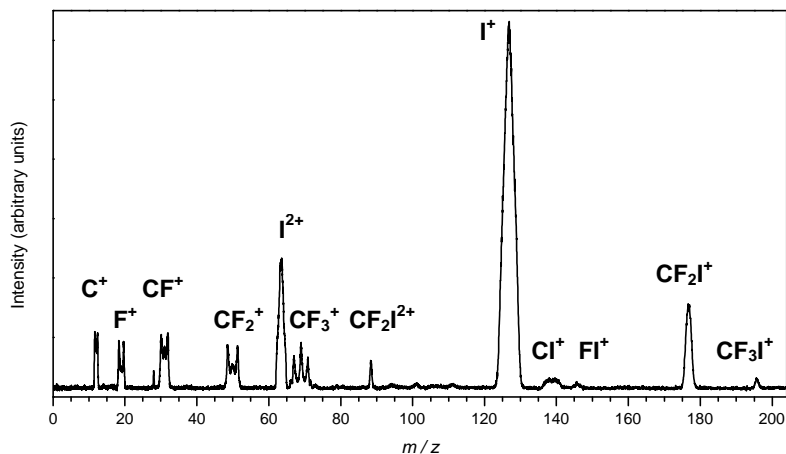


Figure 7.3: Single mass spectrum of trifluoriodomethane showing the major ion fragments and the parent ion formed following photoionization at 37 eV.

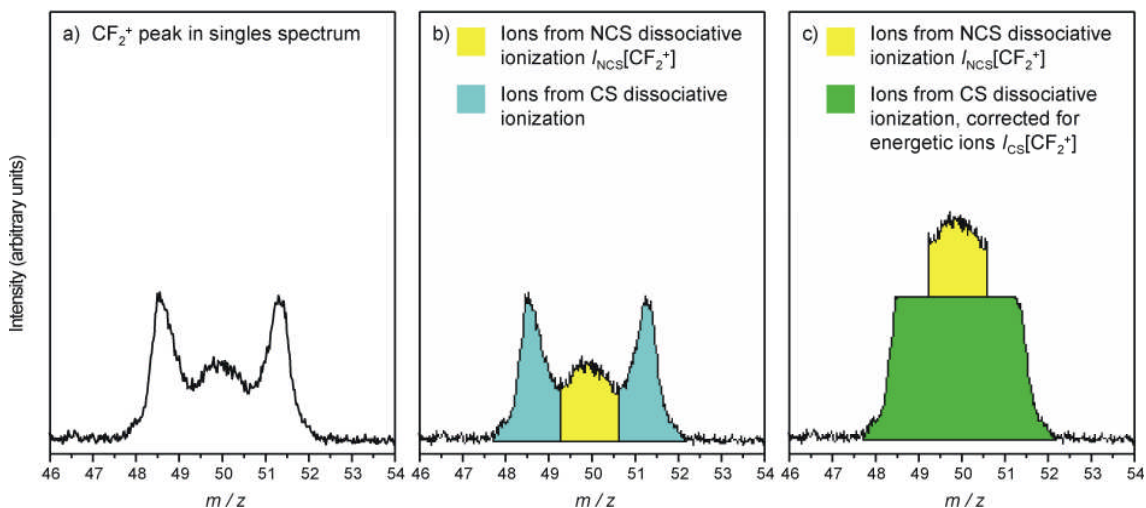


Figure 7.4: A close up of the CF_2^+ fragment ion peak in the single spectra at 37 eV photon energy showing: (a) the “hollowing out” of the peak, (b) the inner (yellow) peak resulting from ions from NCS dissociative ionization $I_{\text{NCS}}[\text{CF}_2^+]$ and the outer (light blue) peaks resulting from ions from CS dissociative ionization, and (c) the energetic ion loss correction to the outer peaks (green) yielding $I_{\text{CS}}[\text{CF}_2^+]$. The total counts of CF_2^+ in the single spectra $I_{\text{n}}[\text{CF}_2^+]$ is given by the sum of $I_{\text{NCS}}[\text{CF}_2^+] + I_{\text{CS}}[\text{CF}_2^+]$.

7.3.2 Pairs Spectra

A pairs spectrum of CF_3I recorded at a photon energy of 37 eV, in which the major ion pair channels can be seen, is shown in Figure 7.5. At this energy a total of 16 different ion pairs are observed: 11 monocation-monocation pairs and 5 dication-monocation pairs (Table 7.1).

The contribution of a particular ion to the pairs spectra, $P_n[X^{m+}]$, was extracted using the procedure described in Section 3.2.2. As mentioned above, due to the high count rates employed a large number of false coincidences are observed in the pairs spectra. These false coincidences are subtracted manually for each peak using the autocorrelation of the singles spectrum, as described in Section 3.2.2.1. This method of false coincidence correction has been shown to be effective by successfully removing counts from known false coincidences in the pairs spectra.

Corrections are also made to the pairs peaks to account for energetic ion losses. As described in Sections 3.2.2.2 and 7.2.3, these energetic ion losses appear as a “hollowing out” of the ion pair peak, as can be seen in Figure 7.5.b. The correction is made by first constructing a time-of-flight difference (Δ TOF) plot for a particular ion pair peak, and then using an appropriate geometric construction to include any energetic ions lost, as described in Section 3.2.2.2. At 37 eV photon energy, all but three of the ion pairs ($\text{CF}_2\text{I}^+ + \text{F}^+$, $\text{I}^{2+} + \text{F}^+$ and $\text{CF}_2^+ + \text{F}^+$) required a correction due to energetic ion loss, however at the lowest photon energy used (28 eV), no ion pairs required this correction. This indicates that as the photon energy was reduced to 28 eV, the number of ion pairs resulting from dissociative double ionization of CF_3I falls away, resulting in a pairs spectra made up almost entirely from false coincidences. This was confirmed by the false coincidence subtraction, which resulted in zero counts, within the error limits, for the majority of ion pairs observed at 28 eV photon energy.

Table 7.1: Ion pairs observed in the pairs spectrum recorded following photoionization of CF_3I at 37 eV ionizing photon energy.

Monocation-monocation pairs		Dication-monocation pairs	
CF_2I^+	$+ \text{F}^+$	I^{2+}	$+ \text{C}^+$
CI^+	$+ \text{F}^+$		$+ \text{F}^+$
I^+	$+ \text{C}^+$		$+ \text{CF}^+$
	$+ \text{F}^+$		$+ \text{CF}_2^+$
	$+ \text{CF}^+$		$+ \text{CF}_3^+$
	$+ \text{CF}_2^+$		
	$+ \text{CF}_3^+$		
CF_2^+	$+ \text{F}^+$		
CF^+	$+ \text{F}^+$		
F^+	$+ \text{C}^+$		
	$+ \text{F}^+$		

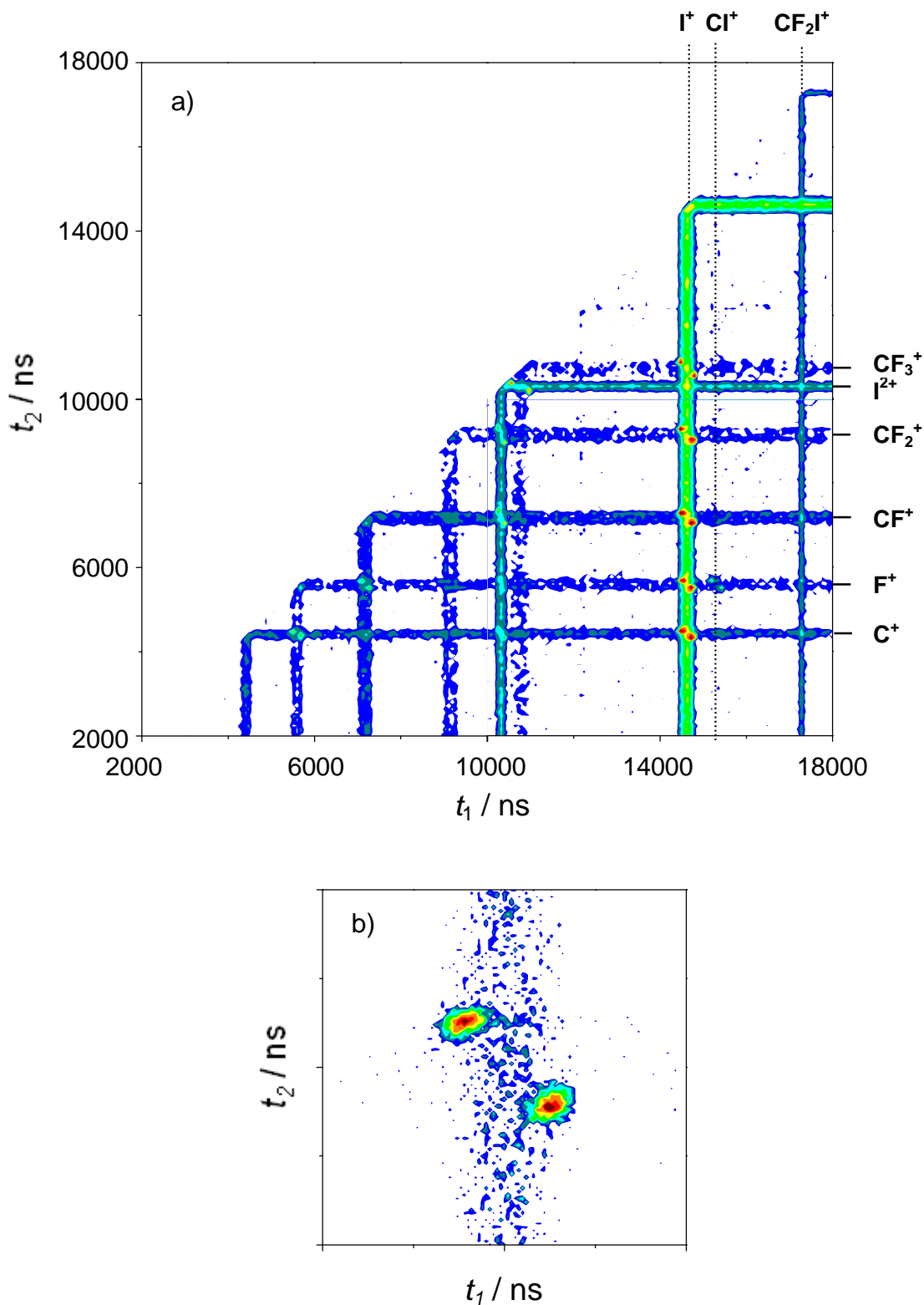


Figure 7.5: Raw pairs spectrum of CF₃I recorded at a photon energy of 37 eV, showing : (a) the full pairs spectra, in which the major ion pairs can be seen, and (b) a close up of the I⁺ + CF⁺ ion pair, in which the hollowing of the pairs peak can be observed.

7.3.3 Relative Ion Yield Determinations

As mentioned above, and discussed in more detail below in Section 7.5.1, the detection of only low energy electrons in these experiments means that the recorded ion intensities favour ions formed from double ionisation events, or single ionization events in which the ion formed has a large degree of internal energy, and/or resulted from a large degree of fragmentation of the parent ion; only in these events is it possible to form a threshold electron. Thus, as not all ions are being detected with equal efficiency, ‘true’ ionization cross-sections cannot be derived from the recorded ion intensities (Section 1.4). Thus, in this chapter we report relative ion yields $RIY[X^{m+}]$ and precursor-specific relative ion yields $RIY_n[X^{m+}]$ for the formation of fragment ions. The relative ion yields (RIYs) are derived using the same set of equations from which relative PICSSs are derived, in Section 3.3, and can be seen in Appendix C.

7.3.4 Determination of Ion Detection Efficiency f_i

As discussed in Section 3.3, in order to determine precursor-specific relative PICSSs $\sigma_n[X^{m+}]$ a value for the ion detection efficiency f_i is required. In a similar manner, in order to determine precursor-specific RIYs, which quantify the contribution dissociative single, double and triple ionization make towards a particular ions total ion yield, the ion detection efficiency of the iPEPICO endstation is also required. As mentioned above, following photoionization of CF_3I , a “hollowing out” of several of the peaks in the singles spectra was observed (Fig 6.2), resulting in inner and outer peaks for several of the ion fragments. As the inner peak will be almost exclusively the result of ions formed from NCS dissociative ionization processes, the counts in this peak are labelled $I_{NCS}[X^{m+}]$. The outer peaks result from ions formed from CS dissociative ionization processes, where the ions are formed with translational energies parallel to the TOF axis (and so will arrive earlier or later than their ideal TOFs), and where one of the ions in the pair is not detected due to the ion detection efficiency being less than unity. Such CS dissociative ionization events in which the ions are formed with translation energies perpendicular to the TOF axis (and so would have arrived close to their ideal TOFs) will miss the detector and so not be counted. It is these translationally energetic ions from CS dissociative ionization events that miss the detector, that result in the “hollowed out” or missing part of the peak. If we correct for the loss of energetic ions to the outer peaks (Fig. 7.4), we obtain a value for the number of ions formed from CS dissociative ionization events in which one ion is not detected due to the ion

detection efficiency of the apparatus, $I_{CS}[X^{m+}]$. This $I_{CS}[X^{m+}]$ value can be related back to the “real” number of X^{m+} ions formed from CS dissociative ionization processes, $N_{2pairs}[X^{m+}] + N_{3pairs}[X^{m+}]$, by Equation 7.1. $N_{2pairs}[X^{m+}]$ and $N_{3pairs}[X^{m+}]$ represent the “real” number of X^{m+} ions formed from dissociative double and triple ionization respectively, in coincidence with one other ion (see Section 3.3). The contribution of a particular ion to the pairs spectra $P_n[X^{m+}]$ can also be related back to the value of $N_{2pairs}[X^{m+}] + N_{3pairs}[X^{m+}]$ by Equation 7.2. A value for f_i can therefore be obtained by rearranging equations 7.1 and 7.2 into equation 7.3.

$$N_{2pairs}[X^{m+}] + N_{3pairs}[X^{m+}] = I_{CS}[X^{m+}] / f_i(1 - f_i) \quad (7.1)$$

$$N_{2pairs}[X^{m+}] + N_{3pairs}[X^{m+}] = P_n[X^{m+}] / f_i^2 \quad (7.2)$$

$$f_i = P_n[X^{m+}] / (P_n[X^{m+}] + I_{CS}[X^{m+}]) \quad (7.3)$$

Using equation 7.3, values of f_i were obtained at 37 eV photon energy for those ions which demonstrated this “hollowing out” in the singles spectra. Spectra at 37 eV photon energy was used as at this energy observed “hollowing” of peaks was greatest. These f_i values are given in Table 7.2, and yield an average value of f_i of 0.065. As can be seen from Table 7.2, there is a noticeable difference between the values of f_i obtained for the different fragment ions. To determine whether these differences indicate a variation of f_i with mass, or are just the result of normal random variation, an estimate of the error in the value of f_i is required. For the electron ionization studies, the error is usually taken as twice the standard deviation of several determinations of f_i ; however as only one determination of f_i could be made for each fragment ion this method can not be used in this case. Another method is to take the counting uncertainty for each ion peak used in the determination of f_i and carry these through, to obtain errors for the value of f_i for each ion fragment. These errors obtained from the counting statistics are also given in Table 7.2. As can be seen from Table 7.2, the statistical error in the individual determinations of f_i are much smaller than the variation between them. Another method to determine an approximate error in the value of f_i is to take the relative percentage error for values of f_i from the electron ionization studies (Chapters 4 – 6), and use it to

calculate an absolute error for the iPEPICO value of f_i . The relative percentage errors for the f_i values in Chapters 4 – 6 is around 5 %. From the f_i value of 0.065 determined above this results in an absolute error of ± 0.003 . Again this error is much smaller than the variation between the individual determinations of f_i for the different ion fragments. This suggests that there may be some variation in the value of f_i with fragment ion mass. Further experiments at the SLS will be able to confirm if there is such a variation, however until then a single value of f_i will be used for the determination of precursor-specific RIYs. The best estimate of the error in the value of f_i we have determined is therefore twice the standard deviation of the values for each fragment ion, resulting in $f_i = 0.065 \pm 0.030$. The possibility that f_i does vary with mass means there will be a larger degree of uncertainty in the RIYs determined below.

Table 7.2: Ion detection efficiencies obtained for fragment ions at 37 eV photon energy. Errors calculated by taking the counting error in each ion peak used and carrying through. Average error taken as twice the standard deviation of the individual determinations.

Ion Fragment	m/z	f_i	Statistical uncertainty
C ⁺	12	0.053	0.001
F ⁺	19	0.048	0.002
CF ⁺	31	0.070	0.001
CF ₂ ⁺	50	0.066	0.001
I ²⁺	63.5	0.062	0.002
CF ₃ ⁺	69	0.090	0.001
Average Value		0.065	0.030

7.4 Results

7.4.1 RIYs and Precursor-Specific RIYs

Mass and coincidence spectra of CF₃I were recorded at photon energies of 28, 31, 34 and 37 eV. These spectra were processed as described above and in Section 3.3 to produce relative ion yields for the formation of all fragment ions observed: C⁺, F⁺, CF⁺, CF₂⁺, I²⁺, CF₃⁺, FI²⁺, CFI²⁺, CF₂I²⁺, I⁺, CI⁺, FI⁺, CFI⁺ and CF₂I⁺. These RIYs are similar to the relative PICSs reported in Chapters 4 – 6, with the key difference being that they are only for ionization events in which a threshold (≤ 800 meV) photoelectron is formed. The RIYs determined are displayed as a function of energy in Figure 7.6 and Tables D.1 and D.2, and are expressed relative to the CF₃I⁺ ion yield. As discussed below in Section 7.5.1, the requirement of detecting a threshold electron in order to

detect an ion results in a very low yield of the parent ion. Such a low parent ion yield results in RIYs following photoionization of CF_3I that are very much larger than the cross-sections obtained following electron ionization of CF_3I reported in Chapter 6.

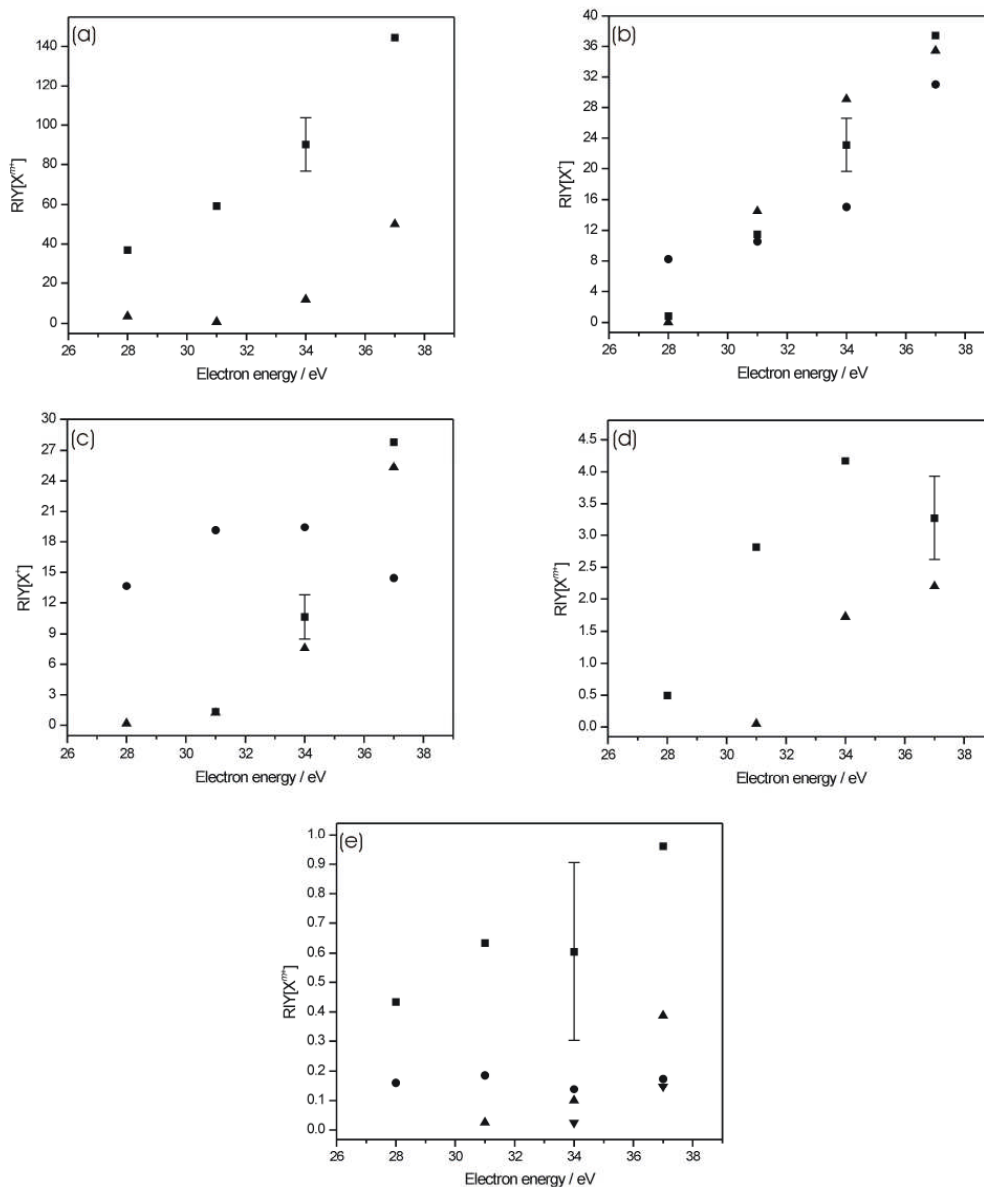
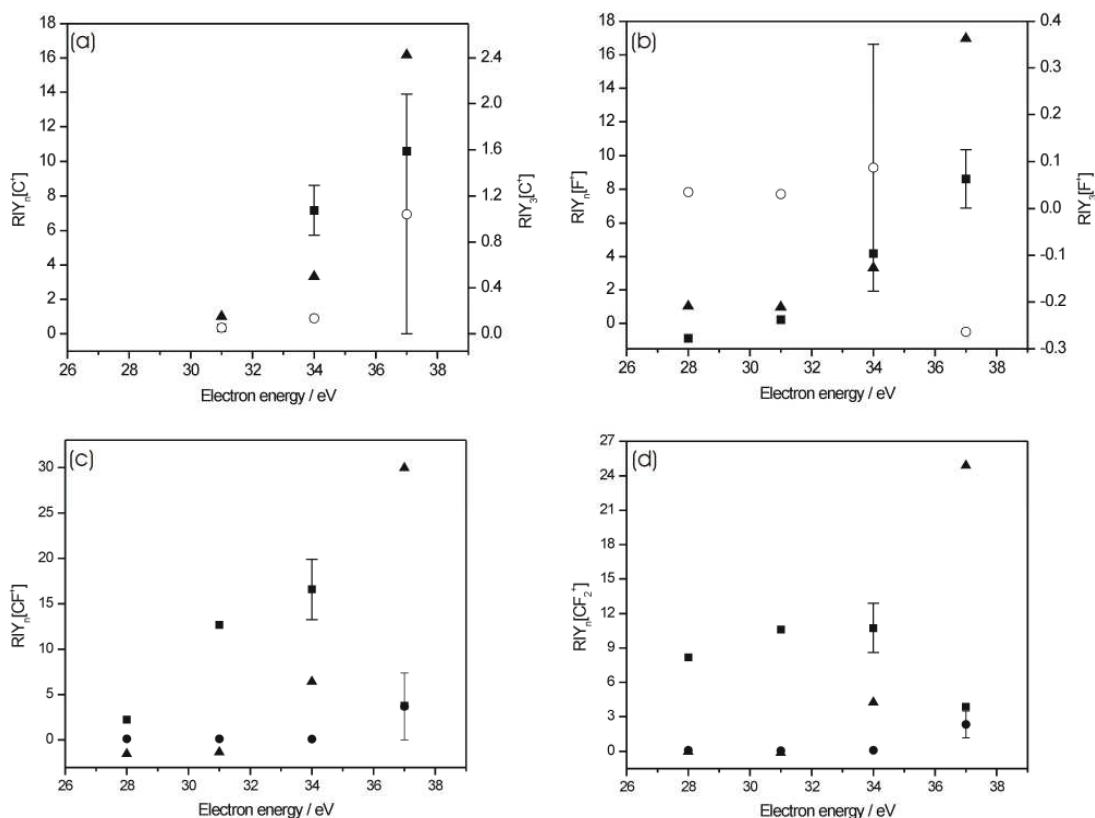


Figure 7.6: Relative ion yields $\text{RIY}[X^{m+}]$ for forming (a) I^+ (■) and I^{2+} (▲), (b) CF^+ (■), CF_3^+ (▲) and CF_2^+ (●), (c) C^+ (■), F^+ (▲) and CF_2I^+ (●), (d) CI^+ (■) and CF_2I^{2+} (▲) and (e) FI^+ (■), FI^{2+} (▲), CF_2I^+ (●) and CF_2I^{2+} (▼) following photoionization of CF_3I in which a threshold electron is formed, relative to the cross-section for forming the parent ion CF_3I^+ .

For the cross-sections reported in Chapters 4 – 6, the error was given by the standard deviation of several determinations. However for the RIYs reported in this Chapter, only one determination was made at each photon energy. By looking at the average relative percentage errors obtained for the cross-sections reported in Chapters 4 – 6, we can obtain an approximate error for the RIYs reported in this Chapter. The cross-sections in Chapters 4 – 6 were split into three rough groups, large, medium and small cross-sections, and the average relative percentage errors of cross-section in these groups taken. From these, we obtained approximate errors for the large, medium and small RIYs derived in this Chapter; RIYs that are above 15 (large RIYs) will have an approximate error of 10 %, those that lie between 15 and 1.5 (medium RIYs) will have an approximate error of 40 %, and those that are below 1.5 (small RIYs) have an approximate error of between 50 and 100 %.



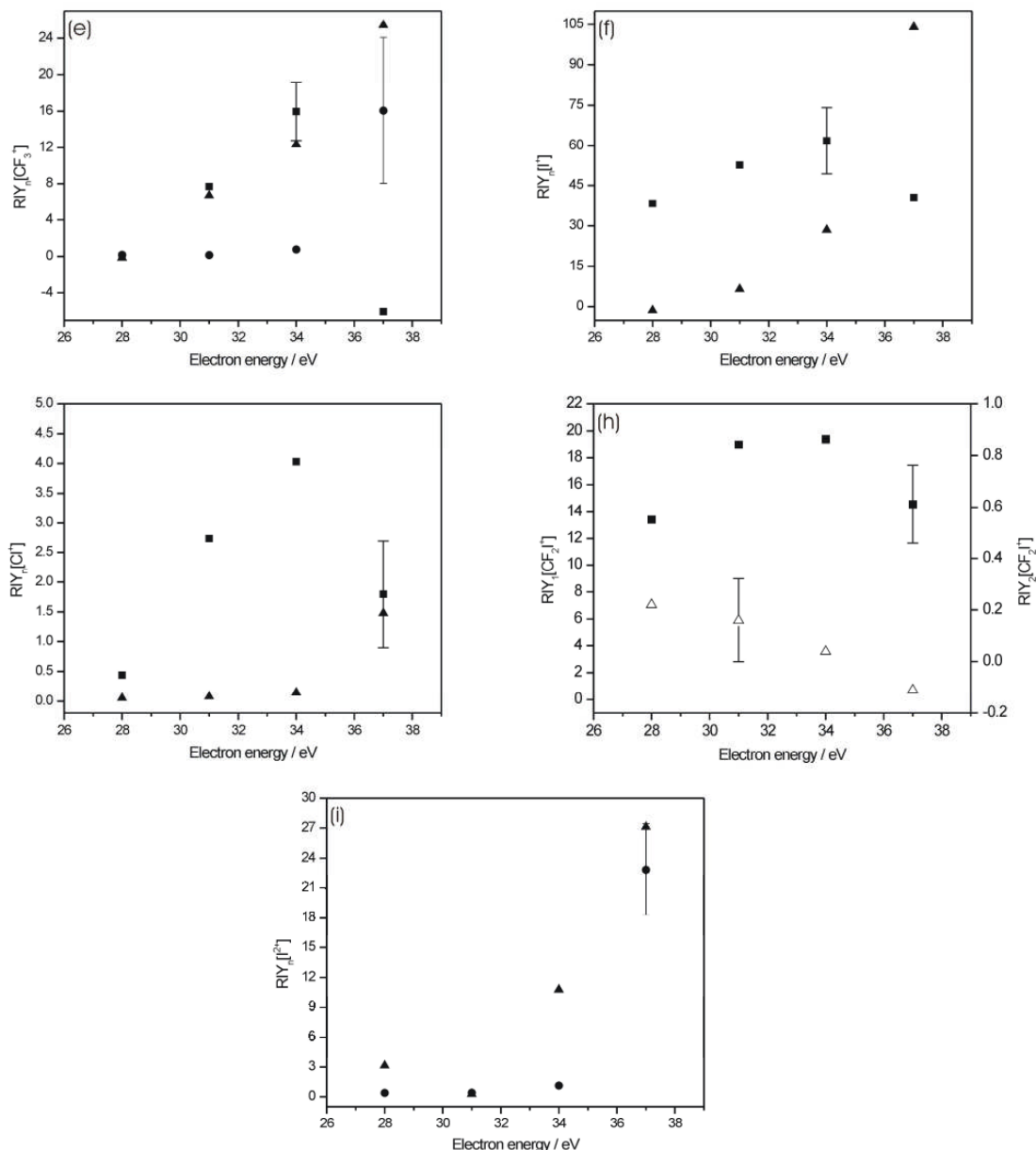


Figure 7.7: Precursor-specific relative ion yields $RIY_n[X^{m+}]$ for forming (a) C^+ , (b) F^+ , (c) CF^+ , (d) CF_2^+ , (e) CF_3^+ , (f) I^+ , (g) Cl^+ , (h) CF_2I^+ and (i) I^{2+} ion fragments via single (\blacksquare), double (\blacktriangle) and triple (\bullet) ionization, following photoionization of CF_3I in which a threshold electron is formed, relative to the ion yield for forming the parent ion CF_3I^+ . Closed symbols relate to the left axis, open symbols to the right.

In our pairs spectra we observe 16 ion pair peaks: 11 monocation-monocation pair peaks and 5 dication-monocation pair peaks (Table 7.1). At the lowest photon energy investigated (28 eV), the pairs spectra is dominated by false coincidences.

Subtraction of these false coincidences shows that contributions to the pairs spectra from true coincidences at this energy are, within error, negligible. Above 28 eV photon energy, the ion pair yield is dominated by ion pairs containing I^+ , the same dominance is also observed following electron ionization of CF_3I . At 31 and 34 eV photon energy, $I^+ + CF_3^+$ is the most intense channel, however as the photon energy is raised to 37 eV the yield of this channel decreases, with the $I^+ + CF^+$ channel becoming the most intense. This greater degree of fragmentation of the CF_3I^{2+} dication with increasing photon energy, is also observed with increasing electron energy. For the observed dication-monocation pairs, at photon energies below 37 eV there is negligible contribution from true coincidences, as is expected as the formation of dication-monocation pairs is not thermochemically accessible^{17,18} at these photon energies. The formation of dication-monocation pairs is also not thermochemically accessible at 37 eV photon energy, however a significant yield of dication-monocation pairs involving I^{2+} is observed at this energy. The most intense of these is by far the $I^{2+} + CF_3^+$ channel, which has the lowest enthalpy of formation at 41.0 eV.^{17,18} It should be noted that uncertainties in the value of the ionization energy of the CF_3 radical and the enthalpy of formation of CF_3^+ ion could result in this value being shifted down by 1 eV.^{19,20} The formation of these dication-monocation pairs at photon energies below their thermochemical thresholds seems to suggest contamination of higher order light in the photon beam. However, if this was the case, dication-monocation pairs should be observed at the lower photon energies investigated, in which we see, within error, negligible yields. Of course it is possible that even a small contamination from higher order light could produce a significant ion yield from triple ionization if a resonant state of the CF_3I trication were accessed. It is therefore possible that such a resonant state of CF_3I^{3+} lies at 74 eV, but not at 68, 62 or 56 eV, resulting in a contribution in the pairs spectra from triple ionization only at 37 eV photon energy.

As discussed in Section 7.3.4, a value for the ion detection efficiency is required to enable us to derive precursor-specific RIYs. Using the methodology described above in Section 7.3.4, we obtain a value of f_i of 0.065 ± 0.030 . The precursor-specific RIYs we obtain, displayed as a function of energy in Figure 7.7 and Table D.2, are for ionization processes forming a threshold electron (≤ 800 meV) and are expressed relative to the CF_3I^+ ion yield. $RIY_1[X^{m+}]$ indicates the contribution from dissociative single ionisation to a particular ions total ion yield. In the same manner, $RIY_2[X^{m+}]$ and $RIY_3[X^{m+}]$ indicate the contributions for dissociative double and triple ionization

respectively. Again, as will be discussed below, the requirement of detecting a threshold electron in order to detect an ion results in a very low yield of the parent ion. Such a low parent ion yield following ionization of CF_3I results in photoionization precursor-specific RIYs that are very much larger than the electron ionization precursor-specific PICSs reported in Chapter 6. Errors for these precursor-specific RIYs are the same as for the RIYs reported above; those that are above 15 have an approximate error of 10 %, those that lie between 1.5 and 15 have an approximate error of 40 %, and those that are below 1.5 have an approximate error of between 50 and 100 %.

The overall contribution to the total ion yield from single, double and triple ionization following photoionization of CF_3I is given in Figure 7.8 and Table D.3. Figure 7.8 shows that as the photon energy increases, the contribution from single ionization decreases. This decrease coincides with an increase in the contribution from double ionization, which becomes the greatest contribution to the total ion yield at 37 eV. Contributions from triple ionization, effectively zero within error at the lowest three photon energies, contributes 12% to the total ion yield at the highest photon energy investigated (37 eV). Such a large contribution to the total ion yield from double ionization highlights how the detection of only low energy electrons significantly disfavours the detection of ions formed from single ionization, as discussed below.

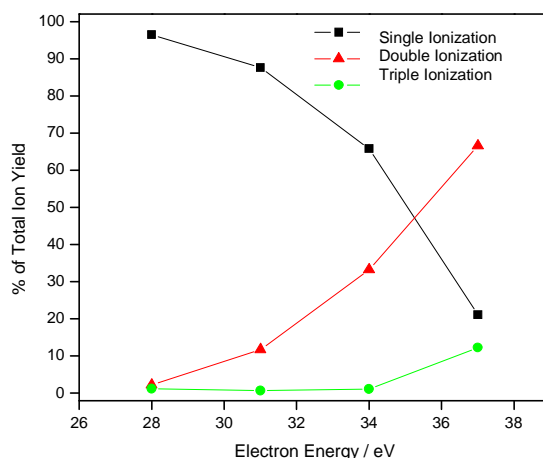


Figure 7.8: Contribution to the total ion yield from dissociative single, double and triple ion ionization, following photoionization of CF_3I .

7.5 Discussion

7.5.1 RIYs for the Formation of a Threshold Electron

As has been discussed above, only ionization events in which a threshold electron is detected (≤ 800 meV) will be recorded, although there will be a small contribution from ionization events forming high energy electrons whose initial velocities are directed towards the detector plate. This data collection technique results in recorded ion intensities that favour ions formed from double ionisation events, or single ionization events in which the ion formed has a large degree of internal energy, and/or resulted from a large degree of fragmentation of the parent ion; only in these events is it possible to form a threshold electron. For example, at all photon energies investigated, the parent ion yield is very low. The ionization energy of CF_3I^+ is 10.3 eV.¹⁷ Therefore, even at the lowest photon energy used (28 eV), in order to form a CF_3I^+ ion with an electron with a translational energy of less than 800 meV, the parent ion must have over 17.6 eV of internal energy. Such highly excited states of the parent ion are very likely to dissociate into an ionic fragment and an excited neutral fragment, which may go on to autoionize and form a second ion fragment. It is likely that only low lying electronic states of the parent cation are non-dissociative, and in order to form such a low lying state the outgoing electron must have considerable energy. This means that only small number of the parent ions formed will be detected; those that form high energy electrons whose initial velocity is directed towards the detector plate. It is due to this data collection technique that the apparent contribution to the total ion yield from double ionization is so high at all photon energies investigated (Figure 7.8).

The detection of only low energy electrons also means that the RIYs reported in this Chapter are not directly comparable to previous photoionization measurements. However, this requirement of detection a threshold electron does allow some further interpretation of ionization events that are being detected. For ions formed by dissociative single ionization, we must be populating only a small subset of excited states of the CF_3I^+ monocation, as only by populating those that lie around the photon energy used will a threshold electron be produced. If the excited monocation states lying around the photon energy investigated were known, branching ratios for how these monocation states decay to form a single ion and other neutral products could be produced. However, it is likely that many such highly excited states of the monocation lie very close together, making identification of which state is being accessed

problematic. For double ionization processes, in which the energy is shared between the two outgoing electrons, less can be said about what electronic states of the dication are being accessed, as the energy of the second electron is unknown.

7.5.2 Dissociation of CF_3I^{2+} and CF_3I^{3+}

As described in Section 3.4, the peak shapes in the pairs spectra can be used, in principle, to determine the mechanism of the dication and trication dissociation. This is done by examining the gradient of the peak in the pairs spectra, which yields the correlation of the fragment ions momenta, and comparing it to a theoretically calculated peak gradient.^{21,22} For example, two-body break ups, where the momenta of the ions are equal and opposite, result in a peak gradient of -1 . However, further fragmentation of one of the primary fragments will, if there is only a small energy release in the secondary decay, result in a reduction in the magnitude of the momentum of the ion along the spectrometer axis and a peak slope which can be used to identify the secondary decay pathway.^{22,23} However, for several of the ion pairs observed in the pairs spectra, we were unable to determine a dissociation pathway. This was either due to there being insufficient counts in a particular pairs channel to determine an accurate peak gradient, or to difficulties in obtaining the dissociation pathway as several possibilities resulted in similar calculated gradients. For the ion pairs for which peak gradients have been investigated, the observed peak gradients were taken from the pairs spectra obtained at a photon energy of 37 eV.

For the ion pair $\text{I}^+ + \text{CF}_3^+$, we observe a peak gradient of -1.02 ± 0.02 , in good agreement with the calculated gradient of -1 required for momentum conservation for a two-body break up. For the ion pair $\text{CF}_3^+ + \text{I}^{2+}$, another two body break up, we observed a peak gradient of -0.49 ± 0.02 . This is also in good agreement with the calculated gradient of -0.5 required for momentum conservation for a two-body break up, in which the ion arriving first is doubly charged.

For the ion pair $\text{I}^+ + \text{CF}_2^+$, a three body dissociation in which a neutral F must also be formed, we observe a peak gradient of -1.01 ± 0.05 . This gradient is consistent with a dissociation pathway in which following photoionization a neutral F fragment is first ejected, forming CF_2I^{2+} . This CF_2I^{2+} species then undergoes a two-body break up to form the $\text{I}^+ + \text{CF}_2^+$ ion pair, and give a calculated gradient of exactly -1 . The same dissociation pathway has been reported by Eland *et. al.*⁷ following photoionization of CF_3I using 40.8 eV photons.

For the ion pair $I^+ + CF^+$, for which either a neutral F_2 or two neutral F fragments must also be formed, a peak gradient of -1.05 ± 0.05 is observed. This peak gradient is again consistent with a dissociation pathway in which one (F_2) or two (2F) neutral fragments are first ejected following photoionization, to form CFI^{2+} , which then undergoes a two-body decay to form the $I^+ + CF^+$ ion pair and give a calculated gradient of exactly -1 . This dissociation pathway is inconsistent with that reported by Eland *et al.*⁷ recorded at a photon energy of 40.8 eV, in which a peak gradient of -1.38 ± 0.05 is observed. Such a peak gradient suggests secondary dissociation from another singly charged ion, suggested to be CF_2^+ . This discrepancy could be the result of the different photon energies used in the two studies, accessing different electronic states of the CF_3I cation.

7.6 Further Work

The results presented in this Chapter demonstrate the viability of determining photoionization ion yields using the iPEPICO endstation on the VUV beam line at the SLS. However, there is considerable scope for improvement of both the experimental setup, allowing the collection of appearance energies and flux normalised ion yields, and the value of the collected data, by reducing the errors and uncertainties in our results. Most importantly, as the ionization yields produced so far are only for events forming a threshold photoelectron, they do not give a full picture of the photoionization process, and cannot be compared with other photoionization measurements.

Firstly, to increase the accuracy in our determination of the ion detection efficiency f_i , experiments on the photoionization of argon or helium could be carried out. Together with singles and coincidence mass spectra obtained following an experimental run, data on the true number of electron-ion coincidences C_{ie} , the total electron counts R_e and the total ion count R_i is also collected. These values can be expressed in terms of the total number of ionization events $IE\nu$, and the electron and ion detection efficiencies, $f_e(E)$ and f_i respectively, as shown in Equations 7.8 – 7.11. A value for the ion detection efficiency can then be found by rearranging equations 7.8 and 7.10, giving equation 7.11. By recording photoionization spectra of argon or helium as a function of energy, we would also be able to determine whether f_i varies with photon energy. Using this method, a value for the electron detection efficiency could also be determined.

$$C_{ie} = IEv \times f_e(E) \times f_i \quad (7.8)$$

$$R_e = IEv \times f_e(E) \quad (7.9)$$

$$R_i = IEv \times f_i \quad (7.10)$$

$$f_i = C_{ie} / R_e \quad (7.11)$$

A second improvement, to increase the confidence in the results presented above, would be to ensure that no contamination from higher order light is present in the photon beam. Although our results suggest that no such contamination is present, the possibility of higher order light remains. By using an aluminium filter, light above an energy of 40 eV would be blocked from the photon beam²⁴. This would allow us to categorically state that there is no contamination from higher order light.

In the preliminary results presented above, photoionization spectra of CF₃I were taken as a function of photon energy, at energy intervals of 3 eV. In order to determine accurate appearance energies, spectra would need to be collected at much smaller energy intervals, such as 0.1 eV. However as the RIYs reported here are presented relative to the yield of the parent ion CF₃I⁺, small variations in the yield of the parent ion could result in large fluctuations in other fragment and ion pair cross-sections. A possible way of removing these fluctuations would be to present ion yields relative to the photon flux. By installing a photon multiplier tube at the end of the photon beam, the photon flux could be monitored during an experimental run and as a function of photon energy. This would allow us to determine ion and ion pair yields relative to photon flux, as a function of energy. Onsets and peaks observed in these flux normalised yields could then be safely reported as true features, rather than oscillations caused by varying photon flux, or variations in the yield of the parent ion.

Finally, as the ionization yields produced so far are only for events forming a threshold photoelectron, they do not give a full picture of the photoionization process, and cannot be compared with other photoionization measurements. By increasing the electric field in the source region of the iPEPICO endstation, it would be possible to collect all the electrons formed, allowing all photoionization processes to be observed. In addition, an increase in the electric field should also improve the ion detection efficiency, particularly with respect to energetic ions. However, a possible problem

with an increase in the electric field would be the reduction in ion flight times, resulting in a reduction in the mass resolution of the singles and pairs spectra. Further experiments would be needed to investigate an appropriate field strength that does not result in poor mass resolution, but does collect electrons of sufficiently high energy for the photon energy under investigation.

7.7 Conclusions

Relative ion yields have been measured for the formation of all positive ion fragments following photoionization of CF_3I , using the iPEPICO end station of the VUV beamline at the SLS. These RIYs are for ionization events in which a threshold electron is formed, and are reported relative to the CF_3I^+ yield, at photon energies between 28 and 37 eV. By determining a value of the ion detection efficiency of the iPEPICO endstation, precursor-specific RIYs were also derived. To the best of our knowledge, this is the first time that both RIYs and precursor-specific relative RIYs have been derived for the photoionization of CF_3I . These RIYs demonstrate the viability of using the iPEPICO endstation in the investigation of multiple ionization processes; however as they are only for ionization events in which a threshold electron is formed, they do not provide the full photoionization picture, and cannot be compared with other experimental photoionization measurements. By increasing the electric field in the source region of the iPEPICO endstation, it should be possible to collect all photoelectrons formed, allowing the full photoionization process to be observed.

7.8 References

- 1 J. C. Yang, M. R. Nyden, and S. L. Manzello, in *Halon Optics Technical Working Conference* (NIST, 2001), pp. 64.
- 2 R. A. Levy, V. B. Zaitsev, K. Aryusook, C. Ravindranath, V. Sigal, S. Kesari, D. Rufin, J. Sees, and L. Hall, *J. Mat. Res.* **13**, 2643 (1998).
- 3 F. Fracassi and R. d'Agostino, *J. Vac. Sci. Technol. B* **16**, 1867 (1998).
- 4 *Fire Suppression System Performance of Alternative Agents in Aircraft Engine and Dry Bay Laboratory Simulations*, Vol. 1, edited by R. G. Gann (NIST, Gaithersburg, 1995).
- 5 L. G. Christophorou and J. K. Olthoff, *J. Phys. Chem. Ref. Data* **29**, 553 (2000).
- 6 S. Solomon, J. B. Burkholder, A. R. Ravishankara, and R. R. Garcia, *J. Geophys. Res.-Atmos.* **99**, 20929 (1994).

- 7 J. H. D. Eland, R. Feifel, and M. Hochlaf, *J. Phys. Chem.* **128**, 234303 (2008).
- 8 P. Downie and I. Powis, *Faraday Discuss.* **115**, 113 (2000).
- 9 P. Downie and I. Powis, *J. Chem. Phys.* **1111**, 4535 (1999).
- 10 P. Downie and I. Powis, *Phys. Rev. Lett.* **82**, 2864 (1999).
- 11 I. Powis, O. Dutuit, M. Richard-Viard, and P. M. Guyon, *J. Chem. Phys.* **92**, 1643 (1990).
- 12 K. G. Low, P. D. Hampton, and I. Powis, *Chem. Phys.* **100**, 401 (1985).
- 13 A. Pilcher-Clayton and J. H. D. Eland, *J. Electron. Spectrosc.* **142**, 313 (2005).
- 14 M. Johnson, A. Bodi, L. Schulz, and T. Gerber, *Nucl. Instrum. Methods Phys. Res., Sect. A* **610**, 597 (2009).
- 15 A. Bodi, M. Johnson, T. Gerber, Z. Gengeliczki, and T. Bear, *Rev. Sci. Instrum.* **80**, 034101 (2009).
- 16 A. Bodi, B. Sztaray, T. Baer, M. Johnson, and T. Gerber, *Rev. Sci. Instrum.* **78**, 084102 (2007).
- 17 *NIST Chemical WebBook; NIST Standard Reference Database Number 69*, Vol., edited by P. J. Linstrom and W. G. Mallard (National Institute of Standards and Technology, Gaithersburg MD, 20899, 2008).
- 18 G. A. Garcia, P. M. Guyon, and I. Powis, *J. Chem. Phys. A* **105**, 8296 (2001).
- 19 R. L. Asher and B. Ruscic, *J. Chem. Phys.* **106**, 210 (1997).
- 20 K. K. Irikura, *J. Am. Chem. Soc.* **121**, 7689 (1999).
- 21 J. H. D. Eland, *Chem. Phys. Lett.* **203**, 353 (1993).
- 22 J. H. D. Eland, *Mol. Phys.* **61**, 725 (1987).
- 23 D. M. Curtis and J. H. D. Eland, *Int. J. Mass Spectrom. Ion Processes* **63**, 241 (1985).
- 24 T. Masuoka, *Phys. Rev. A* **48**, 48 (1993).

Chapter 8 Reactions of I^{2+} with OCS

8.1 Introduction

Iodine is a minor constituent of the Earth's atmosphere, present in both the troposphere and stratosphere as a component of a range of organic and inorganic compounds.¹⁻⁶ A significant portion of this atmospheric iodine is from biological and geochemical marine processes producing organic iodine, which can be photo-oxidised to form soluble inorganic forms.¹ These iodine compounds have been shown to take part in a broad range of chemical reactions,^{1,3,5,7,8} and have a significant role in ozone destruction in both the troposphere and the stratosphere.^{1,6,8} Although there has been no direct detection of multiply charged iodine species in the atmosphere, in environments where monocations occur, dications may also be present, albeit in far lower abundances. Such multiply charged species would be expected to have a markedly different reactivity to their neutral or singly charged analogues. Previous investigations into the reactivity of multiply charged halogens appears to non-existent, with the current work possibly being the first.

Following initial investigations into the reactions of I^{2+} with a range of neutral molecules, this chapter presents further investigations into the reactions between I^{2+} and OCS, over a collision energy range of 2.2 – 6.2 eV in the centre-of-mass (COM) range. Following collisions between I^{2+} and OCS, several product ions are observed, resulting from both electron transfer reactions and bond-forming reactions. Before these results are presented, a brief introduction to dication-molecule reactions is given, followed by an outline of the experimental apparatus and the data analysis procedures used in the study of $I^{2+} + OCS$ collisions. Other available data on the reactivity of I^{2+} appears to be non-existent, as does any investigation into the reactivity of other multiply charged halogen species. Such a lack of data in the literature provides a clear motive for the investigations carried out in this chapter, and pave the way for further investigations involving the other halogens.

8.1.1 Bimolecular Reactivity of Gas Phase Dications

As has been discussed previously in Section 1.3.2, many molecular dications have one or more metastable electronic states, resulting in dications with lifetimes that can be well in excess of 1 s. Thus many molecular dications survive long enough to

take part in bimolecular reactions. In this section, a brief summary of the reactions that may occur between dications and neutral species are presented.

Following the interaction between dications and neutral species, three broad classes of reaction may occur: electron transfer, collision-induced fragmentation and bond-forming reactions.

8.1.1.1 Electron Transfer Reactions

By far the most common reaction to occur following dication-neutral interactions is single electron transfer (SET):



Equation 8.1 represents a non-dissociative SET reaction, however, if the monocation products are formed in dissociative electronic states they may fragment to form an ion-neutral pair.

SET reactions have been successfully understood using the Reaction Window model,⁹ which is based on the Landau-Zener theory^{10,11} of adiabatic transitions. This model is applied to dication-neutral collision systems by picturing the reactants as approaching each other on a potential-energy curve dominated by polarization attraction. The product potential, a purely repulsive potential dominated by electrostatic repulsion between the two monocations, crosses this reactant potential at some interspecies separation, the curve-crossing radii (Figure 8.1). The probability of an electron transfer occurring depends on the coupling between the product and reactant surfaces, which in turn depends on the crossing radii. This relates to the quantity δ , defined as the probability of remaining on a non-adiabatic potential energy surface as it makes an intersection with another surface. In the course of a collision, this intersection will be encountered twice. If the crossing occurs at a small interspecies separation, the interaction between the two surfaces is very large and the probability of the electron being transferred is very high, and so an electron is transferred on both passes through the intersection, resulting in no SET reaction. If the crossing is at a large interspecies separation, there is little probability of the electron tunnelling between the two reactants, and so again there is no SET reaction. Hence, the probability of a SET reaction occurring is maximised when $\delta = 0.5$. The ‘reaction window’ therefore describes a range of curve crossing points at which δ is close to 0.5, thus making a SET reaction likely to occur. The range of interspecies separations that fall into the reaction window

is around 3 – 6 Å. The reaction window may be described in terms of separation or exothermicity since the point of intersection between a dication-neutral potential energy surface and a monocation-monocation surface is determined largely by the asymptotic exothermicity, rather than the exact chemical identity of the species involved.

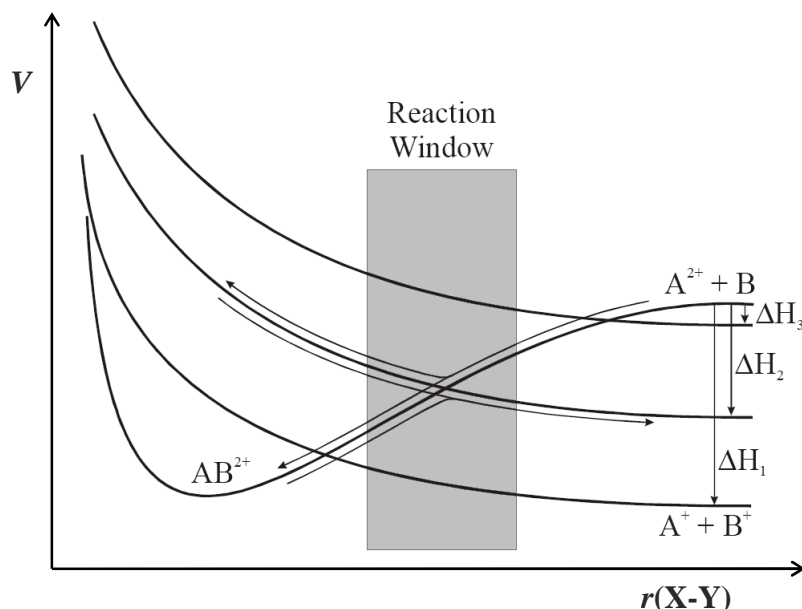


Figure 8.1: Diagram showing the interrelationship between species separation r and asymptotic exothermicity ΔH for SET reactions between a dication and a neutral species. The reaction window is a qualitative region for which SET is most efficient. Only intersections inside the reaction window have a significant probability of resulting in SET (i.e. ΔH_2), typically between 2 – 6 eV. Reproduced from Ref. [12].

Double electron transfer reactions (DET) occur when two electrons are transferred from the neutral species to the dication:



In principle there are three mechanism by which DET reactions can occur; two direct pathways, either concerted or sequential, or *via* a collision complex.¹³

The two direct pathways can again be well understood using the ‘Reaction Window’ model,⁹ based on Landau-Zener theory.^{10,11} Consider the DET reaction between a dication M^{2+} and a neutral AB (Figure 8.2). In the direct, concerted pathway, the two electrons are both transferred at the crossing of the $M^{2+} + AB$ and the $M + AB^{2+}$ potential energy curves (Figure 8.2a), in a concerted process. In this model, the only

differences in the forms of the product and reactant surfaces, beyond the short range repulsive interactions, are due to the differing polarisabilities of the respective neutral species. Therefore, for the curve crossing between the two potential surfaces to occur within the reaction window, the reactant and product asymptotes must lie close in energy, approximately within 1 eV of each other. The alternative direct pathway, involves sequential electron transfer *via* a repulsive $M^+ + AB^+$ potential, which links the attractive reactant and product potentials (Figure 8.2b). In this reaction pathway, the system first crosses from the $M^{2+} + AB$ potential to the $M^+ + AB^+$ potential, then crosses again to the $M + AB^{2+}$ potential. The relevant curve crossings in this sequential pathway will lie within the reaction window for a much greater range of exothermicities than for the concerted pathway. Therefore, if such a sequential pathway was occurring, DET reactions would be expected to be a common result of dication-neutral collisions, which is not the case. The relative scarcity of dication DET reactions therefore points to the concerted mechanism being the most effective direct mechanism.¹⁴

DET reactions between dications and neutral species may also occur *via* the formation of a collision complex:



Experiments in which the angular distribution of products following dication neutral reactions can be extracted, indicates that the majority of DET reactions do not proceed *via* complex formation.¹³ Therefore, any DET reactions observed following collisions between I^{2+} and OCS are assumed to proceed *via* the direct, concerted pathway.

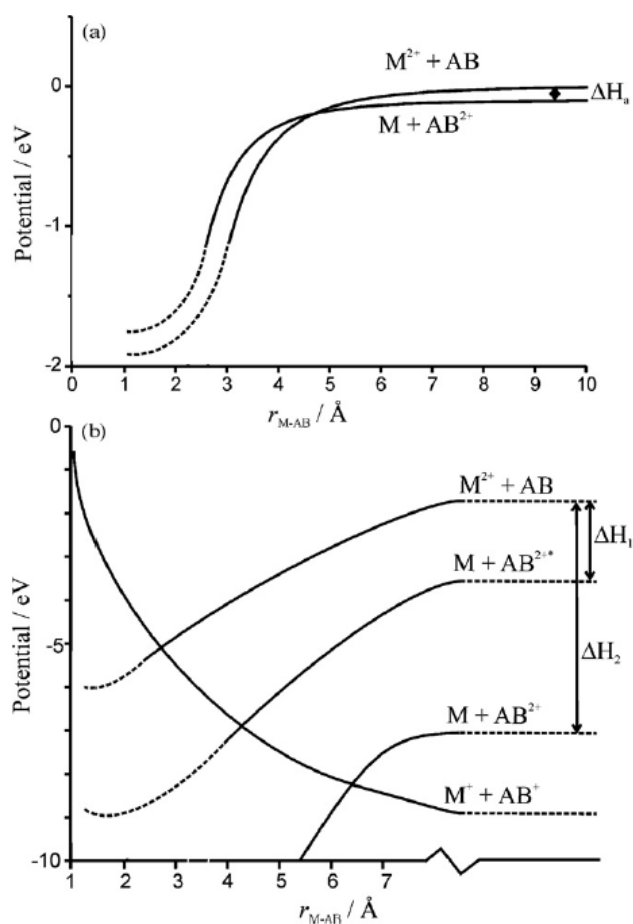


Figure 8.2: Schematic potential energy curves for a direct DET reaction between M^{2+} and AB, showing the concerted (a) and sequential (b) pathways. (a) ΔH_a indicates the small reaction enthalpy which is required for the curve crossing to lie in the reaction window, for the concerted mechanism. (b) ΔH_1 and ΔH_2 schematically indicate the limiting reaction exothermicities for which this pair of curve crossings will lie in the reaction window, a markedly larger range of exothermicities than for the concerted mechanism illustrated in (a). Reproduced from Ref. [13].

8.1.1.2 Collision-Induced Fragmentation

Collision-induced fragmentation reactions occur when some of the energy of a collision is transferred to the dication, exciting it to a pre-dissociative state, while the neutral partner remains intact. The reverse is of course possible, however the neutral fragments formed would not be detected. In the collision system under investigation in this chapter, $I^{2+} + OCS$, collision-induced fragmentation of the I^{2+} is of course not possible, and so this reaction is not discussed further.

8.1.1.3 Bond-Forming Reactions

The final class of reaction that may occur following dication-neutral collisions are bond-forming reactions, in which a new chemical bond is observed. Such bond-forming reactions are generally much weaker than other reaction channels. Two possible types of bond-forming reaction are possible, charge separating and charge retaining (Equations 8.6 and 8.7 respectively):



Most bond-forming reactions are thought to proceed *via* a collision complex because of the broad angular distribution associated with the products.¹⁵⁻¹⁸ However the simplest of bond-forming reactions, hydride transfer to the dication or proton transfer to the neutral, are often considered as ‘heavy’ electron transfer reactions, and treated with Landau-Zener theory.^{10,11,19} However, as hydride or proton transfers are not possible in the collision system investigated in this chapter, these two reactions are not discussed further.

8.2 Experimental

8.2.1 Instrumentation

The experiments reported in this Chapter were carried out using the crossed-beam time-of-flight mass spectrometer¹⁹⁻²¹ shown in Figure 8.3. The dications required for an experiment are generated by electron ionization of a suitable precursor gas. This is done by perpendicularly intersecting an electron beam with a jet of the precursor gas. The electron beam is run at a constant electron current, as measured by an electron trap, by application of a variable current to a tungsten filament. The energy of the electron beam may however be adjusted to between 100 and 200 eV in order to maximise the ion yield. A narrow aperture between the filament and the ionization region restricts the diameter of the electron beam to approximately 2mm; this ensures that ionization only occurs in a very small volume within the source block. Any ions formed will therefore experience the same electric field and so be accelerated to the same kinetic energy as they exit the ion source. A series of ion optics directly after the source block collimates the ion beam. The ion optics also further accelerate the ions so that they reach the

reaction chamber as soon as possible, minimising the amount of unimolecular decay of metastable species. As the kinetic energy spread of the ion beam is very small, selecting the ions by velocity effectively selects them by mass. The velocity filter, a commercial Colutron model,²² is based on the Wien velocity filter²³⁻²⁵ and employs perpendicular magnetic (B) and electrostatic (E) fields to deflect ions away from the filter end. A particle of charge q moving with a velocity v through a magnetic field will experience a force F_B , given by Equation 8.6. Similarly, the same particle moving through an electric field will experience a force F_E , given by Equation 8.7.

$$F_B = qBv \quad (8.6)$$

$$F_E = qE \quad (8.7)$$

The magnetic and electrostatic fields are perpendicular so that F_B and F_E act in opposing directions. This means that an ion can only pass through the velocity filter undeflected if the two forces are equal in magnitude, i.e. $F_B = F_E$, resulting in the condition for the velocity:

$$v = E/B \quad (8.8)$$

As previously mentioned, all the ions will reach the velocity filter with the same kinetic energy KE , depending on the accelerating potential V :

$$KE = qV \quad (8.9)$$

Therefore:

$$\sqrt{2KE/m} = E/B \quad (8.10)$$

From Equation 8.10 it can be seen how for fixed values of B , E , and KE , the trajectory of a particle through the velocity filter depends solely upon its mass. Mass selection can therefore be achieved by simply adjusting B , E , or KE while the others are kept constant. In the current experiment, the accelerating potential V , and thus the KE , and the magnetic field are kept constant, and mass selection is achieved by adjusting the electric field:

$$E = B\sqrt{2KE/m} \quad (8.11)$$

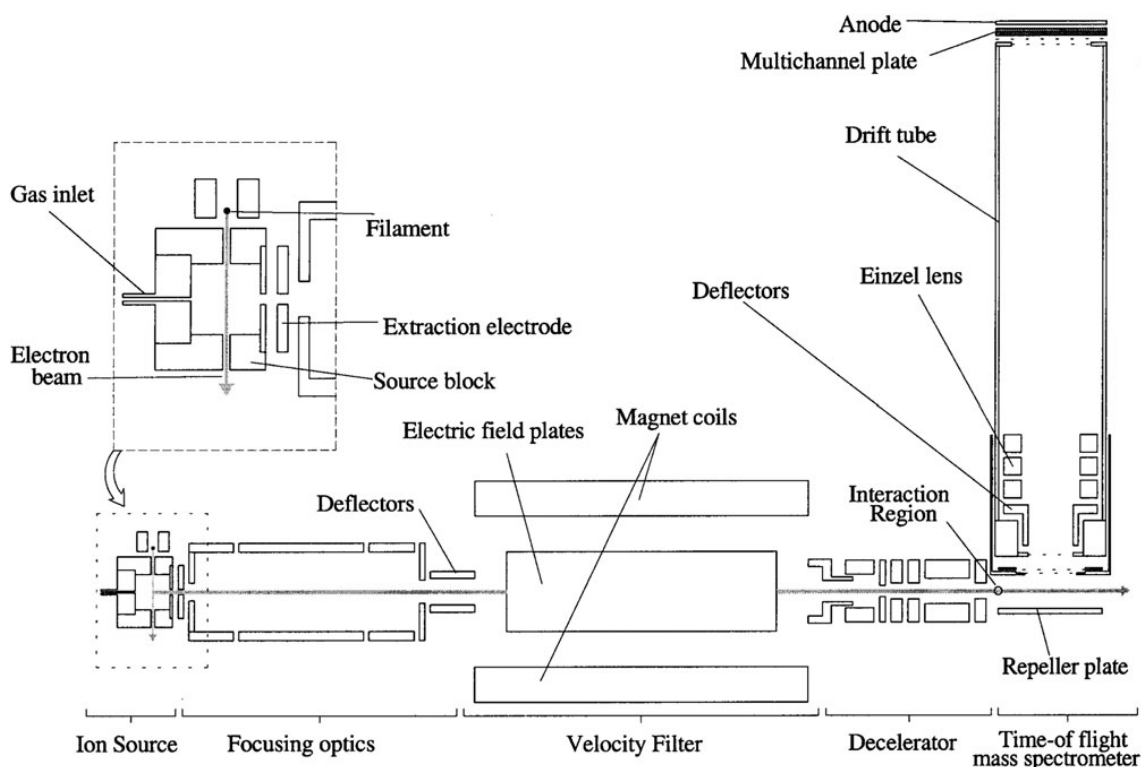


Figure 8.3: Schematic diagram of the crossed-beam time-of-flight mass spectrometer experimental apparatus. Reproduced from Ref. [20].

Following mass selection, the ion beam is decelerated prior to entering the interaction region. This is done in order to increase the interaction time between the reactant particles in an attempt to encourage bond-forming reactions. Retarding electric fields decelerate the ion beam to the desired collision energy, usually between 4 – 20 eV (in the laboratory frame). However, as the fields only retard the on-axis component of the velocity, the off-axis components becomes proportionally larger, which can cause a significant divergence of the ion beam. Therefore, following the decelerating optics, the ion beam is refocused by an Einzel lens.

After deceleration, the collimated, mass selected ion beam enters the interaction region, where it intersects an effusive jet of the neutral collision partner. The interaction region doubles as the source of a Wiley-McLaren²⁶ type TOFMS. A schematic layout of the TOFMS is shown in Figure 8.4, and the electrode voltages and geometrical parameters of the mass spectrometer are given in Table 8.1. Application of 400 V to the repeller plate extracts any ions present in the source region, both products and unreacted dications, into a second accelerating field and subsequently into the field free drift tube and finally onto a multichannel plate (MCP) detector. The repeller plate is pulsed at a frequency of 50 kHz for a duration of 20 μ s, equivalent to 10 μ s on and 10 μ s off.

Although the ion source is continuous, application of the repeller plate voltage deflects the beam, so that only ions already in the source region when the pulse begins are extracted. In order to prevent stray ions from entering the acceleration region before the repeller plate pulse, a small positive bias is applied to a sandwich grid that is positioned just before the extraction electrode. Each repeller plate pulse is triggered by a pulse generator, which simultaneously starts a multi-hit time-to-digital converter (TDC), and starts the timing cycle. Ion signals from the MCP are amplified, discriminated and passed to the TDC. The ion arrival times measured are passed to a PC, where each count is assigned to a channel depending on its flight time.

Table 8.1: Experimental parameters employed under normal operating conditions.

Parameter	Value	Parameter	Value
Neutral target pressure	3×10^{-6} Torr	MCP voltage, front plate	- 2400 V
Repeller plate frequency	50 kHz	MCP voltage, back plate	- 40 V
Repeller plate voltage OFF	0 V	Source length (2S)	20 mm
Repeller plate voltage ON	400 V	Acceleration length (A)	10 mm
Extractor grid voltage	0 V	Drift tube length (D)	280 mm
Drift tube voltage	-1225 V	MCP detector diameter	35 mm

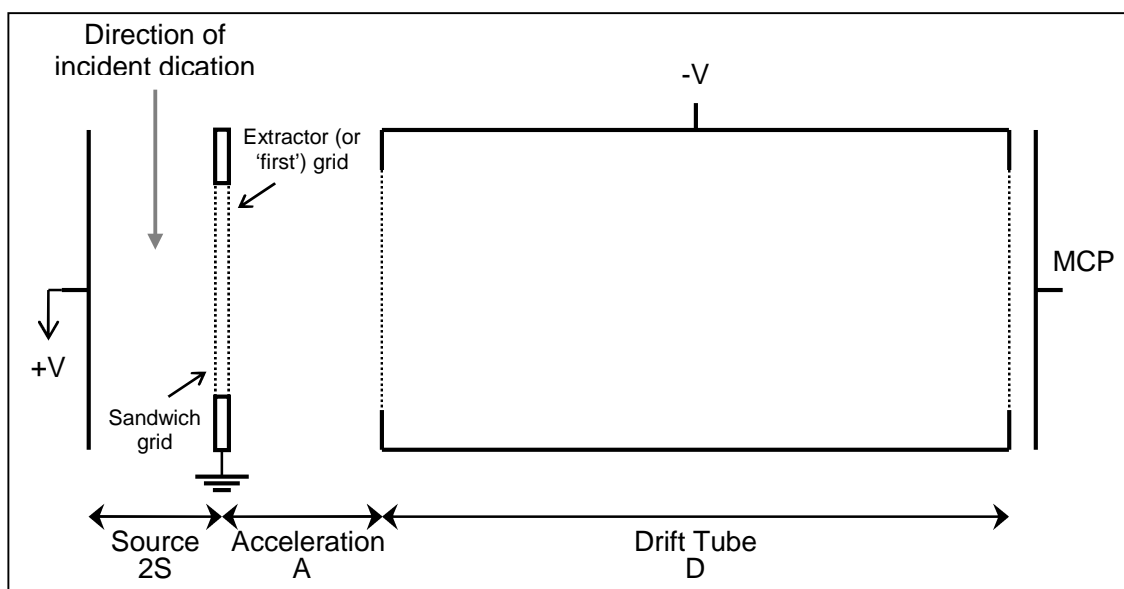


Figure 8.4: Schematic layout of the time-of-flight mass spectrometer.

8.2.2 Experimental Conditions

For all experiments, the OCS gas used was a commercial sample of $\geq 99\%$ purity. In order to produce I^{2+} , iodine vapour (I_2) was introduced to the ion source under its own vapour pressure from a sample of solid iodine, of purity $\geq 99\%$. Typical pressures of I_2 in the ion source and OCS in the interaction region were of the order of 8×10^{-6} Torr and 3×10^{-6} Torr respectively. This pressure of OCS was chosen to ensure that single-collision conditions exist in the interaction region.²⁷ This means that any products of a collision will not be able to react with another neutral molecule. This was confirmed by preliminary experiments in which, at the pressures at which we operate, the intensity of a product ion was shown to have a linear relationship to the pressure of the neutral reactant; if multiple collisions were occurring there would have been a power relationship.²⁷

The time window monitored was set to 9500 ns, corresponding to a maximum m/z of 190, with 2 ns per channel. Spectra were recorded for between 8000 and 10000 cycles, with each cycle comprising 512 kb of data. Typical run times were between 2 and 3 hours.

8.3 Data Analysis

8.3.1 Collision and Background Mass Spectra

Using the experimental apparatus described above, mass spectra were recorded following interactions between a beam of I^{2+} with the neutral reactant OCS at energies between 7.0 and 19.3 eV (in the laboratory frame). In addition background spectra were also recorded in the absence of the neutral reactant. These background spectra are used, in general, to correct the collision spectra for ion signals arising from the unimolecular dissociation of dications in the beam and collisions with residual gas molecules, and impurities in the beam.^{9,28,29} Spectra in which the collision gas is present are called 'collision' or 'gas on' spectra, while those with no collision gas present are called 'background' or 'gas off' spectra. A typical collision spectrum can be seen in Figure 8.5, together with background spectrum.

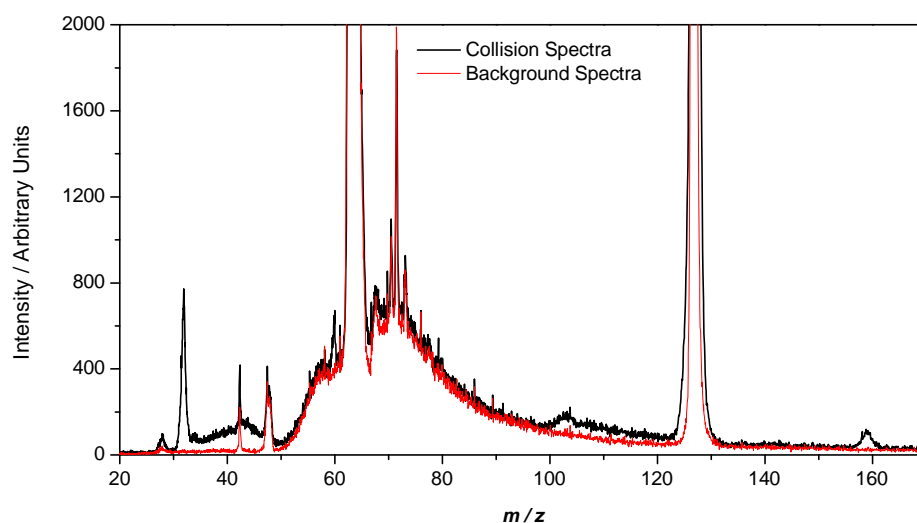


Figure 8.5: A typical collision spectrum (black line) with the collision gas on and a background spectrum (red line) with the collision gas off, for the $I^{2+} + OCS$ collision system.

Ion peaks observed in the mass spectra are identified manually and assigned a ‘start’ and a ‘stop’ channel. The number of counts in the peak is then the sum of the counts in the channels between, and including, the start and stop channels. As with the singles mass spectra in Chapters 4 – 7, a correction is made to the counts in each peak to account for the non-zero baseline which arises due to stray ions. This is done by assessing the level of baseline counts (counts per channel) in a nearby region of the spectrum where no peaks are observed. Using the number of channels each ion peak spans, this baseline level is then scaled to give the number of baseline counts contributing to the peak, and is subtracted from the raw intensity to give the ‘true’ number of counts, also known as the ‘true’ ion intensity I^{TRUE} . As the ‘true’ number of counts in an ion peak in a background spectrum indicate the signal arising from residual background processes, the difference between the ‘true’ number of counts in an ion peak in a reaction spectrum and in a background spectrum is the number of counts of the particular ion resulting from bimolecular reactions between the dication and the neutral gas. In order to provide consistency between different spectra, the values of I^{TRUE} for both the collision and background spectra are normalized relative to the intensity of the dication peak to produce ‘relative ion intensities’ RIs :

$$RII[X^{m+}] = \frac{I^{TRUE}[X^{m+}]}{I^{TRUE}[Dication]} \quad (8.12)$$

The RII for a peak in the background spectra is then subtracted from the RII for a peak in the collision spectra, to produce the ‘observed relative ion intensity’ RII^{OBS} :

$$RII^{OBS} [X^{m+}] = RII_{Collision} [X^{m+}] - RII_{Background} [X^{m+}] \quad (8.13)$$

8.3.2 The Centre-of-Mass Frame

When describing the experimental setup and conditions employed in the investigation of dication neutral reactions, it is most natural and convenient to use the laboratory (LAB) frame as the frame of reference. However, in order to understand the physics of a collision, it is more informative and mathematically straightforward to use the centre-of-mass (COM) frame as the frame of reference.³⁰ For example, it is easy to imagine that the translational energy available for reactive processes following a collision, is the LAB frame collision energy, when in fact a portion of this energy must conserve the linear momentum of the COM of the system relative to the LAB frame. However, in the COM frame linear momentum is always zero, thus all of the kinetic energy of the collision is available for reactive processes. The COM collision energy E_{COM} is related to the kinetic energy of the dication in the LAB frame E_{LAB} by:

$$E_{COM} = \frac{\mu}{m_i} E_{LAB} \quad (8.14)$$

In Equation 8.14, μ is the reduced mass of the collision system and m_i is the mass of the ion. Equation 8.14 is only true when the LAB frame velocity of the dication is significantly greater than that of the neutral collision partner, as is the case for the experiments presented in this Chapter.

8.4 Results

Mass spectra were recorded, as described above, at collision energies from 7.0 to 19.3 eV in the LAB frame, corresponding to 2.2 eV to 6.2 eV in the COM frame. Comparison of the reaction and background mass spectra (Figures 8.5 and 8.6) clearly indicates the formation of CO^+ , S^+ , OCS^+ , I^+ , and IS^+ . Furthermore, small signals located at mass to charge ratios of 30, 44 and 143 indicate the presence of OCS^{2+} , SC^+ and IO^+ respectively. The small size of these ion peaks makes reliable quantification difficult, particularly in the case of the IO^+ peak, which due to its position in the mass spectrum (high mass) is very broad, appearing as a small rise in the baseline. The

largest peak in the spectra at $m/z = 63.5$ can be attributed to I^{2+} (Figure 8.6b) which shows that most of the ion beam does not react, as is typical of the single collision conditions employed in this study. It should be noted that no C^+ or O^+ ions are detected following the bimolecular reaction between I^{2+} and OCS, despite the presence of other dissociative SET channels.

Following $I^{2+} + OCS$ collisions, the reaction channels producing the observed product ions can be split into two broad classes. Firstly, the IO^+ and IS^+ product ions must be formed by bond forming reactions (Equations 8.15 and 8.16):

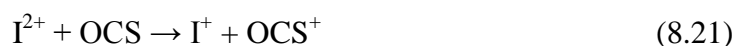
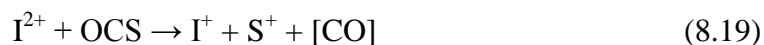


The square brackets in Equations 8.17 and indicate that the other ionic product cannot be unambiguously identified using simple mass spectrometry. This is because two possible partner ions, S^+ (with a neutral C) or SC^+ , are observed in the mass spectra, and may be formed by this chemical reaction, or by other processes such as dissociative electron transfer. However, as discussed further below, models of the possible SET reactions following $I^{2+} + OCS$ suggest that the monocation partner formed in Equation 8.15 is in fact SC^+ .

The second class of reactions producing the observed product ions are electron transfer reactions. For the OCS^{2+} product ion, the only possible reaction channel is DET (Equation 8.17):



The remaining product ions, CO^+ , S^+ , SC^+ , OCS^+ and I^+ , may all be formed by SET reactions (Equations 8.18 – 8.21):



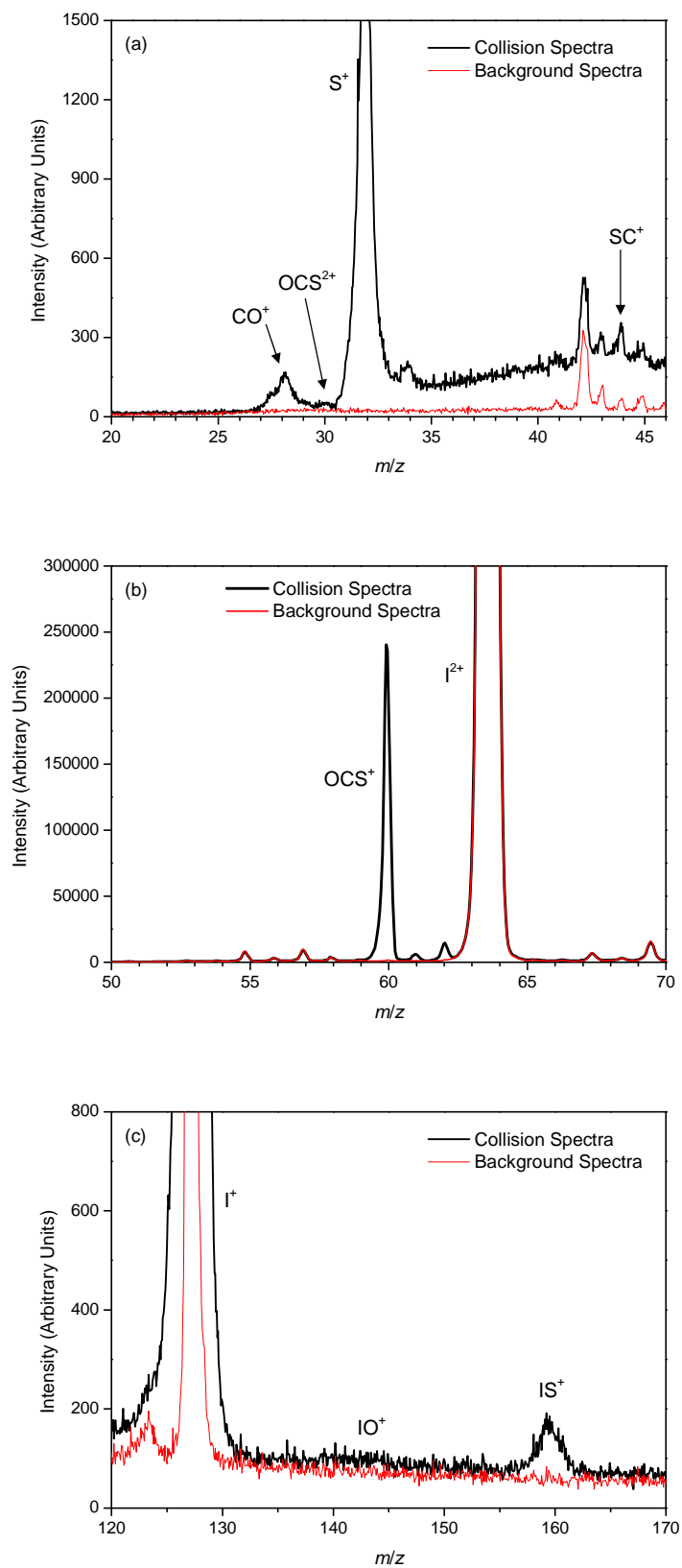


Figure 8.6: Representative collision (black line) and background (red line) spectra for the $\text{I}^{2+} + \text{OCS}$ collision system, showing mass to charge ratio ranges of (a) 20 – 46, (b) 50 – 70 and (c) 120 – 170.

Of these four reactions, only the non-dissociative SET reaction (Equation 8.21) can be unambiguously assigned as a SET reaction, as it is possible that the product ions formed in Equations 8.18 – 8.20 are formed from other reactions. However, given that following dication-neutral interactions, SET reactions usually give rise to the most intense product ion signals^{16,20,21}, with DET and bond-forming reactions typically an order of magnitude or more less intense, it is likely that the majority of the CO^+ , S^+ and CS^+ ion signals are the result of dissociative SET reactions. Despite the usual dominance of SET reactions to a product ions intensity, as discussed in detail below, models of the SET reactions following $I^{2+} + OCS$ collisions suggest that for the CO^+ and SC^+ product ions, there is no contribution from dissociative SET reactions, with these ions being formed solely from the bond-forming reactions shown in Equations 8.15 and 8.16.

For the product ions observed following $I^{2+} + OCS$ collisions, the values of RII^{OBS} obtained are displayed in Figure 8.7 as a function of collision energy, and are given numerically in Table 8.2. As described above, as these RII^{OBS} values have not been corrected for geometric sampling restrictions in the TOF source, and thus the values can only be compared qualitatively, not quantitatively.

Table 8.2: Product ratios RII^{OBS} for product ions observed following $I^{2+} + OCS$ collisions. The values in parenthesis indicate one standard deviation in the last figure.

E_{LAB} / eV	E_{COM} / eV	$RII^{OBS} CO^+ 10^4$	$RII^{OBS} OCS^{2+} 10^5$	$RII^{OBS} S^+ 10^3$	$RII^{OBS} SC^+ 10^5$
7.0	2.2	0.56(5)	0.46(5)	0.65(5)	1.10(21)
10.1	3.3	0.86(8)	0.80(12)	1.02(7)	0.71(36)
13.3	4.3	1.07(7)	0.78(7)	1.28(7)	1.07(19)
16.3	5.2	1.08(4)	0.93(16)	1.37(3)	
19.3	6.2	1.24(10)	1.23(10)	1.48(11)	1.39(15)
E_{LAB} / eV	E_{COM} / eV	$RII^{OBS} OCS^+ 10^2$	$RII^{OBS} I^+ 10^3$	$RII^{OBS} IO^+ 10^6$	$RII^{OBS} IS^+ 10^5$
7.0	2.2	0.02(1)	3.63(89)	4.1(22)	6.96(64)
10.1	3.3	1.81(21)	4.02(70)	8.3(15)	8.56(38)
13.3	4.3	3.46(31)	4.56(39)	9.6(18)	7.98(69)
16.3	5.2	4.38(115)	3.53(14)	7.1(21)	5.71(61)
19.3	6.2	2.38(147)	3.33(40)	4.4(08)	4.39(54)

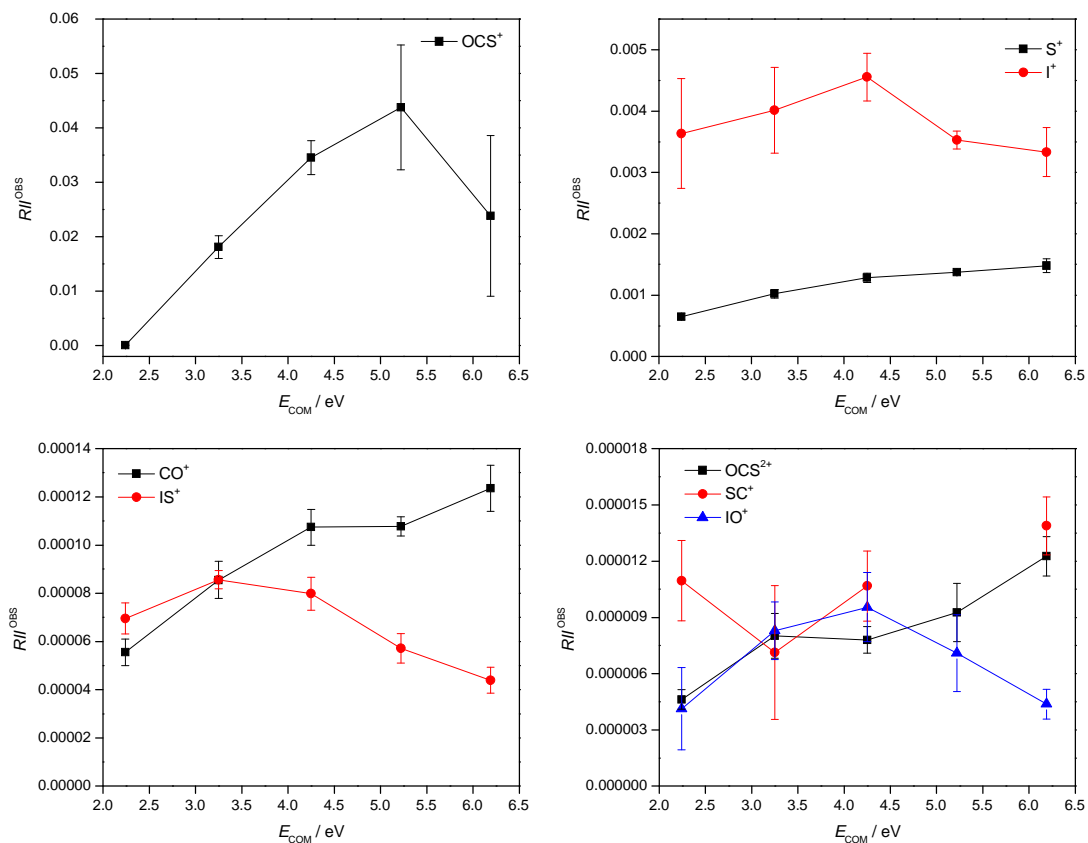


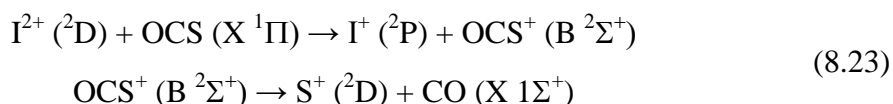
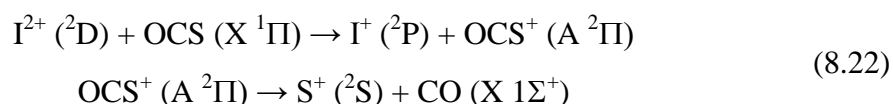
Figure 8.7: Product ratios R_{OBS} for product ions observed following $I^{2+} + OCS$ collisions. Error bars show one standard deviation of four separate determinations.

8.5 Discussion

8.5.1 Single Electron Transfer Reactions

As described above in Section 8.1.1, the ‘reaction window’ model describes how for a SET reaction to be efficient, the reaction exothermicity is expected to be in the range of 2 – 6 eV. Dissociative SET reactions are also likely to proceed *via* a two step process,^{13,31} in which OCS^+ is first formed in a dissociative electronic state, and then goes on to fragment to give the observed ion fragment (with one or more neutral fragments). An energy level diagram giving the enthalpies³²⁻³⁴ of possible SET reactions following $I^{2+} + OCS$ collisions is shown in Figure 8.8. As can be seen from Figure 8.8, the reaction exothermicity to form $I^+ + OCS^+$ in their ground states, from ground state I^{2+} , lies outside of the reaction window range. If the OCS^+ is formed in either of its first two excited states ($A^2\Pi$ or $B^2\Sigma^+$), again with ground state I^+ and from ground state I^{2+} , the reaction exothermicities again lie outside of the reaction window

range. However, the reaction exothermicities for forming ground state I^+ with OCS^+ in either of its first two excited states, from excited I^{2+} (Equations 8.22 and 8.23), do lie within the reaction window range, and therefore have a significant probability of occurring. These two SET reactions (Equations 8.22 and 8.23) would explain the observed S^+ ion intensity, as both the A and B states of OCS^+ are dissociative, forming ground state CO and S^+ .^{35,36} The identification of these two dissociative SET channel from an excited state of I^{2+} is reasonable, as the 2D state of I^{2+} is likely to be relatively long-lived, as relaxation to the ground 4S state is forbidden on the grounds of both spin and orbit quantum number. Therefore it can be concluded that the majority of the S^+ product ion intensity results from dissociative SET reactions involving the first excited state of I^{2+} .



However, any I^{2+} formed in the 2P state following electron ionization of iodine would be expected to radiatively relax to the 2D state, a transition allowed by both spin and orbital angular momentum selection rules, within the time the dications take to traverse the velocity filter and enter the interaction region.

As a significant OCS^+ ion intensity is observed following reactions of I^{2+} with OCS, a SET reaction must also be occurring that produces the ground $X ^2\Pi$ state of OCS^+ , which is bound. As can be seen from Figure 8.10, the reaction exothermicity to form $OCS^+ (X ^2\Pi)$ from ground state I^{2+} does lie within the reaction window range if it is formed with excited I^+ . This suggest that following $I^{2+} + OCS$ collisions significant amounts of excited I^+ is also formed:



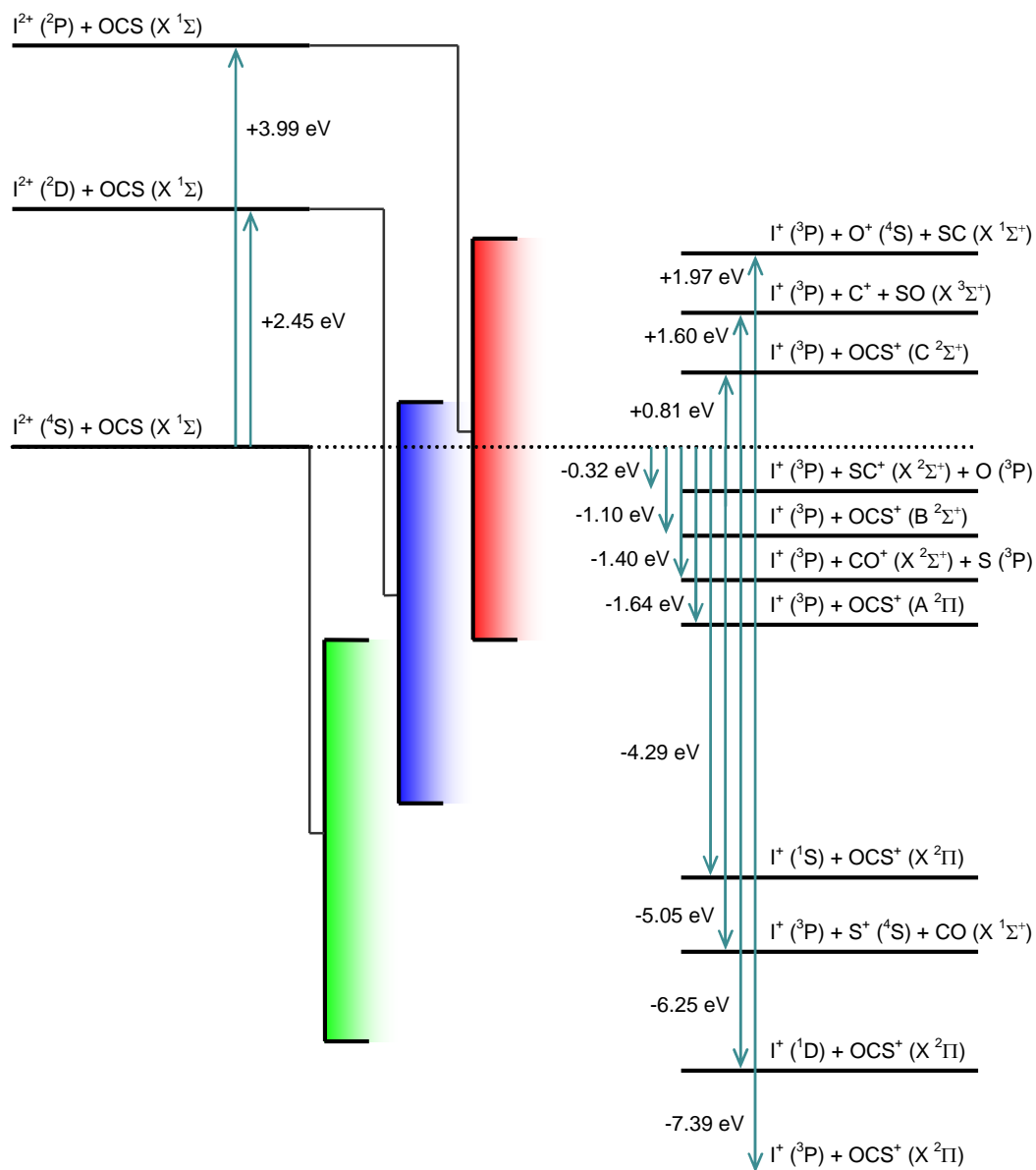


Figure 8.8: Composite energy level diagram for $I^{2+} + OCS$, indicating possible SET reactions. Shaded areas indicate the approximate position of the Reaction Window.

In order to produce CO^+ and SC^+ ions from a SET reaction following $I^{2+} + OCS$ collisions, the $C^2\Sigma^+$ electronic state (or higher) of OCS^+ must be accessed, as of the three electronic states below this, the $X^2\Pi$ is bound, and the $A^2\Pi$ and the $B^2\Sigma^+$ states dissociative to form $S^+ + CO$.^{35,36} For the C state to be accessed in a SET reaction would require the involvement of the second excited state of the iodine dication, $I^{2+} (^2P)$ (Figure 8.8). However, as discussed above, any $I^{2+} (^2P)$ formed by electron impact is expected to radiatively relax to the $I^{2+} (^2D)$ state before it reaches the interaction region. Indeed, if the 2P state of I^{2+} was present in the dication beam, dissociative SET reactions

forming C^+ and O^+ would also be accessible, however no C^+ or O^+ product ions are observed following $I^{2+} + OCS$ collision. This lack of C^+ and O^+ product ions confirmed the absence of the 2P state of I^{2+} in the dication beam. Thus, if the observed product ion intensities for CO^+ and SC^+ are not the result of dissociative SET reactions, they must be the result of the bond forming reactions shown in Equations 8.15 and 8.16. This assignment of CO^+ and SC^+ being formed solely from bond forming reactions is reasonable, as comparison of the R_{OBS} values for these two product ions to those of their correlated bond forming monocation partners, IS^+ and IO^+ respectively, show good agreement, whereas comparison to the R_{OBS} values for product ions from SET reactions (S^+ and OCS^+) show large discrepancies (Figure 8.7).

8.5.2 Double Electron Transfer Reaction

As discussed above in Section 8.1.1.2, there are in principle three mechanisms by which DET reactions can occur.¹³ Of the two direct DET pathways, the concerted “near-resonant” mechanism is the most likely to occur, in which the two electrons are both transferred at the crossing of the $I^{2+} + OCS$ and $I + OCS^{2+}$ potential energy curves (Figure 8.2a). For this direct, concerted DET pathway to be effective requires that the reactant and product asymptotes lie within 1 eV of each other. Therefore, if the dication beam consists of only the ground and first excited states of I^{2+} , as has been confirmed by the SET transfer results discussed above (Section 8.5.1), then the reaction window model states that only the ground and first two excited states of OCS^{2+} can be populated, if we assume that the neutral I atoms formed are in their ground state. Figure 8.9 indicates these possible OCS^{2+} electronic states that are accessible by the reaction window model. All three of these OCS^{2+} states ($X^3\Sigma^-$, $a^1\Delta$ and $b^1\Sigma^+$) are located above the lowest dissociation limit $\{CO^+ (X^2\Sigma^+) + S^+ (^4S)\}$ and so are expected to predissociate, at least to this limit. However, all three of these dicationic states are also metastable, with barriers to dissociation of 1.6 eV, 2.4 eV and 2.1 eV for the X, a, and b states respectively. These three states of OCS^{2+} should therefore have significant lifetimes, hence the observation of OCS^{2+} in the collision spectra.

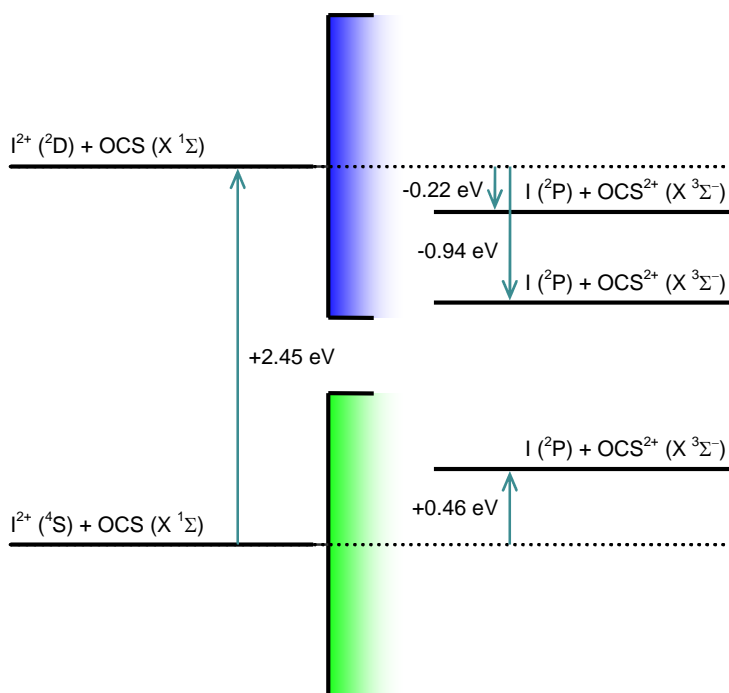


Figure 8.9: Composite energy level diagram for $I^{2+} + OCS$, indicating possible DET reactions. Shaded areas indicate the approximate position of the Reaction Window.

8.5.3 Bond-Forming Reactions

Following collisions between I^{2+} and OCS, two bond forming reactions are observed, forming IO^+ and IS^+ . As previously mentioned, the channel for forming IO^+ is very weak, with the IO^+ ion peak appearing as little more than a rise in the baseline in the collision spectra. However, the data analysis procedures described in Section 8.3 indicated the IO^+ ion peak is real, as does the presence of its correlated monocation partner SC^+ in the collision mass spectra. The channel forming IS^+ is however much more pronounced, with the IS^+ ion peak clearly visible in the collision spectra (Figures 8.5 and 8.6c). Previous studies of the dynamics of bond-forming reactions of molecular dications have shown that most bond-forming processes proceed *via* complexation.¹⁵⁻¹⁸ A schematic model proposed to rationalize the observations of bond-forming reactions has been presented before,³⁷ and is illustrated in Figure 8.10. The diagram represents the possible products of a basic double charged triatomic system. On the left hand side is the asymptotes for the dication X^{2+} and neutral YZ at point '1' and the asymptote for the SET products $X^+ + YZ^+$ at point '2'. On the right hand side is the asymptote for a double-charged product XY^{2+} and accompanying neutral Z at point '4', and the asymptote for the bond-forming monocation product XY^+ with accompanying monocation Z^+ at point '3'. The asymptote at point '3' represents the products of the

observed bond-forming reactions, either $IO^+ + [SC]$, or $IS^+ + [CO]$. In order to reach asymptote '3', the collision system must first pass through the intersection that leads to a SET reaction (point 'A' in Figure 8.10) without crossing between curves. If the system negotiates this crossing without an electron being transferred, then the neutral and dication can interact closely and bonds can be made and broken in a collision complex. Of course, if no reaction occurs, the complex may dissociate back to the reactants. However, if a reaction does occur, the reaction complex may separate along the original bond, and exit towards the right hand side of the diagram. In order to form the observed IO^+ and IS^+ product ions, the separating products must pass through another intersection (point 'B'), this time changing potential surfaces to produce a pair of monocations. Of course if the system negotiates this second crossing at point 'B' without an electron being transferred, then a new dicationic product would be formed. However following collisions of I^{2+} with OCS, no such reactions producing new dicationic products are observed.

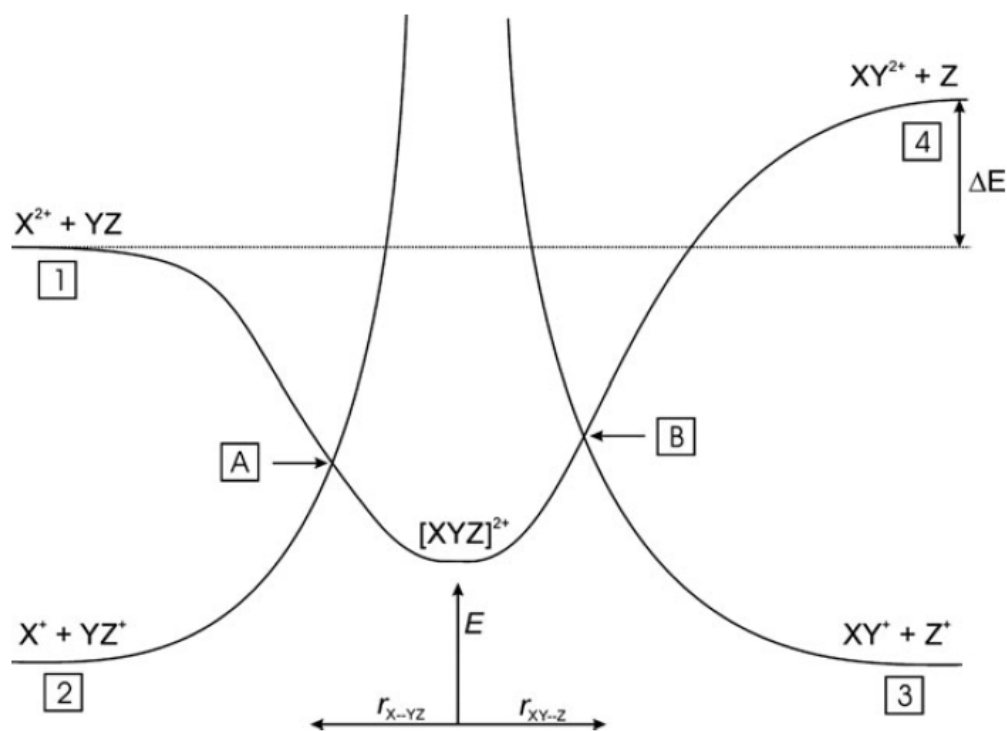


Figure 8.10: Schematic potentials showing the route from $X^{2+} + YZ$ to $XY^+ + Z^+$. The reactants must avoid switching potential surfaces at point A and switch potential surfaces at B. Reproduced from Ref. [20].

Further interpretation of the energetic and dynamics regarding bond-forming reactions observed following $I^{2+} + OCS$ collisions is beyond the scope of this largely qualitative investigation. Indeed the lack of any theoretic or experiential data in the literature on the energetics of many of the key points of the potential curves depicted in Figure 8.10, for the formation of IO^+ and IS^+ , means that further interpretation would require computational calculations of the $I^{2+} + OCS$ system. Future work regarding the bimolecular reactivity of I^{2+} should therefore include theoretical investigations, to give a complete picture of the reactions occurring.

8.6 Conclusions

Collisions between I^{2+} and OCS have been investigated using TOFMS, in the collision range 2.2 – 6.2 eV in the COM frame. The formation of OCS^+ product ions and CO^+ , S^+ and SC^+ product ions from non-dissociative and dissociative SET reactions respectively, have been rationalised by Landau-Zener calculations. These calculations indicate that the CO^+ , S^+ and SC^+ product ions from dissociative SET reactions, are formed from an excited electron state of I^{2+} , and result from the formation of excited electronic states of OCS^+ . These calculations also indicate that the observed OCS^+ product ions must be formed together with excited states of I^+ , in order for the reaction exothermicity to lie within the reaction window range. The formation of OCS^{2+} by DET has also been rationalised by Landau-Zener calculations, indicating that the OCS^{2+} observed may only be in its three lowest electronic states. In addition to electron transfer reactions, two bond-forming reactions have been observed, leading to the formation of IO^+ and IS^+ , with the latter of these being the most intense of the two.

8.7 References

- 1 L. J. Carpenter, *Chem. Rev.* **103**, 4953 (2003).
- 2 R. Fuge and C. C. Johnson, *Environ. Geochem. Health* **8**, 54 (1986).
- 3 B. S. Gilfedder, S. C. Lai, M. Petri, H. Biester, and T. Hoffmann, *Atmos. Chem. Phys.* **8**, 6069 (2008).
- 4 V. D. Korzh, *Atmos. Environ.* **18**, 2707 (1983).
- 5 A. S. Mahajan and e. al., *J. Geophys. Res.* **115**, D20303 (2010).
- 6 J. Stutz, K. Hebestreit, B. Aliche, and U. Platt, *J. Atmos. Chem.* **34**, 65 (1999).
- 7 D. Davis, J. Crawford, S. Liu, S. McKeen, A. Bandy, D. Thornton, F. Rowland, and D. Blake, *J. Geophys. Res. Atmos.* **101**, 2147 (1996).

- 8 M. K. Gilles, A. A. Turnipseed, J. B. Burkholder, A. R. Ravishankara, and S. Solomon, *J. Phys. Chem. A* **101**, 5526 (1997).
- 9 S. A. Rogers, S. D. Price, and S. R. Leone, *J. Chem. Phys.* **98**, 280 (1993).
- 10 L. D. Landau, *Phys. Z. Sowjetunion* **2**, 46 (1932).
- 11 C. Zener, *Proc. Roy. Soc. London, Series A* **137**, 696 (1932).
- 12 P. W. Burnside, **PhD** *Mass spectrometric studies of dication reactions*, University of London, 2007.
- 13 M. A. Parkes, J. F. Lockyear, and S. D. Price, *Int. J. Mass Spectrom.* **280**, 85 (2009).
- 14 D. Smith, N. G. Adams, E. Alge, H. Villinger, and W. Lindinger, *J. Phys. B: Mol. Opt. Phys.* **13**, 2787 (1980).
- 15 S. D. Price, *Phys. Chem. Chem. Phys.* **5**, 1717 (2003).
- 16 S. D. Price, *Int. J. Mass Spectrom.* **260**, 1 (2007).
- 17 J. Roithova, C. L. Ricketts, D. Schroder, and S. D. Price, *Angew. Chem. Int. Ed.* **46**, 9316 (2007).
- 18 J. F. Lockyear, M. A. Parkes, and S. D. Price, *Angew. Chem. Int. Ed.* **50**, 1322 (2011).
- 19 S. D. Price, *J. Chem. Soc. Faraday Trans.* **93**, 2451 (1997).
- 20 P. W. Burnside and S. D. Price, *Phys. Chem. Chem. Phys.* **9**, 3902 (2007).
- 21 P. W. Burnside and S. D. Price, *Int. J. Mass Spectrom.* **249**, 279 (2006).
- 22 L. Wahlin, *Nuc. Instrum. & Methods* **27**, 55 (1964).
- 23 W. Aberth and H. Wollnik, *Mass Spec. Rev.* **9**, 383 (2005).
- 24 M. L. Oliphant, E. S. Shire, and B. M. Crowther, *Proc. Royal Soc.* **A146**, 992 (1934).
- 25 W. Wien, *Ann. Physik.* **65**, 440 (1898).
- 26 W. C. Wiley and I. H. McLaren, *Rev. Sci. Instrum.* **26**, 1150 (1955).
- 27 K. Yamasaki and S. R. Leone, *J. Chem. Phys.* **90**, 964 (1989).
- 28 S. D. Price, S. A. Rogers, and S. R. Leone, *J. Chem. Phys.* **98**, 9455 (1993).
- 29 M. Manning, S. D. Price, and S. R. Leone, *J. Chem. Phys.* **99**, 8695 (1993).
- 30 R. D. Levine and R. B. Bernstein, *Molecular Reaction Dynamics & Chemical Reactivity* (Oxford University Press, 1987).
- 31 D. Schroder and H. Schwarz, *J. Phys. Chem. A* **103**, 7385 (1999).
- 32 V. Brites, J. H. D. Eland, and M. Hochlaf, *Chem. Phys.* **346**, 23 (2008).

-
- 33 N. Kishimoto, T. Horio, S. Maeda, and K. Ohno, *Chem. Phys. Lett.* **379**, 332 (2003).
- 34 *NIST Chemical WebBook; NIST Standard Reference Database Number 69*, Vol., edited by P. J. Linstrom and W. G. Mallard (National Institute of Standards and Technology, Gaithersburg MD, 20899, 2008).
- 35 B. Z. Chen, H. B. Chang, and M. B. Haung, *J. Chem. Phys.* **125**, 054310 (2006).
- 36 S. Morse, M. Takahashi, J. H. D. Eland, and L. Karlsson, *Int. J. Mass Spectrom.* **184**, 67 (1999).
- 37 Z. Herman, *Int. Rev. Phys. Chem.* **15**, 299 (1996).

Chapter 9 Conclusions and Future Work

In Chapters 4-6 of this thesis, results from experiments on the electron ionization of H₂S, CH₃OH and CF₃I have been reported. These experiments employed time-of-flight mass spectrometry coupled with a 2D ion coincidence technique to produce relative partial ionization cross-sections for the formation of positively charged ions following electron ionization of H₂S, CH₃OH and CF₃I in the energy range 30 – 200 eV. The 2D ion coincidence technique also allowed precursor-specific relative PICSs to be derived, cross-sections which quantify the contribution from single, double, triple and quadruple ionization to the yield of each fragment ion. This is the first time such PICSs have been measured for these species. Good agreement is found between the data presented and recent PICS determinations (where available) in which the efficient collection of translationally energetic ions is demonstrated. Information on the energetics and dissociation dynamics of some of the multiply charged species observed was also provided by interpretation of the ion pair peaks observed in the pairs spectra. These results demonstrate the value of the ion coincidence technique employed in Chapters 4-6. However, there is, of course, scope for improvement to the current experimental arrangement. Below, two possible developments to the current experimental setup are discussed, which would allow for an improvement in the quality of the data collected, and enable the investigation of electron interactions not only with neutral molecules, but with more exotic chemical species such as radicals and ions.

In the current experimental setup, information on the energetics and dissociation dynamics of a multiply charged ion produced following electron ionization of a parent molecule are provided by interpretation of the ion pair peaks observed in the pairs spectra. As discussed in Chapters 2 and 3, the gradient of a peak in the pairs spectra yields information on the dissociation mechanism of a given multiply charged ion, while the length of an ion pair peak (Figure 2.9), or equivalently the width of a Δ TOF plot (Figure 3.7), yields information on the kinetic energy release of the multiply charged ion dissociation. As has been discussed in Chapters 4 – 6, interpretation of an ion pair peak can sometimes result in more than one possible fragmentation pathway, particularly for ion pairs in which one or more neutral fragments must have been formed from the dissociation of the parent ion. By replacing the current MCP detector with a position sensitive detector (PSD), the fragmentation pathways in which two (or more) ions are formed together with a single neutral could be unambiguously identified.

A PSD allows information not only on an ion's flight time, but also its arrival position in the plane perpendicular to the axis of the mass spectrometer to be obtained. Such position and timing information for a pair of product ions detected in coincidence would enable the determination of the x , y and z velocity vectors for each ion.¹⁻³ The z velocity would be derived from the deviation in the TOF of an ion from its 'ideal' TOF if the ion had possessed zero kinetic energy, while the x and y velocities would be derived from the position the ion impacts on the detector. Further, for events in which a neutral third body is produced together with the ion pair conservation of momentum allows the velocity of the neutral species can be determined from the velocities of the ionic species. With all three product velocity vectors obtained, correlations between the products can be explored, giving a powerful insight into the dissociation dynamics. In addition as the velocities of the products will be known then KERS can be simply calculated. Though such correlations and KERS can be inferred using the existing instrument use of a PSD would explicitly measure them.

In the current experimental setup, mechanisms and KERS can only be determined for ion pair formation. It is not possible to obtain such information for ion triple formation. Another advantage to using a PSD to directly measure the product velocities is that it would allow detailed information on the mechanisms and kinetic energy releases involving ion triples to be acquired. For example, it would be possible to determine whether an ion triple is formed *via* an instantaneous explosion of a multiply charged parent species, or *via* initial separation of the parent into two daughter ions, followed by the dissociation of one, or both, of these.

There are several designs of PSD that can be employed in the detection of ions in a mass spectrometer. Like the current experimental setup, the majority of these PSDs still employ MCPs. As described in Section 2.3.2, ions impinging on the front surface of an MCP produce a cloud of electrons, which in the current experimental setup is collected by a copper anode. In a position sensitive detector, the anode is able to resolve the position of this electron cloud, thus giving the position of the ion impact. Currently, the two most common types of anode used in PSDs are a combined phosphor screen and video camera, or a delay line anode. The phosphor screen anode works by producing a flash at the position of the cloud of electrons produced by the MCPs, with the camera recording the image of the flashes. In a delay line anode the electron cloud from the MCPs impacts on (usually) two, perpendicularly wound wire anodes of known

lengths.^{4,5} The arrival position of the impacting ion can then be derived from the time of arrival of the charge pulses at the end of each anode wire.

In addition to replacing the current detector with a PSD detector, a relatively simple modification to the experimental setup, large scale modifications could also be made to enable the investigation of electron interactions with radical species. Such modifications would require the assembly of a new piece of apparatus to produce a continuous beam of radicals, which could then be introduced into the source region of the current TOFMS. However, as the current TOFMS is encased in a single stainless steel chamber, it may be easier to assemble a new TOF to attach to the radical producing apparatus. If such a course were taken, the current 2D ion coincidence technique would still be employed, together with the pulsed electron beam.

There are several techniques and apparatus currently employed to generate radical species. One popular technique is the use of flash pyrolysis.⁶⁻⁹ In this method radicals are produced by unimolecular thermal decomposition of a precursor gas. A typical experimental setup would employ a pulsed valve operating at a stagnation pressure between 0.5 – 3 atm to produce a supersonic expansion of precursor gas. This supersonic expansion would be introduced into a pyrolysis tube, a short circular tube heated to temperatures between 800 and 2000 °C. Contact of the precursor gas with the heated pyrolysis tube results in the formation of radical species. A supersonic expansion is used together with a short pyrolysis tube to keep the contact time short, reducing the possibility of secondary reactions. By appropriate selection of the precursor gas, radical species can be produced cleanly and specifically using this technique with little or no secondary reactions.⁹ Of course one drawback of this method is that the formation of a single radical species cannot be guaranteed. For example if CH₃ radicals were produced from the precursor gas CH₃I, I radicals would also be produced. This in itself would not be a problem, and the subsequent ionization and detection of I⁺ from I would not mask any ion peaks produced from the ionization of CH₃. However, if CH₂ radicals were also produced, it would be impossible to say whether any CH_n⁺ ($n = 0 - 2$) ions observed were the result of electron ionization of CH₃ or CH₂.

Another method currently employed in the formation of radical species is termed the fast neutral beam method.¹⁰⁻¹² In this method, ions produced following ionization of a suitable precursor gas are accelerated and focused into a beam. The ion beam is passed through a Wien filter to select a single mass. This mass selected ion beam then

passes into a low-pressure charge exchange cell, in which neutral species are formed by resonant or near resonant charge transfer.¹¹ Any residual ions are removed from the beam by electrostatic deflection. In addition, any species produced in Rydberg states are also ionized and removed from the beam by a region of high electric field. It is again impossible to unambiguously state that only one radical species will enter the source region of the TOFMS, however by careful selection of the precursor gas and charge transfer gas, a pure radical beam should be able to be produced. An additional benefit of this technique is that in addition to enable investigation into electron interactions with neutral radicals, investigations into electron interactions with ionic species¹³ can also be investigated by running the experiment with no charge transfer gas.

In addition to the electron ionization experiments carried out in Chapters 4 – 6, this thesis also reported the results of an investigation into the photoionization of CF₃I, using the vacuum ultraviolet beamline at the Swiss Light Source. These preliminary investigations carried out at the SLS highlighted the potential of this technique in double photoionization studies, as well as some of the issues in the current experimental setup used to measure photoionization spectra. As discussed in Chapter 7, the main issue highlighted by this initial investigation lies in the collection of only threshold (≤ 800 meV) photoelectrons. As discussed in Section 7.6, by increasing the electric field in the source region of the iPEPICO endstation, it would be possible to collect all the electrons formed, allowing all photoionization processes to be observed. Such a modification would also improve the ion detection efficiency, particularly with respect to energetic ions.

The final chapter of this thesis presented result from interactions between I²⁺ and OCS at collision energies between 2.2 – 6.2 eV in the COM frame. These investigations were conducted using a crossed ion beam experiment. Following I²⁺ + OCS collisions, two bond forming reactions producing IO⁺ and IS⁺ were observed, in addition to the more ubiquitous electron transfer reactions. These electron transfer reactions have been rationalised using the Reaction Window model. The observed reactivity of the iodine dication has prompted further investigations into other I²⁺ + neutral collision systems. In addition, due to the paucity of data regarding the reactivity of other multiply charged halogen species, further investigations involving Br²⁺ and Cl²⁺ could also be carried out. As discussed in Chapter 8, results from these investigations may identify trends in the reactivity of multiply charged species down a group.

8.1 References

- 1 M. A. Parkes, J. F. Lockyear, and S. D. Price, *Int. J. Mass Spectrom.* **280** (2009).
- 2 S. D. Price, *Int. J. Mass Spectrom.* **260** (2007).
- 3 W. P. Hu, S. M. Harper, and S. D. Price, *Meas. Sci. Technol.* **13** (2002).
- 4 A. Oelsner, O. Schmidt, M. Schicketanz, M. Klais, G. Schonhense, V. Mergel, O. Jagutzki, and H. Schmidt-Bocking, *Rev. Sci. Instrum.* **72** (2001).
- 5 I. Ali, R. Dorner, O. Jagutzki, S. Nuttgens, V. Mergel, L. Spielberger, K. Khayyat, T. Vogt, H. Brauning, K. Ullmann, R. Moshhammer, J. Ullrich, S. Hagmann, K. O. Groeneveld, C. L. Cocke, and H. Schmidt-Bocking, *Nucl. Instrum. Meth. B* **149** (1999).
- 6 B. Gans, L. A. V. Mendes, S. Boye-Peronne, S. Douin, G. Garcia, H. Soldi-Lose, B. K. C. de Miranda, C. Alcaraz, N. Carrasco, P. Pernot, and D. Gauyacq, *J. Phys. Chem. A* **114** (2010).
- 7 T. Schussler, W. Roth, T. Gerber, C. Alcaraz, and I. Fischer, *Phys. Chem. Chem. Phys.* **7** (2005).
- 8 W. A. Chupka and C. Lifshitz, *J. Chem. Phys.* **48** (1968).
- 9 D. W. Kohn, H. Clauberg, and P. Chen, *Rev. Sci. Instrum.* **63** (1992).
- 10 M. Gutkin, J. M. Mahoney, V. Tarnovsky, H. Deutsch, and K. Becker, *Int. J. Mass Spectrom.* **280** (2009).
- 11 V. Tarnovsky and K. Becker, *Z. Phys. D: Atom Mol. Cl.* **22** (1992).
- 12 R. C. Wetzell, F. A. Baiocchi, T. R. Hayes, and R. S. Freund, *Phys. Rev. A* **35** (1987).
- 13 J. Lecointre, H. Cherkani-Hassani, S. Cherkani-Hassani, D. S. Belic, J. J. Jureta, and P. Defrance, *Eur. Phys. J. D* **60** (2010).

Appendix A

Time-of-Flight Mass Spectrometer

The TOF mass spectrometers used in Chapters 4 – 7 of this thesis are based upon the standard Wiley-McLaren¹ two-field design, shown schematically in Figure 2.1. In this appendix, two important features of this design are discussed. Firstly, the flight time of an ion in the two-field TOFMS is derived using electrostatics and Newtonian mechanics, thus providing a means for the calibration of all mass spectra recorded. Secondly, the conditions for first order space-focusing are derived for the formation of ions with a small spatial distribution in the source.

Derivation of Ion Flight Times for a Two-Field TOFMS

The standard Wiley-McLaren¹ two-field TOFMS consists of three regions: a source region of length $2S_0$, an acceleration region of length A and a field free drift region of length D (Figure 2.1). The two electric fields stated in the name are in the source region, termed E_S , and in the acceleration region, termed E_A . The flight time t_{tof} of an ion of mass m formed in the centre of the source region and detected at the end of the drift tube can be expressed as the sum of the times taken for the ion to traverse each of the three regions in the mass spectrometer:

$$t_{tof} = t_S + t_A + t_D \quad (\text{A.1})$$

The time taken for an ion to travel from the centre of the source region to the start of the acceleration region, t_S , can be expressed in terms of the initial velocity of the ion upon formation, v_0 , the acceleration of the ion, a_S , and the final velocity of the ion, v_S , following acceleration through the distance S_0 :

$$t_S = \frac{v_S - v_0}{a_S} \quad \text{where} \quad v_S^2 = v_0^2 + 2a_S S_0 \quad (\text{A.2})$$

In Equations A.2 and the acceleration a_S of an ion of charge q is given by:

$$a_S = \frac{qE_S}{m} \quad (\text{A.3})$$

The final kinetic energy of an ion, U , formed with an initial kinetic energy, U_0 , after moving through the mass spectrometer can be expressed in terms of the energy gained as it moves through each electric field:

$$U = U_0 + qE_s S_0 + qE_A A \quad (\text{A.4})$$

Thus v_0 and v_s can be expressed in terms of the energy of the ion:

$$v_0 = \left(\frac{2U_0}{m} \right)^{1/2} \quad \text{and} \quad v_s = \left[\frac{2(U_0 + qE_s S_0)}{m} \right]^{1/2} \quad (\text{A.5})$$

Substitution of these expressions for a_s , v_0 , and v_s into Equation A2 yields:

$$t_s = \frac{(2m)^{1/2}}{qE_s} \left[(U_0 + qE_s S_0)^{1/2} - U_0^{1/2} \right] \quad (\text{A.6})$$

Similarly, the time taken for an ion to traverse the acceleration region, t_A , can be expressed in terms of the initial velocity of the ion upon entering the acceleration region, v_s , the acceleration of the ion, a_A , and the final velocity of the ion, v_A , following acceleration through a distance A :

$$t_A = \frac{v_A - v_s}{a_A} \quad \text{where} \quad v_A^2 = v_s^2 + 2a_A A \quad (\text{A.7})$$

In Equations A.8 the acceleration a_A of an ion in the electric field E_A is given by:

$$a_A = \frac{qE_A}{m} \quad (\text{A.8})$$

The final velocity of the ion after passing through both acceleration fields, v_A , can be expressed in terms of the energy of the ion:

$$v_A = \left(\frac{2U}{m} \right)^{1/2} \quad (\text{A.9})$$

Substitution of these expressions for a_A , v_s , and v_A into Equation A.7 yields:

$$t_A = \frac{(2m)^{1/2}}{qE_A} \left[U^{1/2} - (U_0 + qE_s S_0)^{1/2} \right] \quad (\text{A.10})$$

An ion will pass through the field-free drift region with a constant velocity:

$$v_D = v_A = \left(\frac{2U}{m} \right)^{1/2} \quad (\text{A.11})$$

Thus the time taken for an ion to traverse the drift region, of length D , is given by:

$$t_D = \frac{D}{v_D} = \frac{(2m)^{1/2} D}{2(U^{1/2})} \quad (\text{A.12})$$

The total flight time of an ion of mass m is then given by substitution of Equations A.6, A.11 and A.12 into Equation A1:

$$t_{tof} = (2m)^{1/2} \left\{ \left[\frac{(U_0 + qE_S S_0)^{1/2} - U_0^{1/2}}{qE_S} \right] + \left[\frac{U^{1/2} - (U_0 + qE_S S_0)^{1/2}}{qE_A} \right] + \frac{D}{2(U^{1/2})} \right\} \quad (\text{A.13})$$

Equation A.13 illustrates that the ion flight time is proportional to the square root of the ions mass. Thus, the electric fields, dimensions of the TOFMS, and the charge on the ion being constant, Equation A.13 can be abbreviated to yield Equation A.14:

$$t_{tof} = k\sqrt{m} + c \quad (\text{A.14})$$

where k and c are constants. The value of k is dependent on the geometry of the apparatus and voltage conditions used, while c is a constant that quantifies the time delay arising due to the timing electronics. As discussed in Chapters 2 and 3, these constants are determined by solving two simultaneous equations for two ions of different mass.

Space-Focusing

In an ideal TOFMS all ions would be formed in the source at a single point. However, as mentioned in Chapter 2, the ions are formed in the source region with an initial spatial distribution; this may give rise to ions of the same m/z having different flight times, limiting the resolution of the mass spectrometer. Wiley-McLaren¹ designed a two-field design of TOFMS, in order to overcome this spatial resolution. This improvement comes from the fact that ions formed towards the back of the source

region (and further from the detector) are accelerated for longer and thus will reach a greater kinetic energy, than those ions formed towards the front of the source region (and closer to the detector). Thus there exists a plane, defined as the space focus plane, at which the faster moving ions will ‘catch up’ with the slower moving ions. If the detector is positioned at this space focus plane, the resolution of the mass spectrometer will be greatly enhanced.

Wiley-McLaren assumed that an ions initial kinetic energy, U_0 , is zero. They also introduced a new parameter, k_0 :

$$k_0 = \frac{S_0 E_S + A E_A}{S_0 E_S} \quad (\text{A.15})$$

Combination of Equation A.15 with A.4 allows two useful relations of k_0 to be formed:

$$qS_0 E_S = \frac{U}{k_0} \quad \text{where} \quad qA E_A = \frac{U(k_0 - 1)}{k_0} \quad (\text{A.16})$$

Substituting Equations A.16 in A.13 yields an expression for the flight time of an ion of mass m , formed with zero initial kinetic energy ($U_0 = 0$) and at a point in the source region defined by S_0 :

$$t(0, S_0) = (2m)^{1/2} \left[\frac{k_0^{1/2} S_0}{U^{1/2}} + \frac{U^{1/2} (1 - k_0^{-1/2}) k_0 A}{U(k_0 - 1)} + \frac{D}{2(U^{1/2})} \right] \quad (\text{A.17})$$

which, using the identity $(k - 1) = (k^{1/2} - 1)(k^{1/2} + 1)$, gives:

$$t(0, S_0) = \left(\frac{m}{2U} \right)^{1/2} \left[2k_0^{1/2} S_0 + \frac{2k_0^{1/2} A}{(k_0^{1/2} + 1)} + D \right] \quad (\text{A.18})$$

The condition for first order space focusing requires that ions formed in the source with an initial position $S = S_0 \pm \delta S$ gives rise to the identical flight times. To the first order, this condition requires that:

$$\left(\frac{\partial t}{\partial S} \right)_{U_0=0, S} = 0 \quad (\text{A.19})$$

Therefore, an expression for the length of the drift tube at which the space focus plane lies is obtained:

$$D = 2Sk_0 \left(1 - \frac{A}{S(k_0 + k_0^{1/2})} \right) \quad (\text{A.20})$$

Thus, for fixed values of S_0 , A and D , space-focusing can be achieved by adjusting the ratio of E_A/E_S in a two-field TOFMS. This is in contrast to a single-field TOFMS in which there is only a single solution for the position of the plane of space focus, independent of the electric field strengths used.

References

- 1 W. C. Wiley and I. H. McLaren, *Rev. Sci. Instrum.* **26**, 1150 (1955).

Appendix B

Relative Partial Ionization Cross-Section Data

Hydrogen Sulphide, H₂S

Relative PICSS

Table B.1: Relative partial ionization cross-sections $\sigma_i[X^{m+}]$ for forming fragment ions following dissociative electron ionization of hydrogen sulphide, expressed relative to the cross-section for forming H₂S⁺, as a function of electron energy E . The values in parenthesis indicate two standard deviations in the last figure.

E / eV	$\sigma_i[H^+]$	$\sigma_i[H_2^+]$	$\sigma_i[S^{2+}]$	$10^2 \sigma_i[HS^{2+}]$	$10^2 \sigma_i[H_2S^{2+}]$	$\sigma_i[S^+]$	$\sigma_i[HS^+]$
200	0.226 (3)	0.0064 (4)	0.0052 (15)	0.068 (15)	0.589 (46)	0.466 (4)	0.450 (3)
175	0.234 (5)	0.0067 (4)	0.0050 (15)	0.061 (6)	0.596 (29)	0.473 (3)	0.449 (4)
150	0.244 (3)	0.0069 (4)	0.0053 (12)	0.072 (6)	0.604 (26)	0.483 (3)	0.455 (5)
125	0.252 (2)	0.0069 (5)	0.0054 (18)	0.067 (24)	0.618 (26)	0.493 (4)	0.451 (2)
100	0.262 (3)	0.0075 (5)	0.0049 (9)	0.058 (10)	0.632 (11)	0.503 (2)	0.451 (3)
85	0.266 (3)	0.0076 (5)	0.0042 (11)	0.058 (10)	0.634 (10)	0.508 (3)	0.450 (3)
75	0.263 (3)	0.0077 (4)	0.0035 (11)	0.050 (15)	0.615 (20)	0.509 (3)	0.446 (3)
65	0.259 (4)	0.0078 (4)	0.0024 (8)	0.045 (7)	0.590 (6)	0.505 (2)	0.444 (3)
60	0.254 (4)	0.0079 (3)	0.0015 (6)	0.044 (9)	0.553 (12)	0.500 (3)	0.442 (3)
55	0.245 (3)	0.0078 (4)	0.0008 (6)	0.035 (7)	0.500 (13)	0.496 (8)	0.440 (2)
50	0.229 (3)	0.0076 (5)	0.0003 (4)	0.022 (9)	0.430 (18)	0.489 (6)	0.438 (5)
45	0.209 (3)	0.0072 (5)	0.0001 (4)	0.008 (3)	0.294 (25)	0.480 (6)	0.434 (6)
40	0.180 (4)	0.0066 (4)	0.0001 (3)	0.005 (2)	0.144 (12)	0.474 (5)	0.429 (5)
35	0.129 (9)	0.0052 (5)	0.0000 (2)	0.003 (4)	0.016 (15)	0.450 (12)	0.430 (2)
30	0.062 (6)	0.0027 (4)	0.0001 (1)	0.004 (2)	0.002 (9)	0.385 (10)	0.432 (9)

Precursor-Specific Relative PICSS

Table B.2: Precursor-specific relative PICSSs $\sigma_n[X^{m+}]$ for forming fragment ions following dissociative electron ionization of hydrogen sulphide, expressed relative to the cross section for forming H₂S⁺, as a function of electron energy E . The values in parenthesis indicate two standard deviations in the last figure, except for $\sigma_3[S^+]$ for which only one standard deviation is given.

E / eV	$\sigma_1[\text{H}^+]$	$\sigma_2[\text{H}^+]$	$10^2 \sigma_3[\text{H}^+]$	$\sigma_1[\text{H}_2^+]$	$10^2 \sigma_2[\text{H}_2^+]$
200	0.125 (4)	0.0989 (29)	0.167 (98)	0.0045 (4)	0.189 (25)
175	0.132 (5)	0.1009 (42)	0.155 (116)	0.0046 (7)	0.206 (32)
150	0.136 (1)	0.1064 (31)	0.146 (103)	0.0050 (4)	0.192 (23)
125	0.140 (5)	0.1103 (28)	0.157 (118)	0.0048 (6)	0.208 (15)
100	0.147 (5)	0.1138 (24)	0.113 (110)	0.0053 (6)	0.221 (19)
85	0.154 (5)	0.1113 (37)	0.048 (63)	0.0054 (4)	0.224 (11)
75	0.155 (5)	0.1076 (43)	0.020 (44)	0.0056 (5)	0.211 (8)
65	0.160 (3)	0.0988 (12)	0.020 (65)	0.0057 (3)	0.213 (27)
60	0.164 (2)	0.0896 (21)	0.010 (48)	0.0059 (4)	0.194 (20)
55	0.168 (3)	0.0770 (34)	0.011 (28)	0.0061 (6)	0.174 (20)
50	0.170 (1)	0.0586 (27)	0.017 (28)	0.0062 (5)	0.143 (16)
45	0.175 (2)	0.0337 (18)	0.008 (15)	0.0064 (4)	0.081 (8)
40	0.167 (3)	0.0129 (9)	0.001 (3)	0.0063 (4)	0.033 (6)
35	0.127 (8)	0.0022 (9)	0.000 (0)	0.0051 (5)	0.004 (3)
30	0.061 (6)	0.0009 (2)	0.000 (0)	0.0027 (4)	0.001 (1)

E / eV	$\sigma_2[\text{S}^{2+}]$	$10^2 \sigma_3[\text{S}^{2+}]$	$10^2 \sigma_2[\text{HS}^{2+}]$	$10^2 \sigma_3[\text{HS}^{2+}]$	$10^2 \sigma_2[\text{H}_2\text{S}^{2+}]$
200	0.0042 (16)	0.102 (27)	0.067 (15)	0.002 (1)	0.589 (46)
175	0.0041 (13)	0.096 (21)	0.060 (7)	0.001 (2)	0.596 (29)
150	0.0044 (13)	0.092 (18)	0.070 (6)	0.002 (1)	0.604 (26)
125	0.0047 (16)	0.092 (51)	0.065 (21)	0.001 (3)	0.418 (26)
100	0.0045 (12)	0.045 (37)	0.057 (10)	0.001 (1)	0.632 (11)
85	0.0041 (12)	0.009 (25)	0.058 (10)	0.000 (0)	0.634 (10)
75	0.0035 (11)	0.000 (2)	0.050 (15)	0.000 (0)	0.615 (20)
65	0.0024 (8)	0.000 (1)	0.045 (7)	0.000 (0)	0.590 (6)
60	0.0015 (6)	0.000 (1)	0.044 (10)		0.553 (12)
55	0.0008 (6)		0.035 (7)		0.500 (13)
50	0.0003 (4)		0.022 (9)		0.430 (18)
45	0.0001 (4)		0.008 (3)		0.294 (25)
40	0.0001 (3)		0.005 (2)		0.144 (12)
35	0.0000 (2)		0.003 (4)		0.016 (15)
30					0.002 (9)

E / eV	$\sigma_1[\text{S}^+]$	$\sigma_2[\text{S}^+]$	$10^2 \sigma_3[\text{S}^+]$	$\sigma_1[\text{HS}^+]$	$\sigma_2[\text{HS}^+]$
200	0.408 (6)	0.0575 (27)	0.032 (22)	0.410 (1)	0.0400 (26)
175	0.413 (3)	0.0596 (5)	0.029 (26)	0.409 (4)	0.0401 (13)
150	0.419 (4)	0.0632 (22)	0.026 (25)	0.413 (4)	0.0418 (12)
125	0.427 (3)	0.0658 (12)	0.042 (29)	0.408 (2)	0.0437 (8)

E / eV	$\sigma_1[S^+]$	$\sigma_2[S^+]$	$10^2 \sigma_3[S^+]$	$\sigma_1[HS^+]$	$\sigma_2[HS^+]$
100	0.436 (3)	0.0675 (12)	0.034 (27)	0.405 (3)	0.0459 (4)
85	0.443 (4)	0.0656 (12)	0.019 (11)	0.403 (3)	0.0465 (6)
75	0.448 (2)	0.0609 (18)	0.010 (11)	0.400 (2)	0.0464 (18)
65	0.453 (3)	0.0524 (21)	0.010 (16)	0.397 (3)	0.0467 (8)
60	0.454 (4)	0.0459 (17)	0.005 (12)	0.397 (3)	0.0445 (13)
55	0.460 (8)	0.0358 (24)	0.005 (7)	0.398 (3)	0.0421 (13)
50	0.466 (8)	0.0228 (17)	0.009 (7)	0.401 (6)	0.0368 (12)
45	0.470 (6)	0.0091 (11)	0.004 (4)	0.409 (6)	0.0252 (9)
40	0.472 (5)	0.0018 (2)	0.001 (1)	0.418 (4)	0.0111 (10)
35	0.449 (12)	0.0004 (2)	0.000 (0)	0.428 (2)	0.0015 (7)
30	0.384 (10)	0.0004 (2)	0.000 (0)	0.432 (9)	0.0002 (1)

Total Ion Yield from Each Level of Ionization

Table B.3: Percentage contributions to the total ion yield from single, double and triple ionization as a function of electron energy E , following electron ionization of hydrogen sulphide.

E (eV)	Single ionization (%)	Double ionization (%)	Triple Ionization (%)
200	81.7	18.0	0.3
175	81.6	18.2	0.2
150	81.1	18.7	0.2
125	80.6	19.2	0.2
100	80.4	19.5	0.2
85	80.9	19.0	0.1
75	81.6	18.4	0.0
65	82.9	17.0	0.0
60	84.3	15.6	0.0
55	86.4	13.6	0.0
50	89.3	10.7	0.0
45	93.6	6.4	0.0
40	97.5	2.5	0.0
35	99.6	0.4	0.0
30	99.8	0.2	0.0

Methanol, CH₃OH

Relative PICs

Table B.4: Relative partial ionization cross-sections $\sigma_r[X^{m+}]$ for forming fragment ions following dissociative electron ionization of methanol, expressed relative to the cross-section for forming CH₃OH⁺, as a function of electron energy E . The values in parenthesis indicate two standard deviations in the last figure.

E / eV	$\sigma_r[H^+]$	$\sigma_r[H_2^+]$	$\sigma_r[H_3^+]$	$\sigma_r[C^+]$	$\sigma_r[CH^+]$
200	0.612 (11)	0.0624 (11)	0.0112 (4)	0.0664 (6)	0.1062 (5)
175	0.628 (17)	0.0648 (12)	0.0116 (2)	0.0676 (13)	0.1105 (2)
150	0.634 (13)	0.0662 (16)	0.0120 (3)	0.0678 (6)	0.1136 (17)
125	0.629 (5)	0.0676 (14)	0.0119 (3)	0.0666 (9)	0.1170 (15)
100	0.589 (9)	0.0668 (7)	0.0116 (6)	0.0606 (9)	0.1151 (25)
85	0.533 (12)	0.0636 (9)	0.0109 (4)	0.0546 (13)	0.1109 (8)
75	0.480 (8)	0.0594 (14)	0.0101 (5)	0.0493 (7)	0.1049 (24)
65	0.409 (4)	0.0520 (5)	0.0087 (3)	0.0421 (8)	0.0939 (2)
60	0.376 (5)	0.0483 (11)	0.0080 (4)	0.0390 (6)	0.0883 (17)
55	0.324 (15)	0.0411 (17)	0.0068 (3)	0.0340 (13)	0.0793 (45)
50	0.290 (1)	0.0355 (8)	0.0057 (5)	0.0303 (5)	0.0721 (5)
45	0.231 (6)	0.0261 (9)	0.0039 (1)	0.0238 (7)	0.0592 (17)
40	0.165 (9)	0.0162 (18)	0.0019 (1)	0.0144 (11)	0.0388 (32)
35	0.098 (4)	0.0082 (5)	0.0006 (2)	0.0055 (7)	0.0161 (19)
30	0.047 (3)	0.0030 (2)	0.0003 (1)	0.0012 (1)	0.0038 (5)

E / eV	$\sigma_r[CH_2^+]$	$\sigma_r[CH_3^+]$	$\sigma_r[O^+]$	$\sigma_r[OH^+]$	$\sigma_r[OH_2^+]$
200	0.1787 (25)	0.702 (5)	0.0352 (19)	0.0994 (15)	0.0220 (64)
175	0.1828 (22)	0.702 (6)	0.0351 (22)	0.1018 (7)	0.0198 (64)
150	0.1865 (21)	0.702 (3)	0.0349 (8)	0.1049 (11)	0.0230 (25)
125	0.1902 (34)	0.705 (12)	0.0334 (33)	0.1075 (38)	0.026 (13)
100	0.1908 (15)	0.703 (10)	0.0282 (5)	0.1035 (30)	0.0212 (39)
85	0.1868 (24)	0.696 (8)	0.0239 (11)	0.0971 (9)	0.0199 (21)
75	0.1824 (13)	0.692 (3)	0.0190 (5)	0.0892 (16)	0.0197 (43)
65	0.1710 (10)	0.682 (3)	0.0143 (7)	0.0757 (12)	0.0192 (43)
60	0.1655 (17)	0.672 (8)	0.0121 (3)	0.0674 (34)	0.0182 (23)
55	0.1540 (70)	0.655 (32)	0.0095 (14)	0.0559 (36)	0.0172 (27)
50	0.1477 (2)	0.650 (7)	0.0070 (1)	0.0464 (12)	0.0171 (30)
45	0.1345 (16)	0.635 (6)	0.0046 (4)	0.0332 (25)	0.0156 (41)

E / eV	$\sigma_r[\text{CH}_2^+]$	$\sigma_r[\text{CH}_3^+]$	$\sigma_r[\text{O}^+]$	$\sigma_r[\text{OH}^+]$	$\sigma_r[\text{OH}_2^+]$
40	0.1130 (51)	0.609 (11)	0.0030 (14)	0.0191 (22)	0.0147 (52)
35	0.0808 (71)	0.564 (25)	0.0018 (3)	0.0085 (11)	0.0106 (37)
30	0.0477 (59)	0.486 (29)	0.0014 (4)	0.0034 (3)	0.0084 (36)

E / eV	$\sigma_r[\text{CO}^+]$	$\sigma_r[\text{CHO}^+]$	$\sigma_r[\text{CH}_2\text{O}^+]$	$\sigma_r[\text{CH}_3\text{O}^+]$	$\sigma_r[\text{CH}_3\text{O}^{2+}]$
200	0.1226 (36)	1.187 (5)	0.1414 (34)	1.545 (8)	0.0060 (5)
175	0.1272 (58)	1.193 (8)	0.1442 (74)	1.543 (6)	0.0062 (21)
150	0.1315 (45)	1.197 (12)	0.151 (12)	1.540 (8)	0.0078 (27)
125	0.1337 (37)	1.206 (13)	0.1497 (41)	1.546 (6)	0.0065 (17)
100	0.1292 (69)	1.212 (8)	0.1481 (56)	1.549 (12)	0.0060 (20)
85	0.1247 (32)	1.198 (13)	0.1479 (58)	1.546 (28)	0.0050 (10)
75	0.1179 (25)	1.190 (6)	0.1451 (47)	1.555 (7)	0.0045 (8)
65	0.1060 (34)	1.164 (1)	0.1400 (43)	1.553 (2)	0.0039 (1)
60	0.1023 (5)	1.144 (16)	0.1384 (41)	1.553 (18)	0.0037 (8)
55	0.0926 (56)	1.108 (50)	0.1369 (53)	1.532 (85)	0.0029 (13)
50	0.0864 (39)	1.091 (17)	0.1348 (33)	1.550 (27)	0.0021 (12)
45	0.0758 (14)	1.051 (30)	0.1328 (20)	1.548 (4)	0.0015 (6)
40	0.0572 (73)	0.979 (27)	0.1296 (72)	1.529 (38)	
35	0.0318 (42)	0.864 (68)	0.126 (11)	1.49 (11)	
30	0.0167 (94)	0.680 (70)	0.1104 (78)	1.43 (11)	

Precursor-Specific Relative PICSS

Table B.5: Precursor-specific relative PICSSs $\sigma_n[\text{X}^{m+}]$ for forming fragment ions following dissociative electron ionization of methanol, expressed relative to the cross section for forming CH_3OH^+ , as a function of electron energy E . The values in parenthesis indicate two standard deviations in the last figure.

E / eV	$\sigma_1[\text{H}^+]$	$\sigma_1[\text{H}_2^+]$	$\sigma_1[\text{H}_3^+]$	$\sigma_1[\text{C}^+]$	$\sigma_1[\text{CH}^+]$	$\sigma_1[\text{CH}_2^+]$
200	0.286 (9)	0.0066 (15)	0.000(3)	0.0349 (13)	0.0670 (13)	0.1143 (15)
175	0.299 (12)	0.0076 (8)	0.000(4)	0.0372 (26)	0.0710 (9)	0.1171 (18)
150	0.308 (11)	0.0077 (8)	0.000(3)	0.0392 (8)	0.0743 (11)	0.1213 (6)
125	0.317 (6)	0.0094 (17)	0.000(3)	0.0423 (10)	0.0799 (14)	0.1274 (25)
100	0.317 (11)	0.0108 (20)	0.000(3)	0.0445 (20)	0.0852 (22)	0.1345 (21)
85	0.308 (9)	0.0130 (11)	0.000(3)	0.0445 (11)	0.0888 (17)	0.1383 (36)
75	0.296 (8)	0.0149 (2)	0.000(3)	0.0436 (5)	0.0896 (14)	0.1429 (33)
65	0.280 (5)	0.0158 (5)	0.000(2)	0.0402 (9)	0.0867 (4)	0.1447 (13)
60	0.273 (4)	0.0167 (11)	0.000(1)	0.0379 (6)	0.0841 (11)	0.1459 (1)
55	0.253 (11)	0.0179 (10)	0.000(1)	0.0337 (14)	0.0774 (47)	0.1425 (57)

E / eV	$\sigma_1[\text{H}^+]$	$\sigma_1[\text{H}_2^+]$	$\sigma_1[\text{H}_3^+]$	$\sigma_1[\text{C}^+]$	$\sigma_1[\text{CH}^+]$	$\sigma_1[\text{CH}_2^+]$
50	0.240 (1)	0.0181 (7)	0.000(1)	0.0301 (5)	0.0713 (3)	0.1410 (4)
45	0.207 (6)	0.0169 (3)	0.000(1)	0.0237 (7)	0.0589 (18)	0.1323 (15)
40	0.157 (8)	0.0136 (14)	0.000(1)	0.0143 (11)	0.0386 (33)	0.1126 (52)
35	0.096 (4)	0.0077 (5)	0.000(1)	0.0055 (7)	0.0160 (19)	0.0805 (71)
30	0.046 (3)	0.0026 (3)	0.000(1)	0.0012 (1)	0.0038 (5)	0.0475 (60)

E / eV	$\sigma_1[\text{CH}_3^+]$	$\sigma_1[\text{O}^+]$	$\sigma_1[\text{OH}^+]$	$\sigma_1[\text{OH}_2^+]$	$\sigma_1[\text{CO}^+]$	$\sigma_1[\text{CHO}^+]$
200	0.646 (3)	0.0089 (6)	0.0167 (39)	0.0154 (71)	0.0769 (37)	1.008 (3)
175	0.644 (5)	0.0084 (21)	0.0180 (19)	0.0128 (66)	0.0810 (60)	1.010 (11)
150	0.644 (4)	0.0113 (7)	0.0205 (16)	0.0162 (25)	0.0858 (42)	1.013 (13)
125	0.646 (12)	0.0126 (37)	0.0235 (29)	0.019 (12)	0.0904 (34)	1.022 (10)
100	0.648 (8)	0.0136 (3)	0.0263 (8)	0.0152 (34)	0.0952 (71)	1.037 (12)
85	0.648 (7)	0.0146 (3)	0.0293 (6)	0.0143 (22)	0.0994 (25)	1.042 (12)
75	0.651 (3)	0.0131 (2)	0.0316 (14)	0.0148 (39)	0.0997 (30)	1.053 (2)
65	0.650 (2)	0.0116 (7)	0.0335 (14)	0.0156 (42)	0.0973 (30)	1.055 (4)
60	0.646 (7)	0.0104 (2)	0.0339 (19)	0.0151 (19)	0.0970 (7)	1.052 (15)
55	0.637 (29)	0.0085 (16)	0.0334 (10)	0.0151 (27)	0.0904 (56)	1.040 (45)
50	0.637 (8)	0.0062 (2)	0.0317 (13)	0.0156 (29)	0.0854 (39)	1.042 (17)
45	0.628 (6)	0.0041 (3)	0.0267 (16)	0.0149 (41)	0.0752 (14)	1.027 (30)
40	0.607 (11)	0.0025 (10)	0.0174 (22)	0.0146 (52)	0.0567 (71)	0.973 (26)
35	0.563 (26)	0.0015 (3)	0.0078 (12)	0.0106 (37)	0.0314 (42)	0.863 (68)
30	0.485 (29)	0.0012 (3)	0.0030 (4)	0.0083 (36)	0.0164 (90)	0.677 (70)

E / eV	$\sigma_1[\text{CH}_2\text{O}^+]$	$\sigma_1[\text{CH}_3\text{O}^+]$	$\sigma_2[\text{H}^+]$	$\sigma_2[\text{H}_2^+]$	$\sigma_2[\text{H}_3^+]$	$\sigma_2[\text{C}^+]$
200	0.1123 (33)	1.527 (8)	0.3259 (59)	0.0558 (14)	0.0142 (6)	0.0315 (11)
175	0.1149 (62)	1.526 (7)	0.3292 (67)	0.0572 (4)	0.0152 (6)	0.0304 (15)
150	0.120 (10)	1.522 (8)	0.3258 (29)	0.0585 (12)	0.0153 (7)	0.0286 (7)
125	0.1198 (33)	1.528 (6)	0.3116 (33)	0.0582 (25)	0.0150 (7)	0.0243 (8)
100	0.1187 (54)	1.531 (11)	0.2718 (45)	0.0560 (23)	0.0148 (7)	0.0160 (15)
85	0.1201 (50)	1.529 (28)	0.2249 (29)	0.0506 (11)	0.0135 (8)	0.0100 (11)
75	0.1200 (45)	1.540 (7)	0.1838 (23)	0.0445 (16)	0.0127 (10)	0.0057 (4)
65	0.1184 (46)	1.540 (2)	0.1296 (46)	0.0362 (1)	0.0105 (5)	0.0020 (2)
60	0.1199 (42)	1.541 (17)	0.1035 (10)	0.0316 (3)	0.0094 (10)	0.0011 (1)
55	0.1223 (49)	1.523 (85)	0.0710 (37)	0.0233 (7)	0.0079 (6)	0.0003 (1)
50	0.1241 (28)	1.543 (27)	0.0496 (8)	0.0174 (12)	0.0066 (6)	0.0002 (1)
45	0.1268 (18)	1.543 (4)	0.0243 (7)	0.0092 (6)	0.0042 (2)	0.0001 (1)
40	0.1279 (71)	1.527 (38)	0.0076 (19)	0.0025 (5)	0.0017 (2)	0.0000 (1)
35	0.125 (12)	1.49 (11)	0.0020 (1)	0.0005 (1)	0.0003 (1)	0.0000 (1)
30	0.1103 (78)	1.43 (11)	0.0010 (4)	0.0003 (1)	0.0001 (1)	0.0000 (1)

E / eV	$\sigma_2[\text{CH}^+]$	$\sigma_2[\text{CH}_2^+]$	$\sigma_2[\text{CH}_3^+]$	$\sigma_2[\text{O}^+]$	$\sigma_2[\text{OH}^+]$	$\sigma_2[\text{OH}_2^+]$
200	0.0392 (9)	0.0645 (16)	0.0560 (24)	0.0263 (13)	0.0827 (24)	0.0066 (8)
175	0.0395 (9)	0.0657 (5)	0.0581 (11)	0.0267 (2)	0.0837 (24)	0.0070 (7)
150	0.0393 (7)	0.0652 (15)	0.0582 (7)	0.0236 (8)	0.0844 (16)	0.0068 (3)
125	0.0371 (1)	0.0628 (24)	0.0586 (8)	0.0208 (1)	0.0840 (22)	0.0070 (7)
100	0.0299 (6)	0.0563 (17)	0.0543 (23)	0.0146 (7)	0.0772 (39)	0.0060 (5)
85	0.0221 (12)	0.0485 (13)	0.0482 (13)	0.0094 (12)	0.0678 (6)	0.0056 (5)
75	0.0153 (1)	0.0395 (20)	0.0417 (8)	0.0059 (3)	0.0575 (22)	0.0048 (5)
65	0.0072 (3)	0.0263 (6)	0.0319 (7)	0.0027 (3)	0.0423 (22)	0.0037 (2)
60	0.0043 (6)	0.0196 (16)	0.0262 (5)	0.0017 (3)	0.0335 (16)	0.0031 (5)
55	0.0018 (2)	0.0115 (14)	0.0183 (26)	0.0010 (2)	0.0225 (28)	0.0021 (1)
50	0.0008 (2)	0.0067 (6)	0.0126 (2)	0.0008 (1)	0.0147 (13)	0.0015 (1)
45	0.0003 (1)	0.0022 (4)	0.0061 (4)	0.0005 (1)	0.0065 (9)	0.0006 (1)
40	0.0001 (1)	0.0005 (1)	0.0019 (6)	0.0005 (4)	0.0017 (2)	0.0001 (1)
35	0.0001 (1)	0.0003 (1)	0.0007 (1)	0.0003 (1)	0.0007 (1)	0.0001 (1)
30	0.0000 (1)	0.0002 (1)	0.0005 (1)	0.0003 (1)	0.0004 (1)	0.0000 (1)

E / eV	$\sigma_2[\text{CO}^+]$	$\sigma_2[\text{CHO}^+]$	$\sigma_2[\text{CH}_2\text{O}^+]$	$\sigma_2[\text{CH}_3\text{O}^+]$
200	0.0457 (10)	0.1788 (41)	0.0291 (5)	0.0176 (5)
175	0.0462 (9)	0.1833 (43)	0.0293 (18)	0.0177 (10)
150	0.0457 (6)	0.1846 (5)	0.0307 (17)	0.0177 (4)
125	0.0433 (4)	0.1841 (27)	0.0310 (14)	0.0178 (7)
100	0.0340 (5)	0.1748 (39)	0.0303 (13)	0.0177 (11)
85	0.0252 (8)	0.1556 (11)	0.0278 (10)	0.0164 (5)
75	0.0182 (6)	0.1373 (36)	0.0252 (6)	0.0148 (5)
65	0.0087 (5)	0.1089 (30)	0.0216 (34)	0.0130 (2)
60	0.0053 (4)	0.0922 (20)	0.0185 (10)	0.0114 (7)
55	0.0021 (1)	0.0675 (48)	0.0146 (6)	0.0095 (4)
50	0.0009 (2)	0.0490 (5)	0.0107 (6)	0.0077 (12)
45	0.0006 (1)	0.0241 (10)	0.0060 (3)	0.0049 (3)
40	0.0005 (4)	0.0066 (11)	0.0018 (3)	0.0019 (4)
35	0.0004 (1)	0.0012 (4)	0.0002 (1)	0.0002 (2)
30	0.0003 (4)	0.0007 (2)	0.0001 (1)	0.0000 (1)

Total Ion Yield from Each Level of Ionization

Table B.6: Percentage contributions to the total ion yield from single and double ionization as a function of electron energy E , following electron ionization of methanol.

E (eV)	Single ionization (%)	Double ionization (%)
200	80	20
175	80	20
150	80	20
125	81	19
100	83	17
85	85	15
75	87	13
65	90	10
60	92	8
55	94	6
50	96	4
45	98	2
40	99	1
35	100	0
30	100	0

Trifluoroiodomethane, CF₃I

Relative PICSSs

Table B.7: Relative partial ionization cross-sections $\sigma_r[X^{m+}]$ for forming fragment ions following dissociative electron ionization of trifluoroiodomethane, expressed relative to the cross-section for forming CF₃I⁺, as a function of electron energy E . The values in parenthesis indicate two standard deviations in the last figure {those with an ^(a) indicate one standard deviation, due to the small value of these cross-sections}.

E / eV	$\sigma_r[C^+]$	$\sigma_r[F^+]$	$\sigma_r[CF^+]$	$10^2 \sigma_r[F_2^+]$ ^(a)	$\sigma_r[CF_2^+]$
200	0.2510(82)	0.3328(92)	0.401(18)	0.078(37)	0.230(5)
175	0.2390(112)	0.3067(116)	0.403(17)	0.050(3)	0.229(8)
150	0.2275(92)	0.2754(122)	0.406(12)	0.037(18)	0.230(2)
125	0.2021(46)	0.2242(54)	0.397(5)	0.059(30)	0.227(6)
100	0.1494(78)	0.1410(56)	0.357(10)	0.036(7)	0.215(3)
85	0.1084(80)	0.0883(38)	0.314(16)	0.037(8)	0.208(26)
75	0.0826(16)	0.0596(29)	0.283(9)	0.021(10)	0.196(23)
65	0.0562(11)	0.0346(14)	0.247(11)	0.019(8)	0.183(22)
60	0.0428(29)	0.0262(26)	0.226(11)	0.018(8)	0.173(22)
55	0.0318(38)	0.0192(12)	0.205(5)	0.026(23)	0.164(21)
50	0.0209(32)	0.0129(4)	0.175(2)	0.024(24)	0.152(19)
45	0.0123(24)	0.0054(76)	0.145(7)	0.003(5)	0.130(20)

E / eV	$\sigma_r[C^+]$	$\sigma_r[F^+]$	$\sigma_r[CF^+]$	$10^2 \sigma_r[F_2^+]$ ^(a)	$\sigma_r[CF_2^+]$
40	0.0041(42)	0.0034(2)	0.118(7)	0.002(5)	0.105(19)
35	-0.0002(31)	0.0006(20)	0.089(8)		0.086(17)
30	0.0001(10)	0.0003(1)	0.046(7)		0.068(12)

E / eV	$\sigma_r[CF_3^+]$	$\sigma_r[I^+]$	$\sigma_r[CI^+]$	$\sigma_r[FI^+]$	$10^2 \sigma_r[CFI^+]$ ^(a)
200	0.757(17)	1.936(23)	0.0233(8)	0.0158(16)	0.425(32)
175	0.754(30)	1.913(55)	0.0230(18)	0.0159(15)	0.393(36)
150	0.757(19)	1.914(3)	0.0252(19)	0.016(15)	0.390(49)
125	0.751(16)	1.873(11)	0.0258(24)	0.0156(14)	0.407(26)
100	0.739(15)	1.757(15)	0.0246(39)	0.0148(22)	0.352(166)
85	0.728(25)	1.634(10)	0.0222(22)	0.0141(8)	0.358(151)
75	0.719(19)	1.545(10)	0.0212(13)	0.0134(15)	0.352(14)
65	0.713(23)	1.450(10)	0.0200(26)	0.0136(10)	0.353(37)
60	0.706(19)	1.391(27)	0.0194(18)	0.0131(20)	0.353(49)
55	0.705(20)	1.346(16)	0.0192(21)	0.0132(31)	0.345(24)
50	0.695(13)	1.257(20)	0.0190(18)	0.0131(27)	0.326(390)
45	0.673(16)	1.149(13)	0.0167(28)	0.0120(22)	0.322(53)
40	0.636(32)	1.003(8)	0.0124(5)	0.0111(26)	0.313(22)
35	0.594(28)	0.824(21)	0.0058(11)	0.0090(13)	0.276(54)
30	0.570(7)	0.629(16)	0.0005(3)	0.0070(7)	0.204(12)

E / eV	$\sigma_r[CF_2I^+]$	$10^2 \sigma_r[C^{2+}]$ ^(a)	$10^2 \sigma_r[F^{2+}]$ ^(a)	$10^2 \sigma_r[CF^{2+}]$ ^(a)	$10^2 \sigma_r[CF_2^{2+}]$
200	0.5003(25)	0.055(1)	0.074(32)	0.086(12)	0.114(20)
175	0.4795(59)	0.035(7)	0.026(3)	0.080(13)	0.113(28)
150	0.4609(11)	0.023(5)	0.010(3)	0.071(11)	0.112(33)
125	0.4373(29)	0.012(1)	0.003(2)	0.060(15)	0.066(29)
100	0.4054(28)	0.006(2)	0.003(3)	0.038(13)	0.033(20)
85	0.3813(22)	0.000(1)		0.000(10)	0.032(18)
75	0.3647(14)	0.000(1)		0.004(9)	0.009(1)
65	0.3448(30)				
60	0.3335(49)				
55	0.3215(43)				
50	0.3028(39)				
45	0.2808(30)				
40	0.2537(14)				
35	0.2148(47)				
30	0.1657(42)				

E / eV	$\sigma_r[\text{I}^{2+}]$	$10^2 \sigma_r[\text{FI}^{2+}]^{(a)}$	$10^2 \sigma_r[\text{CFI}^{2+}]^{(a)}$	$10^2 \sigma_r[\text{CF}_2\text{I}^{2+}]^{(a)}$	$10^2 \sigma_r[\text{I}^{3+}]$
200	0.1190(3)	0.097(24)	0.055(42)	0.554(9)	0.043(8)
175	0.1091(15)	0.107(18)	0.044(6)	0.544(22)	0.031(10)
150	0.0991(17)	0.103(18)	0.049(14)	0.574(34)	
125	0.0821(8)	0.076(50)	0.040(20)	0.551(53)	
100	0.0492(14)	0.053(18)	0.029(7)	0.518(15)	
85	0.0271(5)	0.047(36)	0.032(22)	0.478(13)	
75	0.0167(37)	0.020(25)	0.035(13)	0.442(130)	
65	0.0059(5)	0.004(4)	0.026(3)	0.402(38)	
60	0.003(5)		0.026(9)	0.334(14)	
55	0.0016(6)		0.021(16)	0.292(26)	
50	0.0007(5)		0.013(10)	0.200(34)	
45	0.0000(1)			0.142(13)	
40				0.065(7)	
35				0.002(4)	
30					

Precursor-Specific Relative PICSS

Table B.8: Precursor-specific relative PICSSs $\sigma_n[X^+]$ for forming monocation fragment ions following dissociative electron ionization of CF_3I , expressed relative to the cross section for forming CF_3I^+ , as a function of electron energy E . The values in parenthesis indicate two standard deviations in the last figure {those with an ^(a) indicate one standard deviation, due to the small value of these cross-sections}.

E / eV	$\sigma_1[\text{C}^+]$	$\sigma_2[\text{C}^+]$	$\sigma_3[\text{C}^+]$	$10^2 \sigma_4[\text{C}^+]^{(a)}$	$\sigma_1[\text{F}^+]$	$\sigma_2[\text{F}^+]$
200	0.0200(52)	0.1330(61)	0.0930(64)	0.509(15)	0.0062(20)	0.1216(133)
175	0.0204(57)	0.1378(156)	0.0776(76)	0.318(37)	0.0063(14)	0.1293(50)
150	0.0200(40)	0.1487(99)	0.0579(25)	0.095(13)	0.0047(33)	0.1518(128)
125	0.0241(28)	0.1409(28)	0.0369(33)	0.014(5)	0.0094(55)	0.1452(51)
100	0.0303(31)	0.1111(76)	0.0080(13)	0.000(1)	0.0178(28)	0.1044(61)
85	0.0361(83)	0.0716(35)	0.0007(2)		0.0231(26)	0.0609(29)
75	0.0367(12)	0.0458(20)	0.0001(1)		0.0241(20)	0.0342(15)
65	0.0348(7)	0.0214(14)	0.0000(1)		0.0219(14)	0.0124(7)
60	0.0318(19)	0.0110(30)	0.0000(1)		0.0198(7)	0.0062(20)
55	0.0278(30)	0.0041(8)			0.0165(12)	0.0027(3)
50	0.0201(28)	0.0008(4)			0.0118(8)	0.0010(6)
45	0.0120(25)	0.0003(1)			0.0049(78)	0.0005(3)
40	0.0039(42)	0.0002(2)			0.0030(2)	0.0004(4)
35	-0.0004(32)	0.0002(1)			0.0004(19)	0.0002(2)
30	-0.0001(10)	0.0002(1)			0.0001(1)	0.0002(1)

E / eV	$\sigma_3[F^+]$	$10^2 \sigma_4[F^+]^{(a)}$	$\sigma_1[CF^+]$	$\sigma_2[CF^+]$	$\sigma_3[CF^+]$	$10^2 \sigma_4[CF^+]^{(a)}$
200	0.1930(195)	0.0120(6)	0.112(32)	0.2377(485)	0.0493(35)	0.231(19)
175	0.1638(62)	0.0073(10)	0.104(10)	0.2493(83)	0.0480(16)	0.153(12)
150	0.1162(73)	0.0026(3)	0.109(10)	0.2504(34)	0.0457(33)	0.091(19)
125	0.0691(52)	0.0006(2)	0.113(6)	0.2476(6)	0.0364(15)	0.017(6)
100	0.0188(20)	0.0000(1)	0.126(7)	0.2155(72)	0.0159(12)	0.000(1)
85	0.0042(8)		0.135(13)	0.1737(40)	0.0045(4)	
75	0.0013(4)		0.139(12)	0.1430(33)	0.0009(4)	
65	0.0004(2)		0.141(12)	0.1054(30)	0.0001(1)	
60	0.0002(2)		0.143(10)	0.0832(59)	0.0000(1)	
55	0.0000(2)		0.144(8)	0.0603(39)		
50			0.144(6)	0.0304(36)		
45			0.135(6)	0.0102(16)		
40			0.116(7)	0.0020(5)		
35			0.089(8)	0.0004(4)		
30			0.046(7)	0.0008(2)		

E / eV	$10^2 \sigma_1[F_2^+]^{(a)}$	$10^2 \sigma_2[F_2^+]^{(a)}$	$\sigma_1[CF_2^+]$	$\sigma_2[CF_2^+]$	$\sigma_3[CF_2^+]$	$10^2 \sigma_4[CF_2^+]^{(a)}$
200	0.026(31)	0.053(6)	0.101(4)	0.1183(16)	0.0097(6)	0.032(5)
175	-0.001(3)	0.051(3)	0.101(6)	0.1183(12)	0.0102(4)	0.030(6)
150	-0.016(17)	0.053(7)	0.101(3)	0.1193(17)	0.0098(7)	0.012(5)
125	0.009(33)	0.050(12)	0.098(6)	0.1200(11)	0.0087(2)	0.004(4)
100	-0.004(3)	0.040(4)	0.097(4)	0.1127(10)	0.0050(5)	
85	0.017(19)	0.020(13)	0.105(27)	0.1012(29)	0.0023(2)	
75	0.016(14)	0.005(9)	0.102(25)	0.0927(22)	0.0009(2)	
65	0.015(11)	0.003(5)	0.102(21)	0.0801(25)	0.0001(1)	
60	0.017(7)	0.001(2)	0.101(22)	0.0716(16)		
55	0.027(24)		0.102(22)	0.0620(19)		
50	0.024(25)		0.107(21)	0.0451(20)		
45	0.003(5)		0.103(20)	0.0264(22)		
40	0.002(5)		0.097(20)	0.0084(11)		
35			0.085(17)	0.0012(4)		
30			0.067(12)	0.0008(1)		

E / eV	$\sigma_1[CF_3^+]$	$\sigma_2[CF_3^+]$	$10^2 \sigma_3[CF_3^+]$	$\sigma_1[I^+]$	$\sigma_2[I^+]$	$\sigma_3[I^+]$
200	0.643(15)	0.1068(17)	0.773(13)	1.169(35)	0.647(44)	0.1196(129)
175	0.637(28)	0.1098(32)	0.787(34)	1.142(42)	0.665(17)	0.1054(71)
150	0.635(19)	0.1138(7)	0.796(19)	1.151(5)	0.681(6)	0.0818(40)
125	0.625(15)	0.1184(26)	0.760(37)	1.143(9)	0.679(2)	0.0514(33)

E / eV	$\sigma_1[\text{CF}_3^+]$	$\sigma_2[\text{CF}_3^+]$	$10^2 \sigma_3[\text{CF}_3^+]$	$\sigma_1[\text{I}^+]$	$\sigma_2[\text{I}^+]$	$\sigma_3[\text{I}^+]$
100	0.618(16)	0.1162(25)	0.466(25)	1.150(9)	0.592(15)	0.0152(17)
85	0.617(26)	0.1087(19)	0.237(12)	1.153(5)	0.478(11)	0.0033(6)
75	0.615(21)	0.1038(32)	0.108(5)	1.147(4)	0.397(12)	0.0008(1)
65	0.613(23)	0.0999(30)	0.023(3)	1.140(16)	0.309(7)	0.0002(1)
60	0.609(20)	0.0973(13)	0.005(3)	1.127(24)	0.264(10)	0.0001(1)
55	0.612(19)	0.0926(28)	0.002(2)	1.127(11)	0.219(7)	
50	0.615(10)	0.0796(34)	0.001(1)	1.102(13)	0.156(8)	
45	0.611(14)	0.0615(36)		1.050(10)	0.098(7)	
40	0.599(33)	0.0374(29)		0.955(9)	0.048(4)	
35	0.583(27)	0.0111(18)		0.811(20)	0.013(2)	
30	0.568(7)	0.0019(8)		0.626(16)	0.004(1)	

E / eV	$10^2 \sigma_4[\text{I}^+]^{(a)}$	$\sigma_1[\text{Cl}^+]$	$10^2 \sigma_2[\text{Cl}^+]^{(a)}$	$10^2 \sigma_3[\text{Cl}^+]^{(a)}$	$\sigma_1[\text{FI}^+]$	$10^2 \sigma_2[\text{FI}^+]^{(a)}$
200	0.031(4)	0.0149(11)	0.763(14)	0.077(10)	0.0140(15)	0.183(7)
175	0.009(5)	0.0146(19)	0.760(36)	0.081(15)	0.0142(12)	0.177(13)
150	0.002(4)	0.0167(22)	0.810(50)	0.041(29)	0.0141(15)	0.186(8)
125		0.0179(28)	0.751(37)	0.041(13)	0.0137(14)	0.187(11)
100		0.0186(40)	0.589(10)	0.010(5)	0.0131(21)	0.163(8)
85		0.0181(23)	0.406(10)	0.002(3)	0.0128(6)	0.128(8)
75		0.0185(12)	0.271(10)	0.001(2)	0.0123(15)	0.111(6)
65		0.019(14)	0.094(11)	0.001(1)	0.0128(8)	0.079(12)
60		0.0191(17)	0.031(8)		0.0123(20)	0.078(8)
55		0.0191(21)	0.008(3)		0.0125(31)	0.062(9)
50		0.0190(18)	0.003(2)		0.0126(27)	0.050(6)
45		0.0166(28)	0.001(1)		0.0118(21)	0.029(3)
40		0.0124(5)			0.0110(27)	0.009(4)
35		0.0058(11)			0.0090(13)	0.001(1)
30		0.0005(3)			0.0070(7)	0.000(1)

E / eV	$10^2 \sigma_2[\text{CFI}^+]^{(a)}$	$10^2 \sigma_1[\text{CFI}^+]^{(a)}$	$10^2 \sigma_2[\text{CFI}^+]^{(a)}$	$\sigma_1[\text{CF}_2\text{I}^+]$	$10^2 \sigma_2[\text{CF}_2\text{I}^+]^{(a)}$
200	0.183(7)	0.401(19)	0.024(4)	0.5002(24)	0.009(10)
175	0.177(13)	0.366(23)	0.027(7)	0.4794(60)	0.007(2)
150	0.186(8)	0.360(23)	0.029(3)	0.4608(11)	0.010(5)
125	0.187(11)	0.379(15)	0.027(4)	0.4372(29)	0.011(5)
100	0.163(8)	0.333(83)	0.019(1)	0.4053(28)	0.005(4)
85	0.128(8)	0.343(73)	0.015(3)	0.3812(21)	0.005(3)
75	0.111(6)	0.340(9)	0.012(4)	0.3646(14)	0.008(3)
65	0.079(12)	0.346(18)	0.008(1)	0.3448(30)	0.001(2)

E / eV	$10^2 \sigma_2[\text{CFI}^+]^{(a)}$	$10^2 \sigma_1[\text{CFI}^+]^{(a)}$	$10^2 \sigma_2[\text{CFI}^+]^{(a)}$	$\sigma_1[\text{CF}_2\text{I}^+]$	$10^2 \sigma_2[\text{CF}_2\text{I}^+]^{(a)}$
60	0.078(8)	0.347(23)	0.006(1)	0.3334(49)	0.003(5)
55	0.062(9)	0.342(12)	0.003(1)	0.3214(43)	0.002(2)
50	0.050(6)	0.325(20)	0.001(1)	0.3028(39)	0.002(1)
45	0.029(3)	0.322(27)		0.2808(30)	0.001(1)
40	0.009(4)	0.313(11)		0.2537(14)	0.001(1)
35	0.001(1)	0.276(27)		0.2148(47)	
30	0.000(1)	0.204(6)		0.1657(42)	

Table B.9: Precursor-specific relative PICSS $\sigma_n[X^{m+}]$ for forming multiply charged fragment ions following dissociative electron ionization of CF_3I , expressed relative to the cross section for forming CF_3I^+ , as a function of electron energy E . The values in parenthesis indicate two standard deviations in the last figure {those with an ^(a) indicate one standard deviation, due to the small value of these cross-sections}.

E / eV	$10^2 \sigma_2[\text{C}^{2+}]$	$10^2 \sigma_3[\text{C}^{2+}]$	$10^2 \sigma_4[\text{C}^{2+}]$	$10^2 \sigma_2[\text{F}^{2+}]$	$10^2 \sigma_3[\text{F}^{2+}]$
200	0.002(2)	0.033(5)	0.021(4)	0.017(35)	0.033(12)
175	0.001(2)	0.024(8)	0.010(1)	-0.003(6)	0.023(9)
150	0.006(8)	0.015(5)	0.002(2)	0.000(2)	0.010(1)
125	0.005(4)	0.007(3)		0.002(2)	0.001(1)
100	0.005(2)	0.001(1)		0.003(3)	0.000(1)
85	0.000(1)				
75	0.000(1)				
65					
60					
55					

E / eV	$10^2 \sigma_4[\text{F}^{2+}]$	$10^2 \sigma_2[\text{CF}^{2+}]$	$10^2 \sigma_3[\text{CF}^{2+}]$	$10^2 \sigma_4[\text{CF}^{2+}]$	$10^2 \sigma_2[\text{CF}_2^{2+}]$
200	0.024(4)	-	0.072(10)	0.013(2)	-0.018(30)
175	0.007(5)	-	0.071(12)	0.010(4)	0.000(18)
150	0.001(2)	-	0.066(10)	0.005(2)	0.007(33)
125		-	0.057(14)	0.003(1)	-0.019(27)
100		-	0.037(13)	0.001(1)	-0.013(18)
85		-	0.000(1)	0.000(1)	0.003(23)
75		-	0.004(8)		-0.001(3)
65					
60					
55					

E / eV	$10^2 \sigma_3[\text{CF}_2^{2+}]$	$10^2 \sigma_4[\text{CF}_2^{2+}]$	$\sigma_2[\text{I}^{2+}]^{(a)}$	$\sigma_3[\text{I}^{2+}]^{(a)}$	$\sigma_4[\text{I}^{2+}]^{(a)}$
200	0.099(8)	0.033(3)	0.0216(5)	0.0873(10)	0.0101(39)
175	0.091(5)	0.021(1)	0.0251(29)	0.0776(26)	0.0064(73)
150	0.090(3)	0.015(3)	0.0280(13)	0.0685(41)	0.0025(17)
125	0.080(7)	0.006(1)	0.0297(8)	0.0518(22)	0.005(12)
100	0.045(8)	0.001(1)	0.0280(16)	0.0212(18)	0.000(1)
85	0.023(5)	0.005(10)	0.0197(10)	0.0074(6)	0.000(1)
75	0.009(2)		0.0142(73)	0.0026(4)	
65			0.0055(10)	0.0004(1)	
60			0.0029(9)	0.0001(1)	
55			0.0015(11)	0.0001(1)	
50			0.0006(10)		
45			0.0001(1)		
40					
35					
30					

E / eV	$10^2 \sigma_2[\text{FI}^{2+}]$	$10^2 \sigma_3[\text{FI}^{2+}]$	$10^2 \sigma_3[\text{I}^{3+}]$	$10^2 \sigma_4[\text{I}^{3+}]$
200	0.036(28)	0.061(6)	0.000(4)	0.043(7)
175	0.046(24)	0.061(8)	0.007(12)	0.025(3)
150	0.047(22)	0.056(6)		
125	0.041(42)	0.034(14)		
100	0.041(15)	0.013(3)		
85	0.04(27)	0.007(9)		
75	0.018(23)	0.002(3)		
65	0.004(4)			
60				
55				
50				

Total Ion Yield from Each Level of Ionization

Table B.10: Percentage contributions to the total ion yield from single, double, triple and quadruple ionization as a function of electron energy E , following electron ionization of trifluoroiodomethane.

E (eV)	Single Ionization (%)	Double Ionization (%)	Triple Ionization (%)	Quadruple Ionization (%)
200	56.4	30.6	12.3	0.7
175	56.2	32.4	11.0	0.4
150	56.9	34.1	8.8	0.2

E (eV)	Single Ionization (%)	Double Ionization (%)	Triple Ionization (%)	Quadruple Ionization (%)
125	58.5	35.2	6.2	0.1
100	64.2	33.5	2.3	0.0
85	70.3	29.0	0.7	0.0
75	74.4	25.4	0.2	0.0
65	79.1	20.8	0.1	0.0
60	81.7	18.3	0.0	0.0
55	84.3	15.7	0.0	0.0
50	88.2	11.8	0.0	0.0
45	91.9	8.1	0.0	0.0
40	95.5	4.5	0.0	0.0
35	98.6	1.4	0.0	0.0
30	99.5	0.5	0.0	0.0

Appendix C

Relative Ion Yield Equations

As discussed in Chapter 7, following photoionization of CF_3I , only fragment ions formed in coincidence with a threshold (< 800 meV) electron are detected. This experimental setup means that the recorded ion intensities favour ions formed from double ionisation events, or single ionization events in which the ion formed has a large degree of internal energy, and/or resulted from a large degree of fragmentation of the parent ion, as only in these events is it possible to form a threshold electron. Thus, as not all ions are being detected with equal efficiency, ‘true’ ionization cross-sections cannot be derived from the ion intensities recorded. Thus, in this Chapter 7, relative ion yields $RIY[X^{m+}]$ and precursor-specific relative ion yields $RIY_n[X^{m+}]$ are presented, for the formation of fragment ions, relative to the ion yield for forming CF_3I^+ . The relative ion yields (RIYs) are derived from same set of equations from which relative PICSSs are derived, in Section 3.3. The equations for $RIY[X^{m+}]$ and $RIY_n[X^{m+}]$ are presented below.

Relative Ion Yields $RIY[X^{m+}]$

$$RIY[X^+] = \frac{I_1[X^+] + P_2[X^+] + P_3[X^+]}{I_1[\text{Parent}^+]} \quad (\text{C.1})$$

$$RIY[X^{2+}] = \frac{I_2[X^{2+}] + P_3[X^{2+}]}{I_1[\text{Parent}^+]} \quad (\text{C.2})$$

Precursor-Specific Relative Ion Yields $RIY_n[X^+]$ for Forming Monocations

$$RIY_1[X^+] = \frac{I_1[X^+] - \left(\frac{1-f_1}{f_f}\right)(P_2[X^+] + P_3[X^+])}{I_1[\text{Parent}^+]} \quad (\text{C.3})$$

$$RIY_2[X^+] = \frac{P_2[X^+]}{f_i I_1[\text{Parent}^+]} \quad (\text{C.4})$$

$$RIY_3[X^+] = \frac{P_3[X^+]}{f_i I_1[Parent^+]} \quad (C.5)$$

**Precursor-Specific Relative Ion Yields $RIY_n[X^{2+}]$ for Forming
Dications**

$$RIY_2[X^{2+}] = \frac{I_2[X^{2+}] - \left(\frac{1-f_1}{f_f}\right) P_3[X^{2+}]}{I_1[Parent^+]} \quad (C.6)$$

$$RIY_3[X^{2+}] = \frac{P_3[X^{2+}]}{f_i I_1[Parent^+]} \quad (C.7)$$

Appendix D

Relative Ion Yield Data

Trifluoroiodomethane, CF₃I

RIYs

Table D.1: Relative ion yields $RIY[X^{m+}]$ for forming fragment ions following dissociative photoionization of trifluoroiodomethane, expressed relative to the ion yield for forming CF₃I⁺, as a function of photon energy E .

$h\nu/eV$	$RIY[C^+]$	$RIY[F^+]$	$RIY[CF^+]$	$RIY[CF_2^+]$	$RIY[CF_3^+]$	$RIY[I^+]$	$RIY[CI^+]$
37	27.81	25.33	37.42	31.06	35.43	144.47	3.27
34	10.63	7.58	23.10	15.08	29.07	90.25	4.17
31	1.37	1.22	11.48	10.53	14.50	59.27	2.82
28		0.18	0.84	8.25	0.04	36.95	0.50

$h\nu/eV$	$RIY[FI^+]$	$RIY[CFI^+]$	$RIY[CF_2I^+]$	$RIY[I^{2+}]$	$RIY[FI^{2+}]$	$RIY[CFI^{2+}]$	$RIY[CF_2I^{2+}]$
37	0.96	0.17	14.44	49.95	0.39	0.15	2.20
34	0.60	0.14	19.43	11.92	0.10	0.02	1.72
31	0.63	0.19	19.13	0.69	0.03		0.05
28	0.43	0.16	13.63	3.54			

Precursor-Specific RIYs

Table D.2: Precursor-specific relative ion yields $RIY_n[X^{m+}]$ for forming fragment ions following dissociative photoionization of trifluoroiodomethane, expressed relative to the ion yield for forming CF₃I⁺, as a function of photon energy E .

$h\nu/eV$	$RIY_1[C^+]$	$RIY_2[C^+]$	$RIY_3[C^+]$	$RIY_1[F^+]$	$RIY_2[F^+]$	$RIY_3[F^+]$
37	10.59	16.18	1.04	8.62	16.98	-0.26
34	7.18	3.32	0.13	4.18	3.32	0.09
31	0.34	0.99	0.05	0.21	0.97	0.03
28				-0.88	1.02	0.03

$h\nu / eV$	$RIY_1[CF^+]$	$RIY_2[CF^+]$	$RIY_3[CF^+]$	$RIY_1[CF_2^+]$	$RIY_2[CF_2^+]$	$RIY_3[CF_2^+]$
37	3.78	29.95	3.69	3.86	24.88	2.32
34	16.57	6.44	0.09	10.75	4.24	0.08
31	12.69	-1.33	0.13	10.63	-0.15	0.05
28	2.23	-1.52	0.12	8.19	-0.02	0.08

$h\nu / eV$	$RIY_1[CF_3^+]$	$RIY_2[CF_3^+]$	$RIY_3[CF_3^+]$	$RIY_1[I^+]$	$RIY_2[I^+]$	$RIY_3[I^+]$
37	-6.05	25.41	16.07	40.51	103.97	1.79
34	15.97	12.35	0.75	61.78	28.47	4.03
31	7.67	6.68	0.15	52.76	6.51	2.74
28	0.02	-0.14	0.16	38.27	-1.31	0.44

$h\nu / eV$	$RIY_2[CF_2I^+]$	$RIY_1[CF_2I^+]$	$RIY_2[CF_2I^+]$	$RIY_2[I^{2+}]$	$RIY_3[I^{2+}]$
37	1.48	14.55	-0.11	27.1	22.86
34	0.14	19.39	0.04	10.77	1.15
31	0.08	18.97	0.16	0.28	0.41
28	0.06	13.41	0.22	3.14	0.40

Total Ion Yield from Each Level of Ionization

Table D.3: Percentage contributions to the total ion yield from single, double and triple ionization as a function of photon energy E , following electron ionization of trifluoriodomethane.

$h\nu / eV$	Single Ionization (%)	Double Ionization (%)	Triple Ionization (%)
37	21.1	66.6	12.3
34	65.8	33.2	1.1
31	87.6	11.7	0.7
28	96.5	2.2	1.2

